Distributed Sensing and Observer Design for Vehicles State Estimation

by

Hamidreza Bolandhemmat

A thesis
presented to the University of Waterloo
in fulfillment of the
thesis requirement for the degree of
Doctor of Philosophy
in
Mechanical Engineering

Waterloo, Ontario, Canada, 2009

AUTHOR'S DECLARATION

I hereby declare that I am the sole author of this thesis. This is a true copy of this thesis, including any required final revisions, as accepted by my examiners.

I understand that my thesis may be made electronically available to the public.

Hamidreza Bolandhemmat

Abstract

A solution to the vehicle state estimation problem is given using the Kalman filtering and the Particle filtering theories. Vehicle states are necessary for an active or a semi-active suspension control system, which is intended to enhance ride comfort, road handling and stability of the vehicle. Due to a lack of information on road disturbances, conventional estimation techniques fail to provide accurate estimates of all the required states. The proposed estimation algorithm, named Supervisory Kalman Filter (SKF), consists of a Kalman filter with an extra update step which is inspired by the particle filtering technique. The extra step, called a supervisory layer, operates on the portion of the state vector that cannot be estimated by the Kalman filter. First, it produces N randomly generated state vectors, the particles, which are distributed based on the Kalman filter's last updated estimate. Then, a resampling stage is implemented to collect the particles with higher probability. The effectiveness of the SKF is demonstrated by comparing its estimation results with that of the Kalman filter and the particle filter when a test vehicle is passing over a bump. The estimation results confirm that the SKF precisely estimates those states of the vehicle that cannot be estimated by either the Kalman filter or the particle filter, without any direct measurement of the road disturbance inputs.

Once the vehicle states are provided, a suspension control law, the Skyhook strategy, processes the current states and adjusts the damping forces accordingly to provide a better and safer ride for the vehicle passengers. This thesis presents a novel systematic and practical methodology for the design and implementation of the Skyhook control strategy for vehicle's semi-active suspension systems. Typically, the semi-active control strategies (including the Skyhook strategy) have switching natures. This makes the design process difficult and highly dependent on extensive trial and error. The proposed methodology maps the discontinuous control system model to a continuous linear region, where all the time/frequency design techniques, established in the conventional control system theory, can be applied. If the semi-active control law is designed to satisfy ride and stability requirements, an inverse mapping offers the ultimate control law. The effectiveness of the proposed methodology in the design of a semi-active suspension control system for a Cadillac SRX 2005 is demonstrated by real-time road tests. The road tests results verify that the use of the newly developed systematic design methodology reduces the required time and effort in real industrial problems.

Acknowledgements

I am extremely grateful to my supervisors, Professor Farid Golnaraghi and Professor Christopher M. Clark, for their support and guidance, and to my committee for their helpful comments and suggestions. I would like to thank Professor William J. Wilson and Professor William Melek for their valuable counsel whenever I asked for it. I am also deeply indebted to my previous advisors, Professor Mohammad-Ali Massoumnia, Professor Arya Alasty, Professor Mohammad-Bagher Malaek, and Professor Nasser Sadati, whose teachings have always illuminated my path.

I wish to thank the Phoenix research team at the University of Waterloo who contributed support and assistance in this study. I would also like to thank my friends, Yosuf Ganji, Mohammad Navidpour, Babak Ebrahimi, Nasser Lashgarian, Navid Dadkhah, Keith Leung, Daryoosh Saeedkia, Alireza Bayesteh, Orang Vahid, Siamak Arzanpour, Mohammad Biglarbegian, Fariborz Rahimi, and Brian Koiter for all their help and support.

In addition, the financial support provided by Mechworks Systems Inc. and Ontario Centres of Excellence (OCE), is appreciated. Last but not certainly least, my greatest appreciation to my wife, Minoo, and to my parents for their constant and unconditional love, support, and encouragement.

Dedication

To my beloved wife, Minoo, for her immeasurable support, encouragement, and patience.

Table of Contents

List of Figures

List of Tables

Terms and Definitions

Sprung mass: Mass of all the components supported by the spring (vehicle body)

Unsprung mass: Mass of all the components below or not supported by the spring (wheels)

LF: Front Left suspension system or wheel

LR: Rear Left suspension system or wheel

RF: Front Right suspension system or wheel

RR: Rear Right suspension system or wheel

Nomenclature

I_{xx}	Vehicle body moment of inertia about its longitudinal axis
I_{yy}	Vehicle body moment of inertia about its lateral axis
a	Half of the distance within two suspension system along the x axis
b	Half of the distance within two suspension system along the y axis
h_{CG}	Height of each corner of the car body above the CG along the z direction
m	Mass of the car body
m_{wF}	Mass of the front wheels
m_{wR}	Mass of the rear wheels
c_{LF}	Average damping coefficient of the left front suspension system
c_{LR}	Average damping coefficient of the left rear suspension system
c_{RF}	Average damping coefficient of the right front suspension system
c_{RR}	Average damping coefficient of the right rear suspension system
k_{sF}	Spring coefficient of the front suspension systems
k_{sR}	Spring coefficient of the rear suspension systems
k_{wF}	Front tire spring coefficient
k_{wR}	Rear tire spring coefficient
x_k	State vector at $t = t_k$
$\hat{x}_k(+)$	Updated estimate of the dynamical system state vector at $t = t_k$
$\hat{x}_k(-)$	Predicted estimate of the dynamical system state vector at $t = t_k$
$P_k(+)$	Updated estimation error covariance matrix at $t = t_k$
$P_k(-)$	Predicted estimation error covariance matrix at $t = t_k$
β_{SF}	Bandwidth of the shape filter
$\frac{\alpha_{SF}}{\beta_{SF}}$	DC value of the shape filter
c_s	Variable damping coefficient of a semi-active damper

1 Introduction and Background

In the previous generations of vehicles, the suspension systems were designed and manufactured from materials with fixed properties. Such systems, however, do not provide an optimal comfort ride or an acceptable stability under all circumstances.

For several decades, active and semi-active suspension systems have been developed to improve the ride comfort, road handling and stability[1] of terrain vehicles. Ride comfort is proportional to the absolute acceleration of the vehicle body or the acceleration of the vehicle's Centre of Gravity (CG). A measure of the ride comfort is given by the ratio of the maximum value of the transmitted acceleration to the CG to the maximum value of the excitation acceleration from the road. This ratio, which describes the acceleration level felt by the passengers, is known as the acceleration transmissibility (or the transmissibility ratio) of the vehicle's suspension system. The mathematical formulations, regarding 1 and 2 Degrees Of Freedom (DOF) car models, are given in Appendix A. Road handling is related to the traction between the vehicle's wheels and the road surface, and hence is related to the tires' deflection. Also, the stability of a vehicle is related to the tires' ground contact.

Active suspension systems include powered actuators – in most cases, hydraulic actuators – that are designed to actively control the acceleration and relative motion of vehicle's body. Different control schemes have been proposed by researchers for active suspension mechanisms. In [1] to [4], the active suspension system design is studied from an optimal control theory point-of-view. The Linear-Quadratic Regulator (LQR) approach is applied and it is shown that the ride comfort and road handling of a vehicle are concurrently improved. Yu and Crolla [5] have developed the Linear-Quadratic-Gaussian (LQG) technique that controls an active suspension system by tuning the weighting parameters of the LQG cost function, based on different road conditions. In addition, Fuzzy logic control has also been adopted by Son and Isik [7] and adaptive control technique has been developed by Esmailzadeh and Bateni [8]. Although active systems exhibit many advantages, vehicle manufacturers are distancing themselves from such technologies due to the high costs, the complexity level, and failure mode safety. Active suspension systems are still popular for off-road, high-duty terrain vehicles and fast heavy trains [9].

[1] These factors are referred to as the vehicle's Suspension system Performance Index, or SPI.

Secondly, semi-active suspension systems are also referred to as adaptive-passive systems in some contexts where the characteristics of the system damper or spring can be controlled by supplying a command signal. The command signal can either vary the oil flow rate between the compression chamber and the reverse chamber (i.e., dampers with solenoid valves), or change the properties of the material inside the shock (i.e., dampers with Magneto-Rheological (MR) fluid, known as MR dampers) to provide various levels of resisting forces. One of the key advantages of semi-active suspension systems is their low energy consumption and their vibration control performance that is similar to that of the active systems. Another advantage of semi-active suspension systems is that they are fail-safe; that is, if the system fails for any reason, there is still a functional passive damper. These characteristics make semi-active devices attractive for a wide range of applications, including terrain vehicle suspensions. Specifically, MR dampers are noted for their fairly quick response, longer life, and low energy consumption (compare to their active counterparts).

Due to these features, many techniques have been adopted for the design and control of semi-active suspension systems. Karnopp et al. ([10], [11]) have proposed the Skyhook control strategy to suppress excessive motions of the sprung mass of a simplified vehicle model. They inserted a fictitious damper, called a Skyhook damper, between the sprung mass and the stationary sky to reduce the vehicle's body motions. However, the wheel-hub vibration is neglected. As a result, the technique cannot significantly attenuate the resonant peak that corresponds to the unsprung mass, offering less improvement in the handling performance of the vehicle [12]. To overcome the disadvantage of the original Skyhook concept, Novak et al. [13] added another fictitious damper between the unsprung mass and the ground to increase the traction between the vehicle tire and the pavement to enhance the handling characteristics of the vehicle. Both the original Skyhook strategy and its modified version, the Skyhook-Groundhook control, are effective in terms of the simplicity of the control algorithm [14]. Their other advantage is that they do not require any a priori knowledge of the vehicle's dynamics; that is, they are not model-based.

Cheok et al. [15] used the LQR method to control the semi-active suspensions. The cost function, to be minimized, was a function of the difference between the control damping force and the ideal Skyhook damping force. The sliding mode control has also been capable of controlling the MR semi-active suspension [16], [17] and [18]. Liao et al. [19] and Kim et al.

[20] have employed the LQG method to reduce the excessive vibration of a vehicle and a train body, respectively. The application of the RMS technique in semi-active suspension control has been demonstrated in [21]. Rakheja et al. [22] have utilized the relative semi-active suspension deflection and velocity to adjust the damper force. In [23], Manus et al. have successfully implemented the proposed control law in [22] to attenuate the vibration of a suspension seat. The Fuzzy logic theory has been also adopted to control the vibration of semi-active suspension systems in [24] and [25]. Among the recent research on semi-active suspensions, the works conducted by Ahmadian et al. [26] and Savaresi et al. [27] are notable. In a conventional Skyhook controller, when the relative velocity is zero, a sharp increase in the damping force is created, resulting in a jump in the sprung mass acceleration. In the first paper [26], a method to reduce the jerk is presented. In the second paper, a new simple technique, the Acceleration-Driven-Damper (ADD), is presented to minimize the vertical acceleration of the vehicle body [27].

Although active and semi-active damper technologies offer new opportunities to improve ride comfort, road handling and stability for terrain vehicles, the primary challenge of providing required control system feedback remains. The control techniques require suspension system/vehicle states to determine the control signal. Frequently-used state variables include the absolute vertical velocity and acceleration of the vehicle body (sprung mass) at each corner (shock ends), the absolute velocity and acceleration of the wheel-hubs (unsprung masses), shock deflection, its rate, and the vehicle's center of gravity kinematics, vehicle body attitude angles and the rate of change of the angles, and tire deflections.

Of these, the accelerations, angular velocities, and suspension deflections are measured by mounting the appropriate sensors – namely, an accelerometer, a gyroscope and a displacement sensor, respectively, in the correct locations. The absolute velocity cannot be measured directly because the velocity sensors must have a stationary reference space, which is not applicable in automotive applications. A common technique to obtain the velocity information is to integrate signals from accelerometers attached to the ends of each shock. However, the performance of low-cost automotive grade accelerometers is limited by a high noise level (typically, 50-1000 $\mu g / \sqrt{Hz}$), especially a high rate drift, which makes this extremely challenging in the real world. Furthermore, for some of these states, such as tire deflection or the height of the vehicle CG, no straight-forward measurement tool can be found.

Even if the measurement of all the states, required by a particular controller (i.e., the Skyhook or the modified Skyhook methods) is practical and possible, a high number of fairly accurate sensors equipped with a sophisticated signal processing and conditioning circuitry needs to be deployed. The result is increased costs and decreased integration activities. To reduce these effects, an estimator can be used to produce an accurate estimation of the required states.

To estimate the states of a semi-active suspension system model, a modified Luenberger observer was adopted in [29] and [30]. In [31] and [32], the LQG and LQR techniques, respectively, have been implemented to simultaneously observe and control the states of the active suspension system of a half car model. Despite the proven efficiency of the designed estimators by computer simulations, the authors have employed an incomplete vehicle model, where the estimators cannot capture the full motion dynamics of a real vehicle. Moreover, the estimator requires the LQG/LQR controller, which is not necessarily the most appropriate control technique in the vibration suppression field; applying this method results in a fairly high order controller law, which is seen as a practical drawback. A linear state observer has been adopted to implement the state feedback control law and a H_2 / H_∞ performance-based control command, respectively, for the active suspension system of a full car model (7 DOF) [3], [33]. The designed unbiased observer has been proven to be asymptotically stable but is not guaranteed to have an acceptable estimation quality in real life in the presence of significant road disturbances such as bumps. Donahue et al. [34] have employed a Kalman Filter (KF) to estimate the active suspension system parameters of a military vehicle, equipped with 22 sensors, including two preview sensors to detect the road significant inputs. The optical preview sensors are mounted in front of the vehicle. The sensor measurements are converted to the road height by trigonometric equations and then fed back to the KF. Despite the acceptable estimation performance, the required preliminary computations of the preview signals need high processing power and time. Furthermore, the preview sensor signal is not accessible in any environment, and its performance is affected by dirt or rain, preventing a continual viewing of the ground and the sensor lenses.

Although previous research has been successful in the estimator design, many practical issues have been missed. The estimators have been developed assuming that there is no restriction on the sensor configuration. In contrast, there usually exist firm constraints on the type and number

of vehicle sensors due to the computational power limitations of the processors, the sensor deficiency (i.e., the preview sensor case), or cost. Often, not enough room can be found for another sensor to be installed. Therefore, the estimator must rely on information from only a few feasible sensors, and must still be capable of estimating the vehicle states. The proposed research aims to address this issue and to find an appropriate solution.

2 Problem Definition

Since the quantity and type of sensors mounted on the vehicle are limited, the estimation system needs to be designed such that the reduced information, the sensor data, does not reduce the estimation performance. The ultimate goal of this research project is to develop an estimation mechanism which can tolerate the paucity of vehicle sensors. When incorporating the available sensor signals, the estimator should produce the states required by a vehicle Ride, Handling, and Stability Controller (RHSC). After the controller processes the vehicle states, it sends command signals to the controllable semi-active dampers. Eventually, the desired force, created by the vehicle suspension system, can provide a better and safer ride for vehicle passengers. Figure 1 provides an overview of the system.

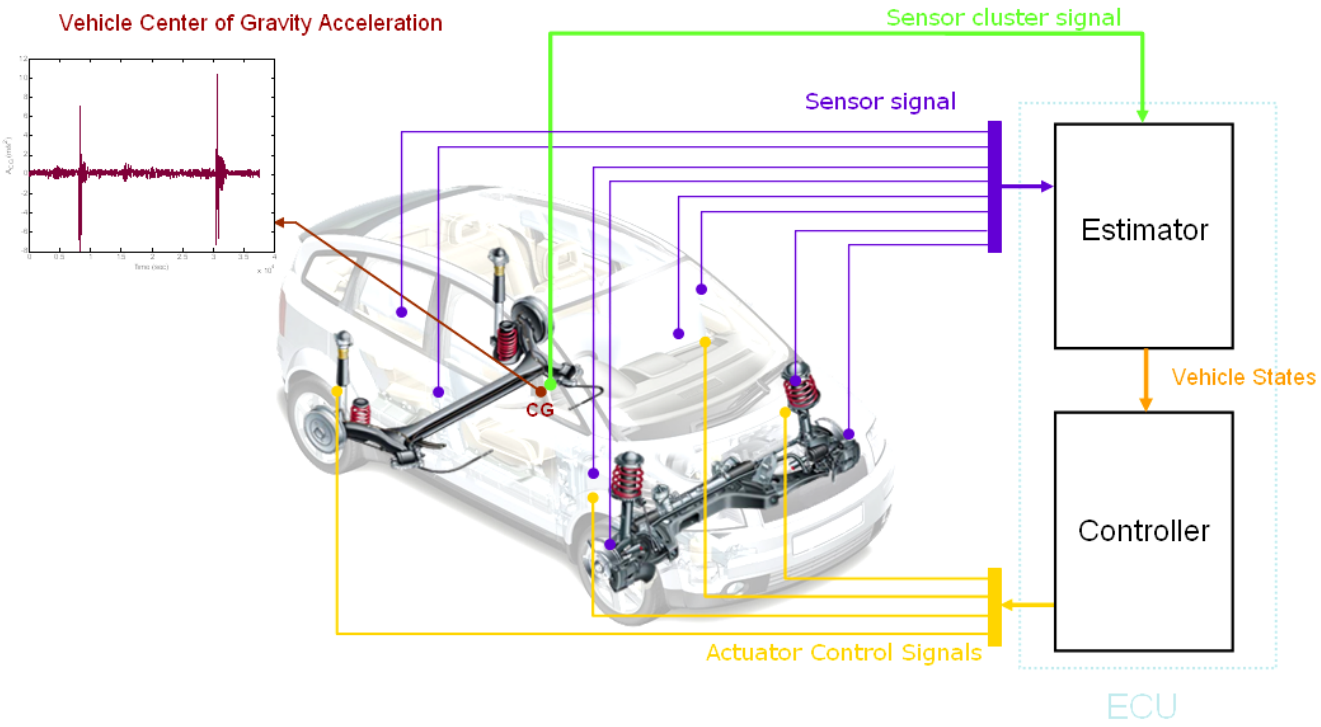

Figure 1: Example of the integrated sensor configuration, estimator and vehicle semi-active suspension controller.

It is expected that the RHSC can minimize the semi-active suspension system acceleration transmissibility at frequencies, where the road input has its maximum power (between 7 to 40 Hz [35], [36] and [37]). It is also recognized that the human body has a minimum tolerance to

vertical accelerations close to 5Hz (4-8Hz according to the ISO 2631) due to the resonance of the abdominal cavity [35]. As a result, the controller technique must pay more attention to the effects of the road's roughness acceleration around the frequency of 5Hz. Furthermore, the resonant peaks, close to the natural frequencies of the sprung and unsprung masses, should be decreased.

Since the development of a novel control technique is beyond the scope of this research, referring to the superiorities of the Skyhook control strategy, this method is adopted to work in series with the estimator to improve the ride comfort and road handling of the vehicle. In general, improved handling implies improved ground force distribution to maximize traction. This results in a reduction of the propensity of the vehicle to either roll over or skid, and hence an enhancement of the vehicle's stability. To better improve road handling qualities, a modified version of the Skyhook strategy, such as the Skyhook-Groundhook method, can also be implemented. It is expected that the structure of the estimator, developed in this research, remains unchanged for modified versions of the Skyhook control strategy (see Appendix A).

The states required by the Skyhook controller are the relative velocity of each suspension as well as absolute velocity of the corresponding wheel-hub[1]. In turn, the Skyhook policy assigns an upper or lower damping level to the semi-active shocks. However, more challenges arise here. First, the damping upper and lower levels are usually set by trial-and-error, and there is no systematic method to determine them. This would make the semi-active suspension system development process time-consuming and sometimes too difficult. Therefore, it would be desirable to establish a systematic methodology to determine the Skyhook damping levels. Second, combining two separately designed sub-systems does not guarantee that the good behaviours embedded in each sub-system are inherited by the final integrated system. This means that although the Skyhook control technique satisfies the frequency domain requirements [11], [12], [13] and [14], incorporating the dynamics of the estimator might deteriorate some of

[1] More precisely, the absolute velocity of the sprung mass (vehicle body at the shock end) can be extracted from the known relative velocity of the shock and the absolute velocity of the corresponding wheel-hub. Concepts and mathematical formulations of the Skyhook control strategy and its modified versions are given in Section 5.3.

these desired behaviours. As a result, the estimator and controller should be designed simultaneously to assure that the required performance is achieved by the integrated system[1].

In order to achieve these goals, the following specific research objectives are planned:

• **Research Objective 1:** Design a feasible reduced number of sensors measurement system which has been distributed strategically throughout the vehicle, thereby producing adequate measurements that can be filtered to provide the vehicle states necessary for RHSC. The ultimate sensor configuration should consist of as few sensors as possible.

• **Research Objective 2:** Development of an estimation mechanism to produce the required states of the RHSC by using the proposed measurement system. The estimator should guarantee that the estimation error remains unbiased and has as small a covariance matrix as possible, specifically at the presence of significant road disturbances (such as bumps). Furthermore, the estimator should be robust enough to withstand uncertainties that arise from varying the weight of the vehicle due to a change in the pay load or in the number of passengers, or varying the tire stiffness due to inflation pressure changes, for real-time applications. Also, the rate of decay of the estimation error should be sufficiently fast compared to the controller bandwidth.

• **Research Objective 3:** Development of a systematic methodology to design and implement semi-active suspension control laws, specifically the Skyhook strategy. The new design methodology must assure that the combined estimator and controller system meets some desired performance requirements defined for a particular RHSC application.

[1] Separation theorem guarantees stability of a system consisting of two stable linear subsystems. However, there is still no guarantee that the desired performance of each individual subsystem would be transferred to the ultimate integrated system.

3 Sensing System

Sensors are essential components of the vehicle RHSC. They provide the integrated estimation and control system with the necessary measurements of the vehicle motion. In the study of the ride and handling quality, the pitch, roll, vertical and lateral motions of a terrain vehicle are focused on. The sensors which can be used include accelerometers, gyroscopes, and displacement sensors to measure the acceleration, angular velocity, and the relative displacement of the moving parts, respectively. Table 1 lists the automobile industry standard sensor configurations.

It is evident that the accelerometers and displacement sensors are the most popular for vehicle RHSC applications. Because of the evolution of Micro Electro-Mechanical Sensors (MEMS), the combination of two or even three direction accelerometers in a simple low-cost sensor is now possible. By utilizing a multi-direction sensor chip with embedded signal-conditioning and temperature compensation, the component count and cost are mitigated. Furthermore, the implementation of a single multi-axes accelerometer facilitates a wide range of automotive auxiliary systems, including the RHSC, air bags, side and rollover crash-sensing, and the Antilock Brake Systems (ABS). The displacement sensors have the third greatest unit sales of all automotive sensors [38]. A displacement sensor can measure the stroke of an active or a semi-active damper. By one-time differentiation of the sensor output, the relative velocity across the damper is obtained, which is a required feedback by almost all suspension control strategies. However, the installation of the displacement sensors is not readily achieved in real practice.

Table 1: Overview of the sensor types and the arrangements in the industry for RHSC applications [38]

Company	Trade Name	Ride and Handling Controller Sensors	Stability Sensors	Applications
ZF Sachs	Continuous Damping Control (CDC)	2 accelerometers per damper, one in the vicinity of tire, the other at the body side of the damper	-	2002 BMW 7 series, Maserati 3200 Coupe, Ferrari Modena, Audi A8, Porshe Cayenne, and Opel Astra
Lord Corp.	Lord damper	4 displacement sensors and 4 vertical accelerometers at the body side of each shock	Lateral acceleration	?
Tenneco-Automotive	Continuously-Controlled Electronic Suspension (CES)	3 body accelerometers – 2 front and 1 rear – and 2-to-4 displacement sensors	Lateral acceleration	Audi A2, A3, A4, also Volvo platforms S60R, V70R, S60, V70 and S80
Delphi	MagneRide	4 displacement sensors	Lateral acceleration	Several GM platforms (i.e., Cadillac STS, SRX XLR and Escalade)
Continental Teves	Electronic Suspension System	4 displacement sensor and 3 body accelerometers in the vicinity of the shocks	-	?
Firestone	IntelliRide	Unknown number of displacement sensors and accelerometers	-	Many of SUVs

In the absence of an estimator, the sensor selection is dictated by a vehicle's type of suspension control strategy. The measurement system should be capable of providing enough information regarding the vertical motion of each wheel and the vehicle body movements. Consequently, a preliminary sensor configuration can include an accelerometer for each vehicle

corner and a sensor cluster at the vehicle body's centre of mass. The accelerometers are connected to one end of each shock in the vicinity of the wheels to measure the vertical acceleration of the wheel-hubs. The desired motion of the body is captured by a vertical direction accelerometer along with two perpendicular gyroscopes in the roll and pitch directions, merged in the sensor cluster. The sensor package can also include a lateral accelerometer to provide feedback for the stability controller.

Of importance are a family of sensor packages, called Inertial Measurement Units (IMU), that consist of triad orthogonal accelerometers and gyroscopes. They are often applied to Inertial Navigation Systems (INS). Since a vertical and lateral accelerometer with two gyros in the roll and pitch axes of the vehicle are required, an IMU mounted at the vehicle CG is proposed. An additional accelerometer[1], positioned along the longitudinal axis, or a gyroscope measuring the yaw rate, can be also employed for the vehicle level control systems and anti-skid systems (i.e., yaw stability applications), respectively. A similar sensor configuration keeps the wheels' accelerometers but replaces the IMU with four accelerometers – one at each corner (shock ends) – in order to measure the vehicle body movements[2].

[1] The x-axis accelerometer is the main feedback of vehicle body level systems during accelerating and braking. During a sharp acceleration, the damping of the rear wheels should be increased to counteract the vehicle to "squatting" [40]. In a hard brake, the front wheel damping should be boosted to prevent the vehicle from "nose-diving".

[2] It can be shown that with four accelerometers, all the motion variables of the body can be extracted.

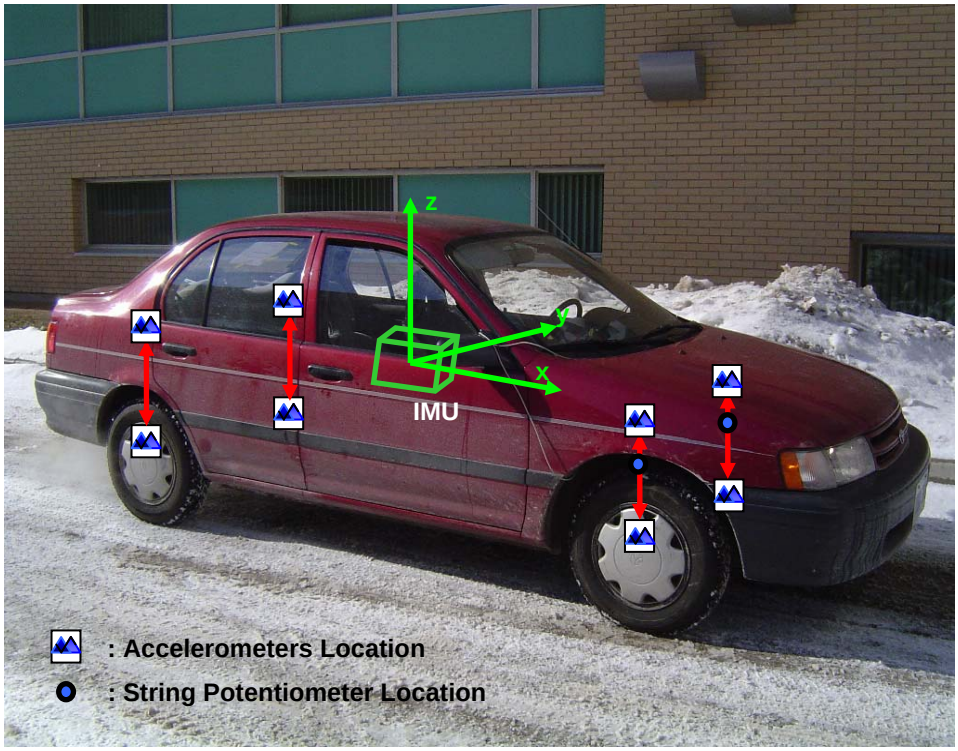

Figure 2: The full sensor configuration consisting of eight accelerometers, displacement sensors, and the IMU mounted on the first test vehicle: a Toyota Tercel 1993. The red arrows locate the vehicle shocks.

Another sensing architecture is composed of an accelerometer and displacement sensor pair, placed at each vehicle corner, totalling eight sensors. The accelerometers capture the vehicle body movements, whereas the displacement sensors measure the relative motion of the body and the wheels. Sometimes, a priori knowledge of only the relative motion between the wheels and the body is adequate. As a result, a configuration including four displacement sensors located at each shock are considered as another possible sensor suite.

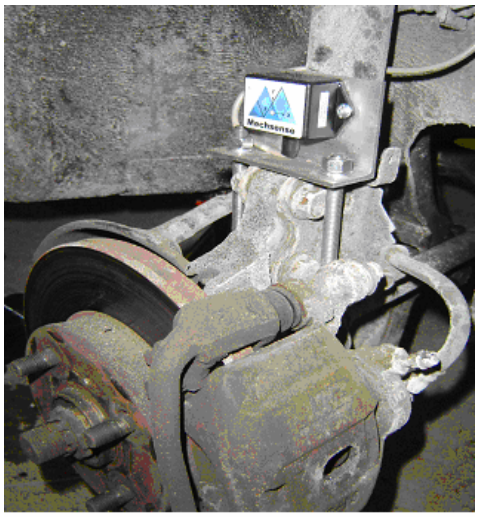

Figure 3: The accelerometer mounted on the bottom of the Toyota Tercel left front damper to measure the acceleration of the wheel-hub.

Therefore, the following preliminary sensor configurations are investigated:

a) one IMU and four accelerometers: the IMU in the vicinity of the vehicle body's CG and one accelerometer on each wheel-hub.

b) nine accelerometers: one accelerometer per each body corner (at the damper end), one accelerometer per each wheel-hub, and the last accelerometer at the CG.

c) four displacement sensors and one accelerometer: one displacement sensor for each shock and the accelerometer at the CG.

d) four displacement sensors and five accelerometers: one displacement sensor for each shock, one accelerometer per each body corner (at the damper end), and the last accelerometer at the CG.

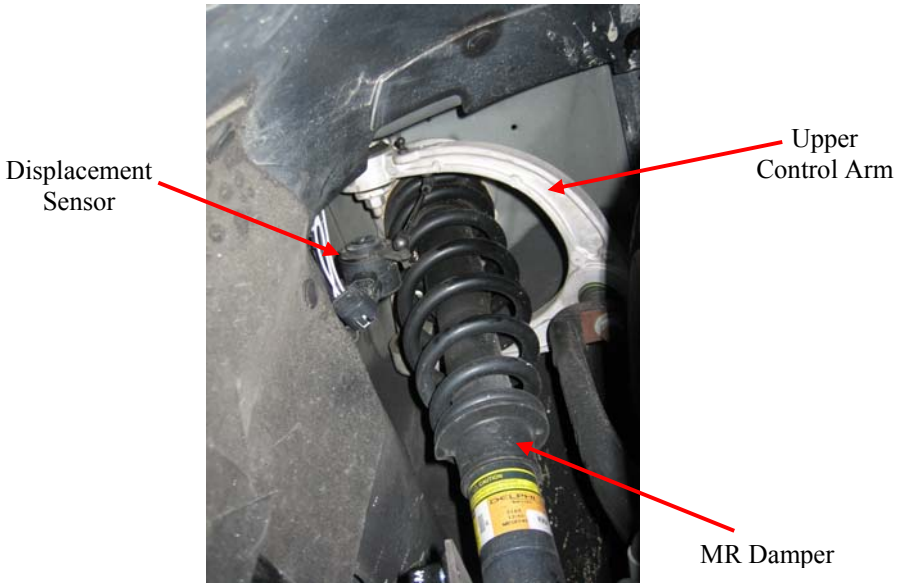

Figure 4: The displacement sensor measures the relative motion across the semi-active shock of a Cadillac SRX.

By using the preliminary sensor configurations, several objectives are pursued. First, to investigate whether fusing the sensors data through the proposed estimator can enrich the data/information package and provide the required states for the RHSC. In this way, the advantages and disadvantages of the particular estimator are extracted, leading to an improved structure.

The second goal is to explore the effects of the individual sensors on the performance of the estimation system and to discover which sensors at which locations have the most positive impact on the estimator's efficiency. Based on that experience, a sensor suite, which consists of as few sensors as possible, is proposed.

4 Estimation

In this chapter, the development of the estimation system is described. The estimator is meant to fuse signals from the sensors, distributed throughout the vehicle, and to provide the RHSC with the required information. In Section 4.1, the optimal estimation problem is defined and its mathematically equivalent form is established. In Section 4.2 to Section 4.4, the structure of a particular estimation algorithm, which is adopted to incorporate available information sources in the current problem, is expanded. Finally, the computer simulations and real-time test results are provided in Chapter 7.

4.1 Optimal Estimation Problem

Consider a linear discrete-time system with the state-space description,

$$x_{k+1} = \Phi_{k+1,k} x_k + G_k u_k + w_k , \tag{4.1}$$

where $w_k \in R^n$ is a zero mean white sequence of power Q_k:

$$E\left\langle w_k w_j^T \right\rangle = Q_k \delta_{k-j} , \tag{4.2}$$

and δ_{k-j} is the Kronecker delta. The power of the model white noise indicates the confidence level of the theoretical model of the system. $u_k \in R^m$ is the known deterministic input sequence which is related to the system state vector, $x_k \in R^n$, by the input matrix G_k. Further, $\Phi_{k+1,k}$ is the state transition matrix between times t_k and t_{k+1}. The transition matrix allows the computation of the state vector at time t_k, given the complete knowledge of the state vector at t_{k-i} for $i > 0$ and the input.

Measurements that capture the dynamical system behaviour are modelled as a linear combination of the system states, corrupted by the zero mean uncorrelated noise, $v_k \in R^p$,with strength R_k, such that

$$z_k = H_k x_k + v_k ,$$

and

$$E\left\langle v_k v_j^T \right\rangle = R_k \delta_{k-j} , \tag{4.3}$$

where $z_k \in R^p$ is the set of p measurements at time t_k. H_k is the measurement matrix that describes how the states and the measurements relate to each other in the absence of the noise.

The goal is to find an estimate of the state vector, denoted by $\hat{x}_k$,based on prior knowledge of the system dynamics and the measurements such that the following optimality criteria is satisfied at each time-step:

$$Min\ E\left\langle [x_k - \hat{x}_k]^T [x_k - \hat{x}_k] \right\rangle, \tag{4.4}$$

or alternatively,

$$J_k = trace\left\langle P_k(+) \right\rangle, \tag{4.5}$$

where $P_k(+)$ is the covariance matrix of the estimation error $x_k - \hat{x}_k$. Furthermore, the estimation error should be unbiased:

$$E\left\langle x_k - \hat{x}_k \right\rangle = 0. \tag{4.6}$$

The following results are proven [41], [42],

- If the system noise sequence, w_k, and the measurement noise sequence, v_k , are Gaussian zero-mean, uncorrelated, and white, then the KF, [43] and [44], provides the desired solution, satisfying the criterion.
- If w_k and v_k are zero-mean, uncorrelated, and white, then the KF is the best linear solution for the optimal estimation problem. There might be a non-linear estimator that offers a more optimal solution, but the KF is the optimal linear estimator.
- Otherwise, for nonlinear systems, or when the system and measurement noise are either correlated or coloured, the KF is no longer optimal but can be modified to approximate the best solution. In this case, KF is a sub-optimal solution for the estimation problem.

For the current estimation problem, it is assumed that the system and measurement noises are zero-mean, uncorrelated, and white. It is also assumed that the vehicle nature is linear in the region of the interest (that is, the vehicle dynamics can be expressed as the form of Equation (4.1))[1]. As a result, wherever the measurement system dynamics is linear, the KF is used for the first trial to tackle the estimation problem. Otherwise, when the optimality condition of the KF is

[1] Note that during the estimator design, it is assumed that the controller is in-line. Also, during the controller design, the estimator is in-line (all the states are provided, accurately). Finally, the nonlinear separation theorem is utilized to design the integrated estimation and control system.

not satisfied due to a non-linearity in the measurement system, modified versions of the KF, called the Extended Kalman Filter (EKF) and the Unscented Kalman Filter (UKF), are adopted [41], [42], [45], [53], [54]. Implementing the well-known filter with proven performance in several linear and non-linear practical applications [41], [46], [47], [48], [49], [50], [54] helps to determine the level of complexity of the problem, and highlights the issues of the particular estimation problem.

In the next section, the structure of the KF is briefly introduced and the underlying concepts are expanded. The structure of the EKF is simply come out from that of the KF by replacing the linear matrices by the corresponding linearized state and measurement matrices (Jacobians). More details are given in Section 4.3. Section 4.4 introduces the structure of the UKF, which fundamentally differs from the EKF. The designated estimator is then applied for state estimation of a simplified vehicle model, known as the quarter car, in Chapter 5 and extended to a full-car state estimation problem in Chapter 6. Each chapter includes modeling of the vehicles and the measurement systems followed by real-time estimation results and conclusions.

4.2 Kalman Filter (KF) Structure

Consider the n-state linear dynamical system:

$$x_{k+1} = \Phi_{k+1,k} x_k + G_k u_k + w_k . \tag{4.7}$$

with the measurements modelled by linear combinations of the states:

$$z_k = H_k x_k + v_k , \tag{4.8}$$

where $w_k \sim N(0, Q_k)$ and $v_k \sim N(0, R_k)$. Assume that the following initial conditions are given:

$$\hat{x}_0^- = E[x_0],$$
$$P_0^- = E[(x - \hat{x}_0^-)(x - \hat{x}_0^-)^T]. \tag{4.9}$$

It is desired to find an unbiased and optimal, in the covariance sense, estimate of the state vector x_k.

The KF works on a prediction-correction basis. First, a prediction is determined based on the system analytical model and the current state vector. In the next step, the predicted state is updated by incorporating the measurements. In this way, the information from the analytical

models and the actual measurements, weighted by their confidence/correctness level, are combined to acquire more reliable and accurate states.

The updated estimate is given by a linear combination of the predicted state and the measurements, that is, [41]

$$\hat{x}_k(+) = \hat{x}_k(-) + K_k[z_k - \hat{z}_k], \tag{4.10}$$

where $\hat{z}_k$ is the KF estimated measurement computed as:

$$\hat{z}_k = H_k \hat{x}_k(-). \tag{4.11}$$

Also, K_k is the Kalman gain and is determined by:

$$K_k = P_k(-)H_k^T[H_k P_k(-)H_k^T + R_k]^{-1}. \tag{4.12}$$

In Equation (4.12), H_k is the measurement matrix and R_k is the covariance of the discrete noise sequence. For an analog sensor with a noise characteristic of R, the equivalent discrete noise power can be simply obtained by [49]:

$$R_k = \frac{R}{\Delta t}. \tag{4.13}$$

The estimation error covariance matrix is corrected by a modified formula which reduces the probability that the covariance matrix can become negative definite, expressed as

$$P_k(+) = (I - K_k H_k)P_k(-)(I - K_k H_k)^T + K_k R_k K_k^T. \tag{4.14}$$

Between measurements, the discrete model of the dynamic system, Equation (4.7), without the noise term, is used to propagate the estimated states. Also, the error covariance matrix is propagated between the measurements by applying the following equality:

$$P_{k+1}(-) = \Phi(k+1,k)P_k(+)\Phi(k+1,k)^T + Q_k, \tag{4.15}$$

where Q_k is the power of the discrete process noise w_k ,and $\Phi(k+1,k)$ is the state transition matrix between the two consecutive time-steps. For a continuous system with a state matrix A, the state transition matrix between the two time-steps is given by the following exponential series [50], [51]:

$$\Phi(k+1,k) = e^{A\Delta T}. \tag{4.16}$$

Also, the equivalent descretized (quantized) noise covariance of an additive continuous white noise $w(t)$ is computed, at each time-step, by:

$$Q_k = \int_{t_k}^{t_{k+1}} \Phi(\rho,k)Q(t)\Phi(\rho,k)^T d\rho,$$

where,

$$E\left\langle w'(t)w'(\tau)^T \right\rangle = Q(t)\delta(t-\tau)\,. \tag{4.17}$$

4.2.1 The Kalman Filter (KF) Characteristics

Lemma 1: Consider the discrete-time system (4.7) with the measurements (4.8). Suppose that the matrix pair $(\Phi_k, Q_k^{1/2})$ is Controllable (Stabilizable) and the pair (H_k, Φ_k) is Observable (Detectable). Then, the estimation error covariance matrix, Equations (4.14) and (4.15), converge to a steady-state matrix value $\bar{P}$,

$$\bar{P} = \lim_{k\to\infty} P_k(+) = \lim_{k\to\infty} P_k(-)\ . \tag{4.18}$$

$\bar{P}$ is the unique positive semidefinite solution of the Discrete Algebraic Riccati Equation (DARE) and is given by Equation (4.19) [42], [45],

$$\bar{P} = \Phi_k \bar{P} \Phi_k^T - \Phi_k \bar{P} H_k^T (H_k \bar{P} H_k^T + R)^{-1} H_k \bar{P} \Phi_k^T + Q_k\,. \tag{4.19}$$

Also, the Kalman gain (Equation (4.12)) converges to a steady-state value $\bar{K}$, which is computed by the following equation,

$$\bar{K} = \bar{P} H_k^T (H_k \bar{P} H_k^T + R_k)^{-1}. \tag{4.20}$$

In this case, the estimation error dynamics is expressed by

$$e_{k+1} = (\Phi_k - \Phi_k \bar{K} H) e_k\,, \tag{4.21}$$

and the steady state Kalman gain guarantees the asymptotic stability of $(\Phi_k - \Phi_k \bar{K} H)$, that is,

$$\left|\lambda_i(\Phi_k - \Phi_k \bar{K} H)\right| < 1\,. \tag{4.22}$$

4.3 Extended Kalman Filter (EKF) Structure

This section extends the discussion of optimal estimation for linear systems to the more general case described by the non-linear stochastic difference equation (4.23):

$$x_{k+1} = f(x_k, u_k, t_k) + w_k\,, \tag{4.23}$$

where w_k is a zero mean Gaussian noise having the spectral density matrix Q_k. The problem is to estimate the state vector x_k from sampled nonlinear measurements of the form:

$$z_k = h(x_k, t_k) + v_k, \tag{4.24}$$

where v_k is the measurements' white random sequence with covariance R_k. Also assume that the initial conditions (4.9) are given.

Like the original KF, the EKF works on a prediction-correction basis. The only difference occurs because the original KF has been derived for linear systems, but the EKF is developed for non-linear dynamics. However, the EKF linearizes the nonlinear system about the most recent estimate of the state vector, and then benefits from the original linear filter concepts[1].

Motivated by the linear estimation problem, the updated estimate is given by a linear function of measurements and the predicted state, i.e., [41]

$$\hat{x}_k(+) = \hat{x}_k(-) + K_k[z_k - \hat{z}_k], \tag{4.25}$$

where K_k is the Kalman gain and is computed by Equation (4.12). For the EKF, matrix H_k in Equation (4.12) is the Jacobian matrix of the nonlinear measurement function, h, resulting from the Taylor series expansion, evaluated at the prior estimate (before measurements are incorporated) of the system state at $t = k$,

$$H_k = \left.\frac{\partial h(x[k], k)}{\partial x[k]}\right|_{x[k]=\hat{x}_k(-)}. \tag{4.26}$$

Also, the estimation error covariance matrix is updated by Equation (4.14).

Between the measurements, the estimated states are propagated by the use of Equation (4.23), the analytical model of the system, without the noise term. Also, the error covariance matrix is propagated by Equation (4.15). However, for the nonlinear system (4.23), the state transition matrix between the two consecutive time-steps is given by:

$$\Phi(k+1, k) = e^{A_k \Delta T}, \tag{4.27}$$

where A_k is the linearized system matrix about the updated estimate:

$$A_k = \left.\frac{\partial f(x[k], k)}{\partial x[k]}\right|_{x[k]=\hat{x}_k(+)}. \tag{4.28}$$

[1] Although the EKF algorithm is derived independently from the original linear filter, the relation between the two filters can be verified by the above-mentioned description.

4.4 Unscented Kalman Filter (UKF) Structure

As explained in Section 4.3, the EKF relies on linearization to update and propagate the mean and covariance of the state vector. This might often lead to unreliable estimates if the system nonlinearities are severe [42], [53], [54]. To eliminate the linearization error, the UKF, an extension of the KF, is developed which propagates mean and covariance information through a nonlinear transformation called Unscented Transformation (UT) [53]. The structure of the UKF is introduced in this section. The next sub-section, 4.4.1, demonstrates how the UKF reduces the linearization errors of the EKF.

Consider the nonlinear system and measurements of Equations (4.23) and (4.24), with the initial conditions given by Equation (4.9). The UKF also consists of two steps: update, followed by prediction. In the first stage, the filter incorporates the received sensors' signal to update the predicted states. In order to do that, $2n$ sigma points $\hat{x}_k^{(i)}$ are specified as the following [42], [53]

$$\begin{aligned}
\hat{x}_k^{(i)} &= \hat{x}_k^- + \tilde{x}^{(i)} \ , \qquad i = 1,...,2n \, , \\
\tilde{x}^{(i)} &= \left(\sqrt{nP_k^-}\right)_i^T \ , \qquad i = 1,...,n \, , \\
\tilde{x}^{(n+i)} &= -\left(\sqrt{nP_k^-}\right)_i^T \ , \qquad i = 1,...,n \, ,
\end{aligned} \tag{4.29}$$

where $\sqrt{P_k^-}$ is the matrix square root of the error covariance matrix P_k^- (i.e., $\sqrt{P_k^-}\sqrt{P_k^-}^T = P_k^-$). Then, the sigma points in Equation (4.29) are transformed by the nonlinear mapping $z_k = h(x_k, t_k)$ to get $2n$ predicted measurement vectors as shown in (4.30)

$$\hat{z}_k^{(i)} = h(\hat{x}_k^{(i)}, t_k) \, . \tag{4.30}$$

In the next step, the $\hat{z}_k^{(i)}$ vectors are combined to obtain the predicted measurement vector at the time $t = k$:

$$\hat{z}_k^- = \frac{1}{2n} \sum_{i=1}^{2n} \hat{z}_k^{(i)} \ . \tag{4.31}$$

In the same fashion, covariance of the predicted measurement is computed by

$$P_z = \frac{1}{2n} \sum_{i=1}^{2n} (\hat{z}_k^{(i)} - \hat{z}_k^-)(\hat{z}_k^{(i)} - \hat{z}_k^-)^T + R_k \ , \tag{4.32}$$

which also takes into account the effect of the measurement noise power. After computation, the cross covariance between $\hat{x}_k^-$ and $\hat{z}_k^-$

$$P_{xz} = \frac{1}{2n}\sum_{i=1}^{2n}(\hat{x}_k^{(i)} - \hat{x}_k^-)(\hat{z}_k^{(i)} - \hat{z}_k^-)^T \ , \tag{4.33}$$

the Kalman gain matrix is given by (4.34)

$$K_k = P_{xz}P_z^{-1}, \tag{4.34}$$

and the update stage is performed through the following equations

$$\hat{x}_k^+ = \hat{x}_k^- + K_k(z_k - \hat{z}_k^-),$$

$$P_k^+ = P_k^- - K_k P_z K_k^T. \tag{4.35}$$

The time propagation stage is initiated by choosing new $2n$ sigma points of the form:

$$\hat{x}_k^{(i)+} = \hat{x}_k^+ + \tilde{x}^{(i)+} \ , \qquad i = 1,...,2n$$

$$\tilde{x}^{(i)+} = \left(\sqrt{nP_k^+}\right)_i^T \ , \qquad i = 1,...,n$$

$$\tilde{x}^{(n+i)+} = -\left(\sqrt{nP_k^+}\right)_i^T \ , \qquad i = 1,...,n \tag{4.36}$$

This time, the nonlinear system equation is used to propagate the sigma points into $\hat{x}_{k+1}^{(i)}$ vectors, as illustrated by (4.37),

$$\hat{x}_{k+1}^{(i)} = f(\hat{x}_k^{(i)+}, u_k, t_k). \tag{4.37}$$

The average of the transformed sigma points yields the a priori state estimate at time $t = k+1$,

$$\hat{x}_{k+1}^- = \frac{1}{2n}\sum_{i=1}^{2n}\hat{x}_{k+1}^{(i)}, \tag{4.38}$$

and an a priori error covariance matrix is given by Equation (4.39)

$$P_{k+1}^- = \frac{1}{2n}\sum_{i=1}^{2n}(\hat{x}_{k+1}^{(i)} - \hat{x}_{k+1}^-)(\hat{x}_{k+1}^{(i)} - \hat{x}_{k+1}^-)^T + Q_k \ , \tag{4.39}$$

where also considers the effect of the system white noise covariance Q_k.

4.4.1 Means and Covariance of Nonlinear Transformation

This section illustrates how linearization approximation (which is implemented in the EKF algorithm) can cause errors in the mean and covariance of nonlinear functions of random variables (RV). Mean and covariance of the same nonlinear function is also evaluated by

employing the UT. The results of the two approaches are then compared. Consider the nonlinear transformation

$$y = h(x), \tag{4.40}$$

where x is a RV with mean $\bar{x}$ and covariance P_x. By using the Taylor series expansion formula, $h(x)$ can be expanded as follows,

$$\begin{aligned} y &= h(x) \\ &= h(\bar{x}) + D_{\tilde{x}}h + \frac{1}{2!}D_{\tilde{x}}^2 h + \frac{1}{3!}D_{\tilde{x}}^3 h + \dots , \end{aligned} \tag{4.41}$$

where $\tilde{x} = x - \bar{x}$ and $D_{\tilde{x}}^k h$ is given by,

$$D_{\tilde{x}}^k h = (\sum_{i=1}^{n} \tilde{x}_i \frac{\partial}{\partial x_i})^k \, h(x)\big|_{\bar{x}} . \tag{4.42}$$

The mean of y can therefore be written as,

$$\begin{aligned} \bar{y} &= E[h(\bar{x}) + D_{\tilde{x}}h + \frac{1}{2!}D_{\tilde{x}}^2 h + \frac{1}{3!}D_{\tilde{x}}^3 h + \dots] \\ &= h(\bar{x}) + E[D_{\tilde{x}}h + \frac{1}{2!}D_{\tilde{x}}^2 h + \frac{1}{3!}D_{\tilde{x}}^3 h + \dots] . \end{aligned} \tag{4.43}$$

A linear mean approximation results in

$$\bar{y} = h(\bar{x}) + E[D_{\tilde{x}}h], \tag{4.44}$$

and since the odd moments of $\tilde{x}$ is zero ($E[D_{\tilde{x}}h] = 0$), equation (4.45) gives the mean value of the nonlinear function.

$$\bar{y} = h(\bar{x}), \tag{4.45}$$

Equation (4.45) is used to propagate the estimated state and the error covariance between measurement times in the EKF routine. It is obvious that the higher order nonlinear terms have been neglected, which can be significant in highly nonlinear dynamical systems [53].

Alternatively, the mean of y can be computed by taking the weighted sigma points of Equation (4.36)

$$\bar{y}_u = \frac{1}{2n}\sum_{i=1}^{2n} y^{(i)} . \tag{4.46}$$

In the next step, the value of $\bar{y}_u$ is computed to see how efficient it matches the exact mean $\bar{y}$. By expanding each $y^{(i)}$ in Equation (4.46) around $\bar{x}$, the above equation can be rewritten as

$$\begin{aligned}\bar{y}_u &= \frac{1}{2n}\sum_{i=1}^{2n}(h(\bar{x}) + D_{\tilde{x}^{(i)}}h + \frac{1}{2!}D^2_{\tilde{x}^{(i)}}h + \frac{1}{3!}D^3_{\tilde{x}^{(i)}}h + ...) \\ &= h(\bar{x}) + \frac{1}{2n}\sum_{i=1}^{2n}(D_{\tilde{x}^{(i)}}h + \frac{1}{2!}D^2_{\tilde{x}^{(i)}}h + \frac{1}{3!}D^3_{\tilde{x}^{(i)}}h + ...).\end{aligned} \tag{4.47}$$

Now, notice that for any integer $k \geq 0$

$$\sum_{j=1}^{2n} D^{2k+1}_{\tilde{x}^{(j)}}h = 0\,, \tag{4.48}$$

since $\tilde{x}^{(j)} = -\tilde{x}^{(n+j)}$, $j = 1,...n$. Therefore, all of the odd terms in Equation (4.47) evaluate to zero and then

$$\bar{y}_u = h(\bar{x}) + \frac{1}{2n}\sum_{i=1}^{2n}(\frac{1}{2!}D^2_{\tilde{x}^{(i)}}h + \frac{1}{4!}D^4_{\tilde{x}^{(i)}}h + ...)\,. \tag{4.49}$$

Now, look at the second term on the right-hand side of the above equation

$$\begin{aligned}\frac{1}{2n}\sum_{i=1}^{2n}\frac{1}{2!}D^2_{\tilde{x}^{(i)}}h &= \frac{1}{2n}\sum_{k=1}^{2n}\frac{1}{2!}(\sum_{i=1}^{n}\tilde{x}_i^{(k)}\frac{\partial}{\partial x_i})^2\, h(x)\Big|_{x=\bar{x}} \\ &= \frac{1}{4n}\sum_{k=1}^{2n}\sum_{i,j=1}^{n}\tilde{x}_i^{(k)}\tilde{x}_j^{(k)}\frac{\partial^2}{\partial x_i \partial x_j}h(x)\Big|_{x=\bar{x}} \\ &= \frac{1}{2n}\sum_{i,j=1}^{n}\sum_{k=1}^{n}\tilde{x}_i^{(k)}\tilde{x}_j^{(k)}\frac{\partial^2}{\partial x_i \partial x_j}h(x)\Big|_{x=\bar{x}}\,,\end{aligned} \tag{4.50}$$

Again, $\tilde{x}^{(j)} = -\tilde{x}^{(n+j)}$, $j = 1,...n$ has been used above to throw out the symmetric terms. Substitute for $\tilde{x}_i^{(k)}$ and $\tilde{x}_j^{(k)}$ from Equation (4.29) in the above equation

$$\begin{aligned}\frac{1}{2n}\sum_{i,j=1}^{n}\sum_{k=1}^{n}\tilde{x}_i^{(k)}\tilde{x}_j^{(k)}\frac{\partial^2}{\partial x_i \partial x_j}h(x)\Big|_{x=\bar{x}} &= \frac{1}{2n}\sum_{i,j=1}^{n}\sum_{k=1}^{n}(\sqrt{nP_x})_{ki}(\sqrt{nP_x})_{kj}\frac{\partial^2 h(x)}{\partial x_i \partial x_j}\Big|_{x=\bar{x}} \\ &= \frac{1}{2n}\sum_{i,j=1}^{n}nP_{ij}\frac{\partial^2 h(x)}{\partial x_i \partial x_j}\Big|_{x=\bar{x}} \\ &= \frac{1}{2}\sum_{i,j=1}^{n}P_{ij}\frac{\partial^2 h(x)}{\partial x_i \partial x_j}\Big|_{x=\bar{x}}\,.\end{aligned} \tag{4.51}$$

Equation (4.49) can therefore be written as,

$$\begin{aligned}\bar{y}_u = h(\bar{x}) + \frac{1}{2}\sum_{i,j=1}^{n}P_{ij}\frac{\partial^2 h}{\partial x_i \partial x_j}\Big|_{x=\bar{x}} + \\ \frac{1}{2n}\sum_{i=1}^{2n}(\frac{1}{4!}D^4_{\tilde{x}^{(i)}}h + \frac{1}{6!}D^6_{\tilde{x}^{(i)}}h + ...).\end{aligned} \tag{4.52}$$

Now, consider the second term in the true mean equation (see Equation (4.43))

$$\begin{aligned}\frac{1}{2!}E[D_{\tilde{x}}^2 h] &= \frac{1}{2!}E[(\sum_{i=1}^{n}\tilde{x}_i\frac{\partial}{\partial x_i})^2\, h(x)\big|_{x=\bar{x}}] \\ &= \frac{1}{2!}E[\sum_{i,j=1}^{n}\tilde{x}_i\tilde{x}_j\frac{\partial^2 h}{\partial x_i\partial x_j}\Big|_{x=\bar{x}}] \\ &= \frac{1}{2!}\sum_{i,j=1}^{n}E(\tilde{x}_i\tilde{x}_j)\frac{\partial^2 h}{\partial x_i\partial x_j}\Big|_{x=\bar{x}} \\ &= \frac{1}{2!}\sum_{i,j=1}^{n}P_{ij}\frac{\partial^2 h}{\partial x_i\partial x_j}\Big|_{x=\bar{x}}\end{aligned} \tag{4.53}$$

$$\begin{aligned}\bar{y} = h(\bar{x}) &+ \frac{1}{2!}\sum_{i,j=1}^{n}P_{ij}\frac{\partial^2 h}{\partial x_i\partial x_j}\Big|_{x=\bar{x}} \\ &\frac{1}{4!}E[D_{\tilde{x}}^4 h] + \frac{1}{6!}E[D_{\tilde{x}}^6 h] + ...\end{aligned} \tag{4.54}$$

Comparing this equation with the one of the $\bar{y}_u$ (the approximated mean of y), it appears that $\bar{y}_u$ matches the true mean correctly up to the third order, whereas linearization matches the true mean only up to the first order (see Equation (4.45)). That is one of the sources that degrade the estimation accuracy of the EKF. It also demonstrated that by implementing the UT, the mean of the nonlinear function is transformed precisely.

Exactly the same argument is valid for the covariance of the nonlinear function. The covariance of y is given by

$$P_y = E[(y-\bar{y})(y-\bar{y})^T], \tag{4.55}$$

by using Equation (4.43), $(y-\bar{y})$ can be written as

$$\begin{aligned}y-\bar{y} = [h(\bar{x}) &+ D_{\tilde{x}}h + \frac{1}{2!}D_{\tilde{x}}^2 h + \frac{1}{3!}D_{\tilde{x}}^3 h + ...] - \\ &[h(\bar{x}) + \frac{1}{2!}E[D_{\tilde{x}}^2 h] + \frac{1}{4!}E[D_{\tilde{x}}^4 h] + ...],\end{aligned} \tag{4.56}$$

Substituting Equation (4.56) into Equation (4.55) results in,

$$\begin{aligned}P_y = &E[D_{\tilde{x}}h(D_{\tilde{x}}h)^T] + \\ &E[\frac{D_{\tilde{x}}h(D_{\tilde{x}}^3 h)^T}{3!} + \frac{D_{\tilde{x}}^2 h(D_{\tilde{x}}^2 h)^T}{2!2!} + \frac{D_{\tilde{x}}^3 h(D_{\tilde{x}}h)^T}{3!}] + \\ &E[\frac{D_{\tilde{x}}^2 h}{2!}]E[\frac{D_{\tilde{x}}^2 h}{2!}]^T + ...,\end{aligned} \tag{4.57}$$

where odd-powered terms have been neglected due to symmetry of the RV's probability density function (pdf). The first term in the above equation can be written as

$$
\begin{aligned}
E[D_{\tilde{x}}h(D_{\tilde{x}}h)^T] &= E[(\sum_{i=1}^{n}\tilde{x}_i\left.\frac{\partial h}{\partial x_i}\right|_{x=\bar{x}})(\sum_{i=1}^{n}\tilde{x}_i\left.\frac{\partial h}{\partial x_i}\right|_{x=\bar{x}})^T] \\
&= E[\sum_{i,j}^{n}\tilde{x}_i\left.\frac{\partial h}{\partial x_i}\right|_{x=\bar{x}}\left.\frac{\partial h^T}{\partial x_j}\right|_{x=\bar{x}}\tilde{x}_j] \\
&= \sum_{i,j}^{n}H_iE[\tilde{x}_i\tilde{x}_j]H_j^T \\
&= \sum_{i,j}^{n}H_iP_{ij}H_j^T \\
&= HPH^T.
\end{aligned}
\tag{4.58}
$$

rewriting Equation (4.57) after incorporating (4.58), covariance of a nonlinear transformation $y = h(x)$ is given by,

$$
\begin{aligned}
P_y = HPH^T + E[\frac{D_{\tilde{x}}h(D_{\tilde{x}}^3h)^T}{3!} + \frac{D_{\tilde{x}}^2h(D_{\tilde{x}}^2h)^T}{2!2!} + \frac{D_{\tilde{x}}^3h(D_{\tilde{x}}h)^T}{3!}] + \\
E[\frac{D_{\tilde{x}}^2h}{2!}]E[\frac{D_{\tilde{x}}^2h}{2!}]^T + ...
\end{aligned}
\tag{4.59}
$$

This is the complete Taylor series expansion for the covariance of a nonlinear transformation [42]. Consider the fact that all of the odd-powered terms in the expected value evaluate to zero. And hence,

$$
P_y = HPH^T . \tag{4.60}
$$

Again, due to linear approximation made in the EKF algorithm, only the first term of Equation (4.59) is used to obtain the covariance of the nonlinear function. This covariance approximation can result in significant errors if the underlying function, $h(x)$, is highly nonlinear. By implementing the UT, it is shown by Equation (4.59), that the approximated covariance, P_y, matches the true covariance up to the third order [53].

5 States Estimation of a Simplified Vehicle Model – the Quarter Car

In this chapter, states estimation of a simple vehicle which has only one wheel is examined. A semi-active suspension attached to the wheel axle and car body frame protects the car from irregularities in the road. This system is usually referred to as a Quarter Car (QC) model. Acceleration of the body and the wheel is measured via accelerometers mounted on each mass. Also, a displacement sensor may be used to measure the relative displacement across the suspension. A KF is utilised to fuse the sensors' data and to output relative displacement and velocity of the vehicle body and the wheel (sprung and unsprung masses), as well as the wheel deflection and the vertical velocity and displacement of the wheel mount (wheel-hub). Sections 5.1 and 5.2 give approximate analytical models of the QC and the measurement system that is embedded within the KF. Section 5.3 explains how the semi-active suspension with the Skyhook control strategy minimizes the effects of road disturbances on the vehicle body. Computer simulation and real-time estimation results are given in Section 5.4

5.1 The Quarter Car Analytical Model

Figure 5 shows a two Degrees of Freedom (DOF) quarter car model.

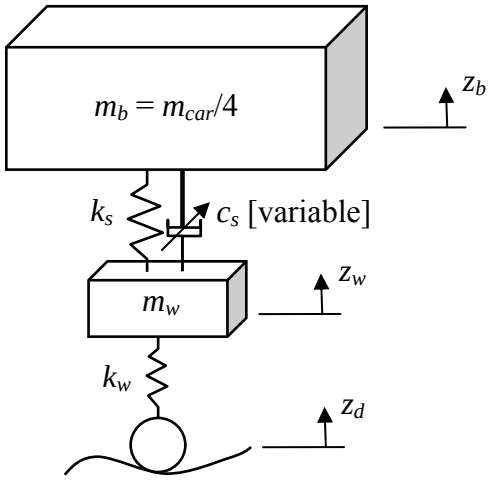

Figure 5: Lumped mass, two degrees of freedom quarter car (2 DOF QC) model.

The equations of motion for this system are given by:

$$m_b \ddot{z}_b = -k_s(z_b - z_w) - c_s(\dot{z}_b - \dot{z}_w) \tag{5.1}$$

$$m_w \ddot{z}_w = k_s(z_b - z_w) + c_s(\dot{z}_b - \dot{z}_w) - k_w(z_w - z_d). \tag{5.2}$$

By choosing the following variables as the states of the system,

$$\begin{aligned} x_1 &= z_b - z_w = z_{rQC} \\ x_2 &= \dot{z}_b = v_b \\ x_3 &= z_w - z_d = \delta_w \\ x_4 &= \dot{z}_w = v_{hQC}\,, \end{aligned} \tag{5.3}$$

the state space formulation of the QC system is derived to be as follows:

$$\begin{bmatrix} \dot{x}_1 \\ \dot{x}_2 \\ \dot{x}_3 \\ \dot{x}_4 \end{bmatrix} = \begin{bmatrix} 0 & 1 & 0 & -1 \\ -\frac{k_s}{m_b} & -\frac{c_s}{m_b} & 0 & \frac{c_s}{m_b} \\ 0 & 0 & 0 & 1 \\ \frac{k_s}{m_w} & \frac{c_s}{m_w} & -\frac{k_w}{m_w} & -\frac{c_s}{m_w} \end{bmatrix} \begin{bmatrix} x_1 \\ x_2 \\ x_3 \\ x_4 \end{bmatrix} + \begin{bmatrix} 0 \\ 0 \\ -1 \\ 0 \end{bmatrix} \dot{z}_d\,, \tag{5.4}$$

where c_s is the damping coefficient of the semi-active suspension; Moreover, $\dot{z}_d$ is the disturbance input coming from the road, and hence,

$$u_d = \dot{z}_d\,, \tag{5.5}$$

The state and input matrices are also given by the following equation

$$A(c_s) = \begin{bmatrix} 0 & 1 & 0 & -1 \\ -\frac{k_s}{m_b} & -\frac{c_s}{m_b} & 0 & \frac{c_s}{m_b} \\ 0 & 0 & 0 & 1 \\ \frac{k_s}{m_w} & \frac{c_s}{m_w} & -\frac{k_w}{m_w} & -\frac{c_s}{m_w} \end{bmatrix}, \quad E = \begin{bmatrix} 0 \\ 0 \\ -1 \\ 0 \end{bmatrix}. \tag{5.6}$$

There is another choice for the state vector of the 2 DOF QC. The alternative state vector contains absolute position and velocity of the sprung and unsprung masses:

$$x_1 = z_b$$

$$
\begin{aligned}
x_2 &= \dot{z}_b = v_b \\
x_3 &= z_w \\
x_4 &= \dot{z}_w = v_{hQC}.
\end{aligned} \tag{5.7}
$$

The corresponding state-space realization is then written as:

$$
\begin{bmatrix} \dot{x}_1 \\ \dot{x}_2 \\ \dot{x}_3 \\ \dot{x}_4 \end{bmatrix} = \begin{bmatrix} 0 & 1 & 0 & 0 \\ -\frac{k_s}{m_b} & -\frac{c_s}{m_b} & \frac{k_s}{m_b} & \frac{c_s}{m_b} \\ 0 & 0 & 0 & 1 \\ \frac{k_s}{m_w} & \frac{c_s}{m_w} & -(\frac{k_s}{m_w}+\frac{k_w}{m_w}) & -\frac{c_s}{m_w} \end{bmatrix} \begin{bmatrix} x_1 \\ x_2 \\ x_3 \\ x_4 \end{bmatrix} + \begin{bmatrix} 0 \\ 0 \\ 0 \\ \frac{k_w}{m_w} \end{bmatrix} u_d \,. \tag{5.8}
$$

where the state and disturbance input matrices are:

$$
A(c_s) = \begin{bmatrix} 0 & 1 & 0 & 0 \\ -\frac{k_s}{m_b} & -\frac{c_s}{m_b} & \frac{k_s}{m_b} & \frac{c_s}{m_b} \\ 0 & 0 & 0 & 1 \\ \frac{k_s}{m_w} & \frac{c_s}{m_w} & -(\frac{k_s}{m_w}+\frac{k_w}{m_w}) & -\frac{c_s}{m_w} \end{bmatrix}, \quad E = \begin{bmatrix} 0 \\ 0 \\ 0 \\ \frac{k_w}{m_w} \end{bmatrix}. \tag{5.9}
$$

The disturbance input of the model, given by Equation (5.8), is the road displacement, that is,

$$
u_d = z_d \,, \tag{5.10}
$$

as opposed to the previous realization (see Equation (5.4)) in which the road velocity is the input.

When weight of the wheel is too small in comparison with the vehicle body, it may be simply overlooked from the QC system, resulting in a 1 DOF vehicle. A schematic of the 1DOF QC is shown in Figure 6. The corresponding equation of motion is given by:

$$
m_b \ddot{z}_b = -k_s^{'}(z_b - z_d) - c_s(\dot{z}_b - \dot{z}_d) \,. \tag{5.11}
$$

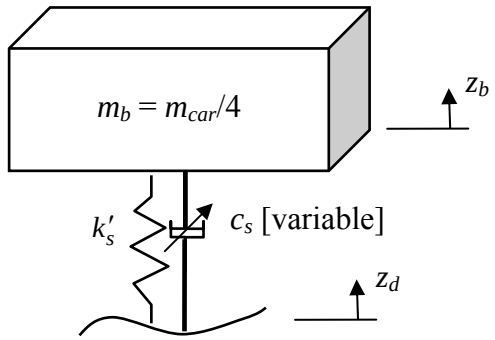

Figure 6: 1 DOF Quarter Car (1 DOF QC) model.

By choosing the following two variables as the vehicle states:

$$x_1 = z_b - z_d$$

$$x_2 = \dot{z}_b - \dot{z}_d \,. \tag{5.12}$$

The equation of motion in the state space form is written as

$$\dot{x} = A(t)x + Eu_d(t)\,, \tag{5.13}$$

where

$$A(c_s) = \begin{bmatrix} 0 & 1 \\ -\dfrac{k_s'}{m_b} & -\dfrac{c_s}{m_b} \end{bmatrix}, \quad E = \begin{bmatrix} 0 \\ -1 \end{bmatrix}, \tag{5.14}$$

and the input to the system, $u_d(t)$, is the road vertical acceleration, that is,

$$u_d(t) = \ddot{z}_d(t)\,. \tag{5.15}$$

In either realization, (5.4), (5.8) or that of the 1 DOF QC, given by (5.13), an extra white noise term $w(t)$ with a strength of Q is added to account for inaccuracies existing in the analytical model. Therefore, the state-space equation of the QC is written as:

$$\dot{x}(t) = A(c_s)x + Eu_d + w(t)\,; \qquad E\left\langle w^T w \right\rangle = Q\,. \tag{5.16}$$

The model base estimator, KF, then benefits from the Equation (5.16), without the noise term, though, to propagate the states estimate between the measurements.

5.2 Measurement System Analytical Model

The measurement system for the 2 DOF QC may consist of two accelerometers measuring the specific forces exerted to each mass. Hence, the measurement system can be described by the following differential equations:

$$\begin{aligned} \ddot{z}_b &= -\frac{k_s}{m_b}(z_b - z_w) - \frac{c_s}{m_b}(\dot{z}_b - \dot{z}_w) \\ \ddot{z}_w &= \frac{k_s}{m_w}(z_b - z_w) + \frac{c_s}{m_w}(\dot{z}_b - \dot{z}_w) - \frac{k_w}{m_w}(z_w - z_d). \end{aligned} \tag{5.17}$$

The measurement vector is:

$$z = \begin{bmatrix} \ddot{z}_b \\ \ddot{z}_w \end{bmatrix}. \tag{5.18}$$

By considering the states set of Equation (5.3), Equation (5.17) can be written in the following compact form

$$z(t) = H(t)x + v(t), \tag{5.19}$$

where $v(t)$ is the sensors noise vector assumed to be zero-mean Gaussian and white, with covariance R. The measurement matrix is also given by Equation (5.20):

$$H = \begin{bmatrix} -\frac{k_s}{m_b} & -\frac{c_s}{m_b} & 0 & \frac{c_s}{m_b} \\ \frac{k_s}{m_w} & \frac{c_s}{m_w} & -\frac{k_w}{m_w} & -\frac{c_s}{m_w} \end{bmatrix}. \tag{5.20}$$

For the 1 DOF case, analog output of the accelerometer mounted on the sprung mass is fed back to the estimator. Hence, the measurement model may be expressed as the following equation

$$z(t) = h^T x^T(t) + v(t), \tag{5.21}$$

where

$$h^T(t) = \begin{bmatrix} -\frac{k_s}{m_b} & -\frac{c_s}{m_b} \end{bmatrix}. \tag{5.22}$$

The next section introduces the Skyhook control strategy to properly adjust the semi-active suspension.

5.3 The Semi-active Damper Control Strategy – The Skyhook Policy

Before defining the Skyhook control policy, it is worth describing the behaviour of a passive system. Considering the 1 DOF QC model in Figure 6 but with a constant damper coefficient, the displacement transmissibility of the passive system can be derived as follows:

$$\left|\frac{x_r}{z_d}\right| = \frac{\omega^2}{\sqrt{(\omega_n^2 - \omega^2)^2 + 4\zeta_s^2\omega_n^2\omega^2}}, \tag{5.23}$$

where x_r is relative displacement across the damper,

$$x_r = x_b - z_d, \tag{5.24}$$

which z_d is the road displacement. ω, ω_n and ξ are frequency, natural frequency, and the damping ratio, respectively. The displacement transmissibility expresses how big the damper relative displacement would be per unit of the base excitation. There exists another ratio which describes the same relation but between acceleration of the mass and the base. This ratio is expressed as,

$$\left|\frac{\ddot{x}_b}{\omega_n^2 z_d}\right| = \frac{\omega^2\sqrt{\omega_n^2 + (2\zeta\omega_n\omega)^2}}{\omega_n^2\sqrt{(\omega_n^2-\omega^2)^2 + 4\zeta^2\omega_n^2\omega^2}}. \tag{5.25}$$

The displacement transmissibility can be plotted as a function of the frequency ratio, ω/ω_n, resulting in Figure 7 for various damping ratios. As one can see from the figure, at low passive damping ratios, the resonant transmissibility (around $\omega = \omega_n$) is relatively large, while the transmissibility at frequencies above the resonant peak is quite low. The opposite is true for relatively high damping ratios. Figure 7 demonstrates the inherent trade-off of passive suspension systems. If the suspension system damping is adjusted to the low values, superior high frequency isolation is gained but poor resonant frequency control.

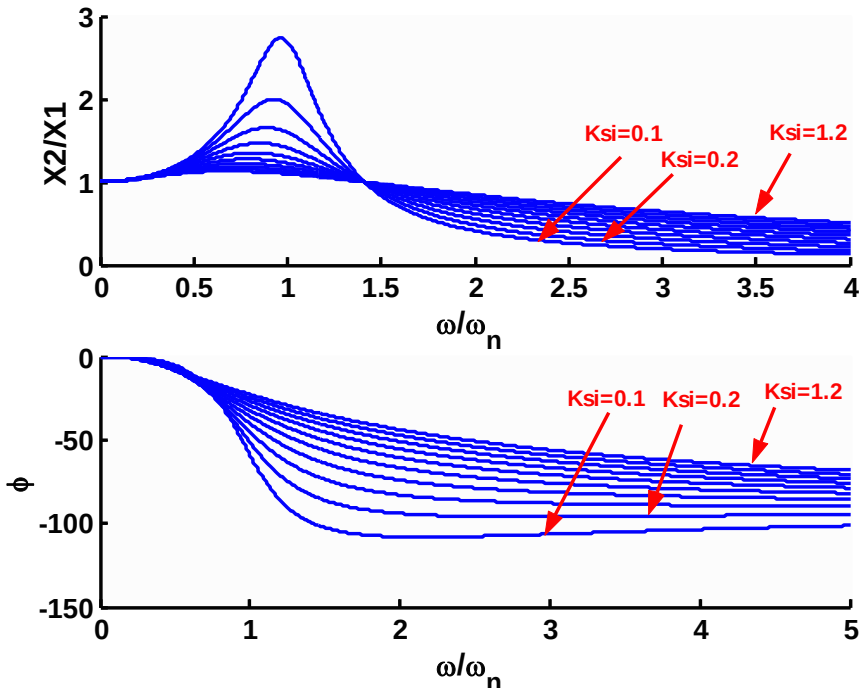

Figure 7: Transmissibility of passive configuration (amplitude and phase) for different damping coefficients.

One method to eliminate the trade-off between resonance control and high frequency isolation in a passive system is to reconsider the configuration of the suspension system. One option is moving the damper from between the suspended mass and the base to the position shown in Figure 8. The damper is connected to an inertial reference in the sky (a ceiling that remains vertically fixed relative to a ground reference). For this to actually happen, the damper must be attached to a reference in the sky that remains fixed in the vertical direction, but is able to translate in the horizontal direction. The transmissibility of the system can be expressed as:

$$\frac{x_b}{z_d} = \frac{1-(\frac{\omega}{\omega_n})^2 - 2(\frac{\omega}{\omega_n})\xi j}{(1-(\frac{\omega}{\omega_n})^2)^2 + (2\xi)^2}. \tag{5.26}$$

Therefore, the amplitude and the phase can be obtained as:

$$\left|\frac{x_b}{z_d}\right| = \frac{1}{\sqrt{(1-(\frac{\omega}{\omega_n})^2)^2 + (2\xi)^2}}, \tag{5.27}$$

$$\tan(\varphi) = \frac{-2(\frac{\omega}{\omega_n})\xi}{1-(\frac{\omega}{\omega_n})^2)^2}. \tag{5.28}$$

where ω_n and ξ are natural frequency of the system and the Skyhook damping ratio, respectively. In order to observe the effect of Skyhook control on the system, transmissibility versus ω/ω_n are plotted, and shown in Figure 9 and Figure 10.

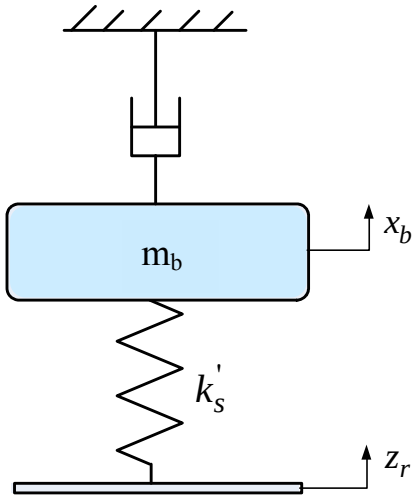

Figure 8: The Skyhook configuration.

As the Skyhook damping ratio increases, the resonant transmissibility decreases. Increasing the Skyhook damping ratio, however, does not increase the transmissibility above the resonant frequency. For sufficiently large Skyhook damping ratios (i.e., above ξ>0.707), the resonance frequency can even be isolated. This is encouraging, since the trade-off associated with the passive systems design has been removed.

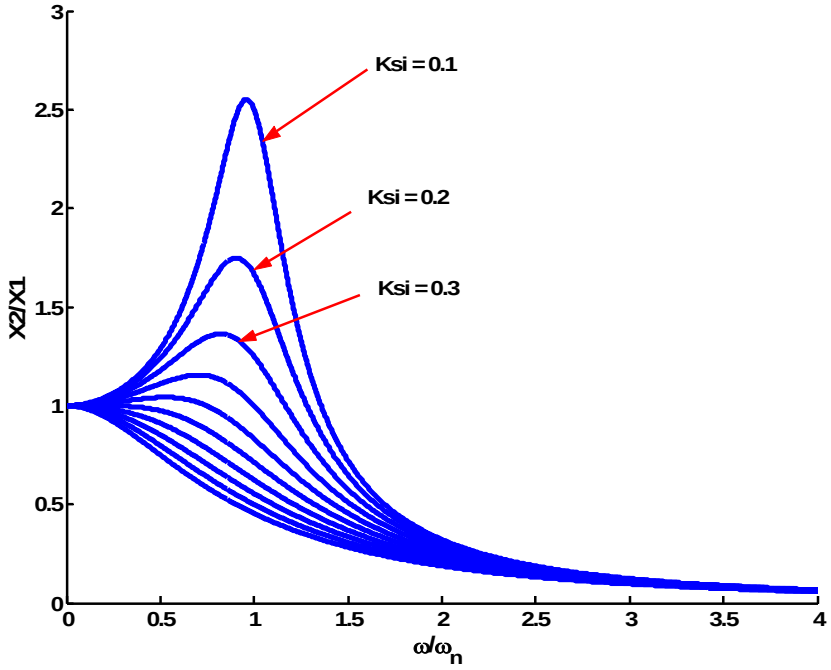

Figure 9: Transmissibility of the Skyhook configuration (amplitude).

To realize the Skyhook control, the relationship between force and the Skyhook damping force is then studied.

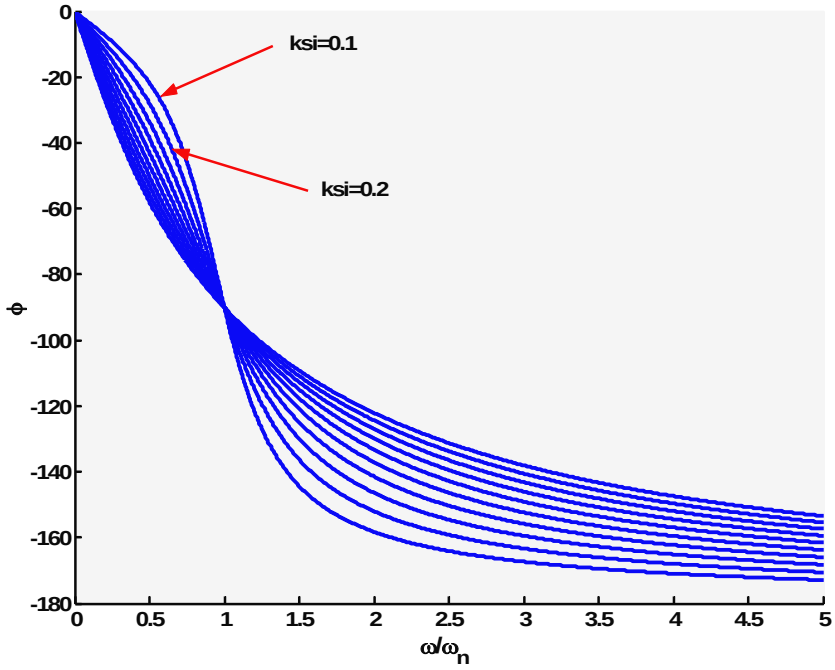

Figure 10: Transmissibility of the Skyhook configuration (phase).

Let us assume that the sprung mass is moving upward (i.e., in a positive direction of the sprung mass movement) and the relative velocity across the damper is positive. At this instance, the Skyhook damper applies a force in the opposite direction of the sprung mass. The relationship between force and the Skyhook damping coefficient, c_{sky}, is as follows [10]:

$$F = -c_{sky} v_b , \tag{5.29}$$

where v_b $(= \dot{x}_b)$ is the absolute velocity of the sprung mass. The negative sign shows that the force is in the opposite direction of the sprung mass motion. The question is how one can relate the variable damping coefficient to the Skyhook damping. Considering Figure 8, the force, applied from the semi-active damper, is written as:

$$F_s = -c_s v_r . \tag{5.30}$$

F_s is a variable force adjusted by the variable damping coefficient. Also, v_r $(= \dot{x}_r)$ is the relative velocity across the semi-active shock. If the semi-active damper needs to provide the same Skyhook force, by equating equations (5.29) and (5.30), the variable damping should be

$$c_s = \frac{c_{sky}}{v_r} v_b . \tag{5.31}$$

As mentioned before, both v_b and v_r should be positive. Now, let us consider the case where v_r is positive and v_b is negative. This means that the spring is stretching while the mass is moving downward. In a similar fashion, the force applied from the Skyhook damper applies in the positive direction of v_b. Referring back to the Figure 8, the equivalent semi-active damper can only apply a force in the negative direction of x_b. Since the equivalent semi-active damper will not be able to produce a force in the direction of the Skyhook damper, the only way to make this possible is to decrease the damping force close to zero. Practically, this can not be achieved completely because there is always a damping force, however slight. This small force applies in the opposite direction of the Skyhook damper. Therefore, when v_b is negative and v_r is positive, one should keep the damping force very close to zero. In another case, when v_b is positive and v_r is negative, the same logic is used. The result is called the Skyhook policy and can be summarized as follows [11]:

$$F_s = \begin{cases} c_{sky}\dot{x}_b & v_b v_r \geq 0 \\ 0 & v_b v_r < 0 \end{cases} . \tag{5.32}$$

F_s is the force applied by the semi-active damper. The Skyhook control implies that when the product of v_b and v_r is positive (either positive or negative), the damping force is proportional to v_b. When the product of the two v_b and v_r is negative (one of them is positive while the other is negative), the damping force should be equal to zero.

For semi-active systems, the Skyhook control strategy, Equation (5.32), is modified to suit the damper capabilities. It adjusts the damping coefficient of the semi-active damper, i.e., an MR damper, by only two damping levels: the high-state damping, c_{max}, and the low-state damping, c_{min}, (ideally zero). When the product of the relative velocity across the shock and the absolute velocity of the sprung mass is positive or zero, the damper is set to the higher level; otherwise, it is set to the lowest level. Mathematically, this is shown by Equation (5.33):

$$c_s = \begin{cases} c_{max} & v_b v_r \geq 0 \\ c_{min} & v_b v_r < 0 \end{cases} . \tag{5.33}$$

The Skyhook control strategy, either Equation (5.32) or (5.33), is undoubtedly the most-used control strategy for vehicles' controllable suspension systems. However, there exist some

drawbacks associated with the implementation of this strategy. As described in Chapter 1, measuring v_b, the absolute velocity of the sprung mass, is not practical. Also, choosing the damping levels (more specifically the upper damping level, c_{max}) should be accomplished by a trial-and-error process which can be difficult and time-consuming. Nevertheless, in the next sections up to Chapter 12, the above-mentioned shortcomings are overlooked, and it is assumed that the damping coefficients of the semi-active dampers are properly altered based on the Skyhook policy. The above-mentioned drawbacks are then addressed in Chapter 12, where a systematic methodology is developed to design and implement the Skyhook control strategy for vehicles' semi-active suspension systems.

5.4 Experimental Results

This section investigates the KF efficiency in estimating the states of the simplified vehicle models. Since the experimental setup on hand is a 1 DOF QC, real-time experiments are carried out on the 1 DOF model. Computer simulations (off-line tests) are accomplished instead on the 2 DOF vehicle model. For the 1 DOF case, a sinusoidal road input stimulates the system, but the exciting function for the 2 DOF QC is a single bump[1]. The next sections present the estimation results.

5.4.1 Off-line Estimation Results of the 2 DOF Vehicle Model

Figure 11 shows the cross section of the bump which excites the 2 DOF QC in the off-line computer simulations. The bump dimensions are selected to be close to that of real bumps on common paved roads (for instance, Ring Road at the University of Waterloo). The quarter car passes over the bump with a speed of 30 km/hr. The damping of the semi-active damper is adjusted following the Skyhook policy to isolate the disturbance input. The most recent damping coefficient is then fed back to the KF to update the embedded system and measurement models. Noisy measurements of the two accelerometers (sprung and unsprung masses), sampled at a rate of 500Hz, are injected into the KF, where the sensors data and the embedded models information are combined to estimate the vehicle states.

[1] A bump input contains a wide range of exciting frequencies up to 40 Hz.

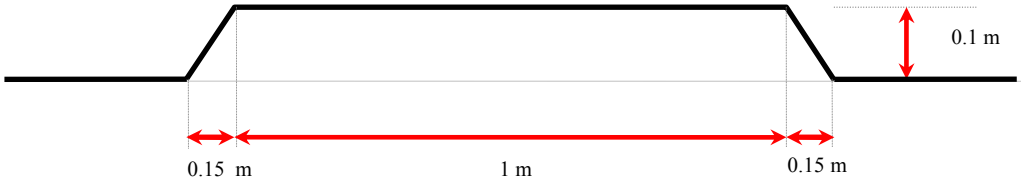

Figure 11: Bump dimensions used in the computer simulations

Figure 12 and Figure 13 display the estimation results by the KF. The top graph of Figure 12 compares the actual and estimated relative displacement of the shock, i.e., z_{rQC}. The bottom graph shows the actual and estimated wheel deflection, δ_w, side by side. In both graphs, the estimated states are reasonably close to the actual quantities.

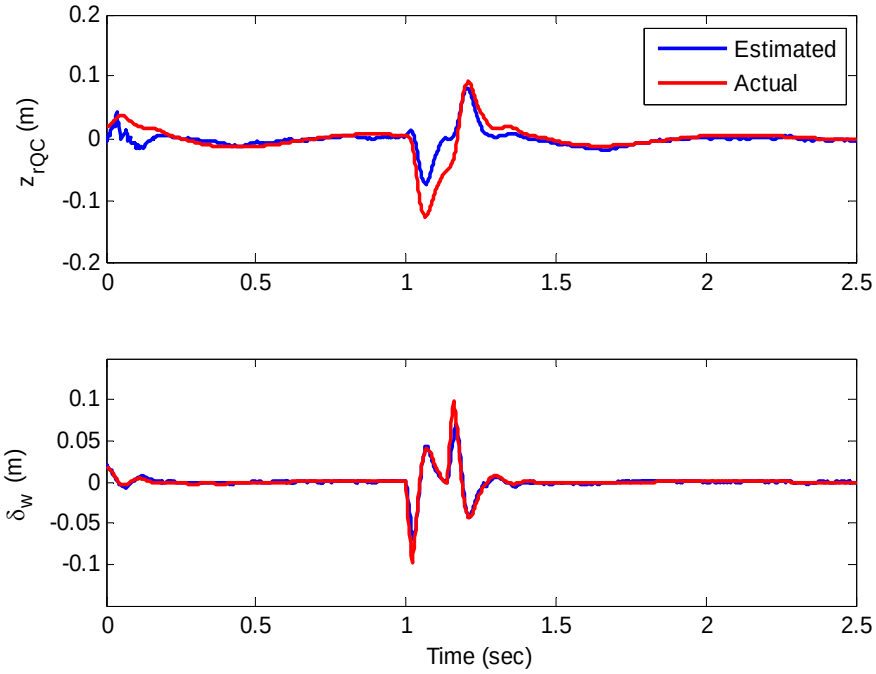

Figure 12: The top graph compares the actual relative displacement of the semi-active damper with the KF estimate. The bottom graph performs the comparison for the QC's tire deflection.

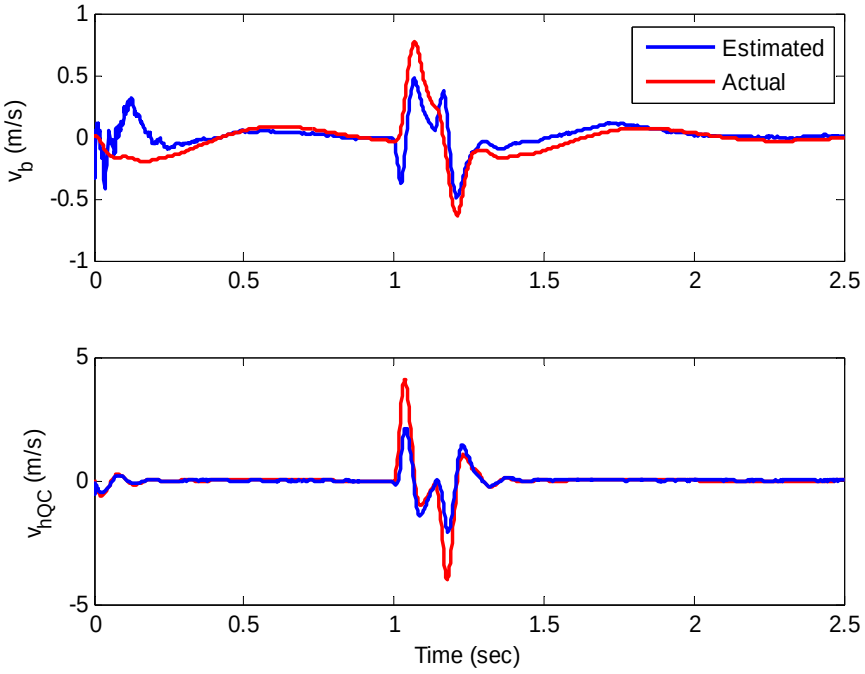

Figure 13: The top graph puts the actual and estimated absolute velocity of the sprung mass side by side. The bottom graph compares the actual absolute velocity of the wheel-hub with the KF estimate.

Figure 13 (the top graph) gives a comparison between the actual and estimated absolute velocity of the sprung mass. The bottom window compares the absolute velocity of the wheel-hub with the KF estimate. From the top graph, it can be seen that the velocity estimate of the sprung mass contains poor knowledge of the actual signal. It is obvious that the separation of the two signal occurs at the time t=1 when the QC hits the bump. Furthermore, the bottom window illustrates that the KF provides a fairly good estimate of the wheel-hub absolute velocity.

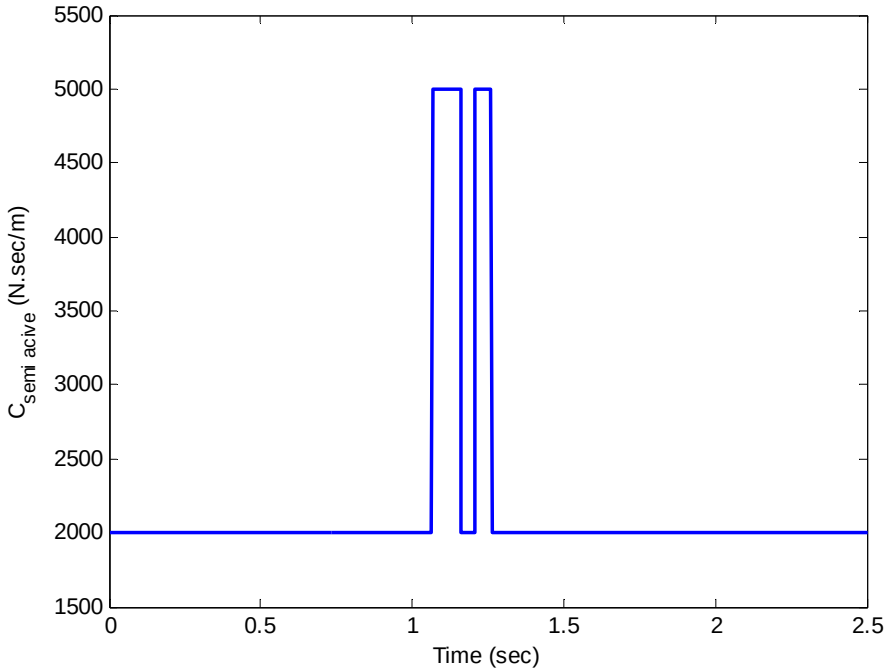

Figure 14: The Skyhook controller command signal

Figure 14 plots the damping coefficient variations made by the Skyhook controller; it is either the permissible lower level, c_{min}, or the upper damping level, c_{max}. The instantaneous damping coefficient of the semi-active damper, c_{min} or c_{max}, may be fed back to the KF to update the embedded models at each time-step (2 milliseconds). However, it can significantly increase the computational burden and the required processing time of the filter, which may not be suitable for real-time applications.

The sensitivity of the KF estimates to the damping coefficient update is studied in the next step. It is done by comparing the estimation results of two KFs; one with time-invariant models, in which a constant damping coefficient equal to the mean value of the entire damping range is set, and the other with time-varying models. For this particular semi-active suspension design, c_{min} and c_{max} are equal to 2000 and 5000 N.sec/m, respectively, and therefore the mean value of the damping range would be 3500 N.sec/m.

It is illustrated by Figure 15, Figure 16, and Figure 18 that the estimation quality of the KF embedding the time-invariant models is comparable to that of the other KF, whose models are updated at each sampling time. Furthermore, both filters are not capable of providing a

reasonable estimate of the sprung mass absolute velocity (please see Figure 17). These results authenticate the use of the KF with time-invariant models whenever lessening the processor burden is vital.

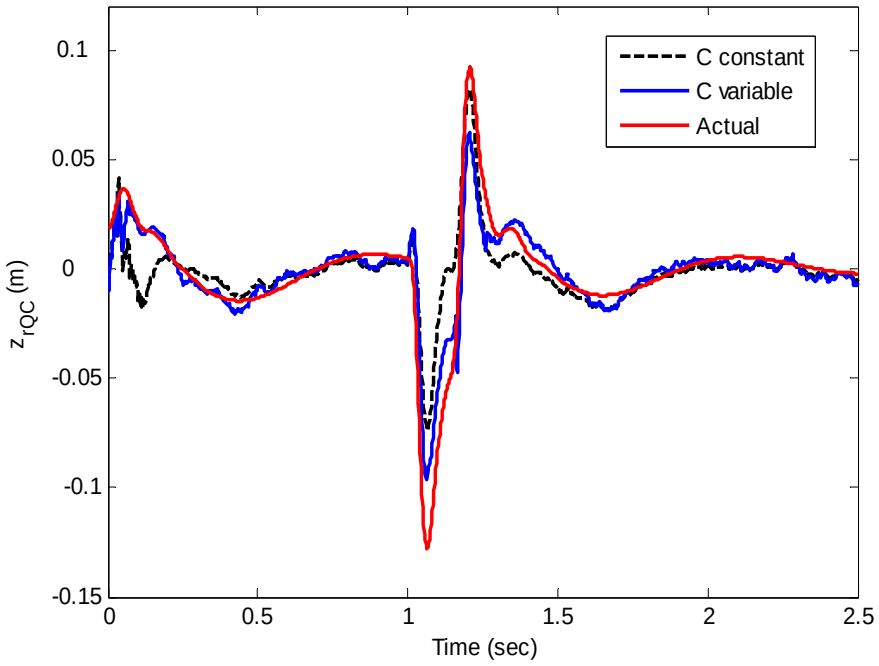

Figure 15: The graph compares the suspension system's actual deflection with its estimations: one is obtained by updating the damping coefficient variations in the KF models, and the other one leaves it as a constant.

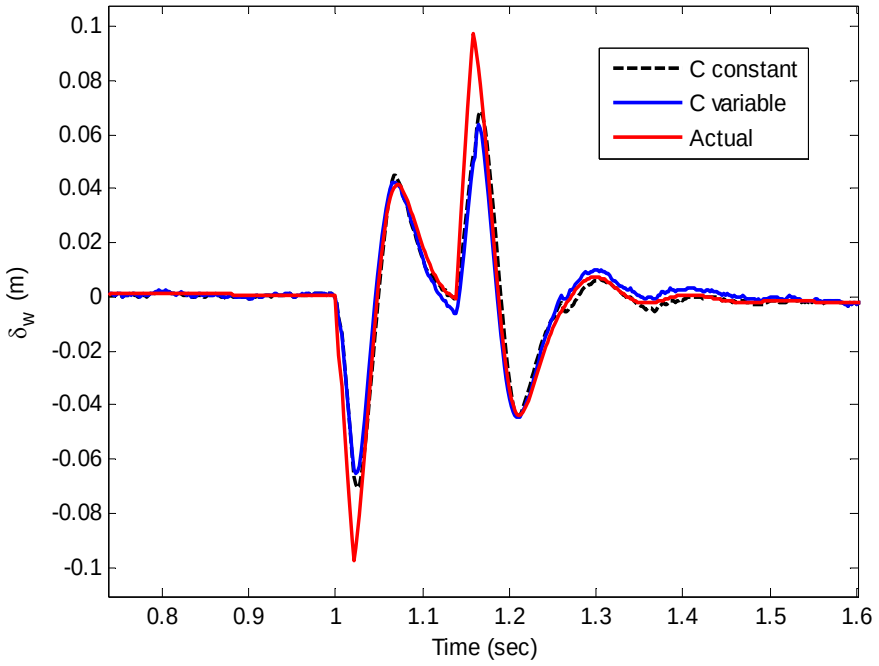

Figure 16: The graph compares the actual deflection of the wheel with its estimations; one is obtained by updating the damping coefficient variations in the KF models, and the other one leaves it as a constant. The plot zoomed in on the bump to provide a better resolution.

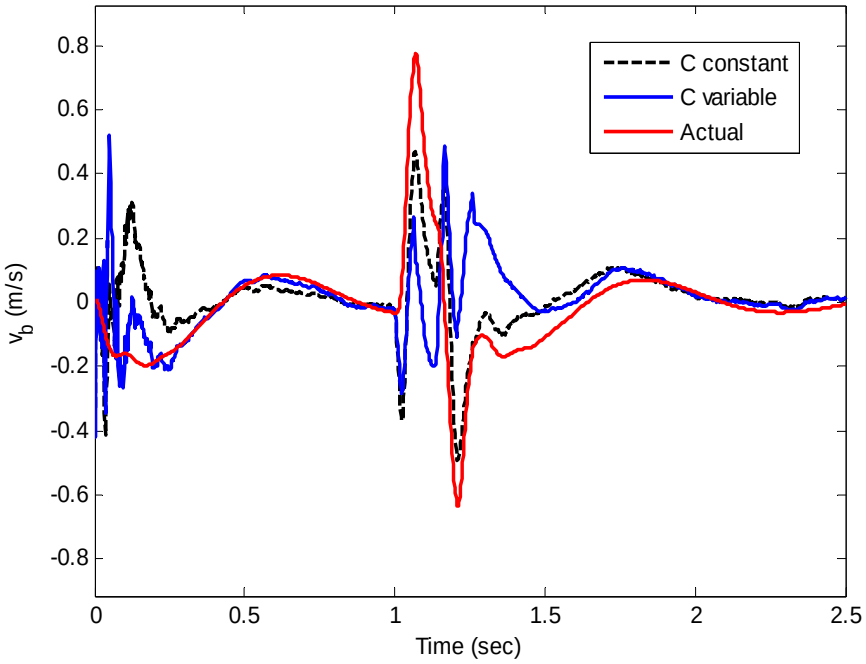

Figure 17: The graph compares the actual sprung mass velocity with its estimations; one is obtained by updating the damping coefficient variations in the KF models, and the other one leaves it as a constant.

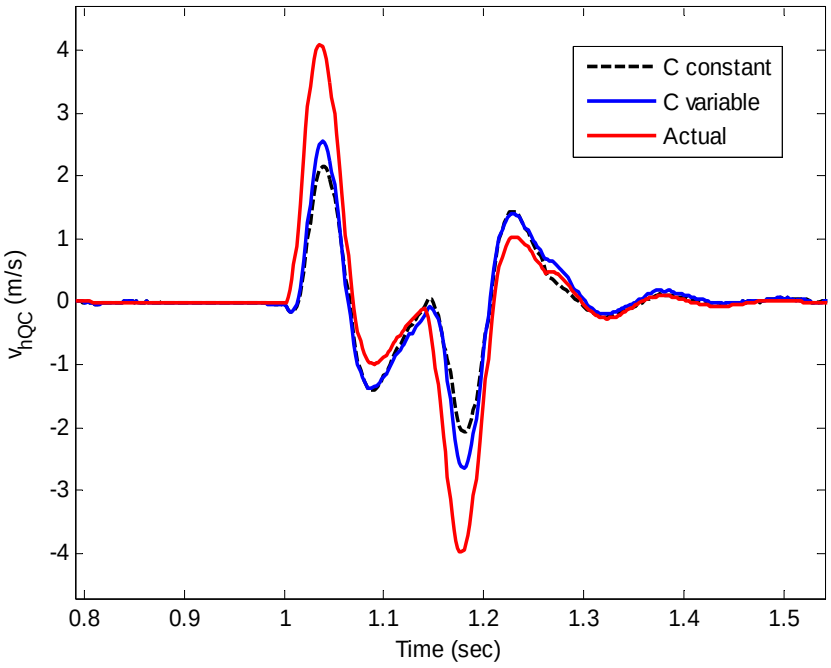

Figure 18: The graph compares the wheel-hub velocity with its estimations; one is obtained by updating the damping coefficient variations in the KF models, and the other one leaves it as a constant. The plot zoomed in on the bump to provide a better resolution.

As Figure 17 demonstrates, the KF is not able to estimate velocity of the sprung mass. Even de-weighting the system model to let the KF rely more on the measurements does not help. This is despite the fact that the Observability matrix of the system and measurement pair, $(H_k, \Phi(k+1,k))$, has full rank[1] (see Equations (5.20), (5.6) and (4.16) for definitions of H_k and $\Phi(k+1,k)$), which means that the states must all be fully observable from the measurements. The discrepancy is attributed to the lack of information of the road input disturbance. The only allowable unknown input to the system in the Kalman filter theory is a zero-mean Gaussian white noise, w_k in Equation (4.7), whereas in the current estimation problem, the unknown input (road disturbance) is not necessarily zero-mean (for instance, consider the case of a bump).

Further simulations confirm that by providing the road input information for the KF, the estimation quality associated with all the states is enhanced significantly. The estimation results are shown in Figure 19 and Figure 20. It is demonstrated in Figure 19 that the sprung mass

[1] It means that the Observability matrix has linearly independent columns or rows.

velocity is estimated accurately in this case. As depicted in this figure, the sprung mass velocity estimate, given by the KF with updated models, exactly matches the real signal. The same thing can be seen for the estimate of the wheel-hub velocity in Figure 20 (compare it with Figure 18). This issue is discussed further in Chapter 7, and solutions are proposed.

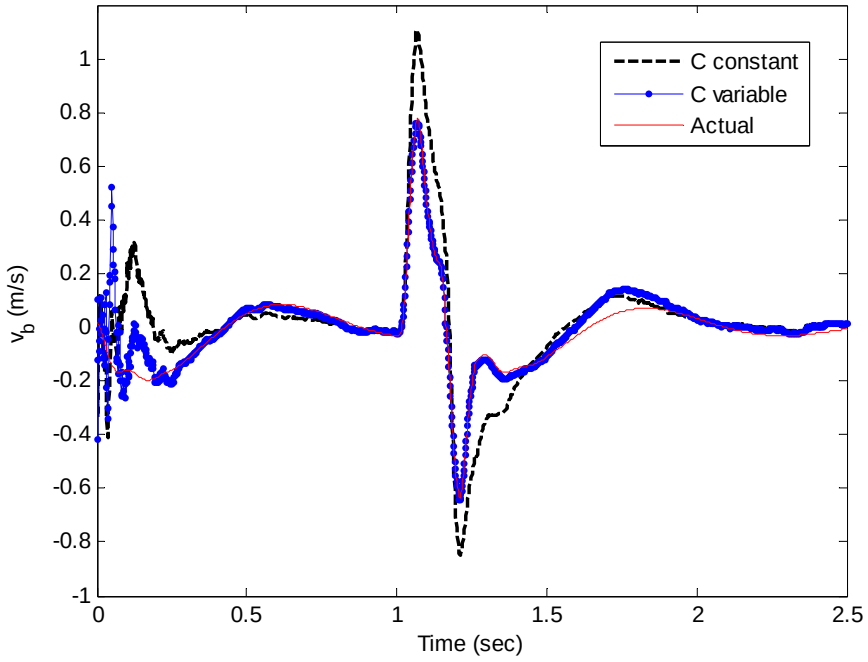

Figure 19: The graph compares the sprung mass velocity estimates obtained by the two different KFs with the real signal. Road profile information is provided for the KF models.

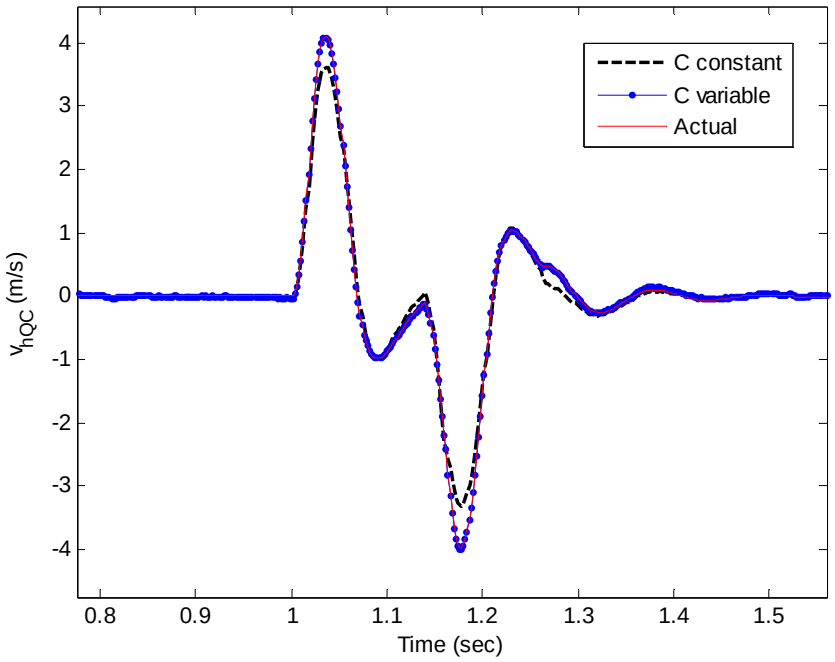

Figure 20: The graph compares the unsprung mass velocity estimates obtained by the two different KFs with the real signal. Road profile information is provided for the KF models. The graph zoomed in on the bump to give a better resolution.

The controllability matrix of the pair $(\Phi(k+1,k), Q_k^{1/2})$ also has full rank (Q_k is given in Equation (4.21)). According to the Lemma 1 of Section 4.2.1 (note that this lemma is only applicable for time invariant estimation problems which, with the assumption of constant damping coefficient, can be applied here), since both Observability and Controllability conditions are satisfied, the estimation error covariance matrix, P_k, and the Kalman gain, K_k, converge to constant matrices $\bar{P}$ and $\bar{K}$, respectively. $\bar{P}$ is the unique solution of the DARE and for this particular problem becomes:

$$\bar{P} = \begin{bmatrix} 0.00005 & -0.0002 & 0.000003 & -0.00001 \\ -0.0002 & 0.002 & 0.00001 & 0.0009 \\ 0.000002 & 0.00001 & 0.000001 & -0.00002 \\ -0.00001 & 0.0009 & -0.00002 & 0.002 \end{bmatrix}. \tag{5.34}$$

The steady-state Kalman gain matrix would then be:

$$\bar{K} = \begin{bmatrix} -0.0001 & 0.00001 \\ -0.0003 & -0.0005 \\ -0.00004 & -0.00009 \\ 0.0009 & -0.0013 \end{bmatrix}. \tag{5.35}$$

Estimation errors associated with the 2 DOF QC states are depicted in Figure 21 and Figure 22. Blue bounds of each plot are plus-minus square root (standard deviation) of the corresponding diagonal element of the error covariance matrix P_k.

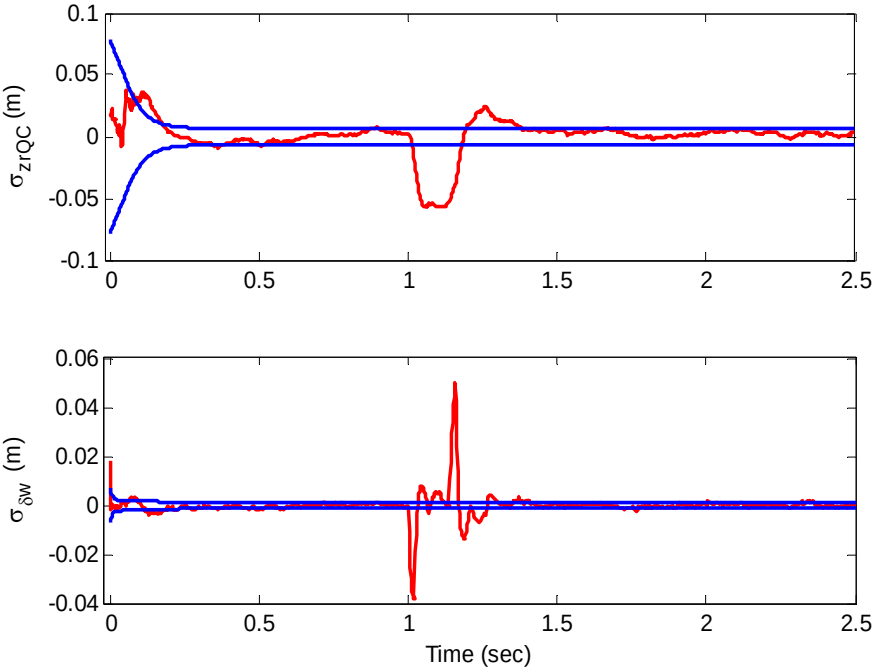

Figure 21: The top graph shows the error in the estimate of the suspension system deflection. The bottom plot was obtained for the tire deflection estimation error. Blue bounds are the corresponding error covariance given by theory.

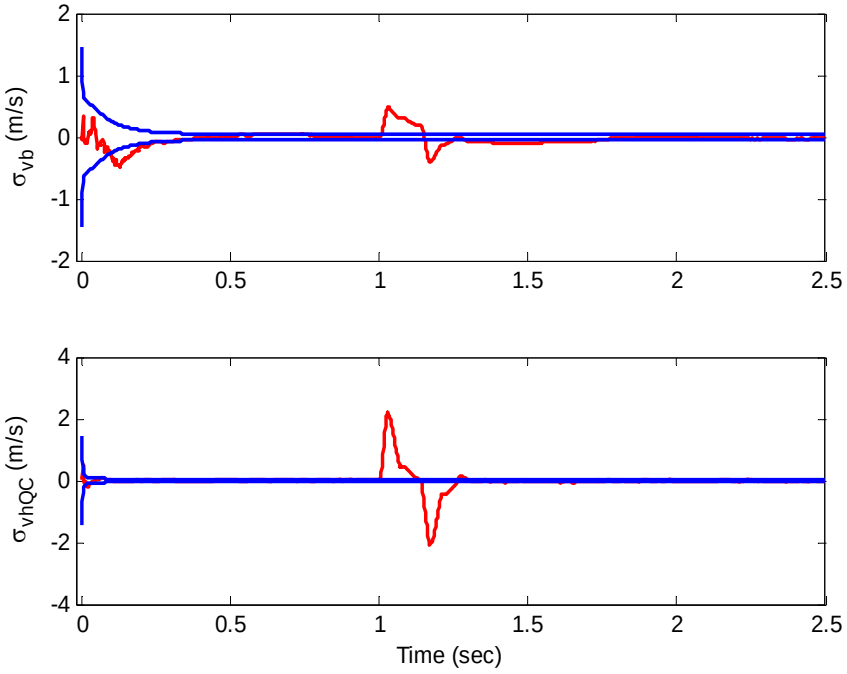

Figure 22: The top plot compares error in the estimate of the sprung mass velocity with the covariance bounds given by the theory. Estimation error corresponding to unsprung mass velocity is shown in the bottom graph.

It is apparent that the error covariance bounds eventually come together and converge to constant quantities. These quantities match the steady state covariance matrix elements (see Equation (5.34)) given by the DARE. Moreover, estimation errors are in agreement with the theoretically expected covariance matrix, which are updated and propagated by Equations (4.14) and (4.15), respectively. These indicate that the KF has been designed and works properly, even though one state is not estimated precisely (see Figure 17).

Measurements residual (or innovation signal), which is the difference between the actual and the estimated measurements vector at each time-step, is also computed. The consistency between the residuals and their theoretically expected covariance bounds is interpreted as the best reliability indicator of the KF (or the EKF). If the Ergodic properties are assumed for the innovation, and the process and measurement noises are uncorrelated, then the covariance and the mean value of the innovation signal are determined by:

$$E\left\langle (z_k - \hat{z}_k) \right\rangle = 0,$$
$$E\left\langle (z_k - \hat{z}_k)(z_k - \hat{z}_k)^T \right\rangle = H_k P_k(-) H_k^T + R_k \,, \tag{5.36}$$

where $\hat{z}_k$ is the estimate of the measurement vector. Figure 23 plots the residuals associated with the sprung and unsprung mass accelerations. The residual of the sprung mass acceleration is given in the top figure and the residual of the unsprung mass measurement in the bottom figure. Covariance bounds corresponding to each residual are also plotted. It can be seen that the measurement residuals are unbiased and there is indeed a consistency between the residuals and the theoretically expected covariance bounds given by Equation (5.36). The existence of this consistency is a firm justification of the KF reliability.

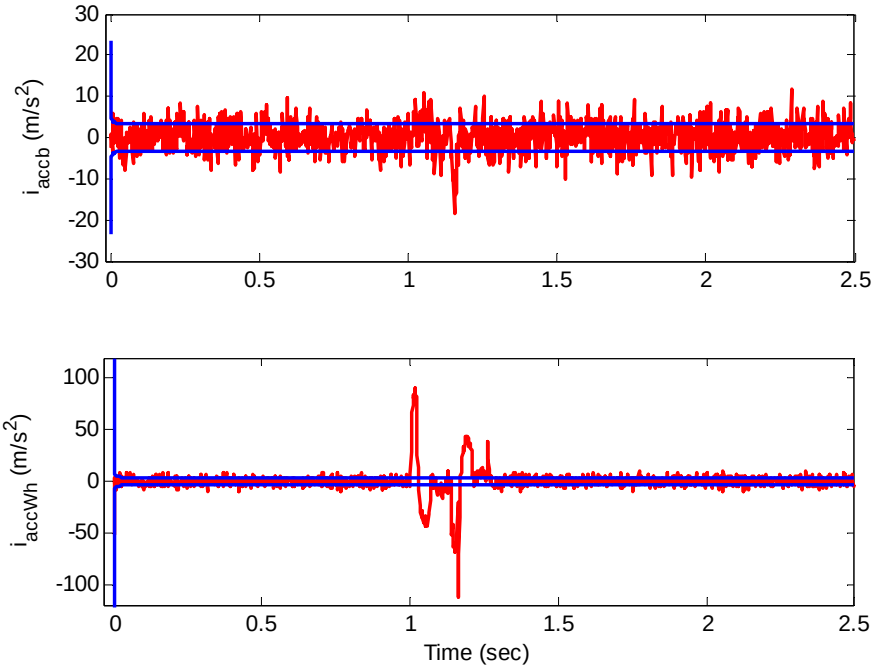

Figure 23: The graph illustrates the innovation signal associated with each accelerometer measurement [red]. Blue curves are expected variances of the residuals.

5.4.2 Real-time Estimation Results of the 1 DOF Quarter Car Model

Figure 24 shows the single DOF QC experimental setup. It consists of four parallel springs and an MR damper which isolate a mass from base excitations. The sprung mass weighs approximately m_b =52 N. The stiffness of each spring is 2346.7 N/m, resulting in a total stiffness of $k_s^{'}$ =9386.798 N/m (compare Figure 6 with Figure 24).

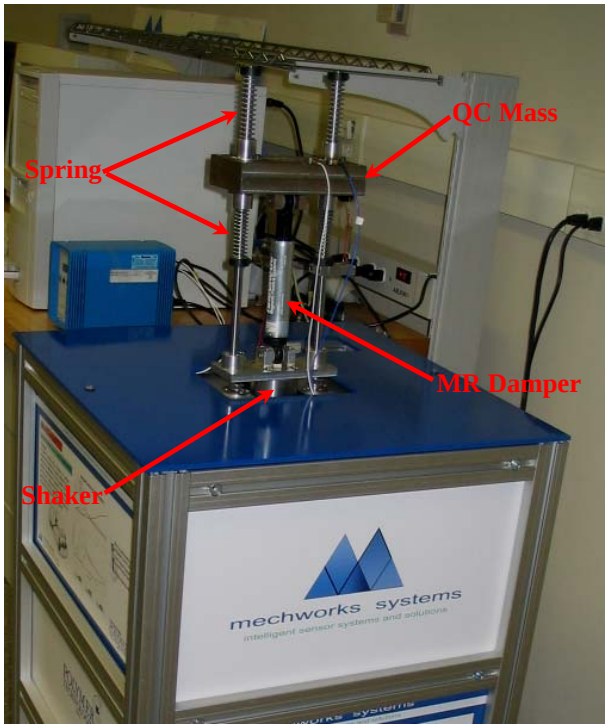

Figure 24: Experimental test rig of the single DOF Quarter car model.

The damper is a Lord Corporation's sponge-based MR damper (model RD-1097-01). Its maximum continuous working current is 0.5 A, and the maximum intermittent input current is 1.0 A. Also, the peak damping force of the damper is approximately 100N. Figure 25 plots the variation of the damper force with the applied current.

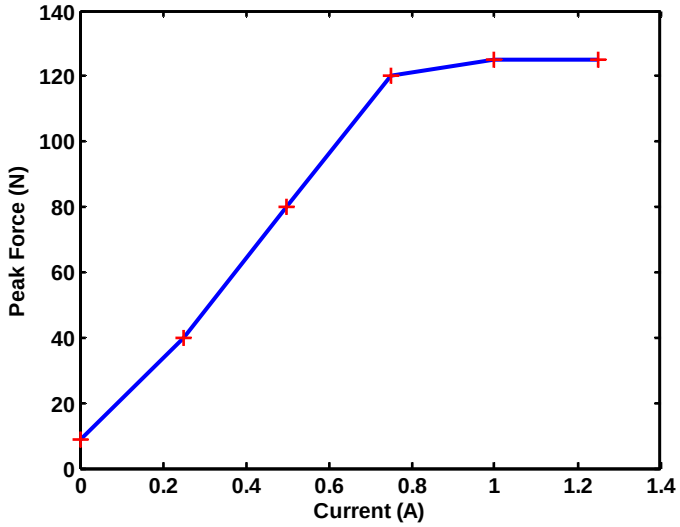

Figure 25: Damper force versus current.

The harmonic excitations to the base are provided by a shaker VTS40 [57]. The shaker is capable of oscillating the base with different amplitude accelerations in different frequencies. Piezoelectric Dactron [58] accelerometers, displayed in Figure 26, are used to measure acceleration of the sprung mass and the base. Furthermore, relative motion across the suspension is measured by an analog string potentiometer. Complete specifications of the experimental setup are provided in Appendix B.

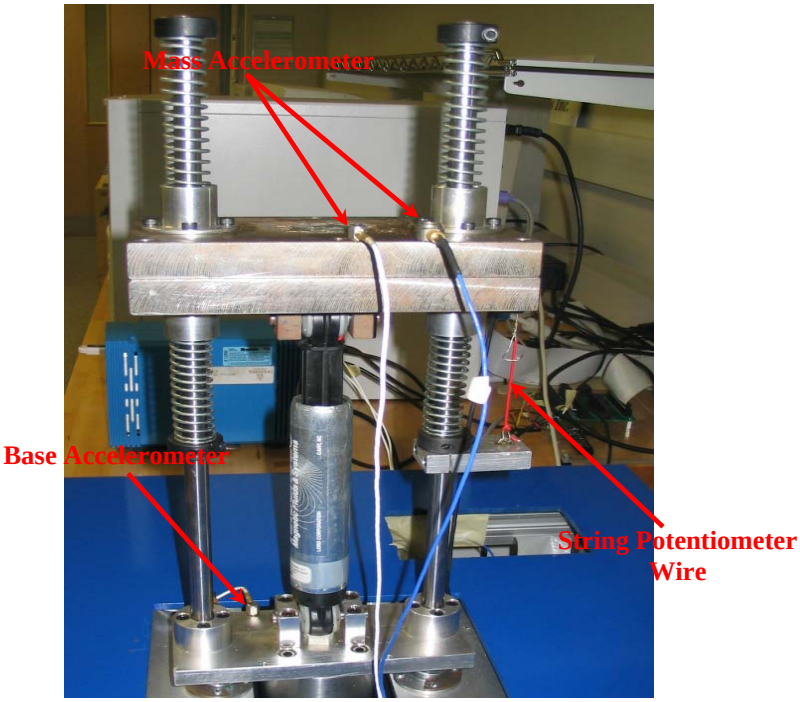

Figure 26: The 1 DOF QC Measurement system.

A software package was generated based on the Simulink®, the Real-Time Workshop® and the Real-Time Windows Target®, modules of the Matlab®, to execute the KF and the Skyhook controller in real-time. While the shaker vibrates the system, data from the sensors are sampled by a PCI-DAS 1602/16 multifunction A/D-D/A board at 500 Hz and transferred to the KF/controller software. Figure 27 shows a sample road input with the frequency of 4Hz and the amplitude of 0.6 m/s^2. Note that for the 1 DOF QC with the states given by Equation (5.12), acceleration of the base is the input to the system (see Equation (5.15)) .

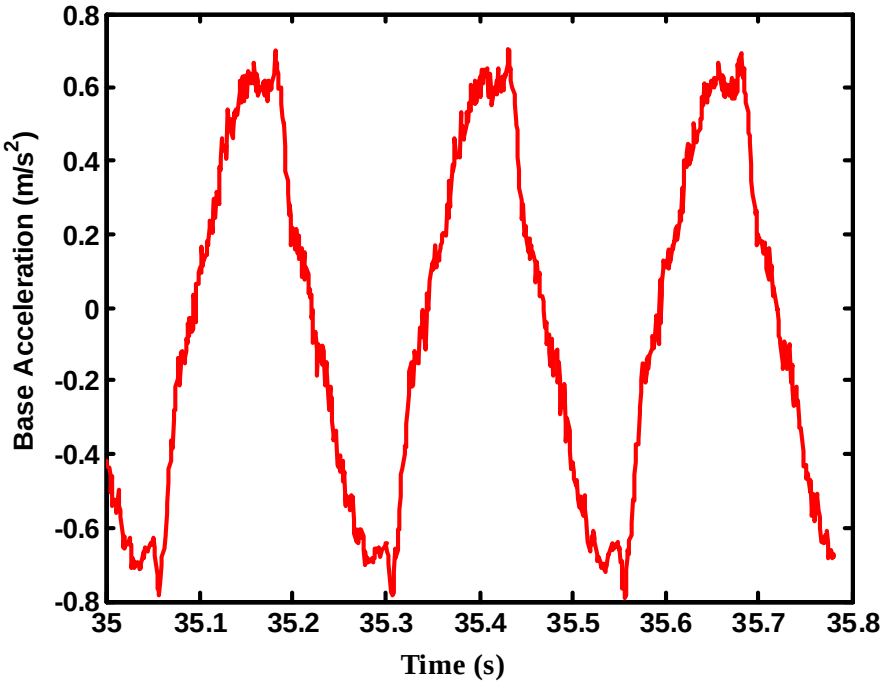

Figure 27: Sinusoidal input to the 1 DOF QC created by the shaker.

Similar to the previous case, without the road input information provided for the KF, the estimation quality is not acceptable. Consequently, the road input to the QC (the base acceleration) is also injected to the KF embedded models. For the acceleration input plotted in Figure 27, the sprung mass acceleration is displayed in Figure 28. The KF fuses this signal with the analytical model of the QC to estimate the states[1]. Estimation results are given in Figure 29, Figure 30 and Figure 31.

[1] From the Skyhook control implementation point of view, the states estimation of the 1 DOF QC is meaningless. But, it is included here just to keep the thesis integrity.

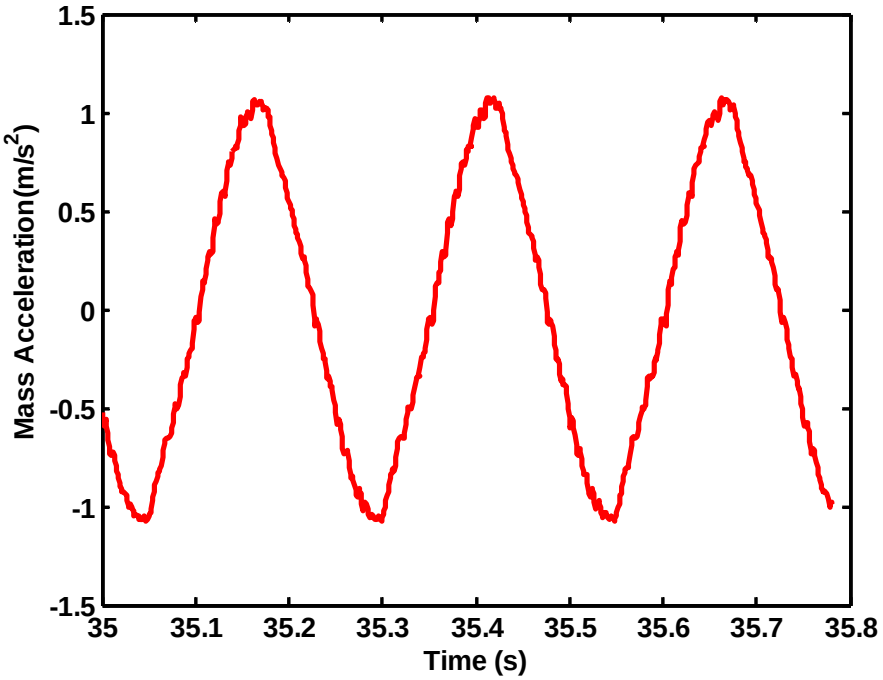

Figure 28: The QC's sprung mass acceleration.

Figure 29 illustrates the effectiveness of the KF in estimating the relative displacement across the shock. The graph has been zoomed in on the last 0.8 seconds to provide a better resolution. It is shown that by using two accelerometers, the KF can accurately provide the relative displacement. Although this state can be simply measured by a string potentiometer, the experiment aims to illustrate how effectively KF can rule out the sensors drift by utilizing the system analytical model. It can also be seen that although the measured relative displacement is being truncated due to the sensor deficiency, the KF estimated signal follows the exact sinusoidal pattern. The corresponding estimation error is plotted in Figure 30. Figure 31 compares the measured relative velocity (obtained by integrating the measurements of the string potentiometer) of the across the shock with the KF estimate. It is apparent that the estimated signal closely tracks the measured signal.

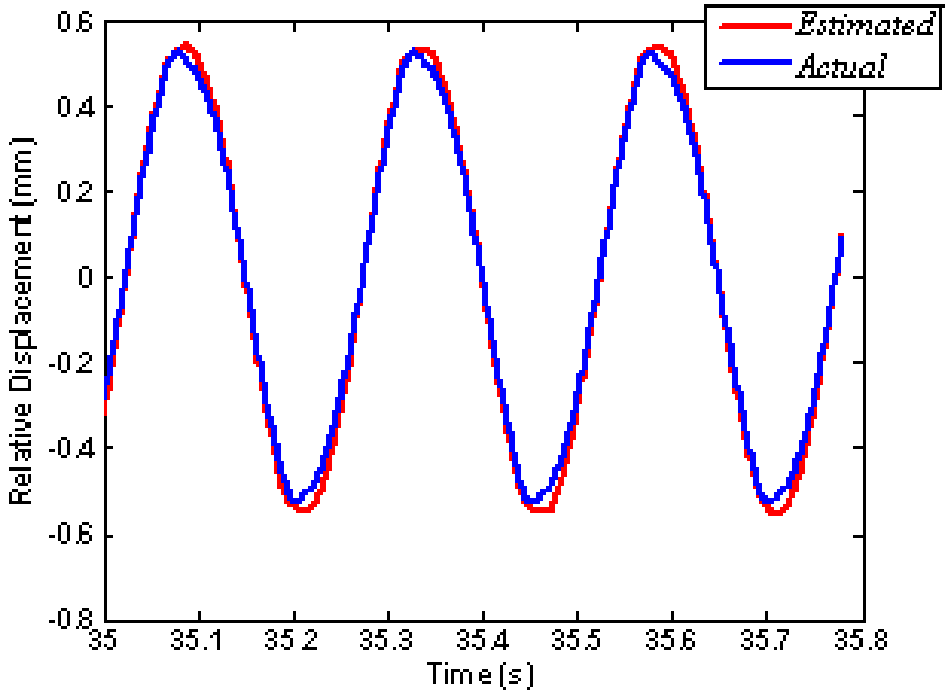

Figure 29: The graph compares the actual relative displacement of the single DOF vehicle suspension with its estimation.

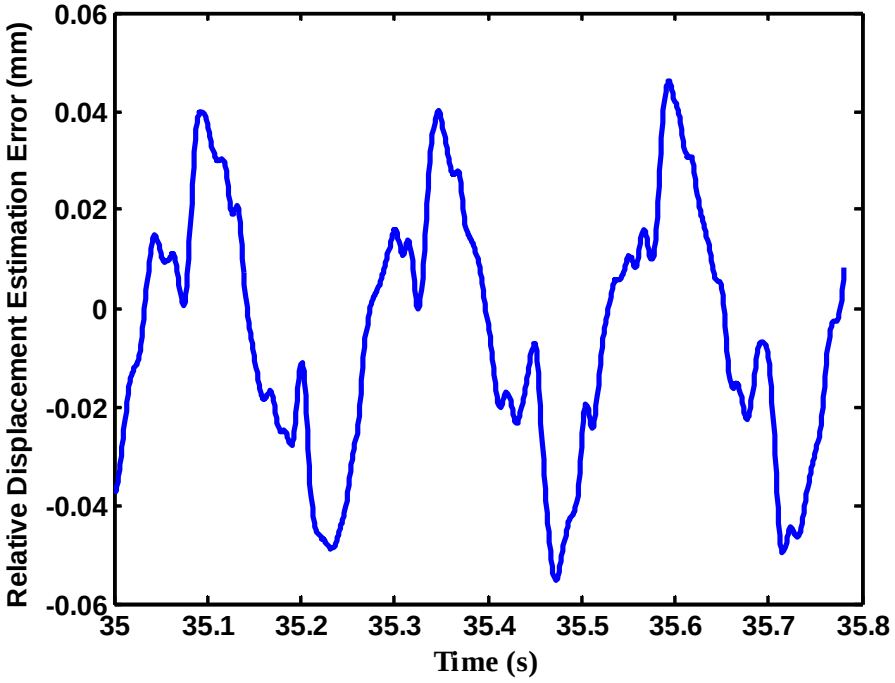

Figure 30: Error of the relative displacement estimate.

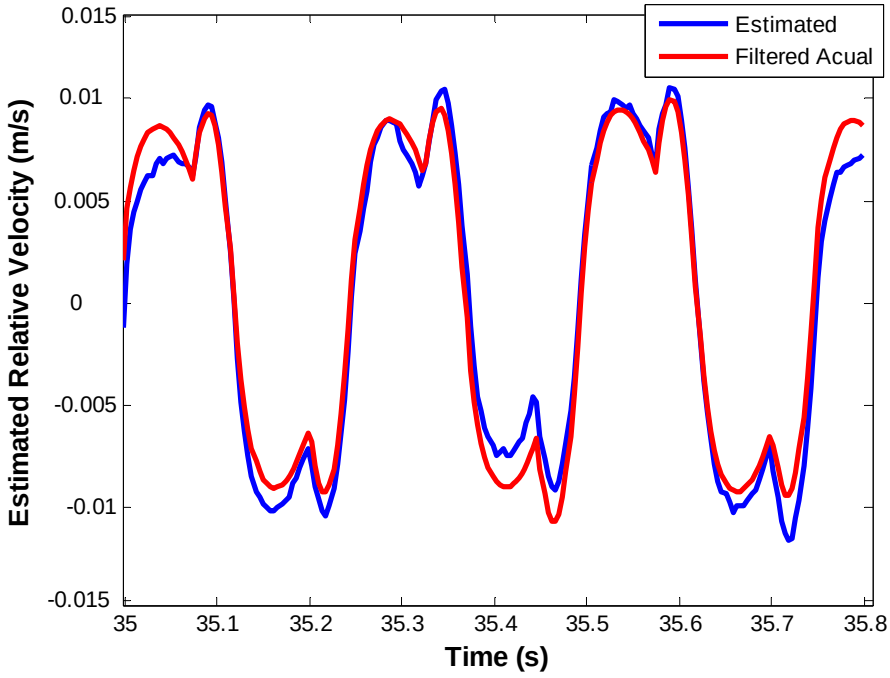

Figure 31: The graph compares measured and estimated relative velocity.

The Skyhook control command is also plotted in Figure 32. The most recent damping coefficient is sent to the KF to update the embedded models. Since the KF embedded models are continuously updated by the last Skyhook damping coefficient, the KF matrices do not converge to any steady-state value (as opposed to the 2 DOF QC's KF discussed in Section 5.4.1). However, they remain bounded (see Figure 33). Note that in this case, both Observability and Controllability matrices have full rank for any accepted value of the semi-active damping coefficient.

The KF appears to be working properly, since estimation errors are within the theoretical bounds, as displayed in Figure 33 . Similar to the last section, the blue bounds are the square root of the appropriate diagonal element of the error covariance matrix, computed by Equations (4.14) and (4.15).

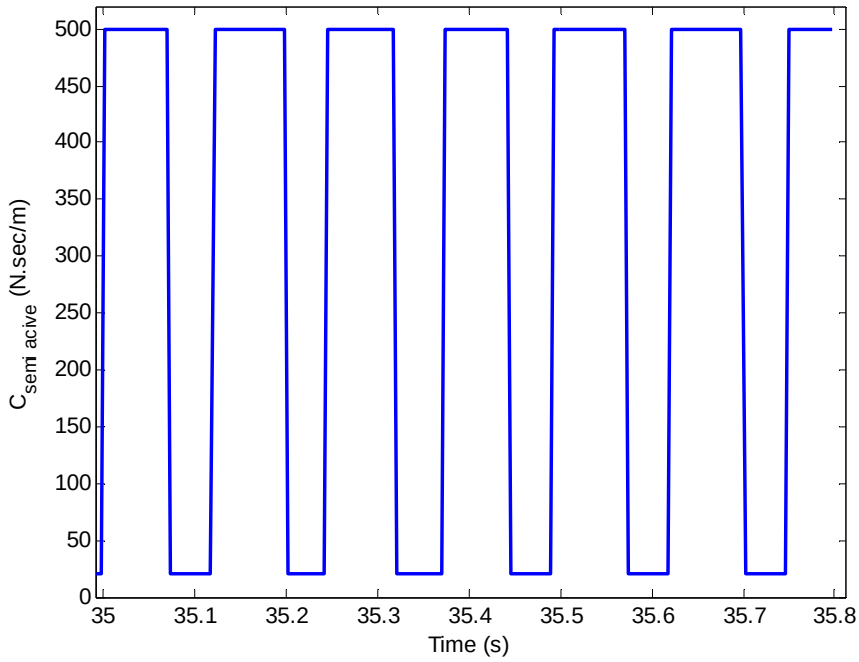

Figure 32: The Skyhook controller damping command

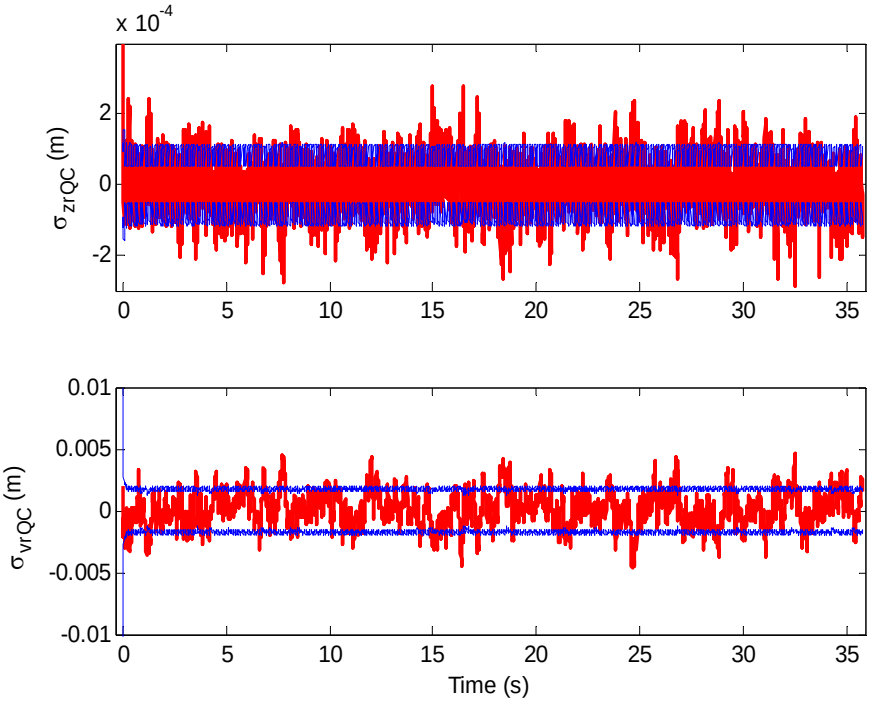

Figure 33: The top graph compares error [red] in the relative displacement estimate with the corresponding covariance bounds [blue] expected by theory. The window below demonstrates the same comparison for the relative velocity state.

Consistency between the sprung mass accelerometer residual and the theoretically expected bounds is illustrated in Figure 34. It is clear that the residual is unbiased and agrees with the covariance bounds. This confirms that the KF has been designed and works properly.

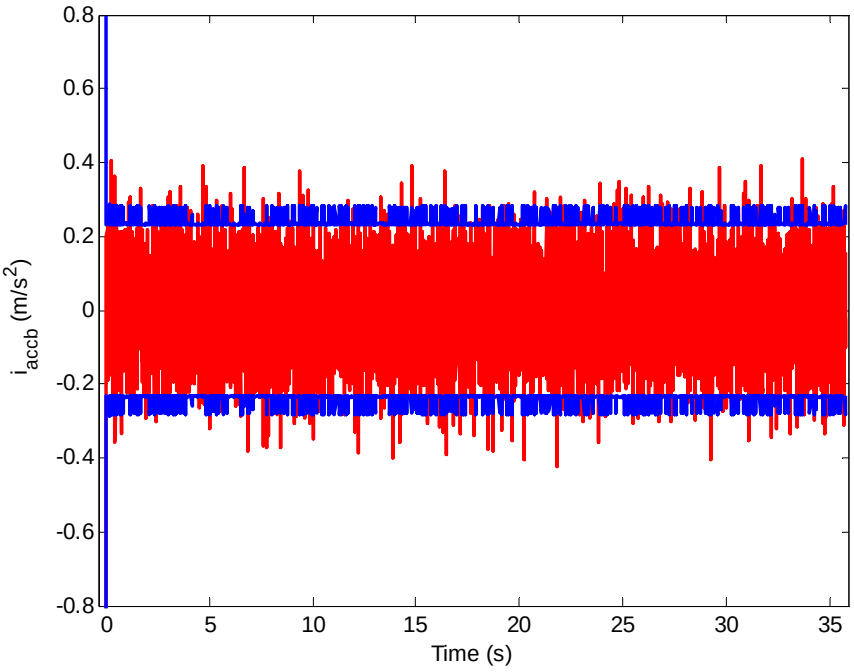

Figure 34: Residual of the accelerometer attached to the sprung mass [red]. Blue bounds are the expected standard deviations from the theory.

6 States Estimation of a Full Car

Chapters 6 and 7 address the states estimation of an actual vehicle equipped with the sensor configurations proposed in Chapter 3. First, an analytical model of the test vehicle in the vertical and lateral modes (wheel bounces, heave, roll and pitch of the body) is derived in Section 6.1. Then, Section 6.2 gives an approximate model for the complete measurement system of the vehicle. Finally, real-time estimation results are presented in Chapter 7.

6.1 Vehicle Dynamics Model

The vehicle dynamics, which are of interest for ride, handling and stability studies, include the vehicle's body heave, roll, and pitch motions, as well as the four wheel bounces. This typical 7 DOF characterization often applies to the design of active and semi-active suspension systems. For an efficient suspension system, the vehicle perturbations in the roll and pitch channels remain small ($\max(\varphi,\theta) < 6^\circ$). Therefore, the vertical and angular motions of the body can be described by the following linear differential equations [59]:

$$\begin{aligned} m\ddot{z}_{CG} = &-k_{sF}(z_{CG}+b\varphi-a\theta-z_1)-c_{LF}(\dot{z}_{CG}+b\dot{\varphi}-a\dot{\theta}-\dot{z}_1)-k_{sR}(z_{CG}+b\varphi+a\theta-z_2)\\ &-c_{LR}(\dot{z}_{CG}+b\dot{\varphi}+a\dot{\theta}-\dot{z}_2)-k_{sF}(z_{CG}-b\varphi-a\theta-z_3)-c_{RF}(\dot{z}_{CG}-b\dot{\varphi}-a\dot{\theta}-\dot{z}_3)\\ &-k_{sR}(z_{CG}-b\varphi+a\theta-z_4)-c_{RR}(\dot{z}_{CG}-b\dot{\varphi}+a\dot{\theta}-\dot{z}_4), \end{aligned} \tag{6.1}$$

$$\begin{aligned} I_{xx}\ddot{\phi} = &-bk_{sF}(z_{CG}+b\phi-a\theta-z_1)-bc_{LF}(\dot{z}_{CG}+b\dot{\phi}-a\dot{\theta}-\dot{z}_1)-bk_{sR}(z_{CG}+b\phi+a\theta-z_2)\\ &-bc_{LR}(\dot{z}_{CG}+b\dot{\phi}+a\dot{\theta}-\dot{z}_2)+bk_{sF}(z_{CG}-b\phi-a\theta-z_3)+bc_{RF}(\dot{z}_{CG}-b\dot{\phi}-a\dot{\theta}-\dot{z}_3)\\ &+bk_{sR}(z_{CG}-b\phi+a\theta-z_4)+bc_{RR}(\dot{z}_{CG}-b\dot{\phi}+a\dot{\theta}-\dot{z}_4), \end{aligned} \tag{6.2}$$

and

$$\begin{aligned} I_{yy}\ddot{\theta} = &\,ak_{sF}(z_{CG}+b\phi-a\theta-z_1)+ac_{LF}(\dot{z}_{CG}+b\dot{\phi}-a\dot{\theta}-\dot{z}_1)-ak_{sR}(z_{CG}+b\phi+a\theta-z_2)\\ &-ac_{LR}(\dot{z}_{CG}+b\dot{\phi}+a\dot{\theta}-\dot{z}_2)+ak_{sF}(z_{CG}-b\phi-a\theta-z_3)+ac_{RF}(\dot{z}_{CG}-b\dot{\phi}-a\dot{\theta}-\dot{z}_3)\\ &-ak_{sR}(z_{CG}-b\phi+a\theta-z_4)-ac_{RR}(\dot{z}_{CG}-b\dot{\phi}+a\dot{\theta}-\dot{z}_4), \end{aligned} \tag{6.3}$$

where z_{CG} stands for the vertical displacement of the body's CG, φ is the vehicle roll angle, and θ is its pitch deflection. The remaining variables and parameters are illustrated in Figure 35.

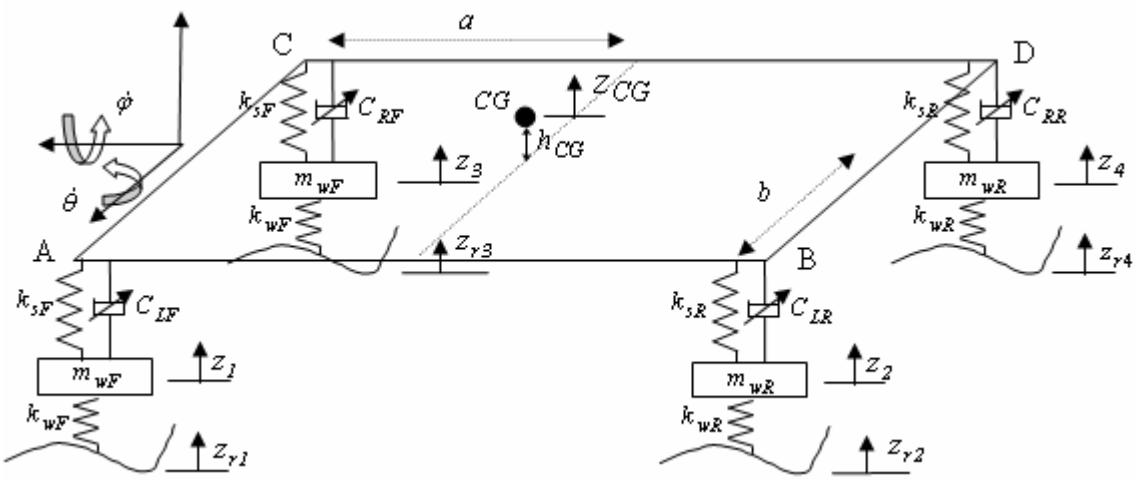

Figure 35: Vehicle multi-body representation. The vehicle is decomposed into five lumped masses with 7 DOF.

The vertical movements of LF, LR, RF and the RR wheel-hubs are denoted by z_1, z_2, z_3, and z_4, respectively. Again, by assuming the linear characteristics for the vehicle springs and shock absorbers, the following linear differential equations govern the wheel bounces:

$$m_{wF}\ddot{z}_1 = k_{sF}(z_{CG} + b\varphi - a\theta - z_1) + c_{LF}(\dot{z}_{CG} + b\dot{\varphi} - a\dot{\theta} - \dot{z}_1) - k_{wF}(z_1 - z_{r1}), \tag{6.4}$$

$$m_{wR}\ddot{z}_2 = k_{sR}(z_{CG} + b\varphi + a\theta - z_2) + c_{LR}(\dot{z}_{CG} + b\dot{\varphi} + a\dot{\theta} - \dot{z}_2) - k_{wR}(z_2 - z_{r2}), \tag{6.5}$$

$$m_{wF}\ddot{z}_3 = k_{sF}(z_{CG} - b\varphi - a\theta - z_3) + c_{RF}(\dot{z}_{CG} - b\dot{\varphi} - a\dot{\theta} - \dot{z}_3) - k_{wF}(z_3 - z_{r3}), \tag{6.6}$$

and

$$m_{wR}\ddot{z}_4 = k_{sR}(z_{CG} - b\varphi + a\theta - z_4) + c_{RR}(\dot{z}_{CG} - b\dot{\varphi} + a\dot{\theta} - \dot{z}_4) - k_{wR}(z_4 - z_{r4}). \tag{6.7}$$

Since any information regarding the relative displacement and velocity of the vehicle dampers is crucial for the semi-active suspension controller; the following state vector is introduced:

$$x = [x_1, ..., x_{16}]^T, \tag{6.8}$$

where x_1 to x_8 are the relative displacements and velocities, corresponding to the suspensions,

$$x_1 = (z_{CG} + b\phi - a\theta - z_1) = z_{r_{LF}},$$

$$x_2 = (\dot{z}_{CG} + b\dot{\phi} - a\dot{\theta} - \dot{z}_1) = v_{r_{LF}},$$

$$x_3 = (z_{CG} + b\phi + a\theta - z_2) = z_{r_{LR}},$$

$$x_4 = (\dot{z}_{CG} + b\dot{\phi} + a\dot{\theta} - \dot{z}_2) = v_{r_{LR}},$$

$$x_5 = (z_{CG} - b\varphi - a\theta - z_3) = z_{r_{RF}},$$

$$x_6 = (\dot{z}_{CG} - b\dot{\varphi} - a\dot{\theta} - \dot{z}_3) = v_{r_{RF}},$$

$$x_7 = (z_{CG} - b\phi + a\theta - z_4) = z_{r_{RR}},$$

and

$$x_8 = (\dot{z}_{CG} - b\dot{\phi} + a\dot{\theta} - \dot{z}_4) = v_{r_{RR}}. \tag{6.9}$$

Moreover, the absolute vertical velocity of each wheel-hub and the tire deflections build the rest of the vehicle state vector as follows:

$$x_9 = (z_1 - z_{r1}) = \delta_{w_{LF}},$$

$$x_{10} = \dot{z}_1 = v_{h_{LF}},$$

$$x_{11} = (z_2 - z_{r2}) = \delta_{w_{LR}},$$

$$x_{12} = \dot{z}_2 = v_{h_{LR}},$$

$$x_{13} = (z_3 - z_{r3}) = \delta_{w_{RF}},$$

$$x_{14} = \dot{z}_3 = v_{h_{RF}},$$

$$x_{15} = (z_4 - z_{r4}) = \delta_{w_{RR}},$$

and

$$x_{16} = \dot{z}_4 = v_{h_{RR}}. \tag{6.10}$$

z_{ri}, with $i = 1,...,4$, represents the road profile (the road vertical displacement) associated with the i^{th} wheel.

Another alternative to the state vector (6.8) is the minimal state vector of the 7 DOF vehicle which contains 14 states:

$$x = [x_1,...,x_{14}]^T, \tag{6.11}$$

where x_1 to x_6 represents kinematics of the body,

$$x_1 = z_{CG},$$

$$x_2 = v_{CG},$$

$$x_3 = \varphi,$$

$$x_4 = \dot{\varphi},$$

$$x_5 = \theta,$$

and

$$x_6 = \dot{\theta}. \tag{6.12}$$

The rest of the states are absolute vertical positions and velocities of the wheel-hubs as follows:

$$x_7 = z_1 = z_{h_{LF}},$$

$$x_8 = \dot{z}_1 = v_{h_{LF}},$$

$$x_9 = z_2 = z_{h_{LR}},$$

$$x_{10} = \dot{z}_2 = v_{h_{LR}},$$

$$x_{11} = z_3 = z_{h_{RF}},$$

$$x_{12} = \dot{z}_3 = v_{h_{RF}},$$

$$x_{13} = z_4 = z_{h_{RR}},$$

and

$$x_{14} = \dot{z}_4 = v_{h_{RR}}. \tag{6.13}$$

By selecting either sets of the states, the vehicle dynamics differential equations, Equations (6.1) to (6.7), can then be expressed in the following state space form:

$$\dot{x}(t) = A(t)x + Eu_d(t) + Lw(t). \tag{6.14}$$

However, with the sixteen states vector (6.8), the disturbance input in the realization (6.14), u_d, contains the road vertical velocities:

$$u_d = [\dot{z}_{r1}, \dot{z}_{r2}, \dot{z}_{r3}, \dot{z}_{r4}]^T, \tag{6.15}$$

but, with the minimal fourteen states vector, u_d is the vector of the road vertical displacements; that is:

$$u_d = [z_{r1}, z_{r2}, z_{r3}, z_{r4}]^T. \tag{6.16}$$

Moreover, $w(t)$ is a zero mean white noise process (random function input) with a spectral density Q, which accounts for the uncertainties in the vehicle's simplified model. System matrix A is shown as a time variable, since it is an explicit function of the semi-active suspensions damping coefficients c_{LF}, c_{LR}, c_{RF} and c_{RR} which are continually adjusted by the RHSC controller.

6.1.1 The Full Car Analytical Model Validation

The vehicle system and its various suspension components are very complex. Hence, the effort is usually focused on developing simple analytical models of the vehicle and the suspension system. The models are then verified and fine-tuned experimentally [60]. Figure 36 depicts a 4-poster test facility where the fully instrumented test vehicle is excited by sweeping frequency excitations created by four base shakers (posters). Moreover, the excitation of each shaker can be in-phase or out-of-phase with respect to the other shakers' excitation.

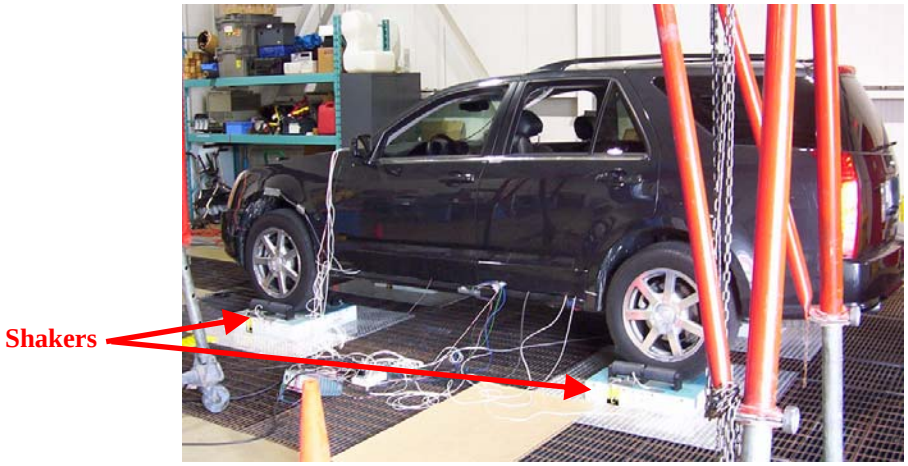

Figure 36: The Cadillac SRX test vehicle in the 4-posters test facility.

Figure 37 portrays acceleration of the LF wheel base shaker. The corresponding frequency content is also shown in Figure 38. The road input exhibits its maximum power in frequencies ranging from around 5 to 35Hz. Accordingly, the primary frequency components of the shaker excitation are located in the same frequency range to excite the same mode shapes of the vehicle, which are excited by real road disturbances. The real frequency response of the test vehicle is then compared with the spectrum predicted by the analytical models.

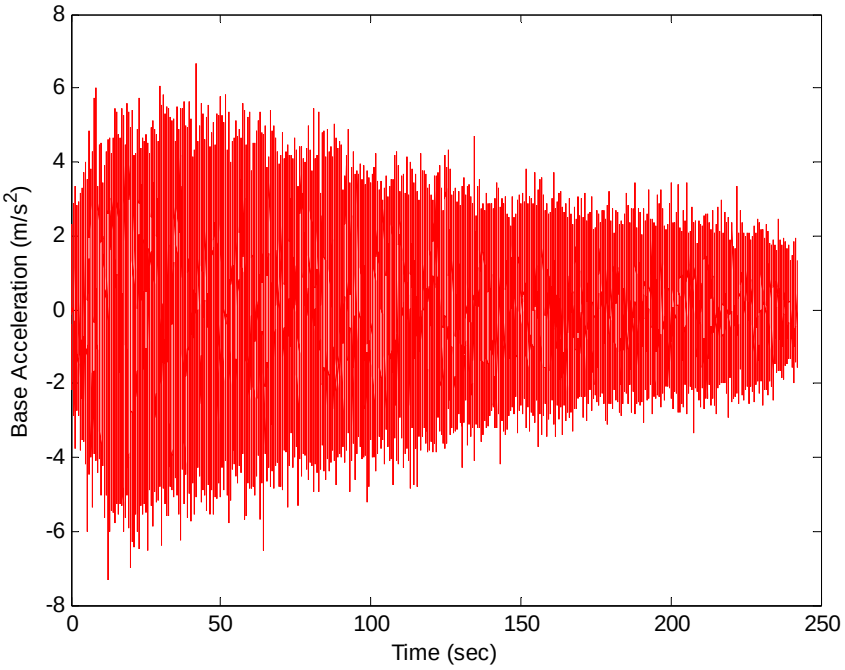

Figure 37: Input acceleration to the LF wheel by the base shaker.

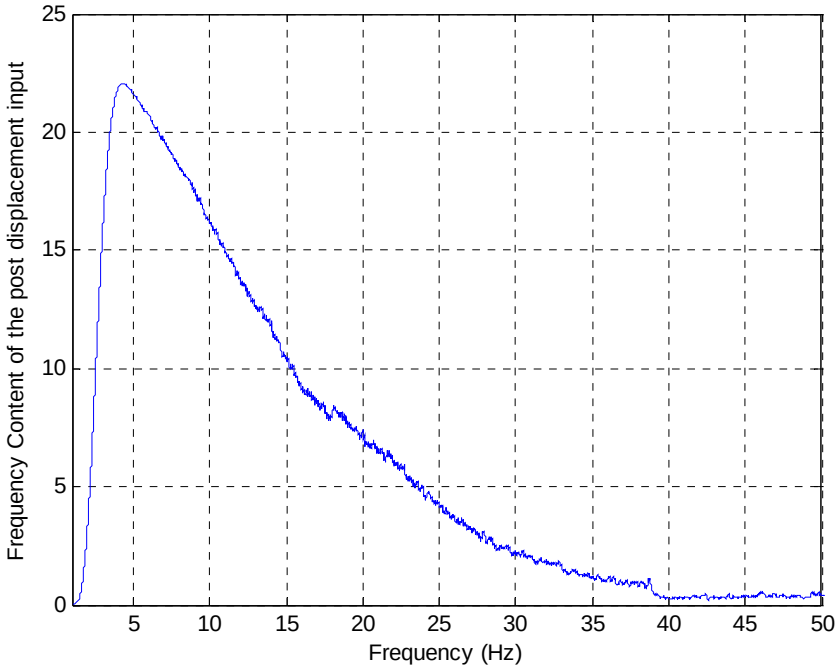

Figure 38: Frequency content of the input acceleration signal depicted in Figure 37.

Eigenvalues of the state matrix A in the vehicle model state space realization (Equation (6.14)) must match the resonance frequencies of the body and those of the wheels. The typical values are between 1 and 3Hz for the body (roll, pitch, and heave mode) and 8 to 12Hz for the wheels. For the Cadillac SRX, the eigenvalues of the state matrix (with minimum semi-active damping coefficients) are repetitively located at (-0.3±j10.5) and (-0.8±j58). The first eigenvalue corresponds to a natural frequency of $\omega_n \approx 1.7$Hz which relates to the body resonance frequencies. The second one, with $\omega_n \approx 9$Hz, represents the resonance frequencies of the wheels.

Figure 39 portrays the accelerometer signal, mounted on the LF corner of the vehicle body, in response to the 4-poster excitations. Figure 40 plots the frequency content of the signal. It is demonstrated that the real resonance frequency of the vehicle body is located at somewhere around 2Hz, which is in agreement with the analytical model prediction.

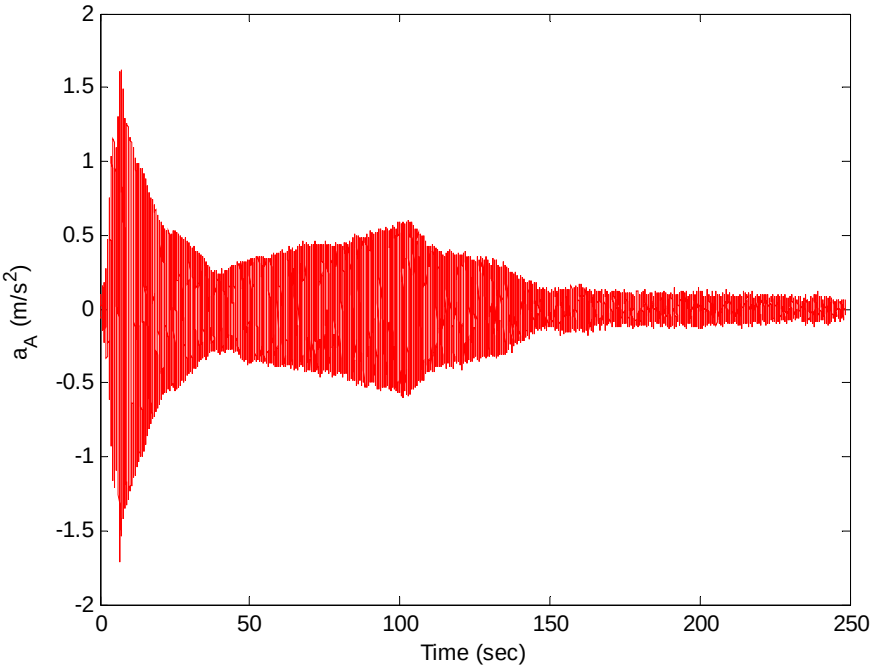

Figure 39: Acceleration of the LF corner of the body (point A, see Figure 35).

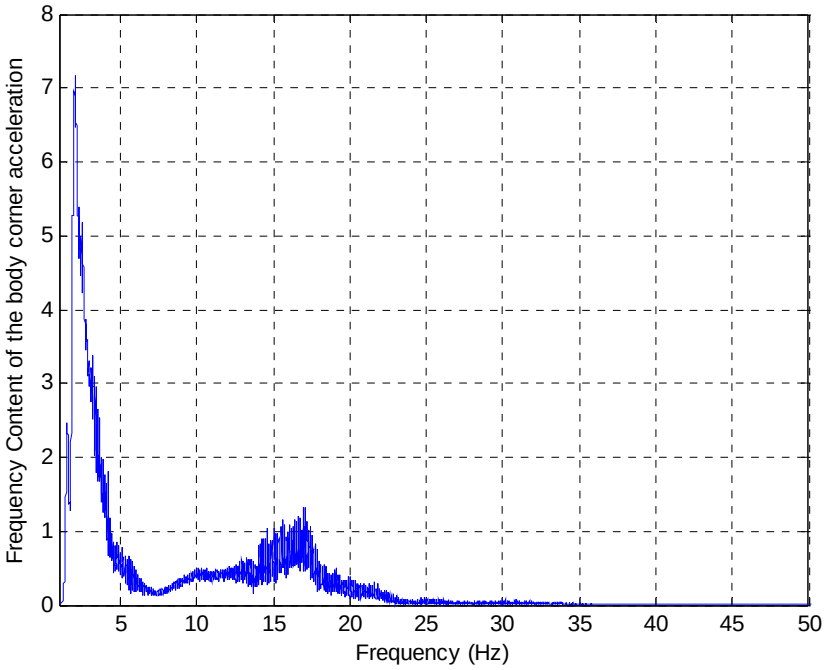

Figure 40: Frequency content of the acceleration of the body's LF corner (point A).

Similarly, a reading of the LF wheel-hub accelerometer is plotted in both time and frequency domains in Figure 41 and Figure 42, respectively. In Figure 42, the peak at the 2Hz belongs to the resonance frequencies of the body. The next peak, occurring at approximately 9Hz, represents the wheel resonant frequency. The vehicle's analytical model also predicts the same natural frequency for the wheels.

As described earlier, the 7 DOF vehicle model, given by Equation (6.14), is a simplified model which cannot express the behavior of the entire vehicle. For instance, there is another resonance peak at approximately 22Hz in Figure 42 which is not predicted by the analytical model. The peak represents the resonance frequency of a solid component of the LF suspension system which has not been considered in the 7 DOF model. However, the role of the additive white noise w in Equation (6.14) is to take into account such inaccuracies in the analytical model.

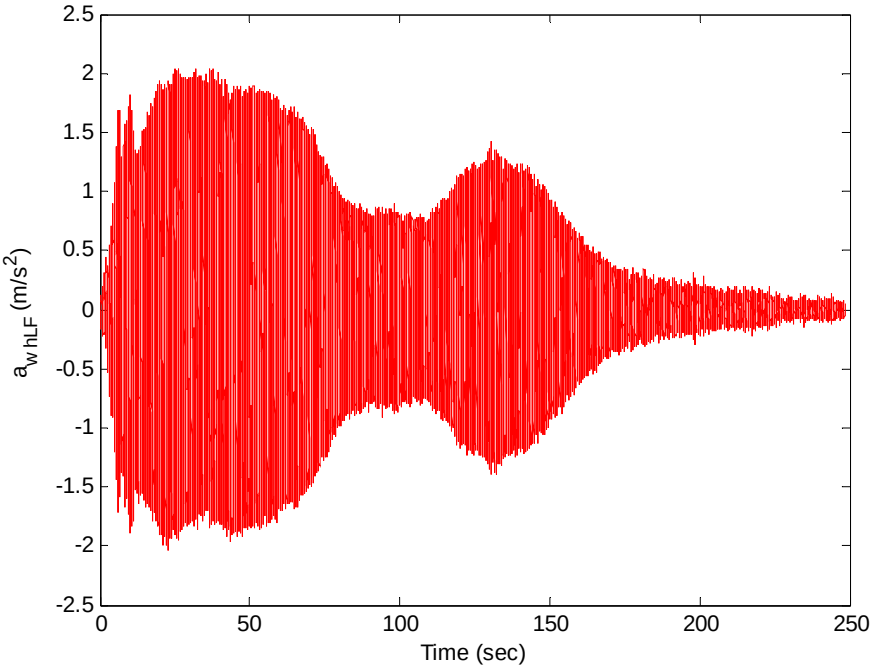

Figure 41: Acceleration of the LF wheel-hub.

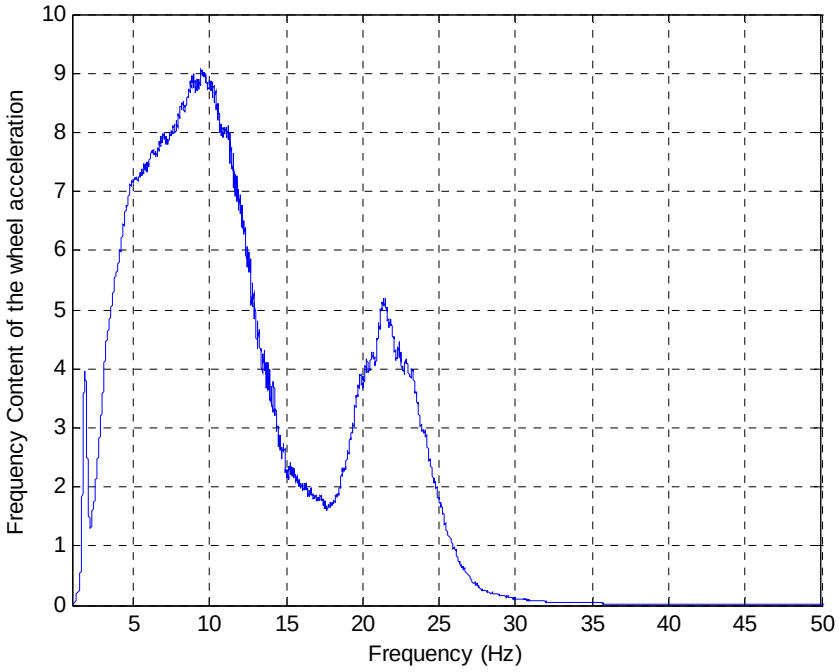

Figure 42: Frequency content of the LF wheel-hub acceleration.

6.2 Sensing System Analytical Model

In this section, an analytical model of the sensor configurations proposed in Chapter 3 is presented. It describes how the sensor measurements relate to the vehicle states. To avoid replication, the measurement model is derived for a complete sensor suite (the union of all the proposed sensor configurations), which consists of one IMU[1], two accelerometers per each vehicle corner, and four displacement sensors. The IMU is installed near the CG, and the accelerometers and the displacement sensors are mounted at the ends of the dampers.

Having considered the aforementioned sensory collection, the measurement vector z_k is then given by:

$$z_k = [\ddot{z}_{CG}, \dot{\phi}, \dot{\theta}, a_A, a_B, a_C, a_D, a_{wh1}, a_{wh2}, a_{wh3}, a_{wh4}, z_{r_{LF}}, z_{r_{LR}}, z_{r_{RF}}, z_{r_{RR}}]^T . \qquad (6.17)$$

In Equation (6.17), $\ddot{z}_{CG}$, $\dot{\phi}$ and $\dot{\theta}$ are the outputs of the vertical accelerometer and the roll-and-pitch rate gyros of the IMU. a_A, a_B, a_C, and a_D are the accelerations at each corner of the vehicle body, which are related to the acceleration of the CG by applying the Coriolis law:

$$a_i^B = a_{CG}^B + \omega^B \times (\omega^B \times r_i^B) + \alpha^B \times r_i^B \qquad (6.18)$$

The superscript B denotes the vectors, expressed in a body reference frame of the vehicle centered at CG. $\underline{r}_i^B$ with $i = A, B, C$, and D is the coordination vector corresponding to each body corner, expressed in the body frame (see Figure 35). Also, ω^B and α^B are the angular velocity and acceleration vector of the vehicle in body frame, respectively, given by:

$$\omega^B = [\dot{\varphi}, \dot{\theta}, \dot{\psi}]^T ,$$

and

$$\alpha^B = [\ddot{\varphi}, \ddot{\theta}, \ddot{\psi}]^T . \qquad (6.19)$$

By assuming a negligible yaw motion of the vehicle[2], after some mathematical manipulation, the accelerations at each corner are described as:

$$a_A = \ddot{z}_{CG} - (\dot{\varphi}^2 + \dot{\theta}^2) h_{CG} - a\ddot{\theta} + b\ddot{\varphi} ,$$

$$a_B = \ddot{z}_{CG} - (\dot{\varphi}^2 + \dot{\theta}^2) h_{CG} + a\ddot{\theta} + b\ddot{\varphi} ,$$

---

[1] Note that only three of the six IMU sensors are utilized by the estimator. The lateral accelerometer signal is directly sent to the stability controller. The yaw rate gyroscope and the longitudinal accelerometer signals are not used in this application.

[2] In a study regarding the RHSC design, this assumption is considered valid.

$$a_C = \ddot{z}_{CG} - (\dot{\varphi}^2 + \dot{\theta}^2)h_{CG} - a\ddot{\theta} - b\ddot{\varphi},$$

and

$$a_D = \ddot{z}_{CG} - (\dot{\varphi}^2 + \dot{\theta}^2)h_{CG} + a\ddot{\theta} - b\ddot{\varphi}, \tag{6.20}$$

where $\ddot{z}_{CG}, \ddot{\varphi}$, and $\ddot{\theta}$ are given by Equations (6.1) to (6.3).

$a_{wh1}, a_{wh2}, a_{wh3}$, and a_{wh4} are the wheel-hub accelerometers measurements which are modelled by Equations (6.4) to (6.7). And finally, $z_{r_{LF}}, z_{r_{LR}}, z_{r_{RF}}$, and $z_{r_{RR}}$ are the outputs of the displacement sensors measuring the relative displacements across the shocks.

After considering either the state vector (6.8) or (6.11), the measurement vector (6.17) is expressed by the following equation:

$$z_k = h(x_k, u_{d_k}, k) + v_k, \tag{6.21}$$

where h is a matrix vector of nonlinear combinations of the vehicle states and the road input disturbances. Nonlinearity of the measurement model (6.21) is due to the accelerometers at each corner (shock-end) of the vehicle body (see Equations (6.20)). Therefore, except the sensor configuration (d), the other sensor configurations of Chapter 3 are linear. For those configurations, the measurement system model, Equation (6.21), is simply rewritten as:

$$z_k = H_k x_k + D_d u_{d_k} + v_k. \tag{6.22}$$

Moreover, with the non-minimal state vector of the vehicle (the state vector (6.8)), the disturbance input matrix, D_d, becomes zero, and the measurement model is reduced to a more compact form of Equation (6.23):

$$z_k = H_k x_k + v_k. \tag{6.23}$$

In the above equations, v_k is the measurements noise vector which is assumed to be zero-mean Gaussian with a covariance of R_k. The power of the measurements noise is initially computed according to the sensor noise characteristics given by the manufacturers [76], [77], [78] and [79], and then fine-tuned during real-time tests. For this application, the Analog Devices MEMS accelerometers and gyroscopes are employed. The accelerometers are chosen from the model ADXL202E, and the gyroscopes are from ADXRS401 [80], [82]. Moreover, the displacement

sensors are[1] non-contact rotary position sensors from the Delphi [83]. Table 2 provides some of the sensors specifications. Complete information can be found in the corresponding data sheets [80], [83].

Table 2**:** Specifications of the measurement system sensors.

Gyroscope	
Scale Factor Error	$0.1\% FS$
Noise Density	$0.05 \text{ deg/ sec/ } \sqrt{Hz}$
Linear Acceleration Effect	0.2 deg/sec/g
Bandwidth	100Hz
Accelerometer	
Scale Factor Error	$0.3\% FS$
Noise Density	$200 \ \mu g / \sqrt{Hz}$
Bandwidth	150Hz
Displacement Sensor	
Noise Variance	0.003 m
Bandwidth	50Hz

Measurements of the accelerometers and the IMU are transferred at a rate of 500Hz with 12 bit resolution to a processing onboard computer. While, displacement sensors are sampled via a 10 bit A/D device at approximately 200Hz. The estimation algorithms presented in Chapter 4 are then applied to fuse the measurements data of a Cadillac SRX test vehicle and provide a central control unit with required states estimate. The real-time estimation results are presented in Chapter 7.

[1] The displacement sensors were originally installed by the Cadillac SRX test vehicle manufacturer (GM).

7 Real-Time States Estimation Results of a Vehicle

A software simulation and real-time processing platform running in VC++ is developed for the off-line simulation and real-time implementation of the estimation algorithms (KF, EKF or the UKF). The onboard processor, where the estimation software processes the sensor signals, is a Pentium 4 desktop with 3.4 GHz computational power (CPU) and 1 GB RAM. The estimation algorithm is executed at a rate of 500Hz, which is the rate that the accelerometers and the IMU signals are sampled[1].

The first test vehicle is a Toyota Tercel model 1993 (see Figure 2) with passive suspensions. It is then replaced by the Cadillac SRX model 2005, which is equipped with a semi-active suspension system. Some of the specifications of the Cadillac SRX are listed in Table 3.

Table 3: Cadillac SRX Exterior Dimensions.

Wheelbase (mm)	2957
Overall length (mm)	4950
Overall width (mm)	1844
Overall height (mm)	1722
Track (mm)	Front: 2957 Rear: 1580
Base Curb Weight (kg)	2013
Weight Distribution (% front/rear)	52/48

In each case, the fully-instrumented test vehicle is driven on a selected segment of Ring Road at the University of Waterloo (UW), with two consecutive bumps.

Figure 43 and Figure 44 reflect the satellite picture of Ring Road and the two bumps. Moreover, the experiments are conducted at various velocities to investigate the effects of the vehicle's longitudinal speed on the performance of the estimator.

[1] The bandwidth of semi-active control systems are restricted to maximum 50 Hz due to the dampers response time limitations [84] and [85]. Therefore, the estimator should not be executed at a rate of slower than five times[1] the controller speed (250 Hz). Since there was a capability of transferring the sensors' data at 500 Hz, the estimator update rate is also selected to be at 500 Hz (ten times greater than the controller).

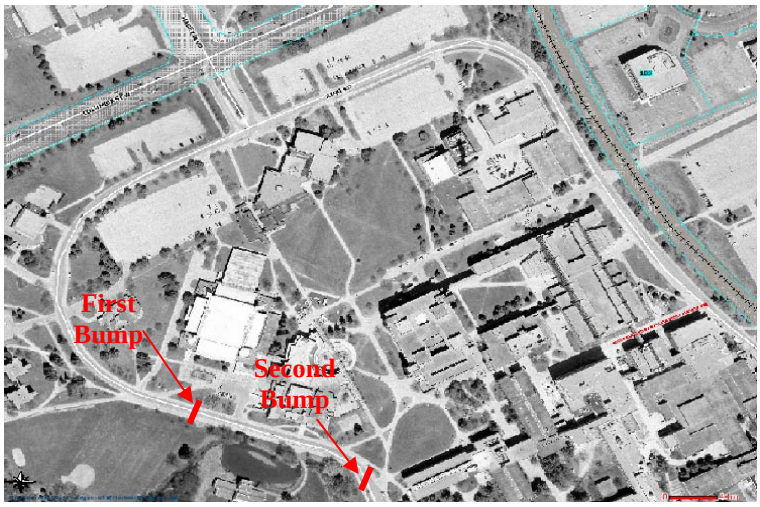

Figure 43: Satellite picture of UW's Ring Road with two bumps.

Figure 44: The first bump on Ring Road.

The vehicle's embedded model is the simplified 7 DOF model, which is given by Equation (6.14) of Section 6.1 (both realizations are examined). The model is digitized by a zero-order hold with a sampling rate of 500Hz. The sampled data form is written as:

$$x_{k+1}(-) = \Phi(k+1,k)x_k(+) + E_d u_{d_k} + w_k', \tag{7.1}$$

where the state transition matrix is expressed by the following exponential series:

$$\Phi(k+1,k) = e^{A\Delta T}. \tag{7.2}$$

The new disturbance input matrix becomes

$$E_d = \int_0^{\Delta T} e^{A\xi} E d\xi = \sum_{k=0}^{\infty} \frac{A^k \Delta T^{k+1}}{(k+1)!} E \,. \tag{7.3}$$

Moreover, the embedded measurement model is given by Equation (6.21) or the linear versions, Equation (6.22) or (6.23), depending on the selected state vector. Also, the road disturbance input should be evaluated in-line and fed back to the estimator embedded models. A preliminary method to provide the information of the road condition is to pass a unit white noise through the following first-order shaping filter:

$$F_{SF} = \frac{\alpha_{SF}}{s + \beta_{SF}} \,. \tag{7.4}$$

The bandwidth and the DC gain of the shape filter are selected as a function of the road roughness and the vehicle speed [14], [86].

The Cadillac MR dampers (see Figure 45) also need to be characterized before any vehicle test. The dampers' characterization is conducted at the UW's MTS test facility.

Figure 45: Cadillac SRX front semi-active damper (left) and the rear damper (right).

Figure 46 portrays a 3-D surface fit to the experimental data of the damper experiments. The curve describes the damping forces with respect to the applied control current and the relative velocity across the damper (relative velocity of the vehicle chassis to the wheel). After the semi-active damper characteristics are identified, the vehicle embedded models are updated at each real-time step. However, during the real-time implementations, it turns out that this increases the

estimation system computational burden without enhancing the estimation performance significantly.

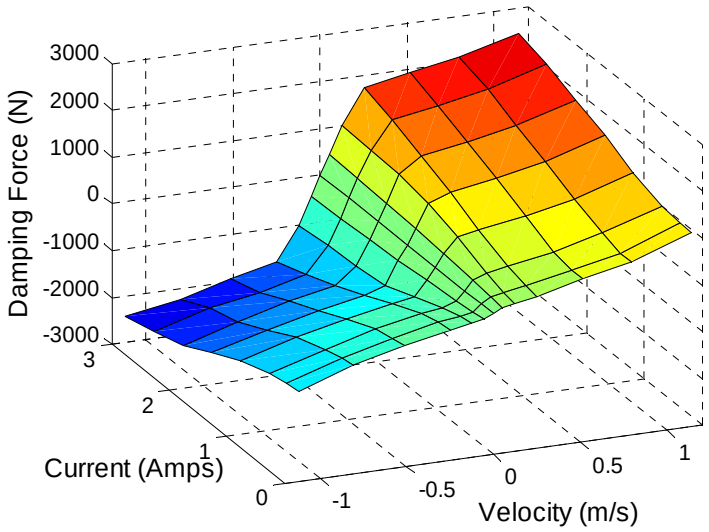

Figure 46: MR damper characteristics curve of the Cadillac SRX.

Figure 47 plots the EKF estimate of the relative displacement of the Toyota Tercel's LF suspension and the measured quantity, side by side. The EKF incorporates measurements of a combination of the sensor suites (a) and (b) – that is, 1 IMU and all the accelerometers. The speed of the vehicle is 40 km/hr during the experiment. Figure 47 shows the EKF estimate on the second bump. Looking at the positive side of the figure, it is apparent that the estimated relative displacement matches the measured data precisely. However, the measured signal is truncated from the negative side due to the mal-installation of the string potentiometer[1]. The rest of the Toyota Tercel's estimation results are also affected by the same reason and are therefore not presented anymore.

[1] It was installed without an offset, which is required to accommodate the compressions of the shock.

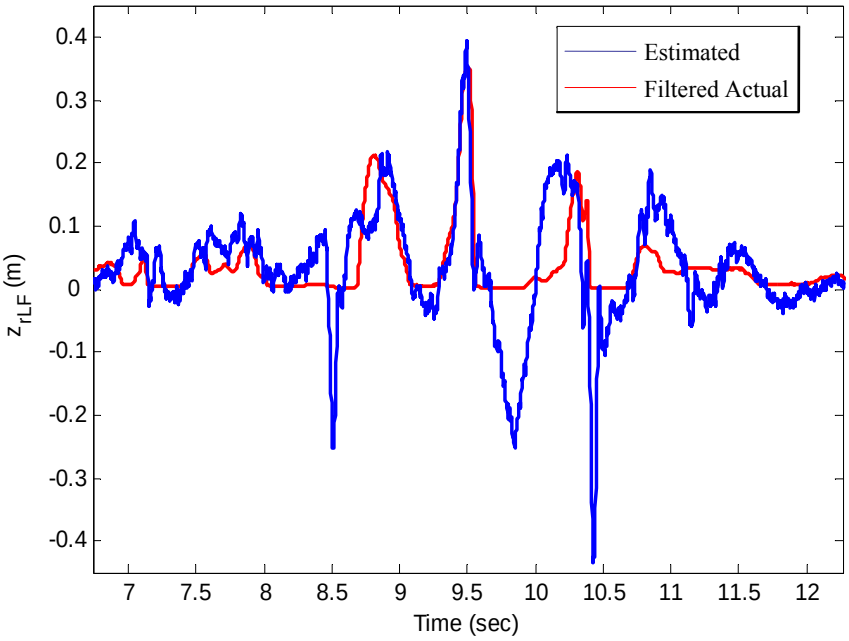

Figure 47: The graph compares the measured relative displacement of the Toyota Tercel's LF suspension with the EKF estimate.

The states estimation results of the Cadillac SRX with different sensor configurations are then presented in the following sections. The estimators performance are investigated for both vehicle models: the model with the state vector (6.8) and the one with the minimal state vector (6.11). In each case, estimation results associated with the states of the vehicle's LF corner are compared with the actual measurement data, except the tire deflection states that no actual information is provided by the existing measurement system.

7.1 State Estimation Results with the Non-Minimal Realization

The non-minimal (sixteen-state) realization of the vehicle model is given by Equations (6.14), (6.15) and (7.1), where the dimensions of the state transition matrix and the input matrix, Φ_k and E_d, are 16×16 and 16×4, respectively. The next sub-section gives the real-time estimation results of the KF, which uses the sensor suite (a).

7.1.1 One IMU and Four Accelerometers Sensor Suite

As described in Chapter 3, the IMU is attached adjacent to the vehicle's CG. It measures the vehicle's body roll and pitch rate, and also the vertical acceleration of the CG. The accelerometers, mounted on the wheel-hubs, measure the vertical acceleration of each wheel due to the road disturbances. The analytical model of the sensor suite (a) is given by the linear Equation (6.23). In this case, the Observability matrix is not full rank, and therefore it is expected to have some states of the vehicle not estimated properly.

During the experiments, the speed of the Cadillac is maintained at around 40 km/hr. The state estimation results are compared with the real sensors data in Figure 48 to Figure 57. As Figure 48 demonstrates, the estimate of the LF suspension relative displacement does not match the actual measurement. It is apparent that the relative displacement state is not observable through measurements of the sensor suite (a) and hence the corresponding estimation error grows over time[1].

[1] However, passing the estimated state through a high-pass filter recovers the true signal.

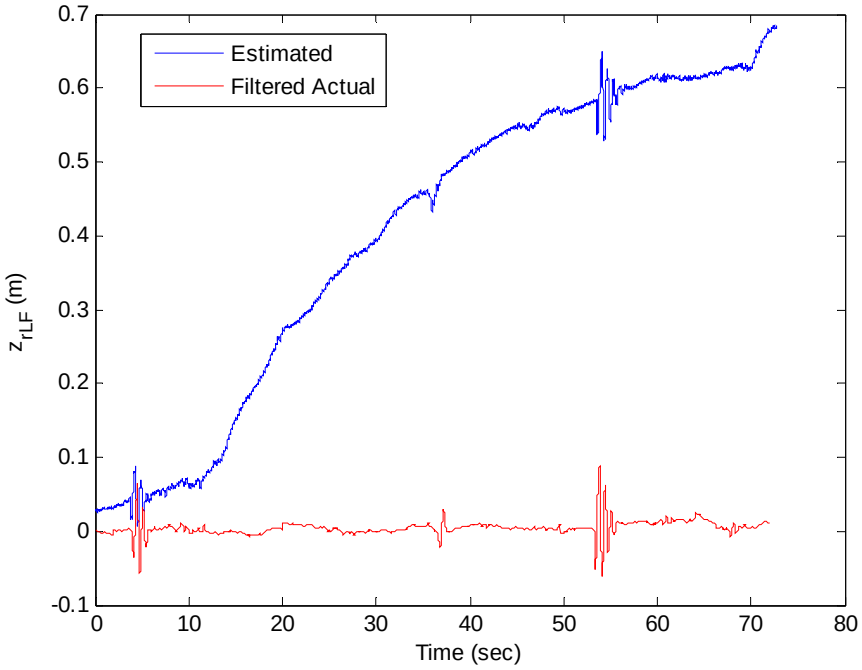

Figure 48: Performance of the KF with 1 IMU and four accelerometers in real time. The graph compares the actual relative displacement of the vehicle suspension with its estimation.

The measured and estimated relative velocity is displayed in Figure 49. The plots have been zoomed in on the first bump to show the estimation performance with a better resolution. It appears that the KF does a much better job in estimating the relative velocity state. The differences between the two signal peaks are attributed to the fact that no knowledge regarding the bump input is provided for the estimator's embedded models in real time.

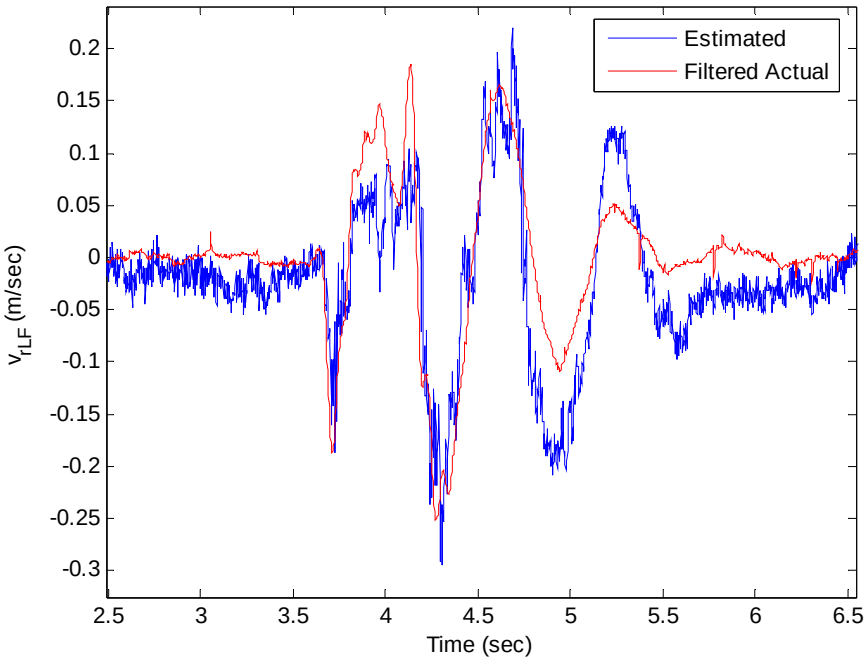

Figure 49: The graph relates the actual relative velocity with its estimation zoomed in on the first bump.

From Figure 50 and Figure 51, it is obvious that the KF cannot estimate the wheel-hub velocity. It is apparent that, specifically, at the leading edge and tailing edge of the bump (at approximately t = 3.7 sec and t = 4.1 sec, respectively), the estimated state travels in an inverse direction. However, after a fairly long transient time, the estimated signal finally attains the same pattern as that of the actual one. Looking at the experimental data reveals that the deviation of the estimated signal from the actual signal occurs when the significant disturbance input (the bump) is introduced to the vehicle. Indeed, the coloured output noise of the shape filter (7.4) is not able to resemble the bump input information for the KF embedded models[1]. This is also explained by the wheel accelerometer residuals (see also the measured and the KF estimate of the LF wheel-hub acceleration in Figure 53). As illustrated in Figure 52, residuals are reasonably small and within the theoretically expected bounds until the vehicle hits the road irregularities (see the residuals at approximately t = 5 sec (first bump), t=40 sec (hole) and t=60 sec (second

[1] Note that with the non-minimal realization, u_d is the road vertical velocity which is non-zero only at the leading and trailing slopes of the bump. For the the rest of the bump u_d is zero. That's why at the leading and trailing slopes of the bump, deviation of the measured and estimated signals occurs.

bump)). At these moments, the residuals are sharply increased, which indicates that the KF does not work properly and that some states are not estimated accurately.

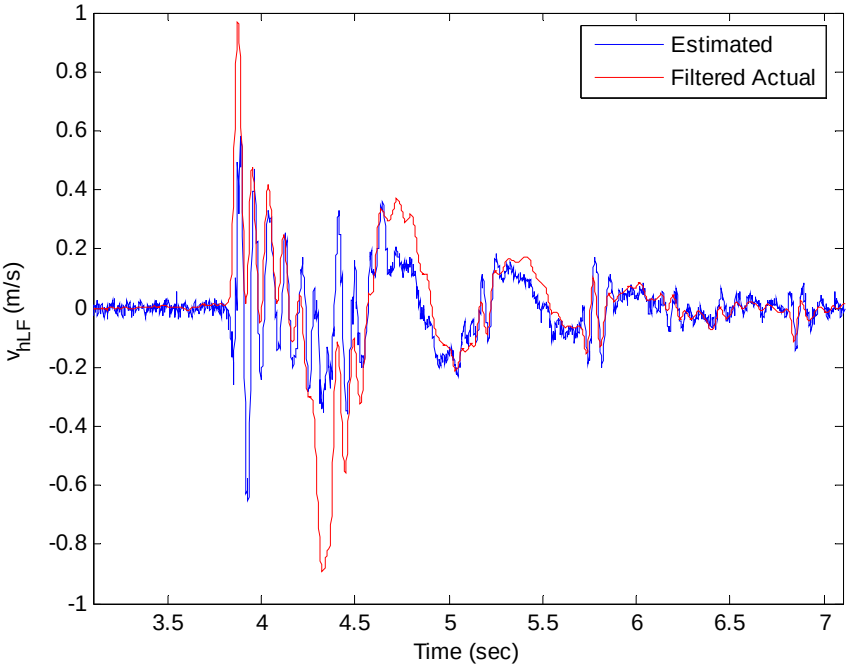

Figure 50: The graph compares the actual velocity of the wheel-hub with its estimation zoomed in on the bump.

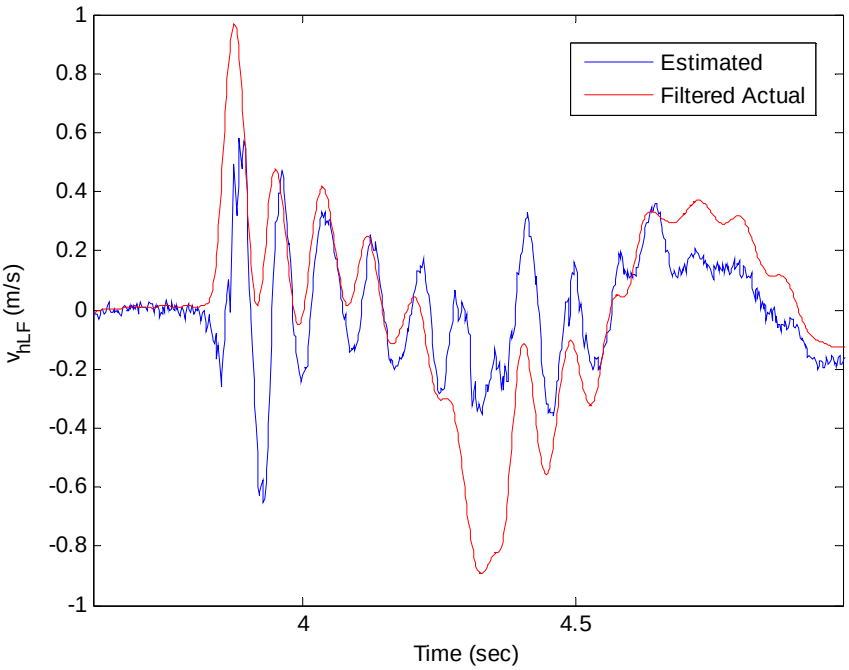

Figure 51: The graph compares the actual velocity of the wheel-hub with its estimation zoomed in on the bump.

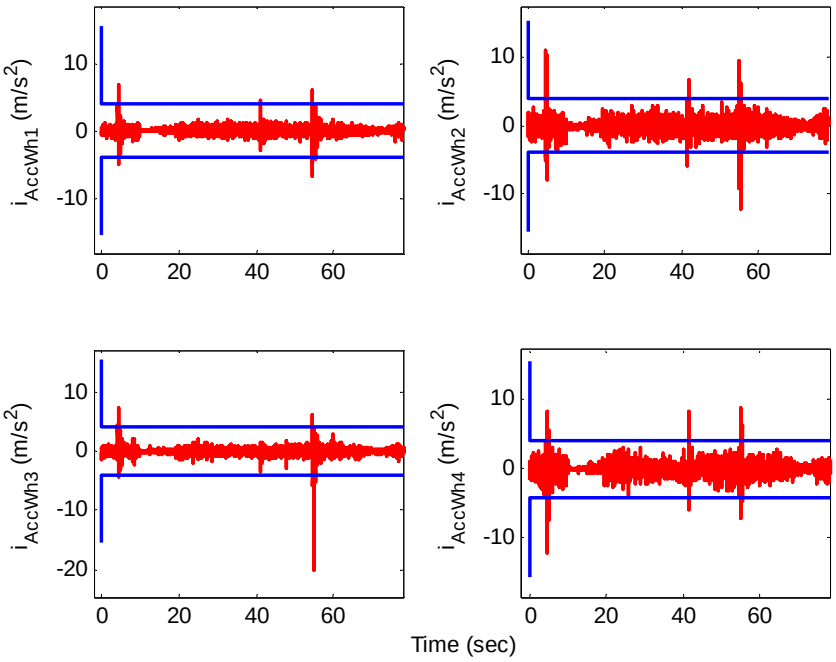

Figure 52: Innovation signal (residual) of each accelerometer measurement [red] and expected variances of the residuals given by the KF [blue].

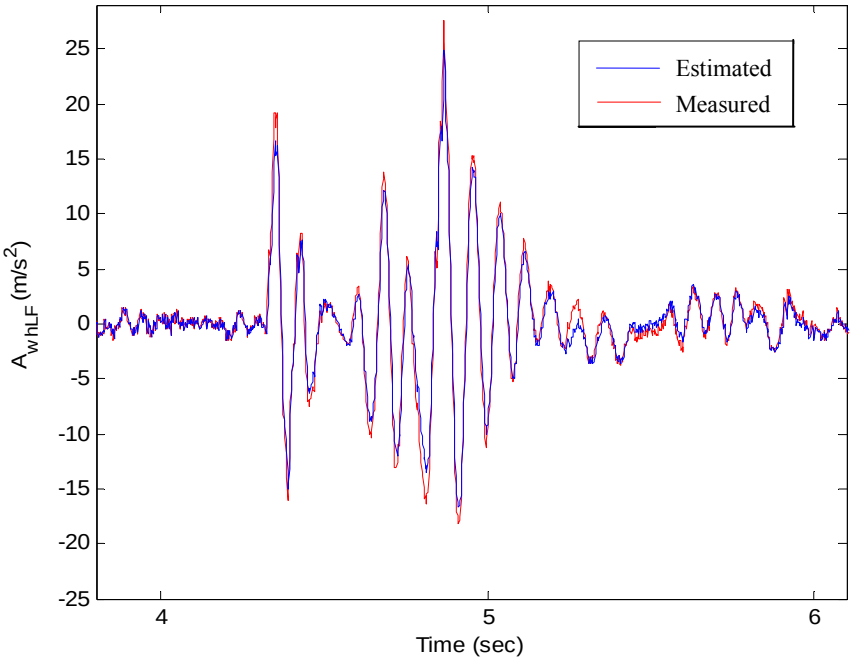

Figure 53: The graph compares the measured LF wheel-hub (wheel No.1) accelerometer and the KF estimate.

Figure 54 and Figure 55 also compare two measurements of the IMU, pitch rate and acceleration of the CG, with the corresponding KF estimates.

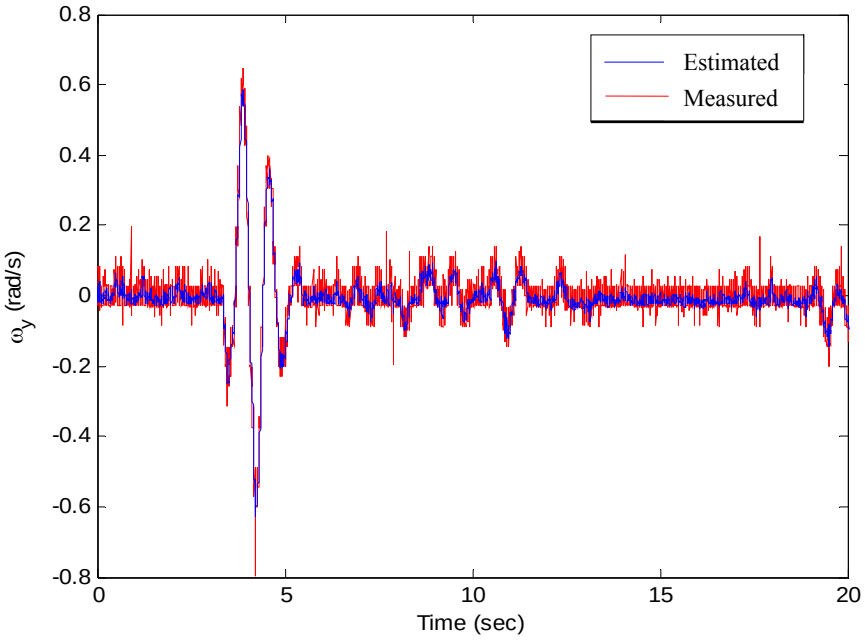

Figure 54: The graph compares the measured pitch rate of the test vehicle with the KF estimate.

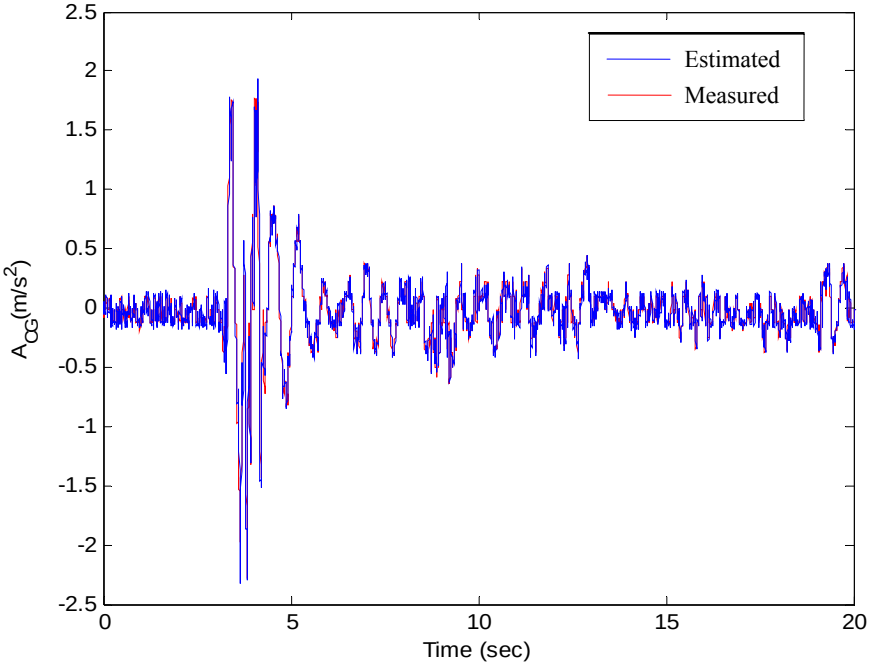

Figure 55: The graph compares the actual measurement of the vehicle body's CG with the KF estimate.

Figure 56 depicts the estimation error, associated with the LF suspension relative displacement. As illustrated earlier in this section, the relative displacement is not evaluated correctly by the KF, resulting in an unstable estimation error. The blue bounds have been obtained by taking the square root of the appropriate diagonal element of the error covariance matrix. They indicate how confident the KF is with respect to the corresponding estimation product. The expansion of the error covariance bounds, reported by the KF, implies that it confirms the unobservability of the state.

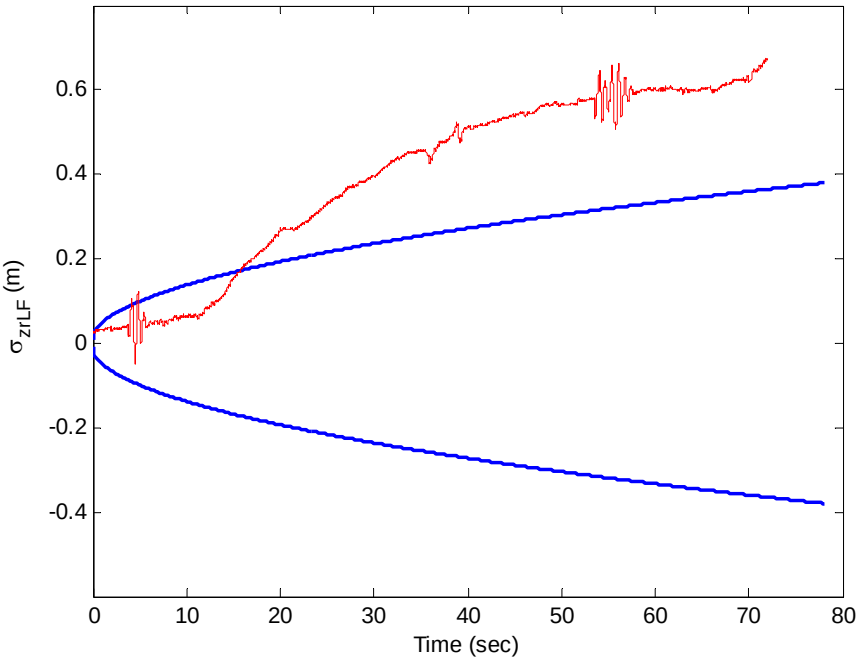

Figure 56: The graph illustrates estimation error [red] corresponding to the estimate of the LF shock relative displacement and the error covariance bounds [blue].

The estimation errors of the suspension relative velocity and the absolute velocity of the LF wheel-hub are given in Figure 57. The convergence of the covariance bounds[1] in Figure 57 denotes that both states are observable by the KF using the measurement system (a). However, it is demonstrated by Figure 50 and Figure 51 that, due to the lack of information of the road disturbance input, the KF cannot provide the absolute velocity state efficiently. In this case, not only the KF estimate is poor, but the KF thinks (on the basis of the computed error covariance)

[1] It implies that the KF remains confident to its estimates accuracy.

that the estimate is better than what it really is (observe the moments where the estimation errors are out of the bounds).

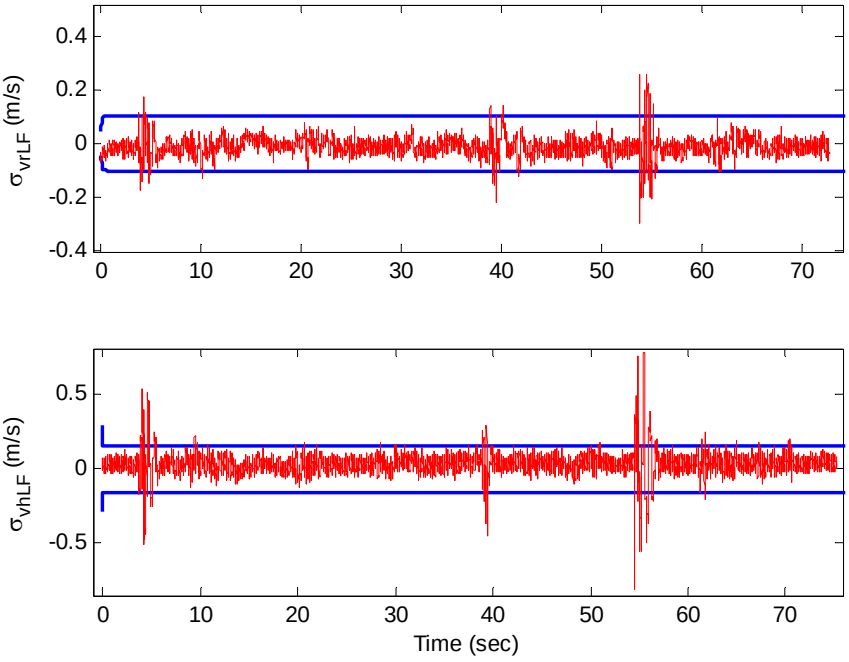

Figure 57: Performance of the EKF with 1 IMU and four accelerometers. The state estimation errors are red and the KF evaluated error covariance bounds are blue.

7.1.2 Four Displacement Sensors and One Lateral Accelerometer Sensor Suite

This section describes performance of the KF incorporating four displacement sensors (sensor suite (c)). The lateral accelerometer, mounted at the vehicle CG, produces the required information for the stability controller. The Observability matrix of the system with this sensor configuration has full rank. Therefore, it is expected that the KF provides an accurate estimate of all the states this time. The real-time experiments are carried out at a speed of 30 km/hr at the UW's Ring Road. The vehicle state estimation results are recorded in Figure 58 to Figure 65. Figure 58 illustrates that even though the measurement is a noisy signal with sharp spikes, the KF extracts the true signal efficiently. Indeed, the KF offers signal smoothing to a great extent,

free of any phase lag. However, to completely eliminate the spikes[1], a digital Butterworth low-pass filter with the appropriate bandwidth is implemented for the remaining experiments.

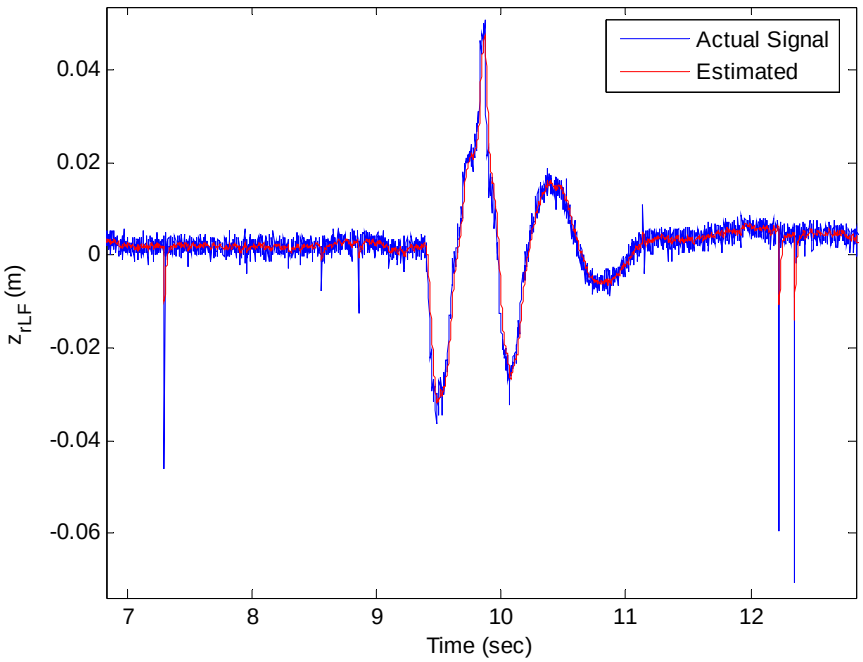

Figure 58: Performance of the KF with four displacement sensors in real time. The graph compares the measured relative displacement of the vehicle LF suspension with its estimate zoomed in on the first bump.

[1] The control system performance is degraded due to the spikes.

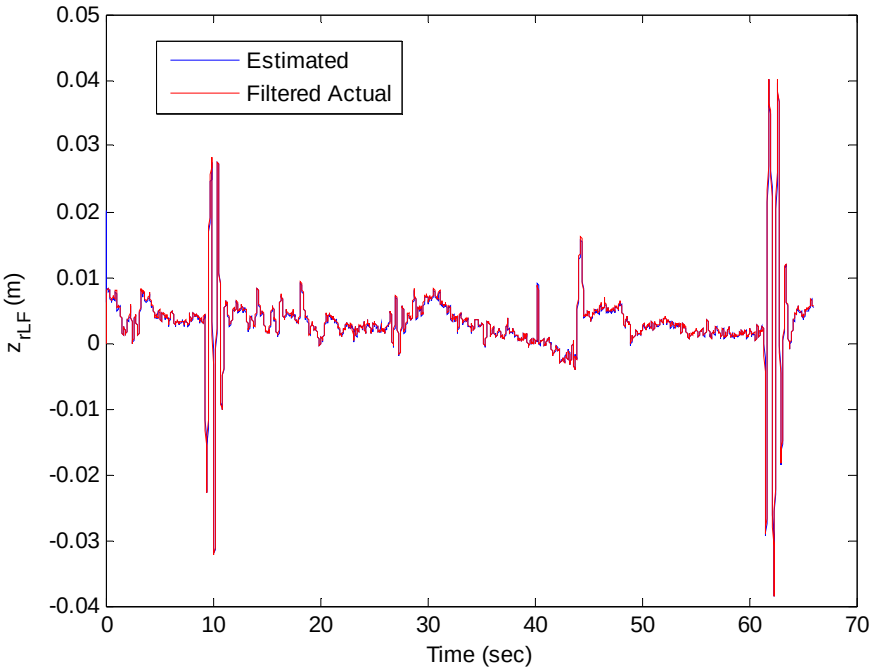

Figure 59: Performance of the KF with four displacement sensors in real time. The graph compares the actual relative displacement of the vehicle LF suspension with its estimate.

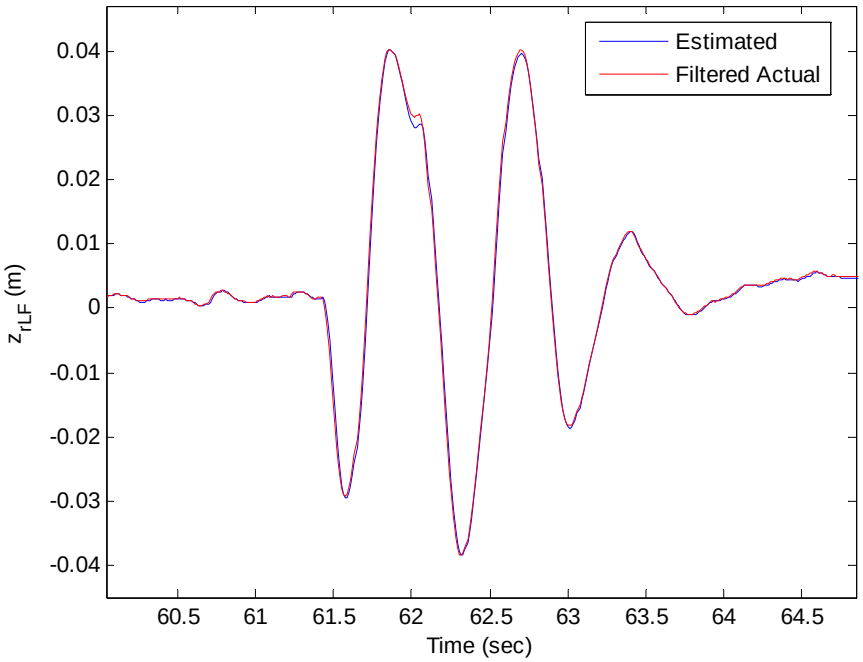

Figure 60: Performance of the KF with four displacement sensors in real time. The graph compares the actual relative displacement of the vehicle LF suspension with its estimation zoomed in on the second bump.

Opposed to the KF with the sensor configuration (a), the relative displacement of the shock is estimated accurately by utilizing the four displacement sensors suite (see Figure 59, Figure 60 and Figure 60). The actual and estimated relative velocity of the LF suspension is compared in Figure 61. In this case, the plots have zoomed in on the second bump to offer a closer view of the KF's performance. It is apparent that the actual relative velocity signal is followed by the considerably attenuated KF estimate, shifted by a small phase angle. However, during the real-time experiments, it is revealed that magnifying the estimated signal by a simple gain (which is a function of the vehicle speed) can decrease the estimation error significantly. Figure 62 demonstrates that the KF/4 displacement sensors poorly estimate the absolute velocity of the wheel-hub.

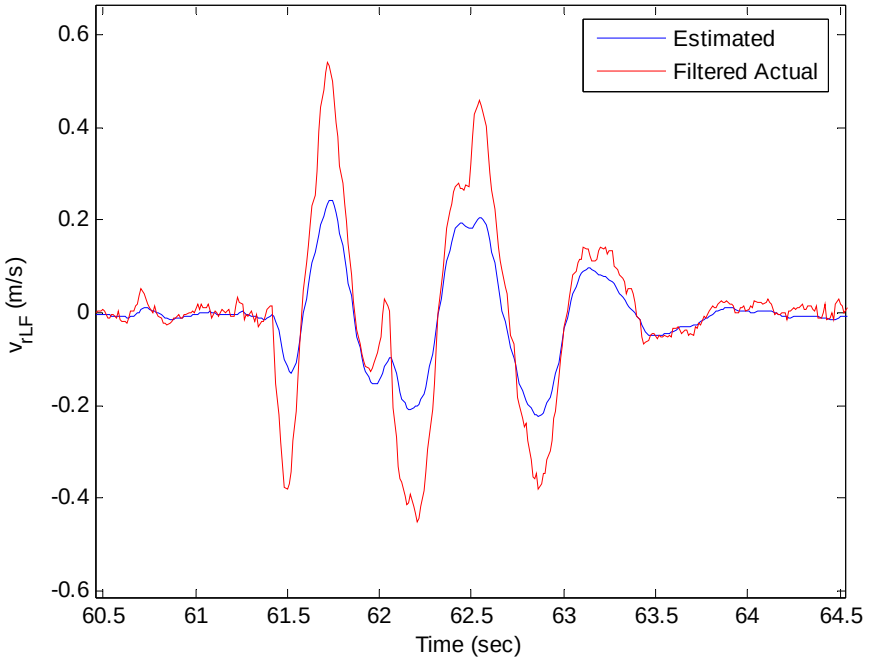

Figure 61: Performance of the KF with four displacement sensors in real time. The graph compares the actual relative velocity with the KF estimation zoomed in on the second bump.

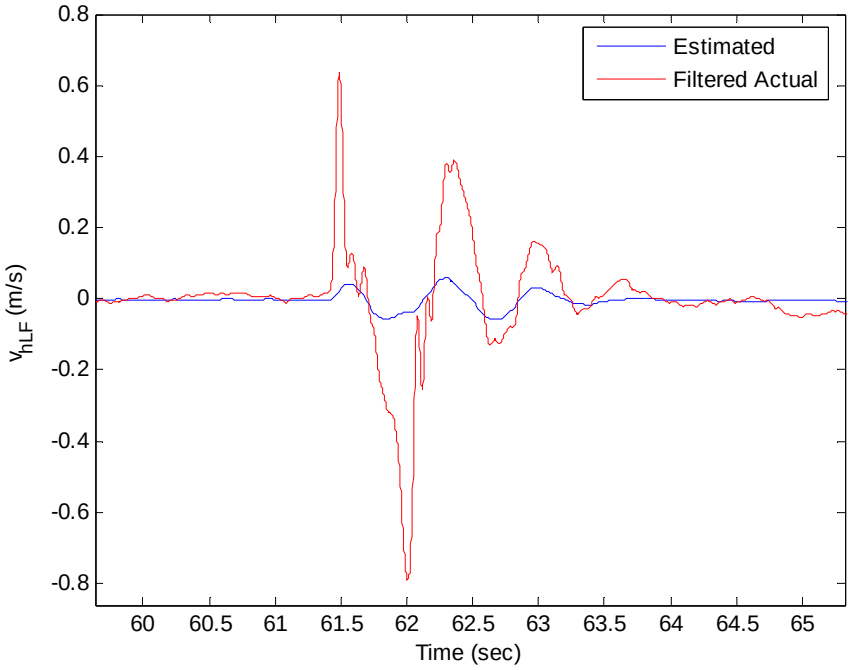

Figure 62: Performance of the KF with four displacement sensors real time. The graph compares the measured absolute velocity of the wheel-hub with the KF estimate zoomed in on the second bump.

The KF estimation errors and the corresponding covariance bounds are displayed in Figure 63 and Figure 64. Similar to those in the previous section, the blue bounds are obtained by taking the square root of the appropriate diagonal element of the error covariance matrix. As displayed in the figures, the error covariance bounds remain bounded, which implies that the KF feels confident with respect to all the estimation products. This is already suggested by the Observability analysis of the KF. In this case, the error covariance bounds are much wider than those generated by the previous KF (compare Figure 57 with Figure 64). In fact, the strength of the plant noise sequence, w_k' in Equation (7.1), has been increased to compensate for the model uncertainties due to lack of information of the road disturbances (de-weighting the system model). This causes the KF to rely more on the measurements of the sensing system than the information from the analytical model (a more conservative design, since the road input information is not available). However, it is illustrated in Figure 62 that the KF still cannot provide a useful estimate of the wheel-hub absolute velocity.

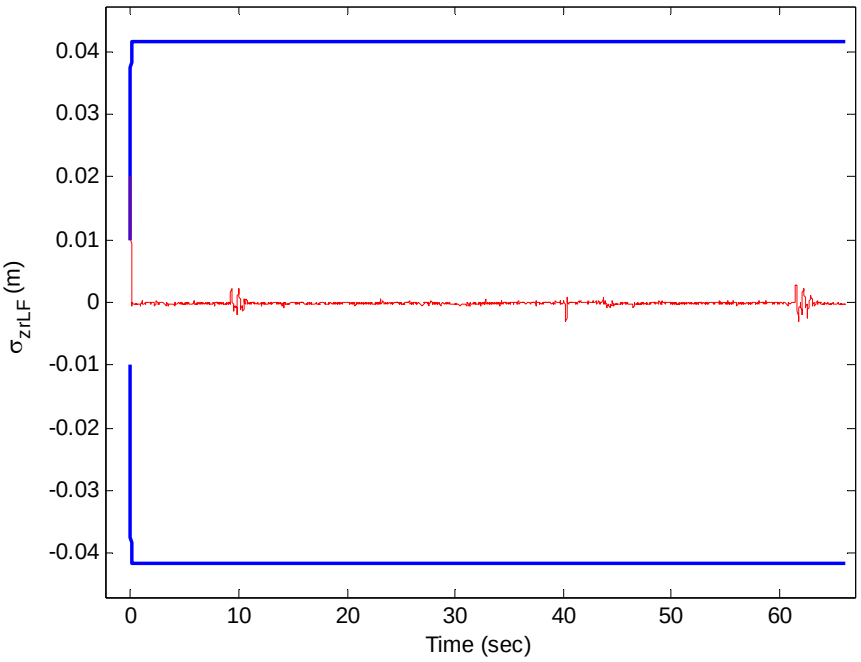

Figure 63: The graph illustrates the estimation error [red] corresponding to the LF shock relative displacement and the KF evaluated error covariance bounds [blue].

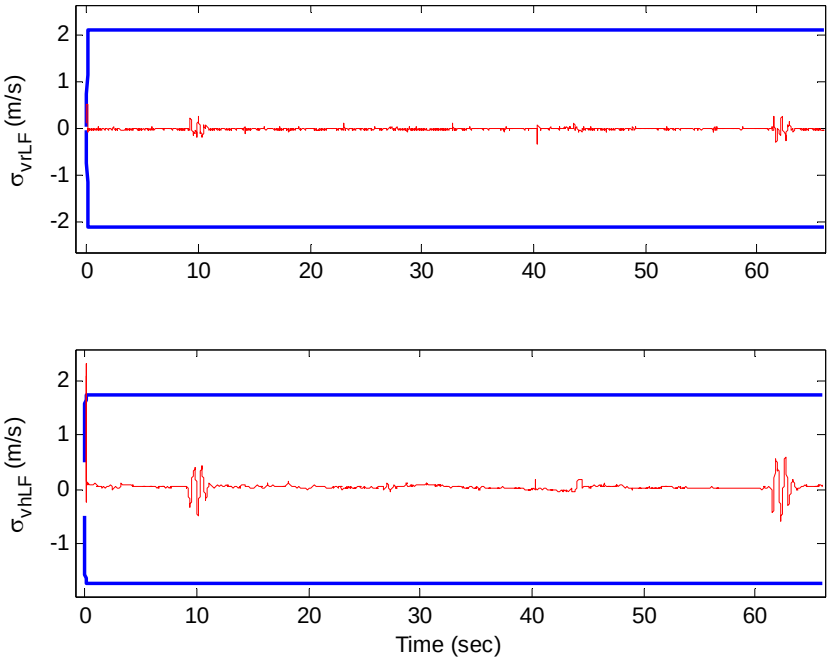

Figure 64: The graph portrays the estimation errors [red] corresponding to the LF shock relative velocity and the wheel-hub absolute velocity. Blue bounds are the KF evaluated covariance quantities for the estimation errors.

The covariance bounds of the measurement residuals are also increased by increasing the plant noise covariance. It is obvious in Figure 65 that the measurement residuals are unbiased, but there is no consistency between the residuals and the expected covariance bounds (the residuals should be within the 1σ bounds for 68% of the time).

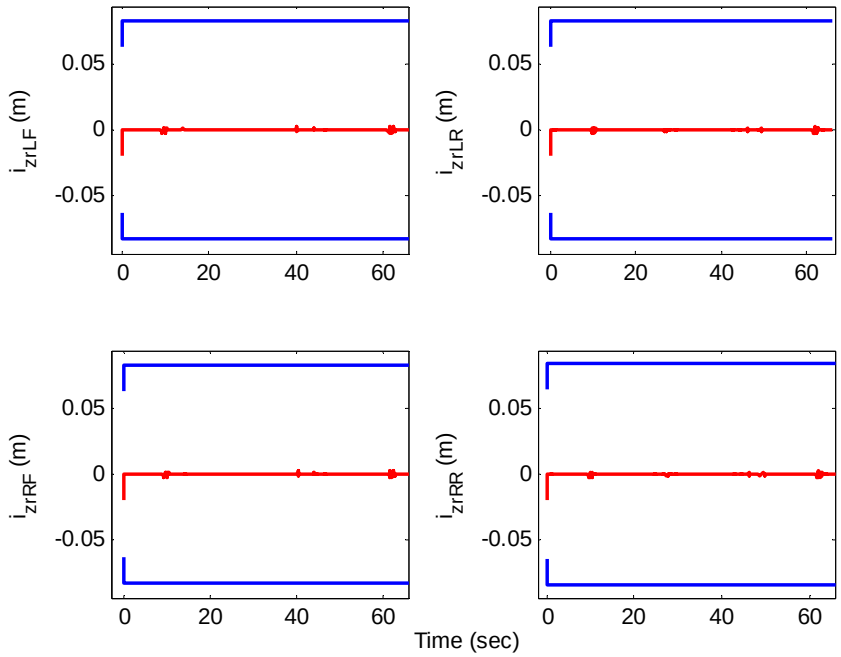

Figure 65: The graph illustrates the innovation signals (residuals) [red] corresponded to the displacement sensor measurements. Blue bounds are the theoretically expected covariance.

7.2 State Estimation Results with the Minimal Realization

This section provides estimation results of the KF which embeds the minimal realization of the vehicle's model, Equation (7.1) with the fourteen-state vector (6.11). The measurement model is also given by Equation (6.22). First, the estimation results with the sensor configuration (a) are presented in Section 7.2.1. Next, Section 7.2.2 investigates performance of the KF with the sensor suite (c).

7.2.1 One IMU and Four Accelerometers Sensor Suite

Similar to Section 7.1.1, the experiments are carried out at the speed of 40 km/hr. Inputs to the KF are the measurements of the IMU and the four wheel accelerometers. Since the pair

(H_k, Φ_k) is Observable, the KF is expected to provide all the states accurately. Figure 66 illustrates that the KF, embedding the minimal model, effectively estimates the wheel-hub absolute velocity, which the previous KF cannot do. Also, Figure 67, Figure 69, and Figure 70 demonstrate that the KF does a good job in estimating the absolute velocity of the CG, the body pitch rate, and the LF shock relative velocity, respectively.

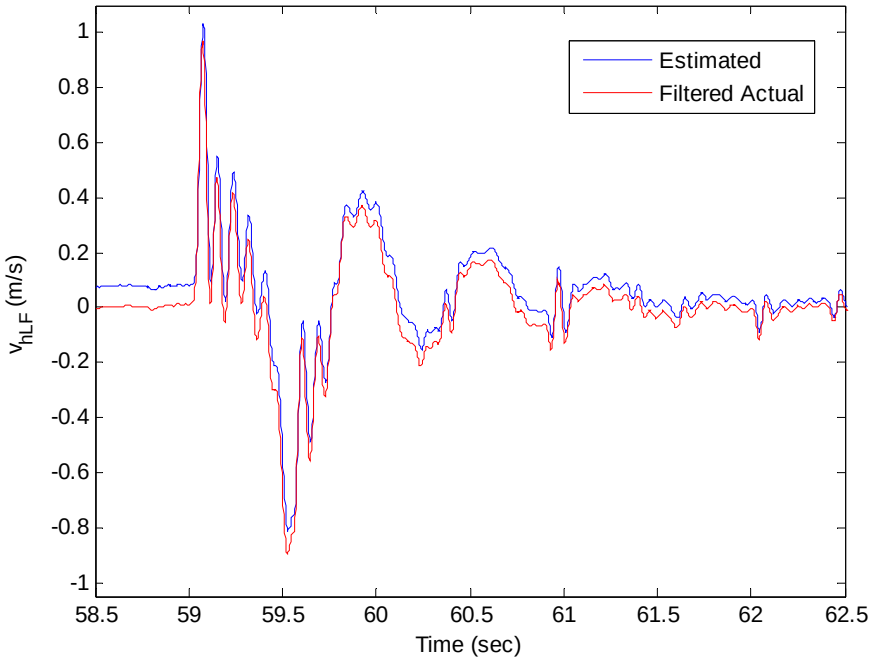

Figure 66: Performance of the KF using the minimal realization and the sensor suite (a). The graph compares the KF estimate of the LF wheel-hub absolute velocity with the measured signal, on the second bump.

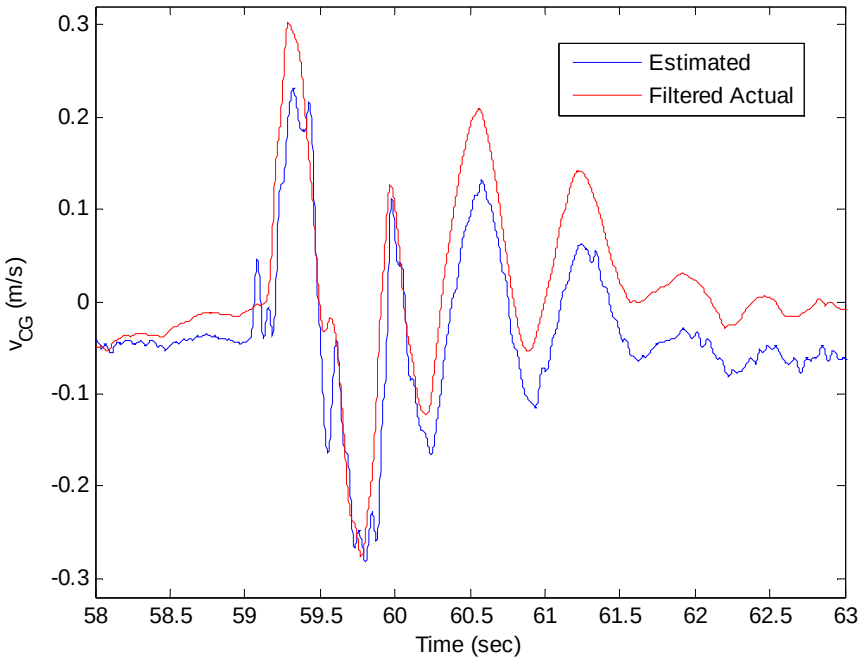

Figure 67: Performance of the KF using the minimal realization and the sensor suite (a). The graph compares the measured velocity of the vehicle's CG with the KF estimate zoomed in on the second bump.

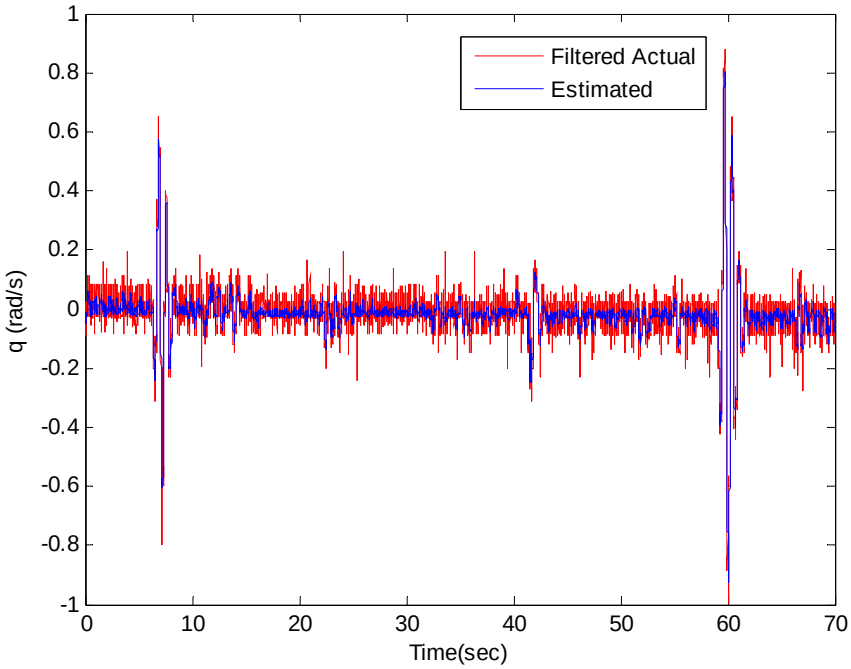

Figure 68: Performance of the KF using the minimal realization and the sensor suite (a).The graph compares the measured pitch rate of the vehicle's body with the KF estimate.

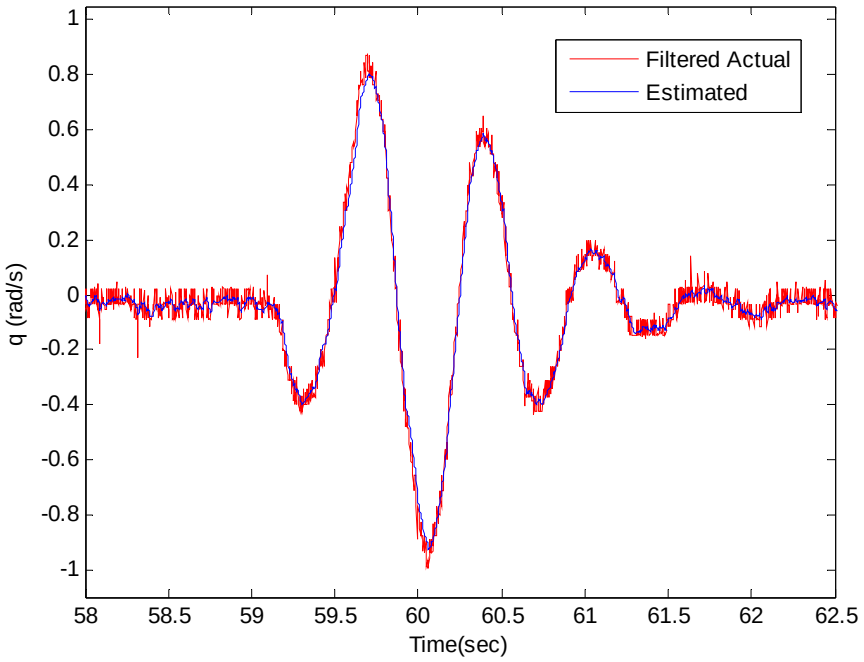

Figure 69: Performance of the KF using the minimal realization and the sensor suite (a).The graph compares the measured pitch rate of the vehicle's body with the KF estimate zoomed in on the second bump.

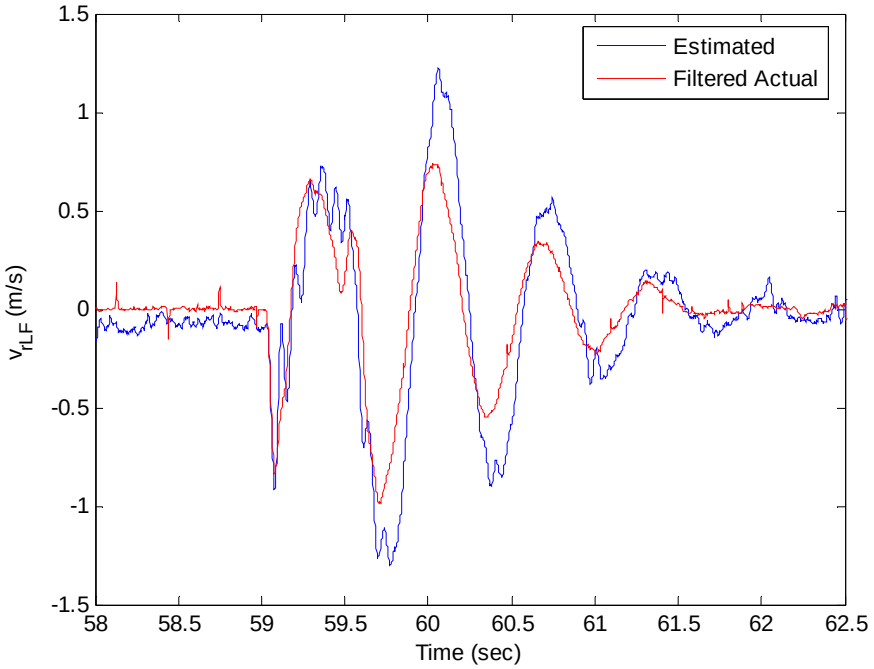

Figure 70: Performance of the KF using the minimal realization and the sensor suite (a). The graph compares the LF suspension relative velocity with its estimation zoomed in on the second bump.

Figure 71 provides a comparison between the measurement and the KF estimate of the pitch angle of the vehicle body. A closer view to the estimation performance on the second bump is also provided by Figure 72. Unlike the anticipation of the Observability analysis, the KF estimate of the pitch angle is not accurate. Further experimental results demonstrate that the estimates of the body's roll angle, the position of the CG, and the absolute positions of the wheel-hubs are also inaccurate. The discrepancy between the expectation of the theory (Observability analysis) and the actual results are described by considering the KF update equation, Equation (4.10). The measurement residual, $(z_k - \hat{z}_k)$, is written as:

$$z_k - \hat{z}_k = z_k - (H_k \hat{x}_k(-) + D_d u_{d_k}), \tag{7.5}$$

where the estimated measurement, $\hat{z}_k$, is computed based on the measurement model (6.22). However, the road input disturbance, u_{d_k}, is unknown. Since, the KF makes the residual white, in the absence of u_{d_k}, it manipulates the state estimate $\hat{x}_k$ in a way to compensate for the lack of information of the road disturbances. Moreover, as pointed out earlier in Section 6.1, with the minimal state vector, u_{d_k} contains road vertical displacements (see Equation (6.16)). This results in erroneous estimates of the displacement type states such as body pitch and roll angles, absolute displacement of the CG, and the absolute positions of the wheel-hubs[1].

[1] Here, KF provides accurate estimates of the states required for implementation of the Skyhook control strategy (relative and absolute velocities). However, in a more general case, other control strategies, like those specifically designed to enhance handling and stability of the vehicle, work parallel with the Skyhook controller. These controllers may need the other states of the vehicle; hence, the estimator is expected to provide estimates of all the vehicle states in a precise manner.

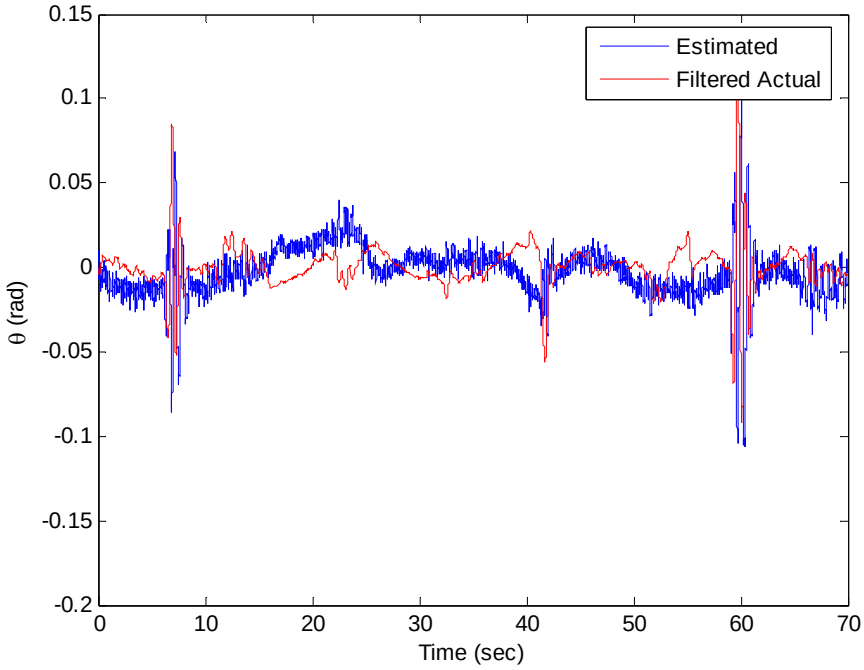

Figure 71: Performance of the KF using the minimal realization and the sensor suite (a). The graph compares the vehicle's measured pitch angle with the KF estimate.

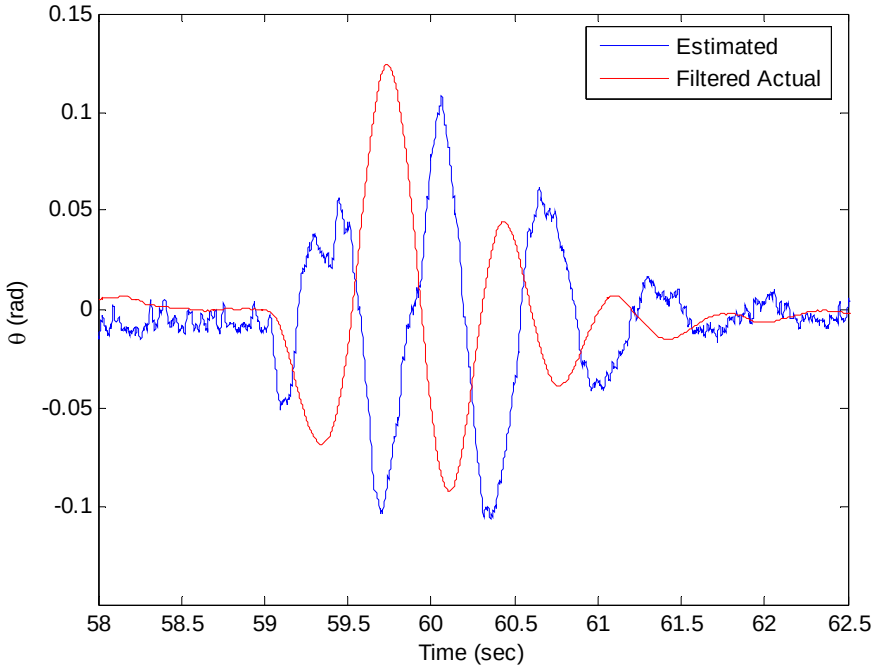

Figure 72: Performance of the KF using the minimal realization and the sensor suite (a). The graph compares the vehicle's measured pitch angle with the KF estimation zoomed in on the second bump.

7.2.2 Four Displacement Sensors and One Lateral Accelerometer Sensor Suite

The estimation performance of the KF incorporating the measurements of the sensor configuration (c) is investigated in this section. The vehicle speed during the road tests is maintained at approximately 30 km/hr. The Observability matrix of the pair (H_k, Φ_k) has full rank. However, as explained in Section 7.2.1, due to the lack of information of the road disturbances, the KF does not provide accurate estimates of all the states. Since the sensor configuration (c) measures the relative displacement of each shock, estimates of the displacement type states are provided with acceptable quality. Figure 73 illustrates the estimation accuracy associate with the LF shock relative displacement. However, the other states such as roll and pitch rates of the body, absolute velocity of the CG, and the absolute velocity of the wheel-hubs, are not estimated precisely. Figure 74 compares the KF estimate of the LF wheel-hub absolute velocity with its measurement. The same comparison is given for LF shock relative displacement in Figure 75[1].

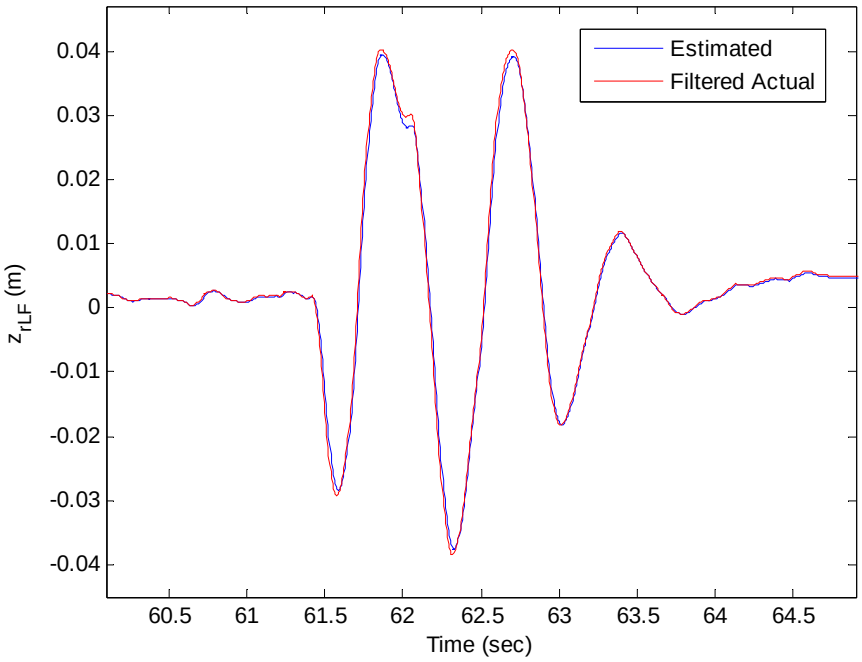

Figure 73: Performance of the KF using the minimal realization and the sensor suite (c). The graph compares the measured relative displacement of the vehicle suspension with its estimation zoomed in on the second bump.

[1] Note that the relative velocity is an indirect estimate for the KF of the current section.

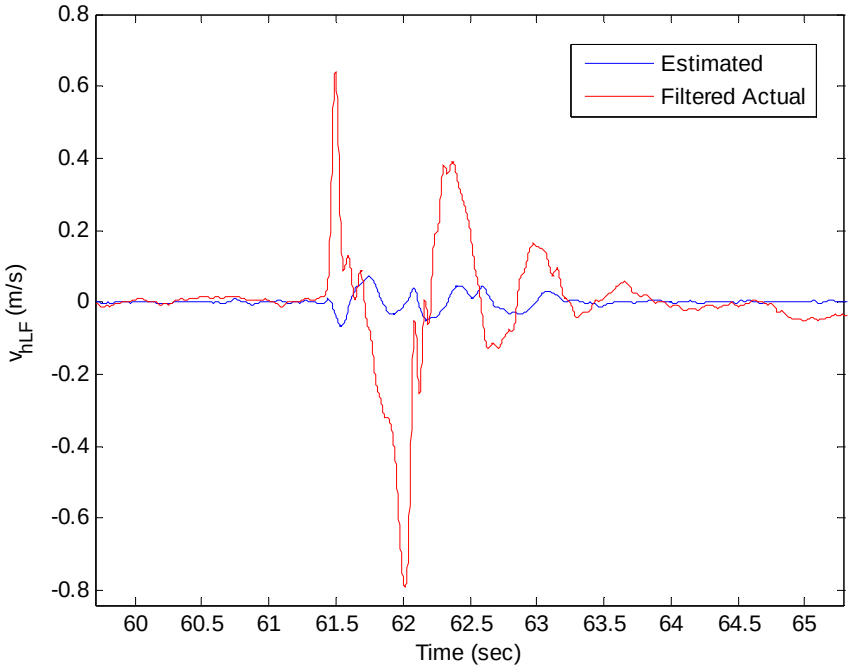

Figure 74: Performance of the KF using the minimal realization and the sensor suite (c). The graph shows the KF estimate of the LF wheel-hub absolute velocity and the measured signal, on the second bump.

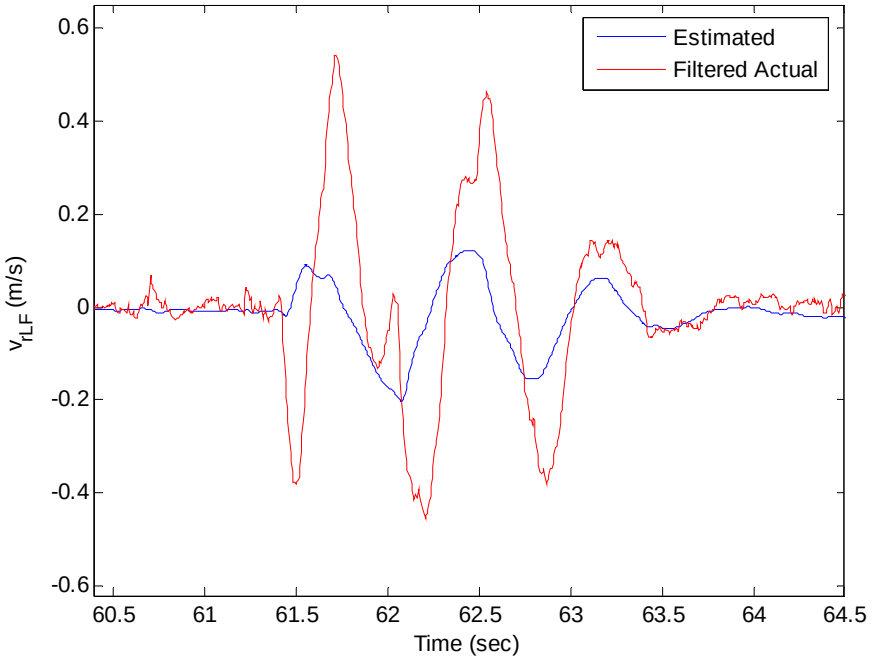

Figure 75: Performance of the KF using the minimal realization and the sensor suite (c). The graph compares the measured relative velocity of the LF shock with the KF estimate on the second bump.

7.2.3 Nine Accelerometers Sensor Suite

As described in Section 6.2, the sensor configuration (b), consisting of nine accelerometers, is nonlinear. The nonlinearity of the measurements model arises from the centrifugal acceleration terms, terms $-(\dot{\phi}^2 + \dot{\theta}^2)h_{CG}$ in Equation (6.20), of the body accelerometers. h_{CG} is usually in the order of 0.1m to 0.25m for SUVs, which makes the effect of the centrifugal terms considerable. For the current nonlinear state estimation problem, the UKF[1] algorithm, presented in Section 4.4, is implemented. Computer simulation results are given by Figure 76 to Figure 84. The Cadillac is driven in the same road of Section 5.4.1 with a bump, shown in Figure 11, at a speed of 30 km/hr. There are two reasons to exhibit the computer simulation results instead of those of the real-time road tests. First, measuring some of the vehicle states such as absolute positions of the CG and the wheel-hubs are almost impossible by the use of the sensor configurations of Chapter 3. The only way is to integrate the corresponding accelerometer output twice. But, in the presence of the high noise level, the resultant position signal is too inaccurate to be compared with the estimated state. Second, by comparing the estimation results of the computer simulations and the real-time experiments, the consistency between the simulations and the experiments is confirmed.

Measurements of the sensor configurations (a) and (b) are almost the same. Both measure the wheel-hubs accelerations. IMU of the sensor configuration (a) provides the roll and pitch rate of the vehicle body and also acceleration of the CG. These measurements are related to the four body accelerometer measurements of the sensor suite (b) by the Coriolis law (Equation (6.18) of Section 6.2). Therefore, in the absence of the road input information, due to the same reason explained in Section 7.2.1, the UKF is expected not to be able to provide accurate estimates of the displacement type states (compare Figure 72 and Figure 78). This is illustrated by Figure 76, Figure 78, and Figure 80. Figure 76 compares the actual position of the body's CG and the UKF estimate. Figure 78 does the comparison for the pitch angle of the body. As well, the comparison between the actual and the estimated LF wheel-hub absolute position is provided in Figure 80. None of the UKF estimates are acceptable.

Similar to the KF with the sensor configuration (a), the UKF provides high quality estimates of the velocity type states by incorporating the measurements of the configuration (b). This is

[1] Estimation results of the EKF for the current problem are very similar to the results of the UKF which are presented in this section.

demonstrated by Figure 77, Figure 79, and Figure 81 plotting the estimates of the CG's velocity, pitch rate of the body, and the absolute velocity of the LF wheel-hub. Finally, the estimation errors and the corresponding covariance bounds are portrayed in Figure 82 to Figure 84. While the Observability analysis is not applicable for the nonlinear estimation problem, the convergence or non-convergence covariance bounds are used for the same purposes. The convergent error covariance bounds indicate that all the states must be estimated precisely. However, it is illustrated that due to lack of information of the road disturbances, this expectation is not met.

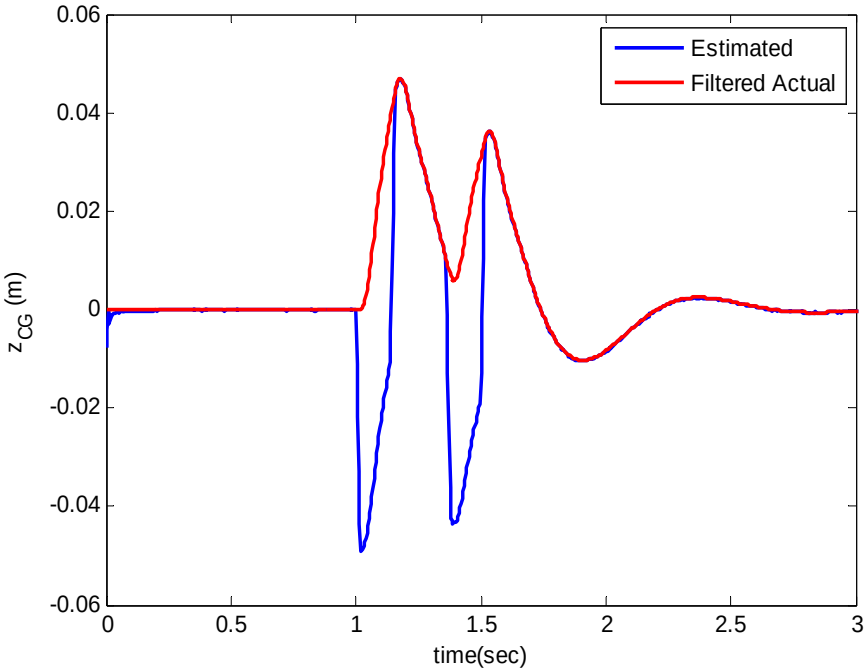

Figure 76: Estimation performance of the UKF with the sensor configuration (b). The graph compares the actual position of the CG with the UKF estimate.

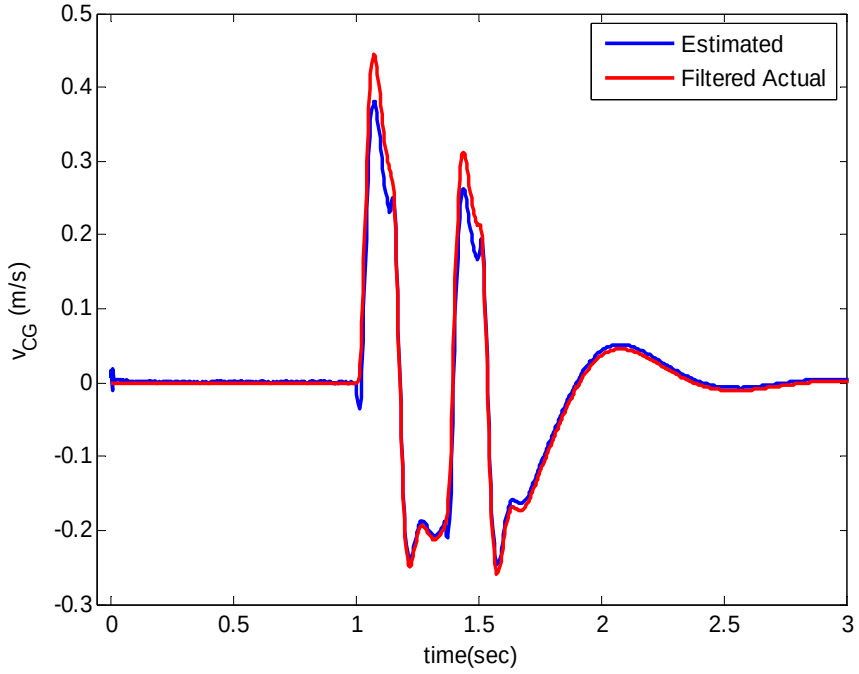

Figure 77: The graph compares the absolute velocity of the body's CG with the UKF estimate.

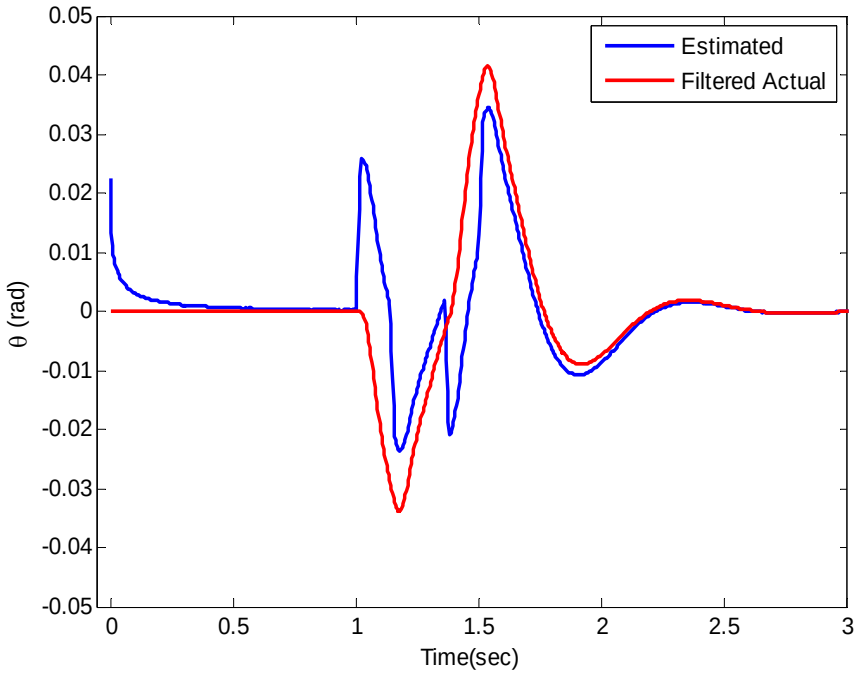

Figure 78: The graph provides a comparison between the actual and the UKF estimate of the body's pitch angle.

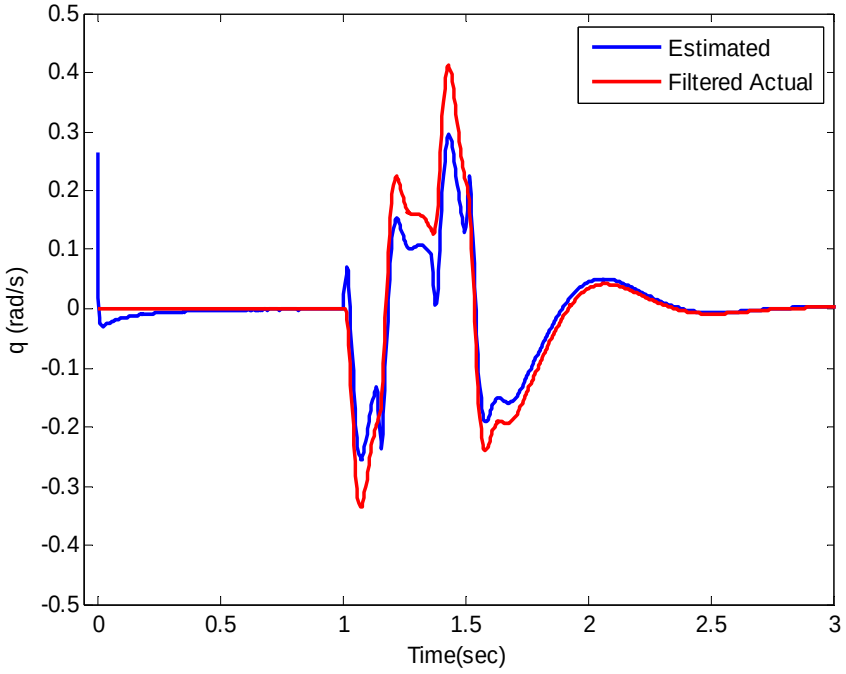

Figure 79: The graph compares the actual and the estimated pitch rate of the vehicle.

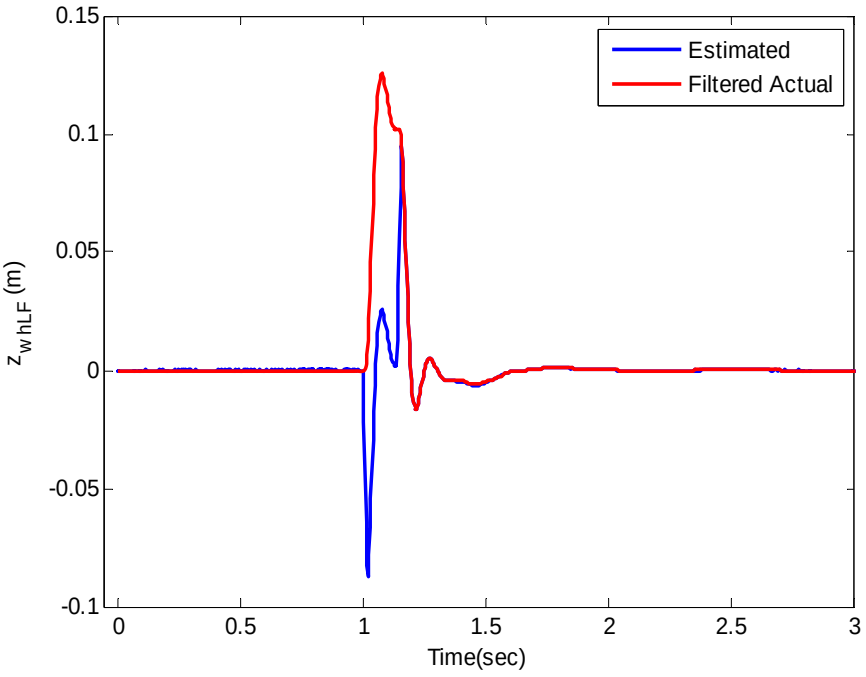

Figure 80: The graph shows the absolute position of the LF wheel-hub and the UKF estimate.

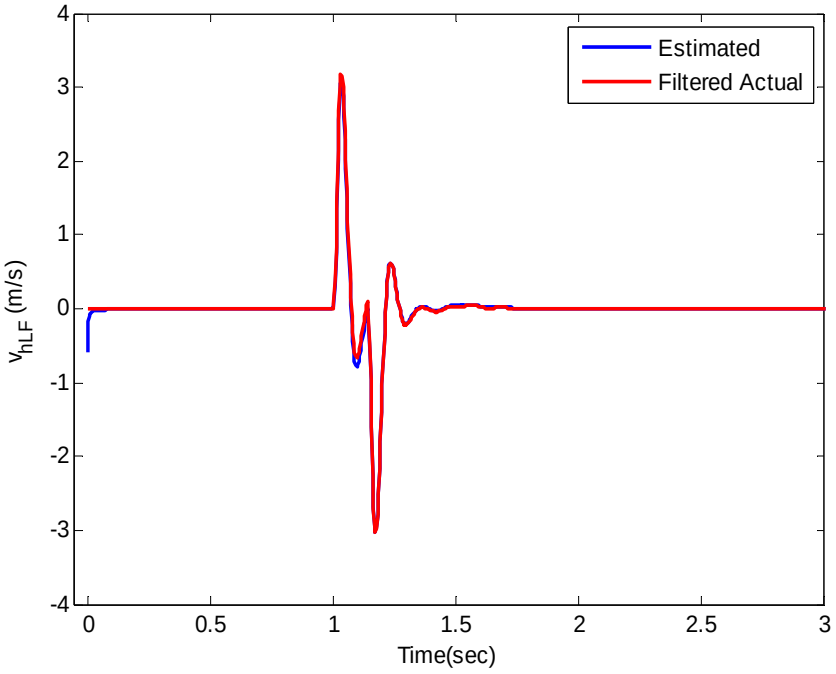

Figure 81: The graph compares the actual and estimated LF wheel absolute velocity.

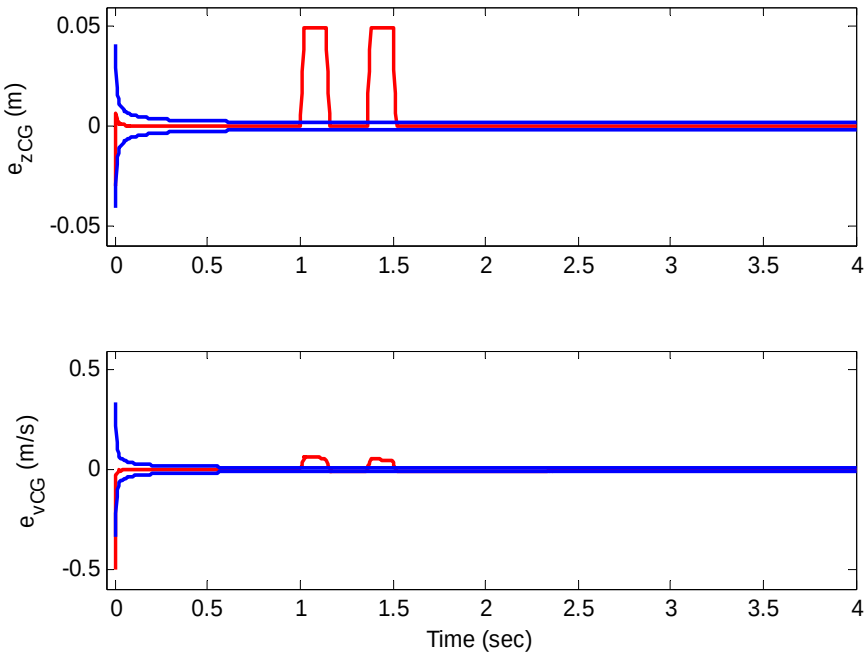

Figure 82: The estimation errors [red] of the absolute position and velocity of the CG and the corresponding covariance bounds [blue].

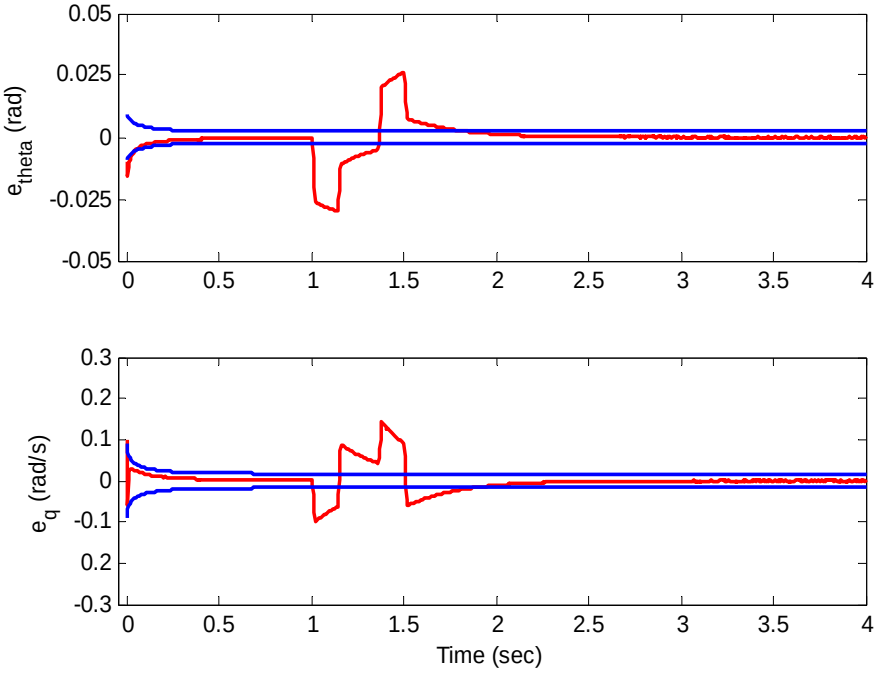

Figure 83: The pitch angle and pitch rate estimation errors [red] and the corresponding covariance bounds [blue].

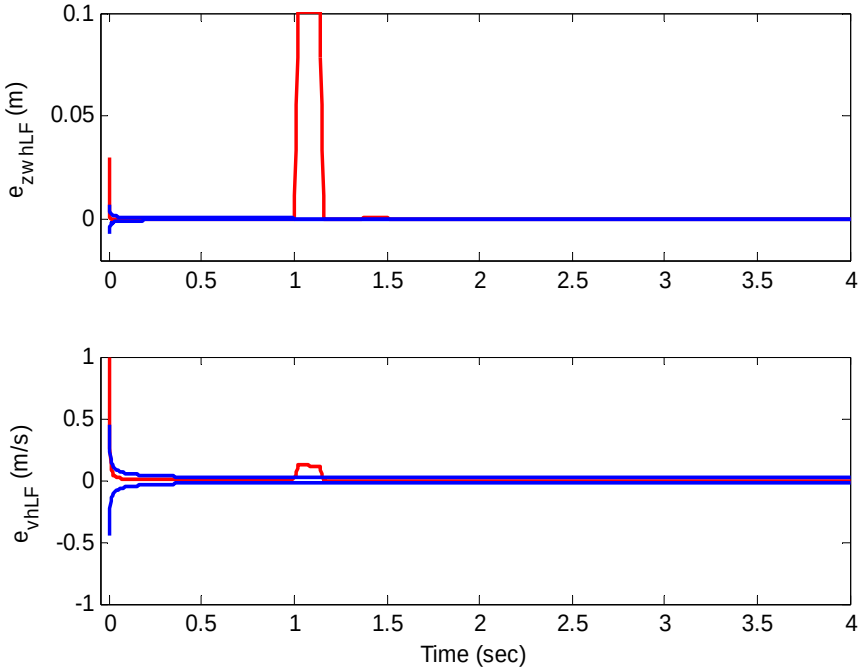

Figure 84: Estimation errors [red] associated with the absolute position and velocity of the LF wheel-hub and the error covariance bounds [blue].

8 Road Input Determination

As demonstrated in Chapter 7, there are always some states of the vehicle that are not accurately provided by the estimator. Indeed, at the presence of the unknown non-zero mean disturbances from the road, there is no guarantee that the dynamics of the KF estimation error, given by Equation (4.21), remain asymptotically stable. The objective of this chapter is to estimate the significant inputs from the road and then feed them back to the estimator embedded models. Two different approaches are examined: Estimation of the road input by a nonlinear estimator such as an UKF, and filtering the wheel accelerometer data through the inverse dynamics of the tire.

8.1 Estimation of the road Inputs

In the first approach, the road disturbance to each wheel is modeled as a Markov process [41]. The new state is then concatenated to the original vehicle realization. With the minimal realization of the vehicle model (which uses the fourteen-state vector), the dimension of the augmented system becomes eighteen. Now, consider a combination of the sensor suites (b) and (c); that is, a measurement system of nine accelerometers and four displacement sensors. The test vehicle is driven at 30 km/hr on the same road and over the same bump used in the computer simulations of Section 7.2.3. The UKF estimate of the bump is plotted in Figure 85. It appears that even with such a complete sensor system, the estimator cannot provide an acceptable estimate of the bump geometry. This is attributed to the fact that no direct information regarding the position profile of the bump (the road displacement)[1] is being provided for the UKF, either by the embedded models or by the measurement system.

[1] For the minimal realization, the road displacement is the input to the system.

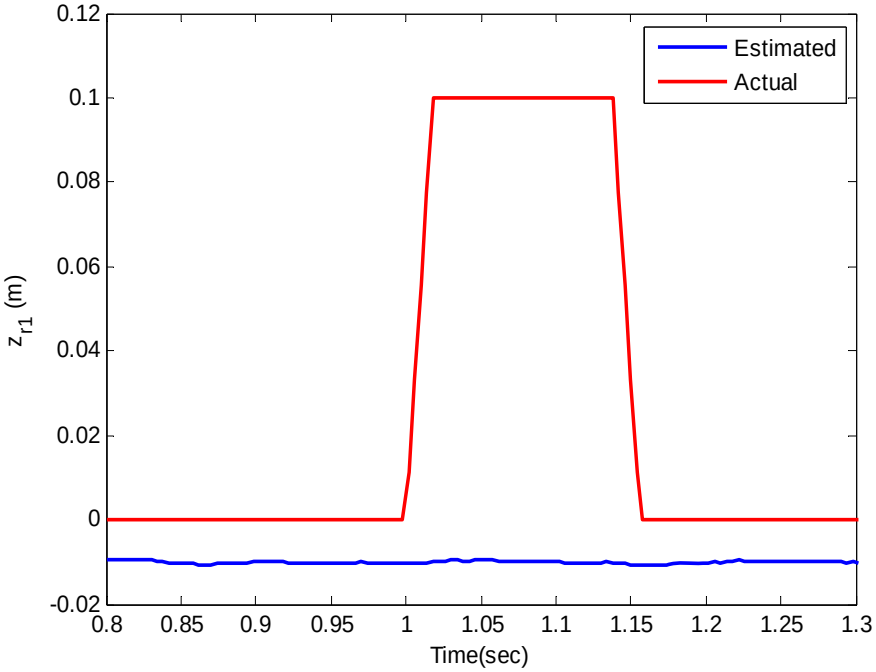

Figure 85: The actual bump, used in the computer simulations, and the UKF estimate.

8.2 Tire Inverse Dynamics

Assume that a linear transfer function G_{wh_i} can be found that relates the road disturbances to the i^{th} wheel, to the acceleration of the same wheel-hub, a_{wh_i}, as:

$$G_{wh_i}(s) = \frac{a_{wh_i}}{u_{d_i}}; \quad i = 1,...,4, \tag{7.6}$$

where u_{d_i} is the road displacement (the road position profile) input to the wheel (see Equation (6.16)). Theoretically, by measuring the wheel-hub acceleration and filtering it by the inverse dynamics of the tire, $G_{wh_i}^{-1}$, the road displacement should be extracted; that is:

$$u_{d_i} = G_{wh_i}^{-1}(s) a_{wh_i}. \tag{7.7}$$

The transfer function of the wheel is obtained by processing the experimental data of the Cadillac 4-poster tests. Figure 42 portrays the frequency content (FFT plot) of the LF wheel-hub acceleration in response to the base poster displacement, shown in Figure 40. The

magnitude plot of the LF wheel transfer function is then achieved by dividing the corresponding components of the acceleration plot by the disturbance input plot.

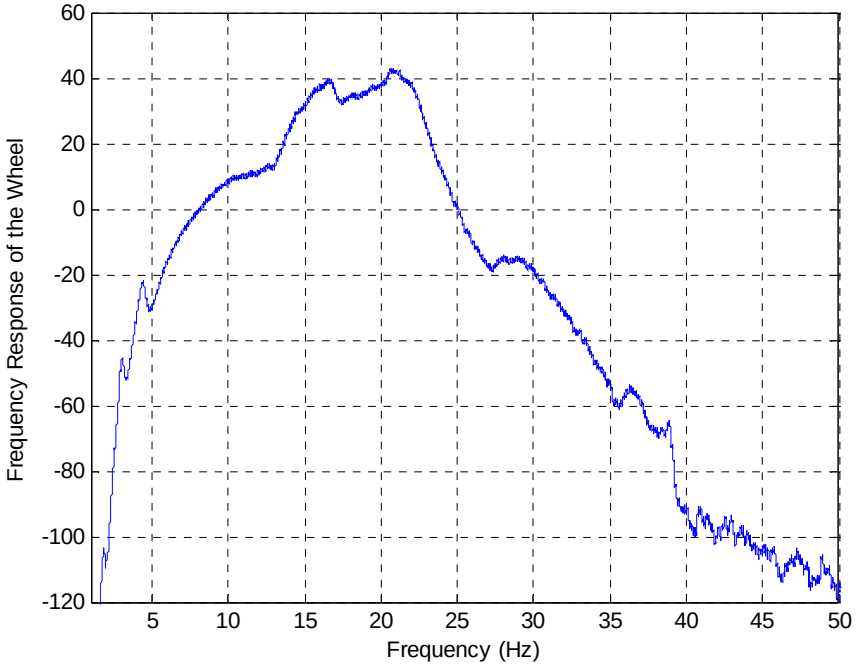

Figure 86: Frequency response (magnitude plot) of the LF wheel.

Figure 86 illustrates the magnitude plot (in dB) of the Cadillac LF wheel transfer function. In the next step, a suitable transfer function is fitted to the magnitude plot of Figure 86. However, prior to doing so, it is worth assuming that the transfer function is given and therefore investigate the feasibility of the proposed idea. Equation (7.8) is the transfer function from the road displacement input to the hub acceleration of the 2 DOF quarter car wheel of Section 5.1:

$$G_w(s) = \frac{\ddot{z}_w}{u_d} = \frac{4500(s^2 - 6.039\times10^{-12}\, s + 3.188\times10^{-10})(s^2 + 3.657s + 56)}{(s^2 + 3.018s + 51.47)(s^2 + 32.64s + 4896)}. \qquad (7.8)$$

This is computed based on the simple analytical model of the quarter car, Equations (5.8) and (5.19), for a damping coefficient equal to $c_s \cong 2000$ N.sec/m. The magnitude and the phase plot of the transfer function (7.8) are exhibited in Figure 87. It is demonstrated that the wheel behaves analogous to a high-pass filter with a cut-off frequency at 1 rad/sec (0.15Hz). Therefore, the inverse of such a filter, $G_w^{-1}(s)$, is a low-pass filter which passes through only frequency components below the 0.15Hz, and the other significant frequency components of

the road disturbance input (up to approximately 15Hz, see Figure 40) are all eliminated. Figure 88 plots the filtered signal of the wheel-hub accelerometer by the tire inverse dynamics $G_w^{-1}(s)$. It is obvious that the computed road profile (the filtered signal) does not contain all the frequency components required to build the actual bump geometry[1].

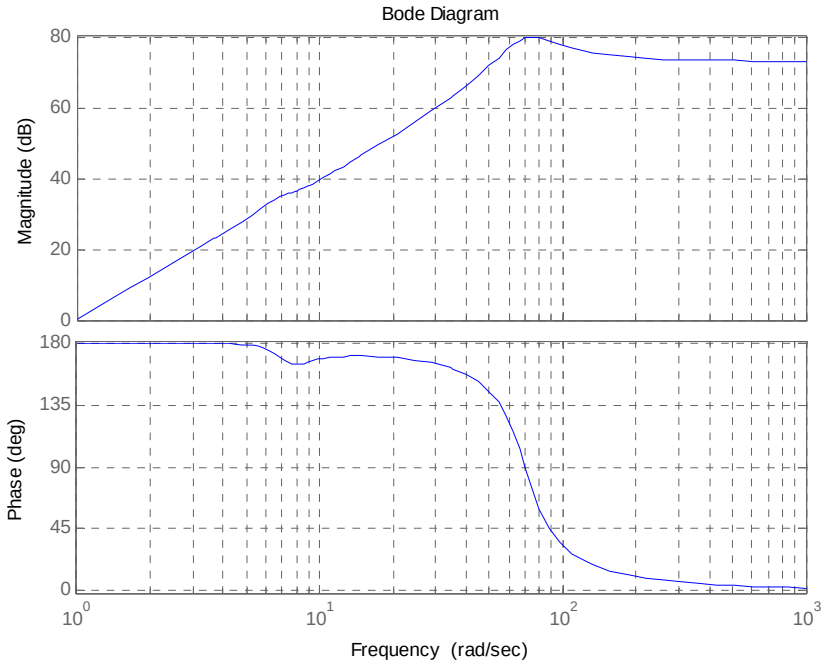

Figure 87: Bode plot of the QC wheel transfer function.

[1] The high frequency components are required to build the sharp edges of the bump.

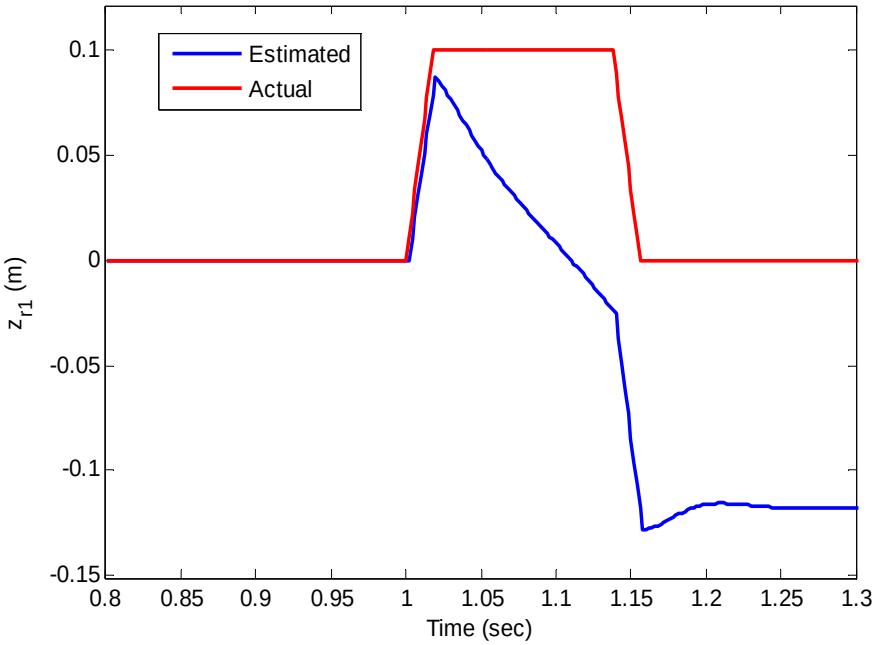

Figure 88: The actual and the estimated road geometry.

9 Beyond the Kalman Filter

Chapter 7 described how, due to lack of information on road disturbances, the estimators are not able to provide accurate estimates of all vehicle states. Chapter 8 is intended to predict the road profile and then feed it back to the estimators embedded models. However, it is demonstrated that none of the proposed approaches provides rich information regarding the road disturbances to the vehicle. Chapters 8, 9 and 10 develop estimation mechanisms which are effective for systems with unmeasurable (or unknown disturbance) inputs, such as the vehicle systems subjected to the unknown road disturbances.

9.1 Bayesian Estimation and Particle Filtering

Suppose that the system and measurement equations are given as follows:

$$x_{k+1} = f_k(x_k, w_k)$$
$$z_k = h_k(x_k, v_k), \tag{9.1}$$

where w_k and v_k are uncorrelated Gaussian white noise sequences with known probability density functions (pdf's). The initial conditions are also given by Equation (4.9). It is also assumed that:

$$p(x_0 \mid z_0) = p(x_0), \tag{9.2}$$

where $p(x_0 \mid z_0)$ denotes the conditional pdf of the initial state vector based on the initial measurement. The goal is to approximate the pdf of the state vector at time $t = t_k$, conditioned on the available measurements set $Z_k = \{z_1, z_2, ..., z_k\}$, that is $p(x_k \mid Z_k)$, given (9.1) and (9.2).

Similar to the filters described in Chapter 4, a Bayesian estimator consists essentially of two steps: prediction and update. In the prediction step, a priori conditional pdf of x_k is evaluated by incorporating all the measurements before the time t_k. This is accomplished by considering the fact that the density function of a random variable can be found from the joint density function of the same random variable and another [42]:

$$p(x_k \mid Z_{k-1}) = \int p[(x_k, x_{k-1}) \mid Z_{k-1}] dx_{k-1}. \tag{9.3}$$

The right side of Equation (9.3) is then rewritten as the product of two conditional pdf's by applying the Chapman-Kolmogorov formula [62] as:

$$p(x_k \mid Z_{k-1}) = \int p[x_k \mid (x_{k-1}, Z_{k-1})] p(x_{k-1} \mid Z_{k-1}) dx_{k-1}\,, \tag{9.4}$$

where, the first pdf is computed by the use of the system analytical model, Equation (9.1), independently of the measurements Z_{k-1},i.e.,

$$p[x_k \mid (x_{k-1}, Z_{k-1})] = p(x_k \mid x_{k-1})\,. \tag{9.5}$$

The second pdf is given by Equation (9.2) for the initial time-step.

In the update step, upon receiving the new measurement, a posteriori conditional pdf of the state is computed by using the Bayes's rule [62]:

$$p(x_k \mid Z_k) = \frac{p(Z_k \mid x_k) p(x_k)}{p(Z_k)}\,. \tag{9.6}$$

By substituting for the $p(x_k)$ in the above equation from:

$$p(x_k) = \frac{p(x_k \mid Z_{k-1}) p(Z_{k-1})}{p(Z_{k-1} \mid x_k)} \frac{p(x_k, z_k)}{p(x_k, z_k)}, \tag{9.7}$$

after some mathematical manipulations, the updated estimate in Equation (9.6) is rewritten as:

$$p(x_k \mid Z_k) = \frac{p(z_k \mid x_k) p(x_k \mid Z_{k-1})}{p(z_k \mid Z_{k-1})}\,. \tag{9.8}$$

On the right side of Equation (9.8), $p(z_k \mid x_k)$ is known from the measurement model. The term $p(x_k \mid Z_{k-1})$ is the predicted pdf of the state vector already evaluated by Equation (9.4). Furthermore, $p(z_k \mid Z_{k-1})$ is computed as follows [42]:

$$p(z_k \mid Z_{k-1}) = \int p[(z_k, x_k) \mid Z_{k-1}] dx_k\,. \tag{9.9}$$

By employing the Chapman-Kolmogorov equation, and considering the fact that $p[z_k \mid (x_k, Z_{k-1})] = p(z_k \mid x_k)$, Equation (9.9) is rewritten as:

$$p(z_k \mid Z_{k-1}) = \int p(z_k \mid x_k) p(x_k \mid Z_{k-1}) dx_k\,. \tag{9.10}$$

Now, both pdf's inside the integration operator of Equation (9.10) are known; the first one from the knowledge of the measurement model, and the second one from Equation (9.4).

Equations (9.4) and (9.8) are the kernels of the Bayesian state estimator. They should be recursively implemented, given the initial condition (9.2), to predict and update the conditional pdf of the state vector by incorporating the new measurement data. However, analytical

solutions to these equations are only available for a few special cases [41], [56], [55]. For linear systems ($f(.)$ and $h(.)$ are both linear) with uncorrelated Gaussian white noise sequences, the solution is the Kalman filter [56], [55]. For other cases, the recursive Bayesian estimator should be implemented numerically.

Similar to the basic idea of the UT, presented in Section 4.4, the Bayesian estimator can be implemented by the use of N randomly generated particles. Each particle is an individual state estimate with an associated probability which indicates its likelihood. The initial particles, $\hat{x}_{0,i}^{+}\,(i=1,...,N)$, are generated based on the initial pdf $p(x_0)$, given by Equation (9.2). The particles are then propagated between the measurements using the process equation $f(.)$ [42], [54], [61], [55]:

$$\hat{x}_{k+1,i}^{-} = f_{k-1}(\hat{x}_{k,i}^{+}, w_k^i), \qquad (i=1,...,N) \tag{9.11}$$

In the update step, the latest measurement is used to identify the particles with higher likelihoods. This is done by computing the relative likelihood q_i that the measurement is equal to the specific measurement $z_k = z^*$, conditioned on the state x_k is equal to the particle $\hat{x}_{k+1,i}^{-}$, that is, $p[(z_k = z^*) \,|\, (x_k = \hat{x}_{k+1,i}^{-})]$. For example, for the following measurement system:

$$z_k = h(x_k) + v_k, \qquad v_k \sim N(0, R) \tag{9.12}$$

the relative likelihood q_i is obtained as [41], [42]:

$$\begin{aligned} q_i &= p[(z_k = z^*) \,|\, (x_k = \hat{x}_{k+1,i}^{-})] \\ &= p[v_k = z^* - h(\hat{x}_{k+1,i}^{-})] \\ &\propto \frac{1}{(2\pi)^{m/2} \,|\, R \,|^{1/2}} \exp\left(-\frac{[z^* - h(\hat{x}_{k+1,i}^{-})]^T R^{-1} [z^* - h(\hat{x}_{k+1,i}^{-})]}{2}\right). \end{aligned} \tag{9.13}$$

The symbol $\propto$ means that the likelihood is proportional to the right side of the above equation. Now, a new set of particles $\hat{x}_{k+1,i}^{+}\ (i=1,2,...,N)$ are refined out of the previous particles, $\hat{x}_{k+1,i}^{-}$, based on the (normalized) relative likelihoods q_i. This is called resampling and must guarantee that the ensemble pdf of the new particles $\hat{x}_{k+1,i}^{+}$ converges to the pdf $p(x_k \,|\, z_k)$, when N is sufficiently large. Several algorithms have been developed to perform the resampling stage [42], [54], [55] . A simple algorithm is given by the following two steps [42], [54]:

For $i = 1, 2, ..., N$,

1. Pick a random number $r \in [0,1]$ which is uniformly distributed.
2. Find j such that, $\sum_{m=1}^{j-1} q_m < r$, but $\sum_{m=1}^{j} q_m > r$. Select the old particle $\hat{x}_{k+1,j}^{-}$ to be in the resampled set, that is $\hat{x}_{k+1,i}^{+} = \hat{x}_{k+1,j}^{-}$.

The required statistical characteristics of the state vector at each time-step are then approximated from that of the resampled particles. For example, the estimated state at the time $t = t_{k+1}$ is given by Equation (9.14):

$$\hat{x}_{k+1}^{+} = E[x_{k+1} \mid z_{k+1}] \approx \frac{1}{N} \sum_{i=1}^{N} \hat{x}_{k+1,i}^{+} . \tag{9.14}$$

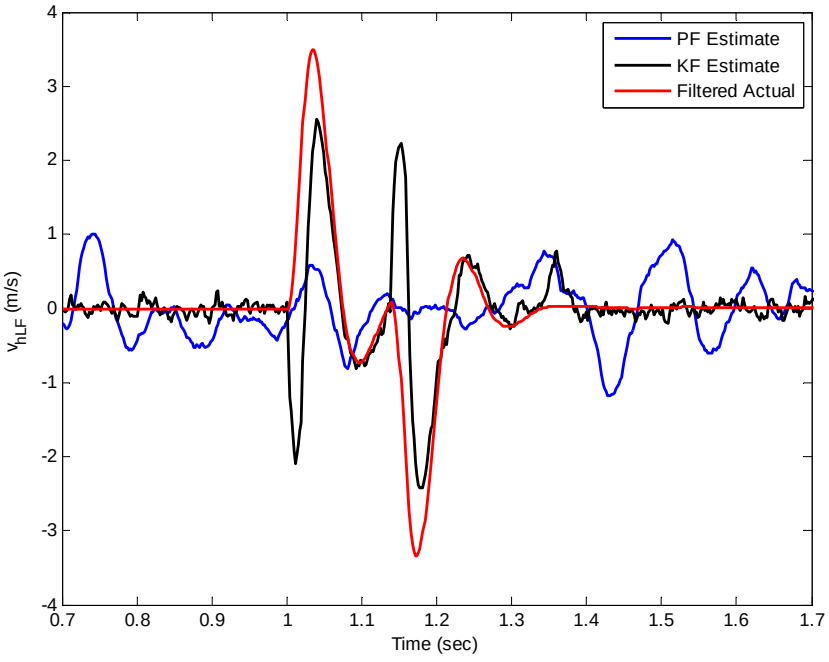

Figure 89: The Particle Filter (PF) and the Kalman Filter (KF) estimation performance for the absolute velocity of the LF wheel-hub.

The estimation algorithm, presented by Equations (9.11) to (9.14), is known as Particle Filter (PF). Figure 89 plots the PF estimate of the Cadillac LF wheel-hub velocity. The simulation is performed on a 1.8 GHz processor PC with 1 GB RAM. It is assumed that the vehicle is moving on the same road and the bump is that used in previous experiments (see Figure 43 and Figure 44). The PF is initiated by 10,000 randomly generated particles ($N = 10000$). The non-minimal (sixteen-state) realization of the vehicle model, Equation (7.1), is used to propagate the

particles with time. Measurements of nine accelerometers of the sensor configuration (b) (see Chapter 3) are captured every two milliseconds (500Hz sampling rate) to evaluate the particles' relative likelihoods (see Equation (9.13)). The resampling stage is accomplished by the resampling algorithm presented in this section. It almost takes fifteen minutes for the 1.8 GHz processor to perform the 1.8 sec simulation length, approximately one second for each cycle (prediction-update) of the PF algorithm.

From Figure 89, it is evident that the PF is not able to provide an accurate estimate of the wheel-hub absolute velocity, even at the price of higher computational effort. Increasing the number of particles and using more efficient resampling algorithms may improve the PF estimation performance [42], [54], [55], [56][1]. However, the required processing time by the PF per each cycle cannot be even moderately decreased. As described in Chapter 12, the control system loop (estimator-controller) must be performed at a rate of at least 60Hz to be able to suppress the resonant frequencies of the wheels. This is the bottleneck to the real-time implementation of the PF for the current state estimation problem.

9.2 Observers for Linear Systems with Unmeasurable Inputs[2]

Consider the linear time-invariant system:

$$\dot{x}(t) = Ax(t) + Bu(t) + Eu_d(t)$$
$$z(t) = Hx(t) \tag{9.15}$$

where, $x \in R^n$ is the state vector, $u \in R^m$ is the control input vector, $u_d \in R^q$ is the unmeasurable disturbance vector, and $z \in R^p$ is the measurement vector. Without the loss of generality, assume that $rank(H) = p$ and $rank(E) = q$. Also assume that the matrix pair (H, A) is observable. The problem is to design an observer to asymptotically estimate the state vector $x(t)$ irrespective of the unknown disturbance vector u_d [3].

Since H has full row rank, a non-singular transformation on the states can be found:

---

[1] For nonlinear or non-Gaussian estimation problems, it has been proven that the PF outperforms both EKF and UKF [42], [54]. However, it is achieved at the price of extremely higher computational effort.

[2] Observer design for Bilinear systems with unknown inputs is also addressed in references [67], [66], and [67]. The solutions are not presented here, since the required conditions are usually too hard to be met.

[3] References [62] and [64] present another solution to this problem by utilising the geometric theory of linear systems. This approach is not reviewed in here.

$$\begin{bmatrix} z \\ \alpha \end{bmatrix} = \begin{bmatrix} H \\ D \end{bmatrix} x, \tag{9.16}$$

such that p states, in the new coordinate system, are directly measurable. In this coordinate system, the system (9.15) is expressed in the following partitioned form [68], [69]:

$$\begin{bmatrix} \dot{z}(t) \\ \dot{\alpha}(t) \end{bmatrix} = \begin{bmatrix} A_{11} & A_{12} \\ A_{21} & A_{22} \end{bmatrix} \begin{bmatrix} z(t) \\ \alpha(t) \end{bmatrix} + \begin{bmatrix} B_1 \\ B_2 \end{bmatrix} u(t) + \begin{bmatrix} E_1 \\ E_2 \end{bmatrix} u_d(t)$$

$$z(t) = \begin{bmatrix} I_p & 0 \end{bmatrix} \begin{bmatrix} z(t) \\ \alpha(t) \end{bmatrix}. \tag{9.17}$$

In the next step, a reduced $(n-p)th$ order Luenberger observer [70] is constructed as follows:

$$\dot{\hat{\beta}}(t) = F\hat{\beta}(t) + Gz(t) + Cu(t) + Ju_d(t) \tag{9.18}$$

where,

$$F = A_{22} - LA_{12},$$

$$G = FL + A_{21} - LA_{11},$$

$$C = B_2 - LB_1,$$

$$J = E_2 - LE_1. \tag{9.19}$$

From the Observability of the pair (H, A), Observability of the pair (A_{12}, A_{22}) is also implied [72]. And hence, in a case, when $u_d(t)$ is available, the Luenberger observer gain, L, is chosen to place eigenvalues of F in desired locations. Consequently, the estimate $\hat{\alpha}$ of α is obtained from $\hat{\beta}$, the estimate of β produced by Equation (9.18), as [68], [69], [70]:

$$\hat{\alpha}(t) = \hat{\beta}(t) + Lz(t). \tag{9.20}$$

However, $u_d(t)$ (the road disturbance input in the current estimation problem) is not available. Therefore, the Luenberger gain matrix, L, is also required to make the unknown disturbance matrix identically zero, that is:

$$\begin{aligned} &\text{i) } J = 0; && \forall t \geq 0, \text{ and} \\ &\text{ii) } \lambda_i(F) < 0; && \forall i \leq n. \end{aligned} \tag{9.21}$$

A general solution to (9.21)(i) is given by [73], [74]:

$$L = E_2E_1^+ + K(I_p - E_1E_1^+), \tag{9.22}$$

where E_1^+ is the pseudo-inverse of E_1:

$$E_1^+ = (E_1^T E_1)^{-1} E_1^T , \tag{9.23}$$

and K is an arbitrary $(n-p)\times p$ matrix which is determined later to satisfy (9.21)(ii). E_1^+ exists if E_1 has full column rank, which means:

$$rank(E_1) = rank(HE) = q \text{ and } p \geq q . \tag{9.24}$$

Assuming that (9.24) holds, it implies that there exists an orthogonal matrix S such that:

$$SE_1 = \begin{bmatrix} \bar{E}_1 \\ 0_{(p-q)\times q} \end{bmatrix}, \tag{9.25}$$

where $\bar{E}_1$ is a $(q\times q)$ non-singular matrix. By substituting for E_1 in (9.22) from Equation (9.25) and some mathematical manipulations, the Luenberger gain formula, Equation (9.22), is rewritten as:

$$L = \begin{bmatrix} E_2 \bar{E}_1^{-1} & 0_{(n-p)\times(p-q)} \end{bmatrix} S + KS^T (I_p - \begin{bmatrix} I_{q\times q} & 0_{q\times(p-q)} \\ 0_{(p-q)\times q} & 0_{(p-q)\times(p-q)} \end{bmatrix}) S . \tag{9.26}$$

Let,

$$KS^T = \begin{bmatrix} \bar{K}_1 & \bar{K}_2 \end{bmatrix}, \tag{9.27}$$

Equation (9.26) is finally given by:

$$L = \begin{bmatrix} E_2 (\bar{E}_1)^{-1} & \bar{K}_2 \end{bmatrix} S . \tag{9.28}$$

In the next step, $\bar{K}_2$ is determined such that the eigenvalues of F are located properly. Having considered Equation (9.28), the expression of matrix F in Equation (9.19) is rewritten as:

$$F = F_1 - \bar{K}_2 \bar{A}_{12}^2 , \tag{9.29}$$

where,

$$F_1 = A_{22} - E_2 (\bar{E}_1)^{-1} \bar{A}_{12}^1 , \tag{9.30}$$

and

$$SA_{12} = \begin{bmatrix} \bar{A}_{12}^1 \\ \bar{A}_{12}^2 \end{bmatrix}. \tag{9.31}$$

It is clear from Equation (9.29) that $\bar{K}_2$ can assign all the eigenvalues of F arbitrarily, except unobservable modes of the pair $(\bar{A}_{12}^2, F_1)$.

Lemma 1: Let $rank(HE) = q$, the unobservable polynomial of the pair $(\bar{A}_{12}^2, F_1)$ is equal to the invariant zero polynomial of the triple (H, A, E). The proof of this lemma is given in [74] and [75].

An immediate outcome of the Lemma 1 is that if the triple (H, A, E) has no invariant zeros, then all the eigenvalues of the reduced order observer (9.18) can be arbitrarily assigned. If the triple (H, A, E) has stable invariant zeros (the pair $(\bar{A}_{12}^2, F_1)$ is not observable, but detectable), the Luenberger observer (9.18) would be asymptotically stable. However, some modes cannot be placed arbitrarily. And finally, if the invariant zeros of the triple (H, A, E) are unstable, estimation error dynamics would be unstable, too.

A similar approach is examined to establish the observer existence conditions for discrete systems. Consider a linear discrete system modelled as:

$$x_{k+1} = \Phi_k x_k + G u_k + E_d u_{d_k}$$

$$z_k = H x_k \tag{9.32}$$

where u_{d_k} is the disturbance sequence which cannot be measured. All the vector dimensions are the same as the continuous system (9.15). The problem is to estimate the state vector x_k by using the measurements z_k with no knowledge of the u_{d_k}. The following theorem summarizes existence conditions for a stable reduced-order Luenberger observer [74], [75]:

Theorem 1: Disturbance decoupling conditions for the discrete systems. Consider the *nth* order system (9.32), and assume that $p \geq q$, $rank(H) = p$ (condition for existence of the non-singular transformation (9.16)), $rank(E_d) = rank(HE_d) = q$. If the triple (H, Φ_k, E_d) has no invariant zeros or the invariant zeros are all inside the unit circle, then the following reduced order observer

$$\hat{\beta}_{k+1} = M_k \hat{\beta}_k + N_k z_k + V_k u_k + J_{d_k} u_{d_k}, \tag{9.33}$$

with $J_{d_k} = 0, \forall k \geq 1$, can be implemented to asymptotically estimate the dummy state β_k. Inverse transformations of the estimate $\hat{\beta}_k$ through,

$$\hat{\alpha}_k = \hat{\beta}_k + Lz_k \,, \tag{9.34}$$

and

$$\hat{x}_k = \begin{bmatrix} H \\ D \end{bmatrix}^{-1} \begin{bmatrix} z_k \\ \hat{\alpha}_k \end{bmatrix}, \tag{9.35}$$

yields the states estimate $\hat{x}_k$.

In the next step, the existence conditions are examined for the vehicle state estimation problem with unknown road disturbances. Consider the non-minimal (sixteen-state) realization of the vehicle model[1], given by Equation (7.1), without the additive noise term. The first sensor configuration, which is investigated, consists of one IMU and four accelerometers, i.e., sensor configuration (a) in Chapter 3. The measurement system is modelled by Equations (6.3), (6.7), and (6.23). In this case, the pair (H, Φ_k) is not observable. Matrices H, E_d and HE_d, all have full ranks, and both invariant zeros of the triple (H, Φ, E_d) are on the unit circle. Therefore, the required conditions for the unknown disturbance decoupling $(J_d = 0)$ do not exist. The same result is obtained for the sensor configuration (b).

For the fourth sensor configuration of Chapter 3, four displacement sensors and five accelerometers, the pair (H, Φ) is observable, and matrices H, E_d and HE_d have full ranks. However, the triple (H, Φ, E_d) has four repetitive zeros at $z = 1$. Obviously, the existence conditions are not satisfied for this case, too. Finally, with the sensor configuration (c) of four displacement sensors and one accelerometer, a similar outcome is achieved.

The disturbance decoupling conditions, given in Theorem 1, are all fulfilled only when virtual velocity sensors, measuring vertical velocity of the wheel-hubs, are added to the sensor configurations (d) or (c). In these cases, the triple (H, Φ, E_d) has no invariant zeros. Hence, a reduced-order unknown input (Luenberger) observer exists whose eigenvalues can be chosen arbitrarily. It makes sense, since the KF of Section 7.1.2 was able to provide accurate estimates of all the states except the wheel-hub velocities. The KF resembles a Luenberger observer after a few time-steps when the Kalman gain converges to its steady-state quantity (see Section

[1] The measurement model associated with the 14 states realization, Equation (6.23), does not match the structural requirement for the observer introduced in this section (please see Equation (9.32)).

4.2.1). Clearly, providing the velocity data for the Luenberger observer of Section 4.2.1 renders all the state estimates available, which confirms the last result of this section.

10 Aided Kalman Filter (AKF)

Consider a dynamical system modelled by the following linear difference equation:

$$x_{k+1} = \Phi_k x_k + G u_k + E_d u_{d_k} + L w_k \,, \tag{10.1}$$

where, $x_k \in R^n$ is the state vector, $u_k \in R^m$ contains m-known deterministic control inputs to the system, $u_{d_k} \in R^q$ is the vector of q unknown non-zero mean disturbance inputs (u_d also contains ℓ^{th} control input which is inaccessible ($\ell > m$)), and $w_k \in R^n$ is a zero-mean Gaussian white sequence with a strength of Q. The measurement system is also modelled by:

$$z_k = H_k x_k + v_k \,, \tag{10.2}$$

where $z_k \in R^p$ is the measurement vector and $v_k \in R^p$ is the measurement noise sequence having a strength of R. Assume that the matrix pair (H, Φ_k) is observable. Also, Matrices H, E_d and HE_d, all have full ranks. However, without the information of the disturbance u_d, the KF is not able to provide accurate estimates of some of the states of the system. It is desired to modify the estimation system in a way that accurate estimates of all the states, in an asymptotically stable manner, with no direct measurement of the disturbance vector u_d are rendered.

Suppose that the first $n_1 < n$ elements of the state vector x_k are not estimated precisely[1]. Now, assume that the following linearly independent combinations of these elements can be indirectly provided from the measurements (10.2):

$$z_v(j) = \sum_{i=1}^{n} h_{v_{ji}} x(i) \;; \quad j = p+1, p+2, \ldots \,, \tag{10.3}$$

where $i = 1, \ldots, n_1$. Indeed, the $z_v(j)$'s are the virtual measurements, from fictitious sensors, that are obtained by integrating or differentiating or post processing the measurements of the real sensors. By adding the fictitious sensors to the real sensors, the new measurement model is written as:

---

[1] It is always possible to reaarange the elements of the state vector such that those states, which are not accurately estimated by the KF, are placed as the first n_1 elements of the state vector.

$$\begin{bmatrix} z_k \\ z_{v_k} \end{bmatrix} = \begin{bmatrix} H \\ H_v \end{bmatrix} x_k + v_k^t . \tag{10.4}$$

It is then rewritten in the following more compact form:

$$z_k^t = H^t x_k + v_k^t , \tag{10.5}$$

where superscript t denotes the total measurements of the system.

Corollary (of Theorem 1, Section 9.2): Consider the dynamical system (10.1) with the measurement system (10.2). If there exists the virtual measurements (10.3) such that the triple (H^t, Φ_k, E_d) has no invariant zeros (or, if it does, all of them are inside the unit circle), then the KF[1], incorporating the measurement system (10.5), estimates all the system states in an asymptotically stable manner, with no knowledge (no direct measurement) of the disturbance vector u_d. Since the KF is aided by the fictitious sensors to compensate for the unknown disturbance input u_d, the KF is named Aided Kalman Filter (AKF) in this context.

The next section applies the Corollary for the vehicle state estimation problem in the presence of unknown road disturbances.

[1] Note that at steady state, KF is a Luenberger observer.

10.1 The AKF Estimation Results with the Real Data

Consider the non-minimal (sixteen-state) realization of the vehicle model. As it is illustrated in Section 7.1, the absolute velocity states of the wheel-hubs are not accurately estimated by the KF, regardless which sensor configuration is utilised. Therefore, the first 4 ($n_1 = 4$) elements of a new state vector x^n are the absolute velocity states, x_{10}, x_{12}, x_{14} and x_{16} of the original state vector (6.8):

$$\begin{aligned} x^n(1) &= x_{10} \\ x^n(2) &= x_{12} \\ x^n(3) &= x_{14} \\ x^n(4) &= x_{16}\,. \end{aligned} \tag{10.6}$$

The remaining elements of x^n are filled by the other vehicle states, given by Equations (6.9) and (6.10). To implement the AKF, the first step is to find a sensor configuration such that the matrix pair (H, Φ_k) is observable. Among the possible sensor configurations, presented in Chapter 3, only the sensor suites (c) and (d) satisfy the Observability condition. However, no information regarding the $x^n(i)$'s, $i = 1,...,4$, is obtained from the displacement sensors data of the configuration (c)[1].

Now consider the sensor suite (d) which consists of one displacement sensor for each suspension and one accelerometer for each wheel-hub. Even without one of the displacement sensors, for instance the one on the RF suspension, the pair (H, Φ_k) remains observable. Also, it is assumed that the front and rear wheels always experience the same disturbances, but shifted in time. Therefore, the two rear accelerometers are eliminated. Instead, the front accelerometers signal are used for the rear wheel-hubs by considering the time delay between the front and rear wheels. Finally, the absolute velocity of the wheel-hubs is indirectly measured by integrating the corresponding wheel accelerometer signal. According to the AKF theory, six fictitious sensors, including two accelerometers and four velocity sensors, are added to the original sensor suite. The accelerometers measurement is modelled by:

---

[1] It means that by processing the displacement sensors data of the sensor suite (c), no information regarding the $x^n(i)$'s, $i = 1,...,4$, which are absolute velocities of the wheel-hubs, can be extracted.

$$z_v(j) = \sum_{i=1}^{n} h_{v_{ji}} x(i)\ ; \quad j = p+1, p+2\,, \tag{10.7}$$

where $h_{v_{ji}}$'s are given by Equation (6.7) . The virtual velocity measurements are also modelled by Equation (10.8), as:

$$\begin{aligned} z_v(j) &= x^n(i), \\ j &= i + p + 2 \quad ;\ i = 1,...,4\,, \end{aligned} \tag{10.8}$$

where $p = 5$ is the dimension of the original reduced number sensor suite consisting of two accelerometers and three displacement sensors. Concatenating the models of the fictitious sensors to that of the actual sensors, it is revealed that the triple (H^t, Φ_k, E_d) has no invariant zeros.

First, a computer simulation result is presented in Figure 90. The graph compares the AKF and the KF estimates of the LF wheel-hub absolute velocity.

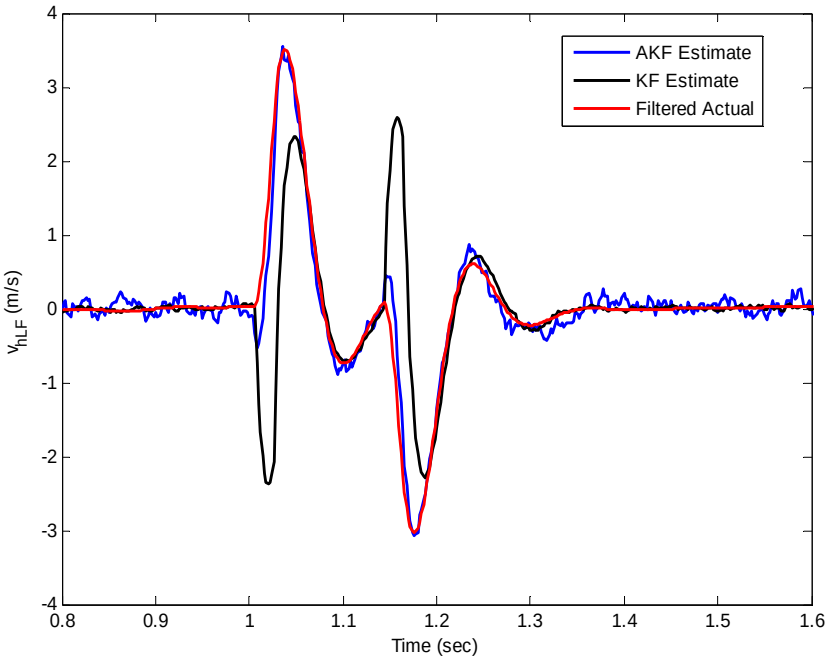

Figure 90: The graph compares the AKF and the KF estimates of LF wheel-hub absolute velocity in a computer simulation.

It is apparent that the AKF does a very good job in estimating the velocity states which the KF can not. Figure 91 to Figure 102 illustrates the AKF estimation efficiency with the real data.

The sensor data, which are fed to the AKF, is a set of data collected from the Cadillac SRX sensors, driven over the bump at a rate of 40 km/hr (see Chapter 7 for further descriptions of the real-time experiments). It is demonstrated by Figure 93 and Figure 94 that even without the RF suspension sensor, the AKF provides fairly accurate estimates of the RF relative displacement and velocity. The AKF estimates of the absolute velocity states associated with the LF and LR wheel-hubs are also plotted in Figure 96 and Figure 98, respectively. It is shown that the AKF effectively estimates the absolute velocities with no direct measurement (no knowledge) of the road disturbances. Finally, the measurement residuals are displayed in Figure 100 to Figure 102. The residuals are unbiased and within the theoretically expected bounds, given by Equation (5.36).

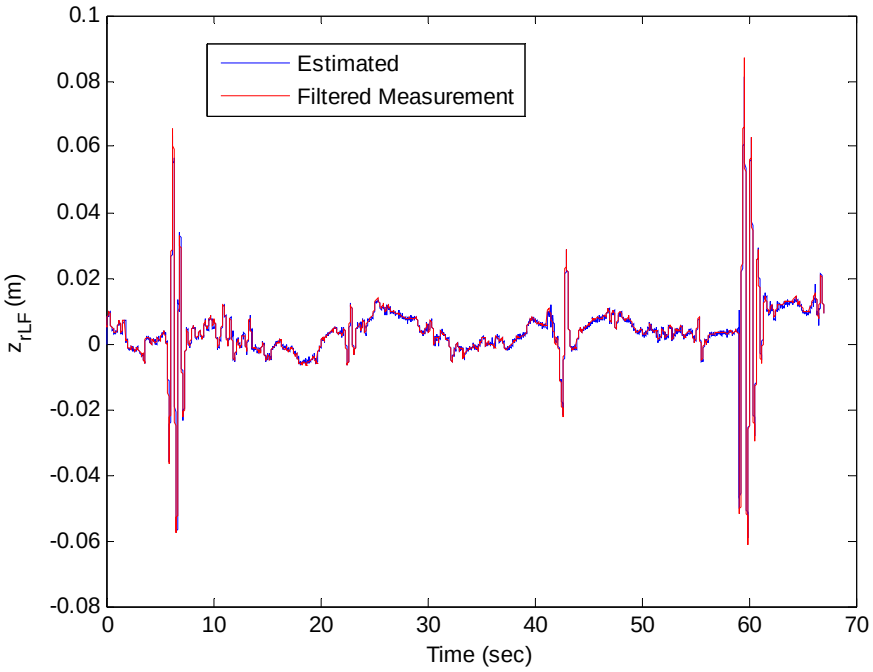

Figure 91: The graph compares the measured relative displacement of the LF shock with the AKF estimate.

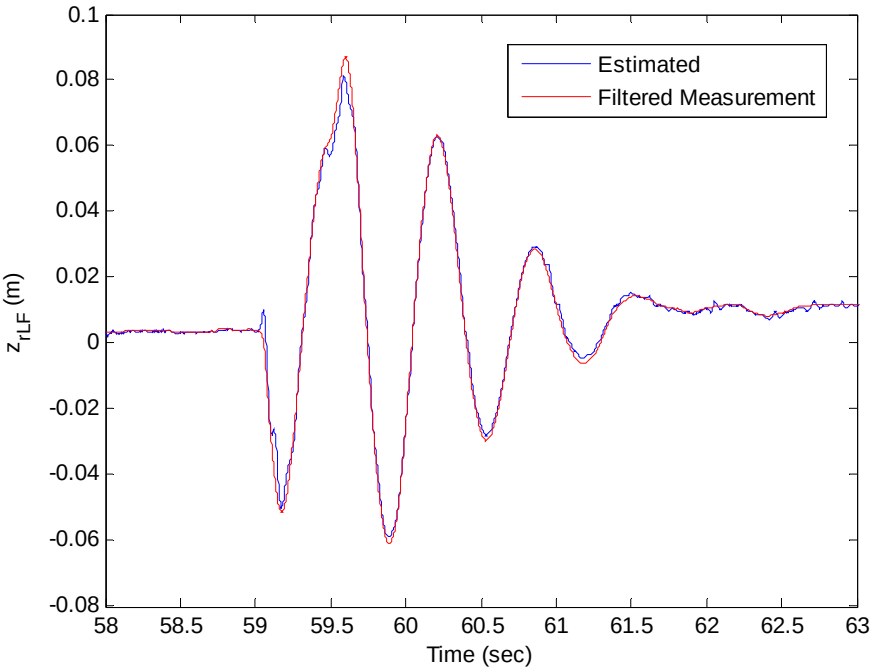

Figure 92: The graph compares the measured relative displacement of the LF shock with its estimation, zoomed in on the second bump.

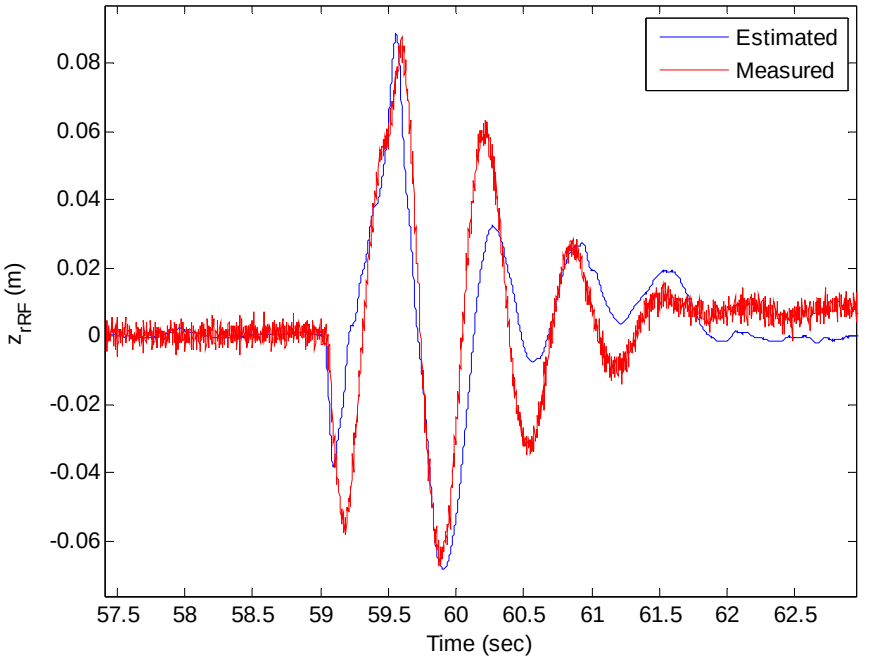

Figure 93: The graph compares the measured relative displacement across the RF shock with the AKF estimate on the second bump.

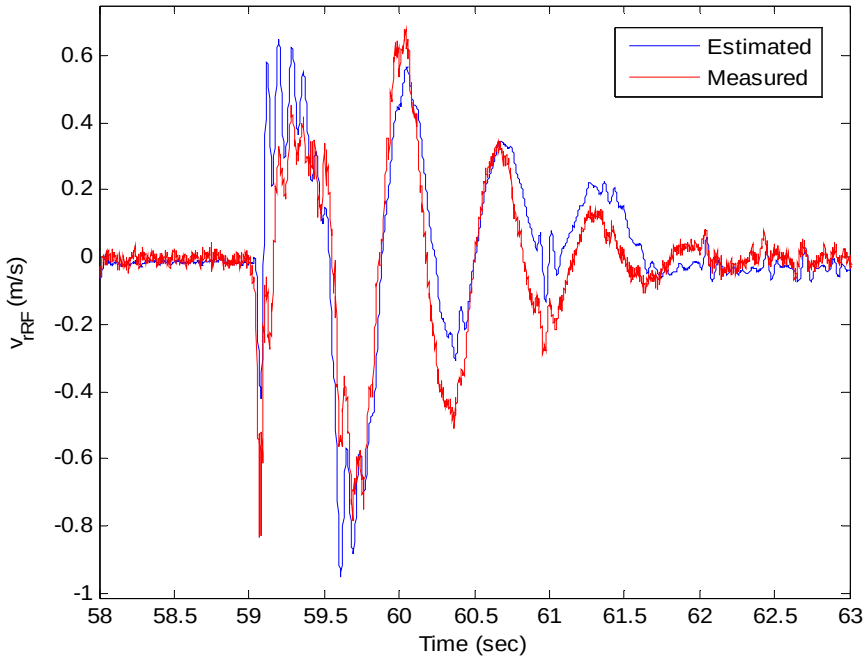

Figure 94: The graph compares the measured relative velocity of the RF shock with the AKF estimate on the second bump.

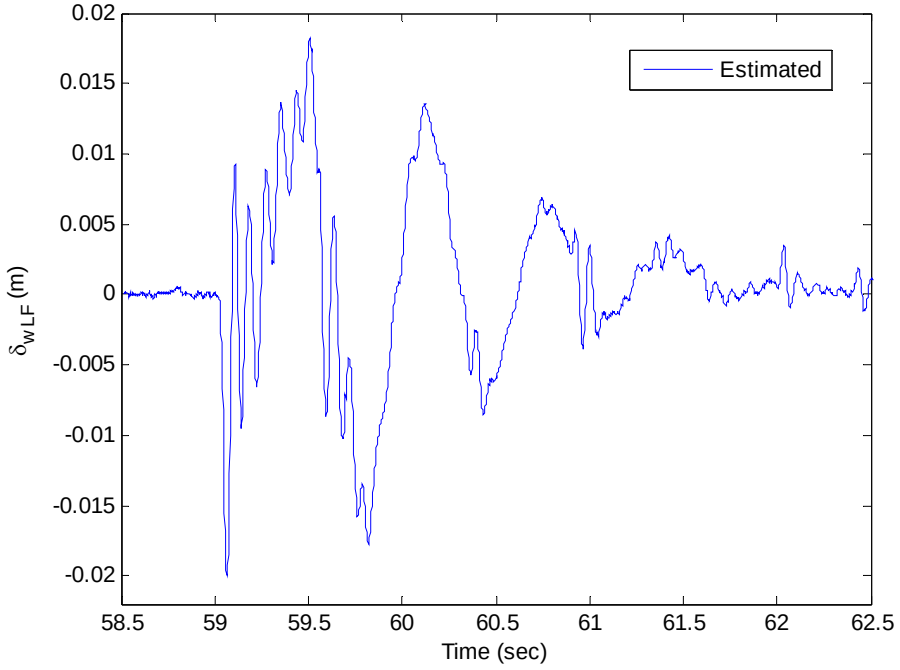

Figure 95: The AKF estimate of the LF wheel deflection on the second bump.

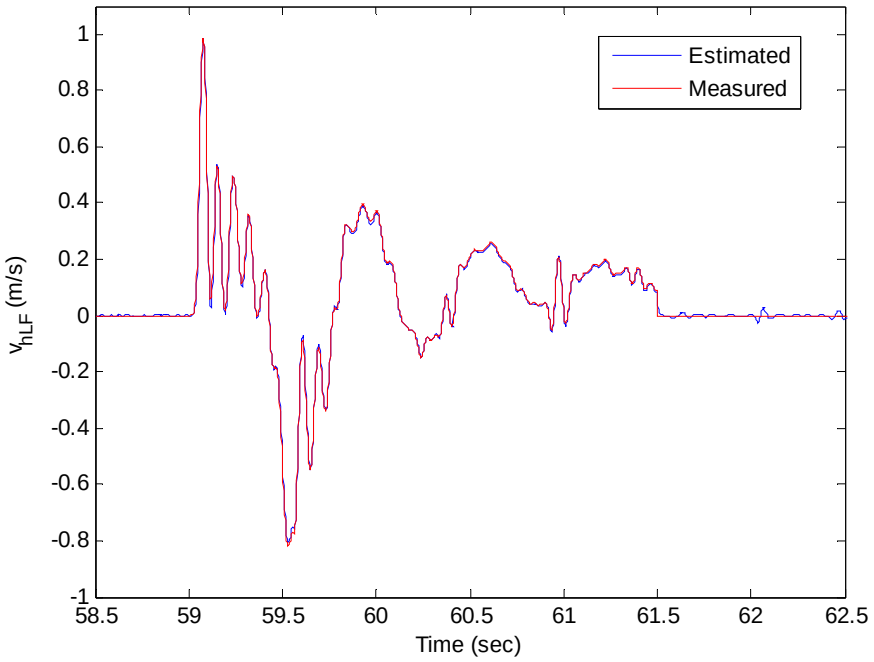

Figure 96: The graph compares the measured absolute velocity of the LF wheel-hub with the AKF estimate.

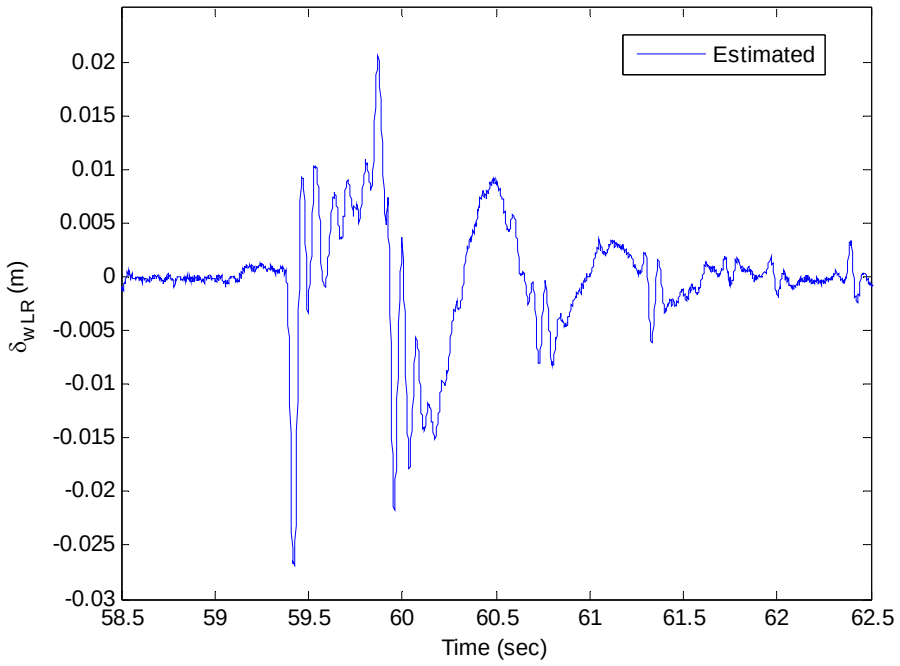

Figure 97: The graph shows the estimate of the LR tire deflection on the second bump.

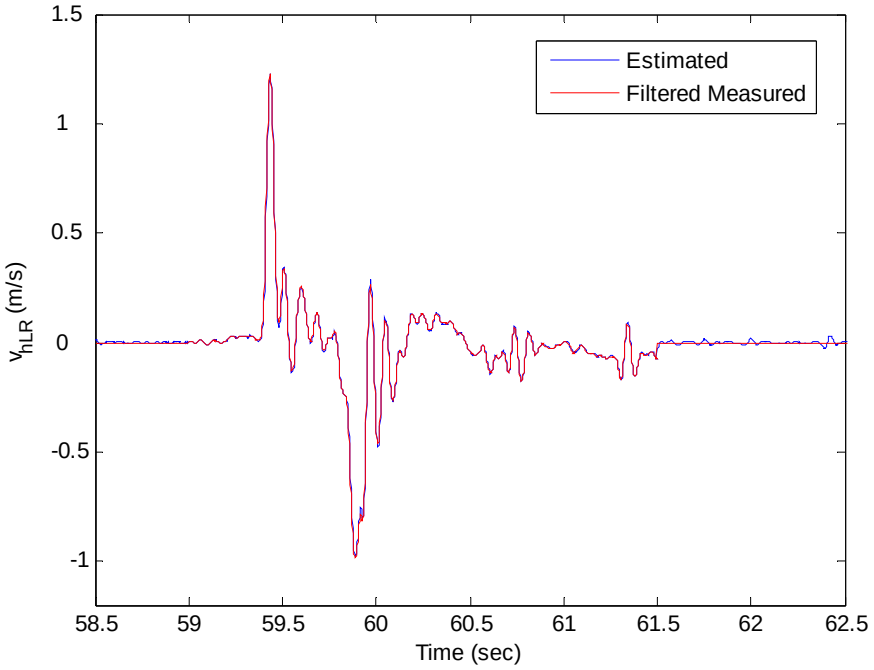

Figure 98: The graph compares the measured absolute velocity of the LR wheel-hub with the AKF estimate.

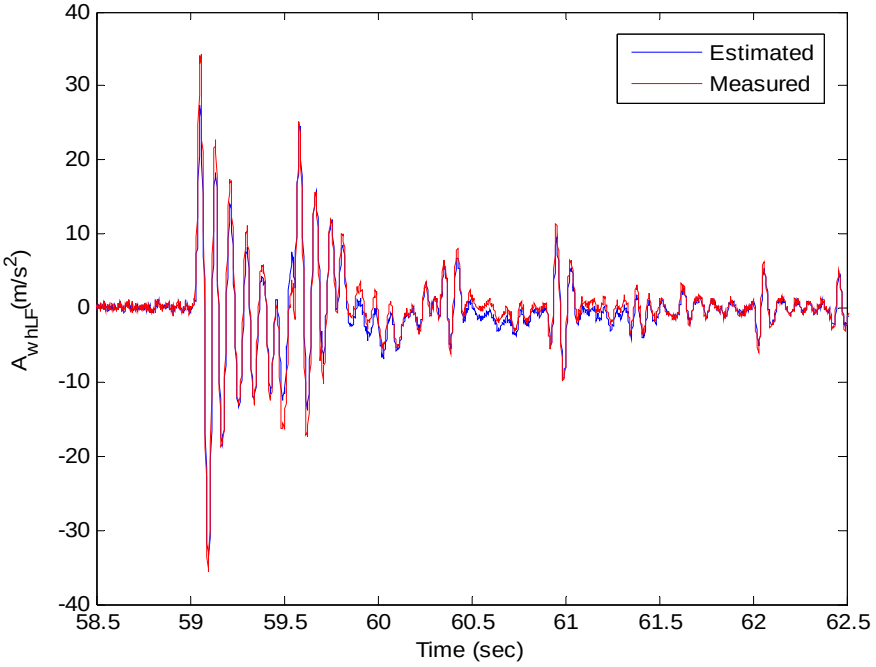

Figure 99 : The graph compares the measured acceleration of the LF wheel-hub with the AKF estimate.

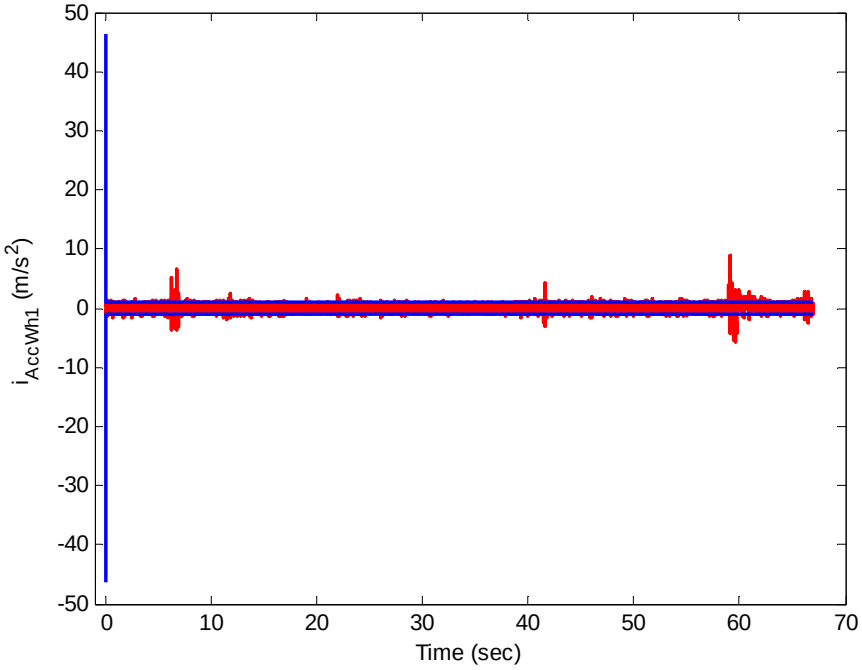

Figure 100: The graph shows the LF wheel-hub acceleration residual [red] and the theoretically expected covariance bounds [blue].

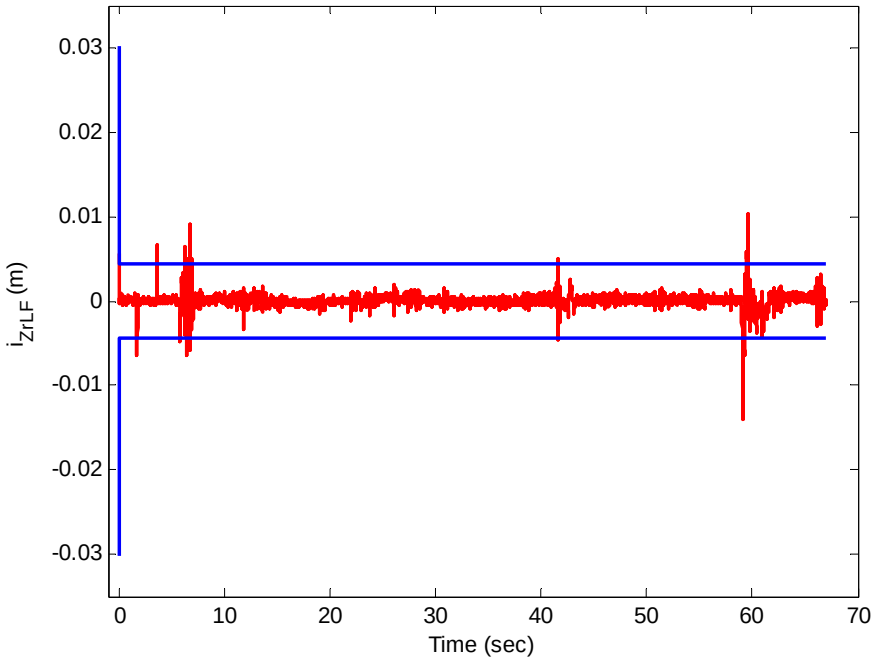

Figure 101: The graph shows the residual [red] corresponding to the measurement of the LF suspension relative displacement and the theoretically expected covariance bounds [blue].

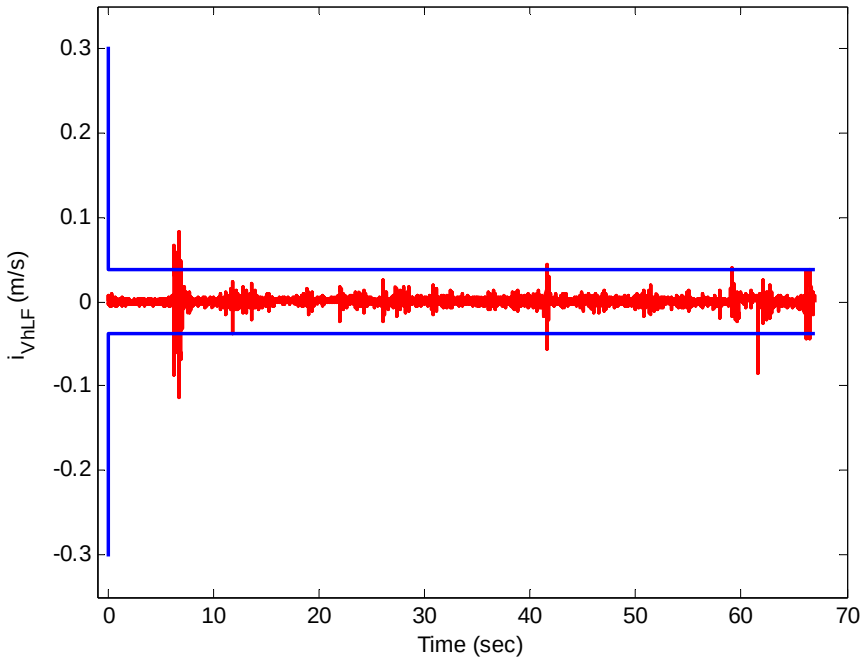

Figure 102: The graph shows the residual [red] corresponding to the measurement of the LF wheel-hub absolute velocity and the theoretically expected covariance bounds [blue].

11 Supervisory Kalman Filter (SKF): A New State-Estimation Scheme for Systems with Unknown Inputs

Consider a dynamical system modelled by the following linear difference equation:

$$x_{k+1} = \Phi_k x_k + G u_k + E_d u_{d_k} + L w_k . \tag{11.1}$$

The measurement system is modelled as:

$$z_k = H_k x_k + v_k . \tag{11.2}$$

In Equation (11.1), $x \in R^n$ is the state vector, $u \in R^m$ is the control input containing m-known deterministic control inputs to the system, $u_d \in R^q$ is the vector of q non-zero mean disturbance inputs which cannot be measured (u_d also contains those control inputs which are inaccessible, $u(\ell)$'s with $\ell > m$), and $w_k \in R^n$ is a zero-mean Gaussian white sequence with a strength of Q. In the measurement model, Equation (11.2), $z \in R^p$ is the vector of measurements corrupted by a Gaussian white sequence $v_k \in R^p$. The covariance (strength) of the measurement noise is R. The subscript k refers to the time-step. It is assumed that the matrix pair (H_k, Φ_k) is observable. Also, the initial condition (4.9) is given. The problem consists of designing an estimator to asymptotically estimate the state vector x_k with no knowledge of the disturbance vector u_d [1].

In the absence of the disturbance input u_d, the KF is the optimal solution to the above estimation problem (see Section 4.2). However, the KF theory is violated when the non-zero mean unknown disturbance u_d is acting on the system. If the KF is implemented for the state estimation of such a system, not all the states of the system are estimated precisely. Suppose that the estimation quality associated with $n_1 < n$ elements of the state vector x_k is unacceptable. A state estimation is defined as unacceptable when the estimation error is unbiased and is not in agreement with the corresponding covariance bounds, calculated by the KF. This is determined by analyzing the off-line computer simulation results. For instance, the UKF estimation errors of the absolute position of the vehicle's CG (see Sections 4.4 and 7.2.3

[1] With no direct measurement of the disturbance vector.

for further descriptions), obtained by the Monte Carlo simulation method, are portrayed in Figure 103. It is apparent that the estimation errors, during the period that the system is hit by the unknown disturbance input due to the bump located at between $t = 1$ and $t = 1.5$ sec, are not unbiased and also do not remain inside the expected covariance bounds (at least for 68% of the times). The comparison of the estimated and the real CG position, given in Figure 76, also confirms that the estimation quality is unacceptable.

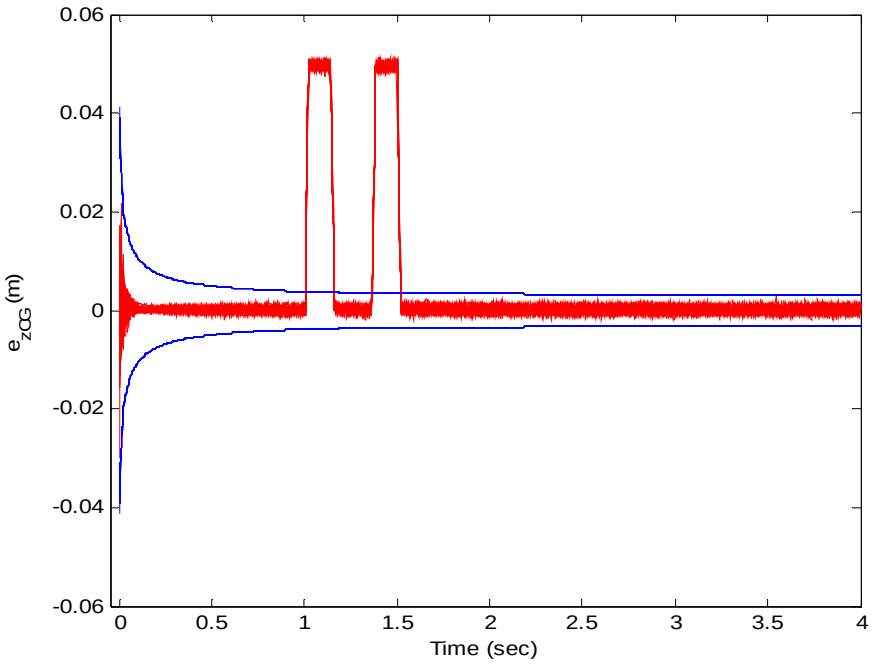

Figure 103: The UKF estimation errors [red] of the CG position obtained by the Monte Carlo simulation method.

The remaining $n_2 < n$ states are assumed to be reasonably estimated by the KF. By rearranging the states, the state vector is rewritten in the following partitioned form[1]:

$$x_k = \begin{bmatrix} x_{1_{n_1 \times 1}} \\ x_{2_{n_2 \times 1}} \end{bmatrix} \; ; \quad n_1 + n_2 = n \, . \tag{11.3}$$

The SKF is a KF with an extra update step whose function is similar to that of the Bayesian estimator (PF), presented in Section 9.1. The extra step, called a supervisory layer, operates on the x_1 portion of the state vector to enhance its estimation accuracy. It is either triggered from

[1] It is always possible to rearrange the elements of the state vector such that those states, which are not accurately estimated by the KF, are placed as the first n_1 elements of the state vector.

the initial time or activated when the disturbance input u_d is introduced to the system and sensed by a responsive sensor[1]. Suppose that $p(x_k \mid z_k)$ is the latest estimated pdf provided by the KF update step immediately prior to the supervisory layer being triggered. The supervisory layer generates N random state vectors $\hat{x}^+_{k,i}$ $(i = 1,2,...,N)$, hereafter referred to as particles, which their first n_1 elements, $\hat{x}^+_{1_{k,i}}(j)$'s $(j = 1,...,n_1)$, are distributed based on the KF updated pdf, that is:

$$E[\hat{x}^+_{1_{k,i}}(j)] = mean[p(x_k(j) \mid z_k)] = \hat{x}^+_k(j);\ i = 1,...,N,$$

$$\frac{1}{N}\sum_{i=1}^{N}(\hat{x}^+_{1_{k,i}}(j) - \hat{x}^+_k(j))(\hat{x}^+_{1_{k,i}}(j) - \hat{x}^+_k(j)) = \alpha \times cov[p(x_k(j) \mid z_k)] = \alpha P^+_k(j,j), \qquad (11.4)$$

where $\hat{x}^+_k$ and P^+_k are the KF updated state and covariance matrix, given by Equations (4.10) and (4.14), respectively. Also, α is a design parameter which is selected such that the particles are spread throughout the variation ranges of the first n_1 states. Since the x_2 portion of the state vector is accurately estimated by the KF, the remaining n_2 elements of each particle, $\hat{x}^+_{2_{k,i}}(j)$'s $(j = n_1 + 1,...,n)$, are identically substituted from the KF last updated estimate, $\hat{x}^+_k$:

$$\hat{x}^+_{2_{k,i}}(j) = \hat{x}^+_k(j);\ \ i = 1,...,N. \qquad (11.5)$$

The following three steps are accomplished recursively. First, the particles are propagated to the next time-step by using the system analytical model, Equation (11.1). However, since estimation quality of the x_1 portion of the state vector is degraded due to the lack of information of the disturbance input, the first n_1 elements of each particle are propagated by including the white sequence in the system model:

$$\hat{x}^-_{1_{k+1,i}}(j) = \varphi(j)\hat{x}^+_{k,i} + g(j)u_k + w_{k,i}(j);\ \ j = 1,...,n_1, \qquad (11.6)$$

where $\varphi(j)$ and $g(j)$ are the j^{th} rows of the state transition matrix Φ_k and the input matrix G, respectively. The elements of x_2 portion of each particle are also propagated by:

$$\hat{x}^-_{2_{k+1,i}}(j) = \varphi(j)\hat{x}^+_{k,i} + g(j)u_k;\ \ j = n_1 + 1,...,n. \qquad (11.7)$$

---

[1] A responsive sensor, in the case of the vehicle systems, can be a wheel accelerometer which immediately senses the significant disturbance inputs by the bumps or holes of the road.

Furthermore, the error covariance matrix is propagated by Equation (4.15) (the regular KF equation).

Upon receiving a new measurement, z^*_{k+1}, each particle is updated by the KF update formula:

$$\hat{x}^+_{k+1,i} = \hat{x}^-_{k+1,i} + K_{k+1}(z^*_{k+1} - \hat{z}_{k+1,i}), \quad i = 1,...,N. \tag{11.8}$$

where the Kalman gain, K_{k+1}, is given by Equation (4.12) and the measurement estimates $\hat{z}_{k+1,i}$ are computed by using the measurement model, Equation (11.2), as:

$$\hat{z}_{k+1,i} = H_{k+1}\hat{x}^-_{k+1,i} \;; \quad i = 1,...,N. \tag{11.9}$$

However, with no direct information of the disturbance input u_d, KF updated estimate of the x_1 portion of the particles are not accurate. Therefore, each $\hat{x}^+_{1_{k+1,i}}(j)$ $(j = 1,...,n_1)$ element of the KF updated particles is replaced by a number picked up from a random distribution with the mean value of the $\hat{x}^+_{1_{k+1,i}}(j)$ itself and the corresponding KF updated covariance times α, i.e., $\alpha P^+_{k+1}(j,j)$.

Finally, the resampling stage (see Section 9.1) is performed to collect the particles with higher belief. First, each particle is assigned a weight depending on how well the estimated measurement fits the actual measurement. This is achieved by evaluating the relative likelihood q_i of each particle given the most recent measurement z^*_{k+1}:

$$q_i \sim p[(z_{k+1} = z^*_{k+1}) \,|\, (x_{k+1} = \hat{x}^+_{k+1,i})]; \quad i = 1,...,N. \tag{11.10}$$

Now, either of the resampling algorithms presented in [42], and [54] or the one in Section 9.1 is utilized to select the particles with higher likelihoods q_i and create a new set of particles. At each time-step $t = t_{k+1}$, after the resampling stage, the SKF estimate, denoted by $\hat{x}^S_{k+1}(+)$, is then approximated by the following expression:

$$\hat{x}^S_{k+1}(+) \approx \frac{1}{N}\sum_{i=1}^{N} \hat{x}^r_{k+1,i}(+), \tag{11.11}$$

where $\hat{x}^r_{k+1,i}(+)$ $(i = 1,2,...,N)$ are the particles in the resampled set.

The above-mentioned three steps are recursively implemented until the supervisory layer function is terminated as a result of diminishing the unknown disturbance input u_d. This is also sensed by the responsive sensor. After turning off the supervisory layer, the SKF is again a

regular KF initiated by the latest SKF estimate, given by Equation (11.11). The SKF algorithm is summarized in

Figure 104 in which operations on the x_1 portion of the state vector are presented above the dashed time-axis and operations on the x_2 portion are below the axis. The same algorithm is used for a nonlinear state estimation problem. However, instead of the KF (the KF is the base estimator for the SKF in a linear estimation problem), a nonlinear estimator like the EKF or UKF is employed as the base estimator. The next section applies the SKF to the current vehicle state estimation problem.

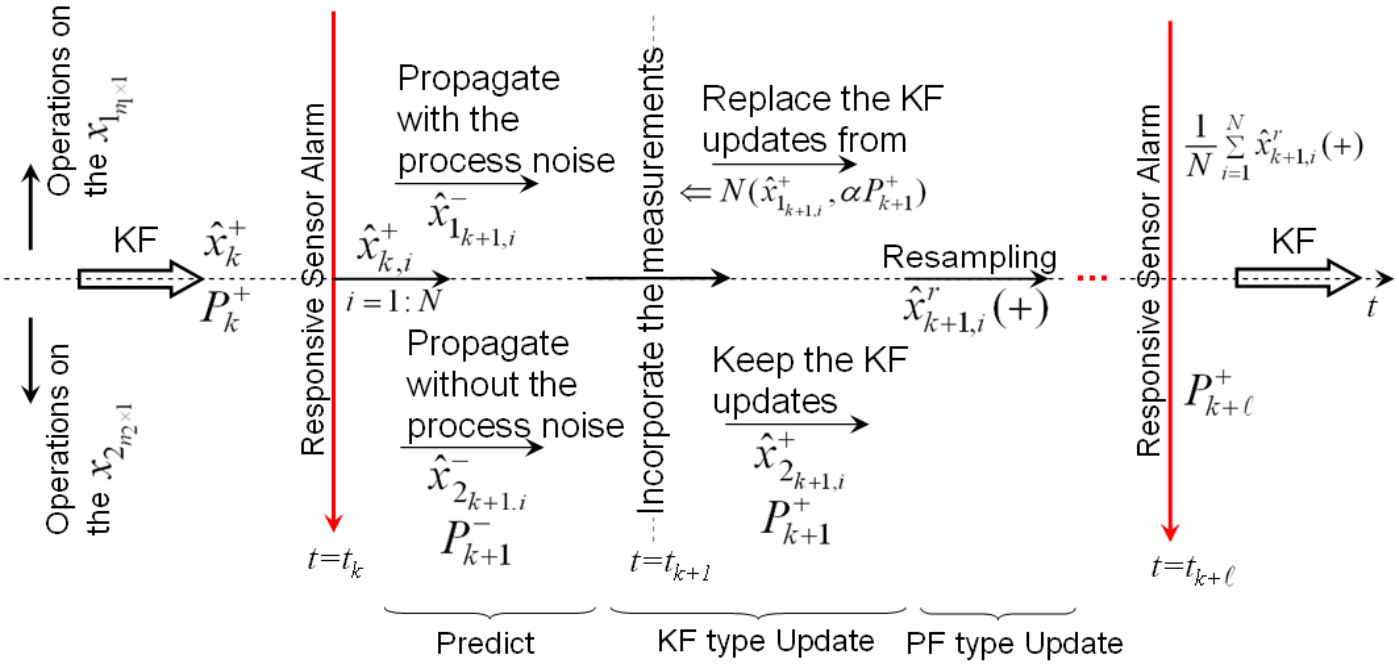

Figure 104: The SKF algorithm.

11.1 SKF Results for the Vehicle States Estimation Problem

As demonstrated earlier, neither the KF estimators (see Chapter 7) nor the PF or the conventional observers for systems with unknown inputs (see Section 9.2) are able to provide high quality estimates of all the vehicle states. The relative displacements of the vehicle shocks are the states that are not satisfactorily estimated by the KF, embedding the minimal fourteen-state realization. With the non-minimal realization, those states not estimated accurately are the absolute velocities of the wheel-hubs.

Consider the test vehicle equipped with the minimized sensor configuration introduced in Chapter 10. It consists of two accelerometers on the front wheel-hubs and three displacement sensors, one on the LF suspension and the two remaining on the rear suspensions. A non-explicit model of the measurement system with respect to the unknown road disturbance u_d is obtained by the use of the non-minimal realization[1] of the vehicle model. Then the pair (H, Φ_k) is also observable. By considering the original state vector, given by Equation (6.8), the x_1 portion of a new state vector x^n includes the four absolute velocity states of the wheel-hubs:

$$x_1 = [x_{10}, x_{12}, x_{14}, x_{16}]^T . \tag{11.12}$$

The rest of the states, given by Equations (6.9) and (6.10), are accurately estimated by the KF and therefore placed in the x_2 portion. For the current estimation problem, the unknown disturbance input is due to the bump in Ring Road. The vehicle velocity is approximately 30 km/hr while passing the bump. The front wheel accelerometers are the sensitive sensors to the bump disturbance.

Figure 105 illustrates how effective the SKF is in estimating the absolute velocity of the LF wheel-hub, the state that neither KF nor PF can accurately estimate. The KF estimation result is also plotted in the figure (Figure 89 shows the PF estimation result). The RMS values associated with the estimation errors are compared in Table 4. It is obvious that the SKF estimate perfectly matches the actual velocity data, specifically during the period when the unknown disturbance is acting on the vehicle. But, at the same period, the KF estimate does not

[1] With the minimized sensor configuration, the measurement model with the 14-states vector would be an explicit function of the unknown disturbance input. This is not in agreement with the structural requirements of the measurement model of this section (see Equation (11.2)).

remain acceptable. Before and after the vehicle hits the bump at the time $t = 1$ sec and approximately at $t = 1.35$ sec respectively, the SKF and the KF results are both reasonably accurate.

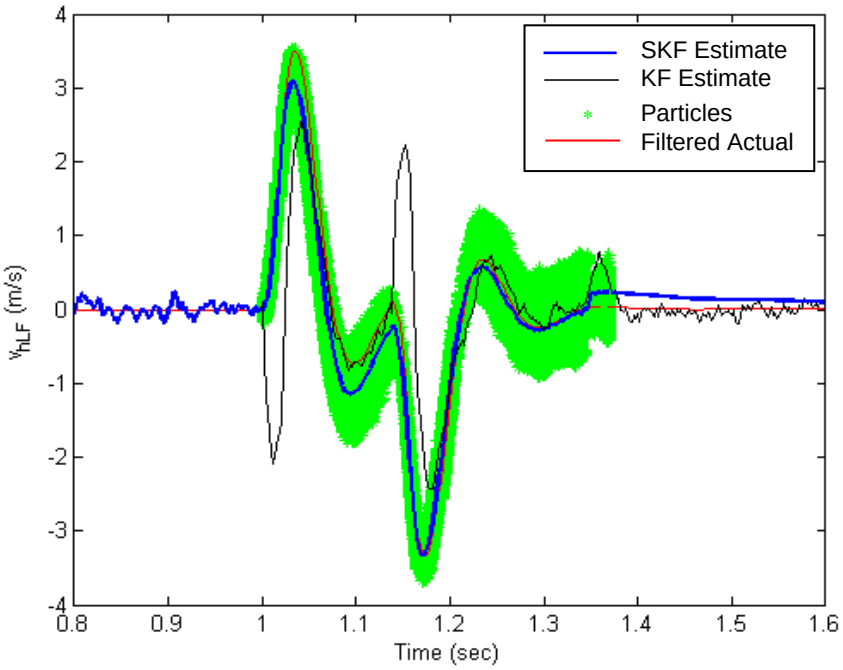

Figure 105: Performance of the SKF in estimating the absolute velocity of the LF wheel-hub.

As demonstrated by Figure 105, before the bump disturbance at $t = 1$ sec, the SKF and the KF estimation results are identical since the SKF works exactly similar to the KF. As soon as the wheel-accelerometer triggers the supervisory layer, random particles, shown by the green stars in the Figure 105, are generated based on the distribution given in Equation (11.4). Here, the magnifying coefficient α in Equation (11.4) is selected to be $3 \times n$, where $n = 16$ is the dimension of the state vector. α should be big enough to assure that the particles are distributed throughout the working space. Afterwards, the particles are recursively processed by the three consecutive steps of the SKF until again the accelerometer turns off the supervisory layer. For the rest, the SKF is the KF initialized by the SKF's last estimate.

The supervisory layer allows the SKF to explore wider regions of the states space than an ordinary KF to find the best estimates of the state vector. However, compared to the PF, the SKF spreads the particles more intelligently based on the updated estimates of a base filter such

as a KF, EKF or UKF. Moreover, the search is accomplished on the only portion of the state vector which is not accurately provided by the base estimator[1] (see Equation (11.4), only the first n_1 elements of the state vector are randomly distributed). Consequently, a fewer number of particles is required to guarantee the convergence of the SKF. This reduces the computational burden of the SKF and makes it suitable for real-time applications. For instance, the accurate estimate of the wheel-hub velocity in Figure 105 is obtained by the SKF which uses 200 particles[2]. With this number of particles, sample impoverishment [54], [55] happens in the PF implementation only after a few steps. The processor in Section 9.1 needs less than six milliseconds (approximately 150Hz) to process the 200 particles at each cycle of the SKF.

The SKF estimates of the states, which are also provided accurately by the KF, are plotted in Figure 106, Figure 107 and Figure 108. Figure 106 compares the SKF and KF estimation results of the relative displacement across the LF shock. The comparison on the LF relative velocity state is given in Figure 107. And finally, the tire deflection estimates are plotted in Figure 108. It is demonstrated that the SKF provides accurate estimates of the tire deflection which are crucial for the vehicle stability controllers.

The performance of the two filters in terms of the RMS value of the estimation error is detailed in Table 4. Other than for the relative displacement estimate, which is marginally degraded, the use of the SKF improves the estimation accuracy of all the other states.

[1] Given the Observability of the pair (H, Φ_k), the base estimator provides accurate estimate for only a portion of the state vector without any knowledge of the unknown disturbance.
[2] Even with only 20 particles, the SKF estimation results remain quite accurate.

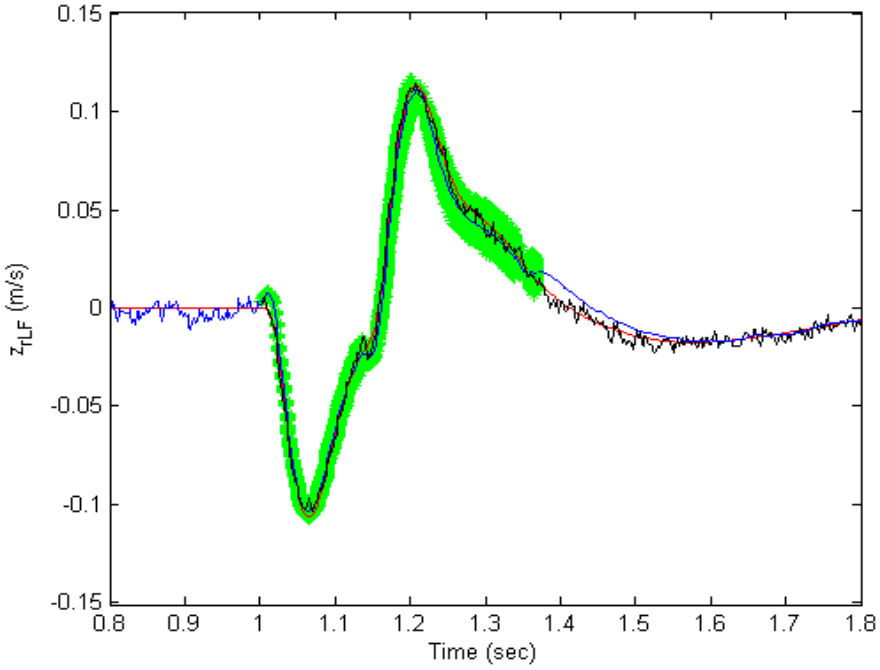

Figure 106: Performance of the SKF in estimating the relative displacement of the LF shock.

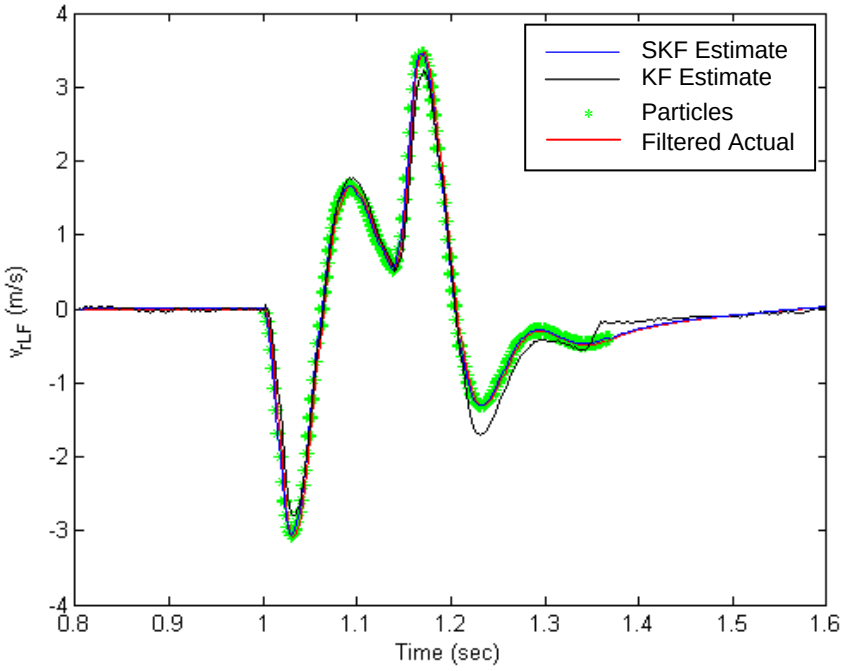

Figure 107: Performance of the SKF in estimating the relative velocity across the LF shock.

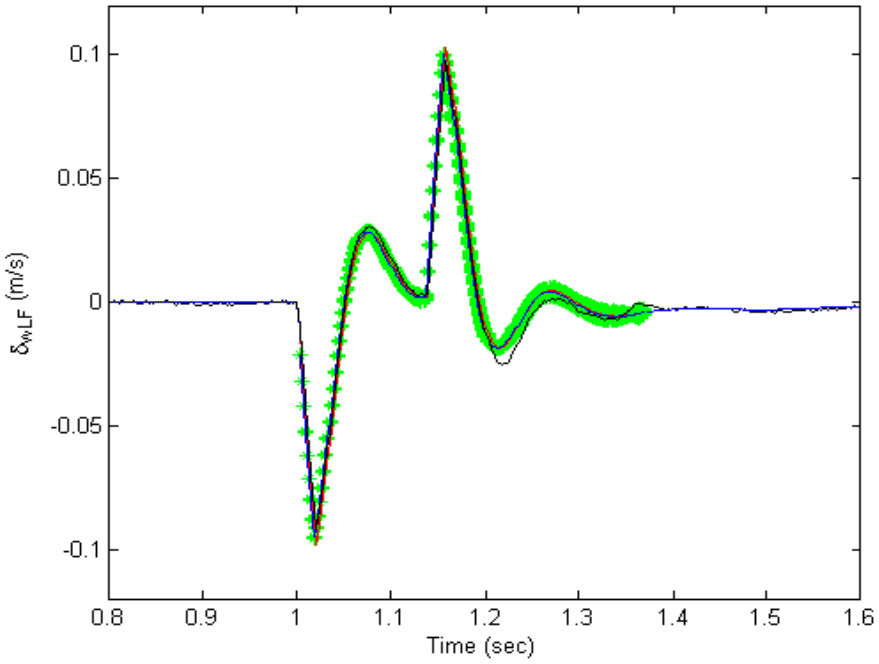

Figure 108: Performance of the SKF in estimating the LF tire deflection.

Table 4: Comparison of the RMS values of the SKF and KF estimation errors associated with the vehicle LF states.

	KF	SKF
Relative displacement	0.0033	0.0039
Relative velocity	0.0962	0.0235
Absolute velocity	0.4851	0.0734
Tire deflection	0.0017	0.0008

12 Control[1]

This chapter develops a novel practical methodology to design and implement vehicle semi-active suspension control systems by using simple analytical models. The proposed design technique is then employed to design a semi-active suspension system for the Cadillac SRX equipped with Delphi Magneto-Rheological (MR) dampers.

Semi-active suspension systems utilize dampers that can change their damping and stiffness properties, given a low power electrical signal, and exhibit high performance vibration isolation. Usually, the command signal is provided by the vehicle computer, or preferably, a low-cost micro-controller module. There are two classes of semi-active dampers in practice. One is a modification of passive dampers that are equipped with external solenoid valves to vary the oil flow rate between the compression chamber and the reverse chamber of the damper. For the second class, the dampers (e.g., MR dampers) change the properties of the material inside the shock to provide different levels of resisting forces.

Sensors are essential components of vehicles semi-active suspension systems. They measure the chassis and wheels motion, relative to the road. The information is then fed back to the vehicle computer, preferably a micro-processor, which in turn sends a control command to the semi-active dampers. It is therefore of great practical interest to develop/implement control strategies that are efficient for embedded programming so that the micro-processor cost and size are reduced.

Various control strategies have been proposed to determine the desired damping forces. The Skyhook control strategy, introduced by Karnopp et al. [11], is undoubtedly, the most widely used control policy for semi-active suspension systems. Following the Skyhook policy, the semi-active damper mounted between the sprung mass and a stationary sky emulates a fictitious damper behavior. It has been established that the Skyhook strategy can significantly attenuate the resonant peak of the sprung mass, enhancing the vehicle's ride comfort. The Skyhook strategy is also effective in terms of the simplicity of the control algorithm. Its other advantage is that, aside from the information regarding the vehicle's shock characteristics, the control

[1] This chapter along with Chapter 13 have been accepted for future publication in the Vehicle System Dynamics journal.

strategy does not require any a priori knowledge about the dynamics of the vehicle; that is, it is not model-based.

The Skyhook policy can be applied either as a bang-bang controller or in a continuous manner by utilizing the sprung mass vertical velocity feedback (however, this version is also discontinuous). The on-off Skyhook controller is usually simpler and better suited for the industrial applications. The control law can be described simply as

$$c_{sky} = \begin{cases} c_{\max} & if \quad v_r v_b \geq 0 \\ c_{\min} & otherwise \end{cases}, \tag{12.1}$$

in which v_b is the absolute velocity of the sprung mass, and v_r is the relative velocity between the sprung and unsprung mass across the suspension. Extensive theoretical and experimental studies of the performances of different types of semi-active Skyhook controllers can be found in the literature [11], [14], [28], [88] and [92].

Nevertheless, the controller's upper and lower gains (that is, $c_{\max}$ and $c_{\min}$, respectively) are usually determined by trial and error, and there is no systematic method to adjust them. This would make the controllable suspension system development process time consuming and sometimes too difficult. Consequently, this chapter introduces a new methodology which allows for the systematic design and implementation of the on-off Skyhook control strategy for semi-active suspensions. Although the design methodology is developed for the Skyhook control strategy, it remains valid for implementation of other semi-active control policies, presented in Appendix A, which have switching natures.

The discontinuous nature of semi-active control strategies, including the Skyhook policy, is the principle barrier in methodical design. The first step of the new methodology is to apply the Fuzzy system theory to create a network with continuous valued outputs to emulate the discontinuous controller law. Once the original control strategy is converted to a continuous form, different well-established frequency or time domain techniques can be employed to design and adjust suspension system controller parameters.

The remainder of the chapter is organized in two sections. In Section 12.1, the structure of a general semi-active suspension system is presented and a proper analytical model is assigned to each element of the closed loop control system. The new design methodology is then introduced in Section 12.2.

12.1 Structure of the Closed Loop Semi-Active Control System

Figure 109 shows a typical configuration of a vehicle's semi-active suspension systems. Vector z contains outputs of the sensors, strategically distributed throughout the vehicle, to capture the vehicle's motions. As described in Chapter 3, the sensing system consists of accelerometers, gyroscopes, and displacement sensors with different configurations. The information sent by the sensors is processed by an estimator (e.g., a KF, UKF or SKF). Outputs of the filtering unit are the vehicle states required for the semi-active controller. Frequently-used state variables include the absolute vertical velocity of the vehicle body at each corner (shock ends), the absolute velocity of the wheel-hubs, relative displacement and velocity across each shock, and the vehicle's CG kinematics. Incorporating the vehicle states (in this case, the relative velocity of the shocks as well as the absolute velocity of the body corners), the Skyhook control strategy determines the damping characteristic suitable for the current time-step. The control command is accordingly fulfilled by the vehicle semi-active shocks.

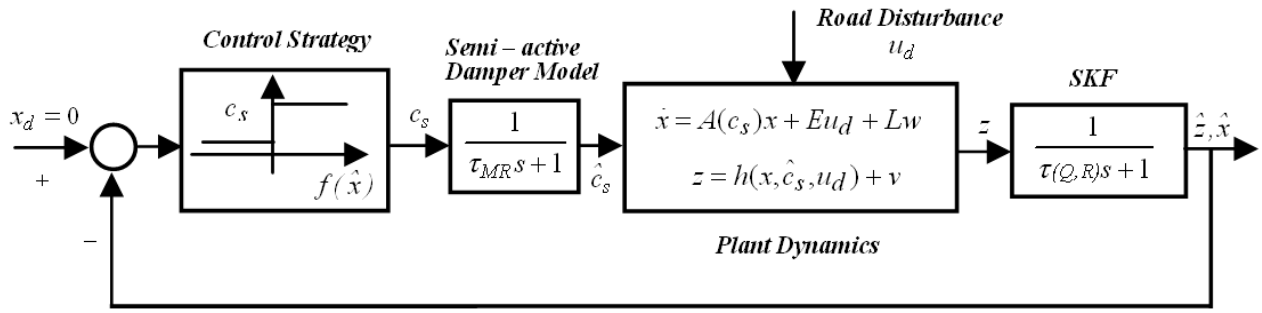

Figure 109: Block diagram of the vehicle's semi-active suspension control system.

As described in Section 6.1.1, simplified vehicle models of the vehicle and the suspension systems are first derived analytically. Next, these models are verified and fine-tuned by the 4-poster experiments. The semi-active dampers behave similarly to low-pass filters with relatively high bandwidths. The bandwidth corresponding to the MR dampers can be experimentally determined [80], [85], as approximately 65 (rad/sec). As described in Section 6.1, the vehicle dynamics is expressed by a linear time-varying formulation with respect to the semi-active damping coefficient, c_s, (which is equal to the c_{sky} in this study) of the following form:

$$\dot{x}(t) = A(c_s)x + Eu_d(t) + Lw(t) \tag{12.2}$$

where $x(t)$ and u_d refer to the vehicle state vector and the inputs to the wheels by the road roughness, respectively. In addition, A and E are the corresponding state and road input matrices.

Typically, the measurement system model is given as a nonlinear combination of the vehicle states, the road disturbances, and the current damping coefficient such that

$$z = h(x, u_d, c_s) + v\,. \tag{12.3}$$

In addition, the sensor data is assumed to be corrupted by a zero mean white noise v with a covariance of R. As described in Chapter 11, by employing a proper sensor configuration, all the vehicle's required states are observed by the SKF[1]. In this case, the SKF simply appears as a low-pass filter whose bandwidth is a function of the Q and R matrices. Consequently, the filtering block can be easily substituted by a suitable transfer function.

The ultimate control objective is to determine $c_{\min}$ and $c_{\max}$, such that the state vector and its derivatives are minimized ($x_d = \dot{x}_d = \ddot{x}_d = 0$). The state variables that need to be regulated, such as absolute position and velocity of the wheel-hubs and relative displacement and velocity of the shocks, have frequency components up 12Hz, which is the typical resonant frequency of the vehicle wheels. Therefore, the control loop must be performed as fast as at least 60Hz (five times faster) to be able to effectively suppress the vibratory motions. Moreover, the closed-loop control system must guarantee to meet some given transient response criteria. However, the lower bound, $c_{\min}$, is limited to the minimum possible damping coefficient (ideally zero) that the semi-active shock offers (determined by the damper characteristic tests). Therefore, the problem is reduced to the determination of $c_{\max}$ so that the desired requirements are satisfied.

The discontinuous block in Figure 109, describing the Skyhook control strategy, is the only module that cannot be classified in the framework of the conventional control system theory. The new approach should bring the discontinuous control strategy into the general framework of the classic control theory. Only then can all the conventional control system theory tools be employed in the design of a semi-active suspension controller. The next section pursues this goal.

---

[1] The early real-time experiments were conducted with the KF in-line. As described in Chapter 7, some of the required states were not provided accurately. Therefore, a combination of a low-pass filter and a differentiator, or an integrator followed by a high-pass filter, were also utilized to calculate the unobserved states. In either way, the entire filter blocks are substituted by an appropriate linear transfer function.

12.2 Fuzzy Skyhook System

It can be proven that a Fuzzy logic system is capable of approximating any non-linear function on a compact set to an arbitrary accuracy [93]. Thus, a continuous Fuzzy system can be developed to mimic the on-off Skyhook control strategy and maintain the controller efficiency. One method to create such a system is to encapsulate the Skyhook control law into the inference engine of the Fuzzy system. This engine is the brain of the Fuzzy system which induces a Fuzzy output, based on a predefined Fuzzy rule base. In this case, the rule base built on the Skyhook strategy consists of the following 4 rules

R^1: IF v_b is "P" AND v_r is "P" THEN c_s is "B"

R^2: IF v_b is "N" AND v_r is "P" THEN c_s is "S"

R^3: IF v_b is "P" AND v_r is "N" THEN c_s is "S"

R^4: IF v_b is "N" AND v_r is "N" THEN c_s is "B",

where P and N are the primary Fuzzy sets defined in the $\mathbb{R}$, which is the universe of discourse of the input variables v_b and v_r. P represents "Positive" and N denotes "Negative", and are selected as follows:

$$\mu_p(v_i) = \frac{\kappa}{1+\exp(-v_i/q)}, \tag{12.4}$$

and,

$$\mu_N(v_i) = \frac{\kappa}{1+\exp(v_i/q)}, \tag{12.5}$$

with $i = b, r$. Figure 110 plots the input membership functions for q equal to 0.01. q determines the growing or decaying rates of the sigmoid functions. Proper values of the q for this particular application are between 0 and 0.1. κ is usually set to 1.

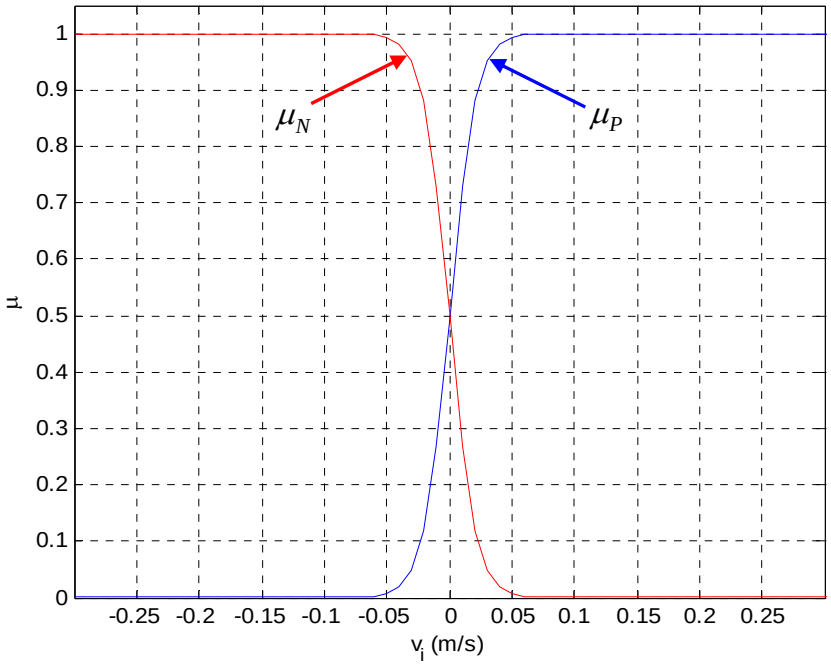

Figure 110: The Positive and Negative membership functions ($q = 0.01$).

The inputs to the Fuzzy system are normalized such that the same membership functions can be employed for both inputs. The normalized crisp input vector $v = [v_b \quad v_r]^T$ is then fuzzified via a Singleton Fuzzifier [93]. Figure 111 shows the basic structure of the Fuzzy system model.

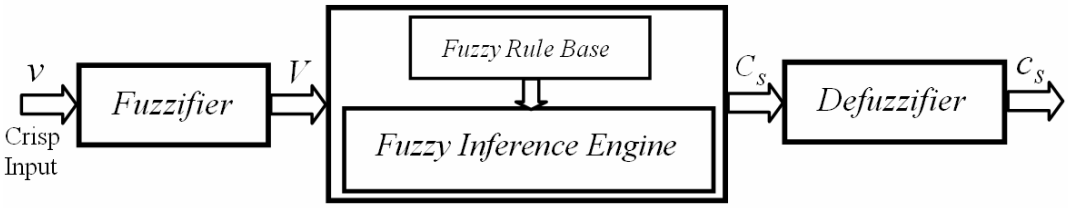

Figure 111: The basic structure of the Fuzzy logic system.

Each IF-THEN rule of the Fuzzy rule base is characterized by a membership function, $\mu_{R^\ell} = \mu_{\mathbb{R}\times\mathbb{R}\times\mathbb{R}}(v, c_s)$, defined in the Cartesian product space $\mathbb{C} = \mathbb{R}\times\mathbb{R}\times\mathbb{R}$. The final structure of the μ_{R^ℓ} is determined by using a particular operation rule of the Fuzzy implication [93]. By employing the product operation rule, the μ_{R^ℓ} is evaluated by

$$\mu_{R^\ell} = \mu_{u_j^\ell}(v_b).\mu_{u_k^\ell}(v_r).\mu_{\Upsilon^\ell}(c_s)\,, \tag{12.6}$$

where $\ell = 1,...,4$, and j,k is either p or N, depending the rule number. In addition, μ_{Υ^ℓ} is one of the two membership functions defined on the output variable c_s; that is, "B" (Big) or "S" (Small). Then, a Fuzzy output is induced from each IF-THEN rule and the fuzzified input vector V by applying the following equation:

$$C_s^\ell = V \circ R^\ell\,, \tag{12.7}$$

where $\circ$ refers to a compositional rule of inference. In this design, the sup-product compositional rule is applied [93], [94]. As a result, C_s^ℓ is evaluated as:

$$\mu_{C_s^\ell} = \sup_{v \in \mathbb{R}\times\mathbb{R}} \left\{\mu_V(v).\mu_{R^\ell}(v, c_s)\right\}. \tag{12.8}$$

The output of the Fuzzy inference engine is the union of each individual IF-THEN rule outcome C_s^ℓ,

$$C_s = \bigcup_{\ell=1}^{n=4} C_s^\ell\,. \tag{12.9}$$

The Fuzzy output set, C_s, is ultimately transformed into a crisp output by a Center Average Defuzzifier (CAD) [93], given by:

$$c_s = \frac{\sum_{\ell=1}^{4} \bar{c}_s^\ell.\mu_{R^\ell}(v, \bar{c}_s^\ell)}{\sum_{\ell=1}^{4} \mu_{R^\ell}(v, \bar{c}_s^\ell)}\,, \tag{12.10}$$

where $\bar{c}_s^\ell$ is the extremum of the output Fuzzy set, $\mu_{\Upsilon^\ell}(c_s)$, (at which the $\mu_{\Upsilon^\ell}(c_s)$ has a maximum value of 1). The substitution of (12.6) in (12.10) results in the crisp output of the Fuzzy system as:

$$c_s = \frac{\sum_{\ell=1}^{4} \bar{c}_s^\ell.\prod \mu_{u_j^\ell}(v_b).\mu_{u_k^\ell}(v_r)}{\sum_{\ell=1}^{4} \prod \mu_{u_j^\ell}(v_b).\mu_{u_k^\ell}(v_r)}\,. \tag{12.11}$$

By defining W^ℓ as

$$W^\ell = \frac{\prod \mu_{u_j^\ell}(v_b).\mu_{u_k^\ell}(v_r)}{\sum_{\ell\ell=1}^{4} \prod \mu_{u_j^{\ell\ell}}(v_b).\mu_{u_k^{\ell\ell}}(v_r)}\,, \tag{12.12}$$

the output of the Fuzzy system is ultimately written in the following compact form:

$$c_s = \sum_{\ell=1}^{4} \bar{c}_s^\ell.W^\ell = W^T.\bar{C}\,. \tag{12.13}$$

In (12.13), $W = [W^{\ell}]$, $\overline{C} = \left[\overline{c}_s^{\ell}\right]$, and $\overline{c}_s^{\ell}$ equals either $c_{\max}$ or $c_{\min}$. Having employed the Fuzzy system, the structure of the semi-active suspension control loop is illustrated as in Figure 112, where the on-off controller is replaced by the continuous nonlinear map N defined by (12.13):

$$c_s = N(\hat{x}, c_{\max}, c_{\min}). \tag{12.14}$$

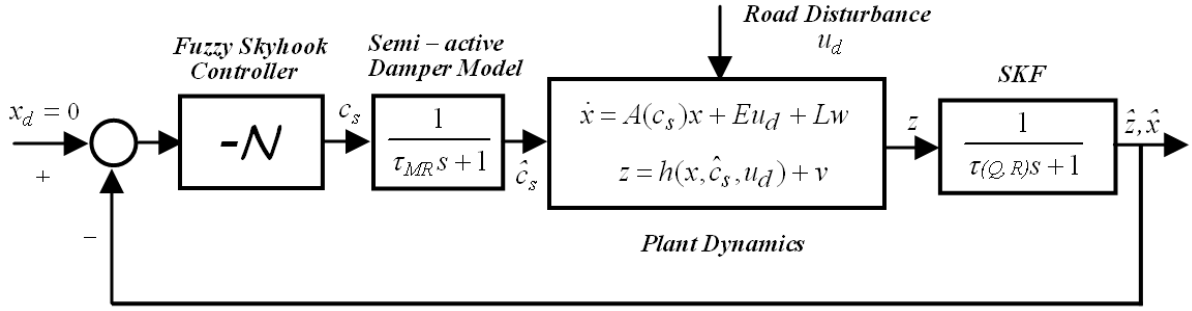

Figure 112: The semi-active suspension control system with the Fuzzy Skyhook controller

In the next step, the nonlinear control law, Equation (12.14), is designed to provide some desired performance around a system equilibrium point. In order to do that, N is expanded around the equilibrium point, x_0, in which

$$v_{b_0} = v_{r_0} = 0. \tag{12.15}$$

After applying the Taylor series expansion formula, the nonlinear function can now be described as follows

$$N \cong N(x_0) + \left.\frac{\partial N}{\partial x_0}\right|_{x_0}^{T} (x - x_0). \tag{12.16}$$

By the use of Equations (12.4), (12.5), and (12.11), after some mathematical manipulation, it can be shown that

$$\left.\frac{\partial N}{\partial x_0}\right|_{x_0} = 0, \tag{12.17}$$

due to the symmetry of the membership functions, defined on the inputs. Moreover, since $c_{\min}$ is much less than $c_{\max}$ (zero in theory), the terms containing $c_{\min}$ are overlooked. And therefore, $N(x_0)$ is obtained by calculating

$$\mathcal{N} \cong \mathcal{N}(x_0) \cong \frac{c_{\max}}{r(\kappa, q)}. \tag{12.18}$$

r is a constant quantity which relates to the membership functions parameters, κ and q. By properly selecting κ and q, r usually falls into a region of [1.5, 2.5].

Now, the original switching control loop is approximated by a linear state-space model described (around the equilibrium point) by

$$\dot{x}_c = A_c x_c + B_c u_c + L_c w_c \ , \tag{12.19}$$

where the state, input and disturbance vectors are given in (12.20)

$$x_c = \begin{bmatrix} x \\ \hat{c}_s \end{bmatrix}, \ u_c = \frac{c_{\max}}{r(\kappa, q)}, \ w_c = \begin{bmatrix} u_d \\ w \end{bmatrix}, \tag{12.20}$$

and the corresponding matrices are as follows:

$$A_c = \begin{bmatrix} A(\hat{c}_s) & 0 \\ 0 & -\tau_{MR}^{-1} \end{bmatrix}, \ B_c = \begin{bmatrix} 0 \\ \tau_{MR}^{-1} \end{bmatrix}$$

and

$$L_c = \begin{bmatrix} E(\hat{c}_s) & L \\ 0 & 0 \end{bmatrix}. \tag{12.21}$$

where subscript c refers to the controller design. Subsequently, all the tools, well-known in the conventional control system theory from the pole placement, LQR/LQG and $H_{2/\infty}$ to the various frequency domain techniques, can be utilized to design the unknown parameter, $c_{\max}$, such that the closed loop control loop satisfies the desired performance requirements in the vicinity of the equilibrium point. For the other points of the universe of discourse, the required performance may not be satisfied. However, the exponential stability of the controlled system is always guaranteed in the entire universe of discourse, due to the passivity property of the suspension system [95].

In practice, either the original bang-bang Skyhook strategy, Equation (12.1), or the nonlinear Fuzzy controller (12.14) is implemented by incorporating the designed $c_{\max}$. However, $c_{\max}$, obtained by the proposed methodology, might need to be fine-tuned during the road tests to assure the desired performance. Also, sensitivity and smoothness of the Fuzzy Skyhook controller can be altered and adjusted by tuning the membership functions parameters. q changes the membership function growth or decay rate. Setting q to small quantities increases

the sharpness of the Fuzzy controller – that is, it behaves more or less similar to the original on-off controller. Moreover, to decrease sensitivity of the Fuzzy controller to the input noises, an offset value γ is introduced to the input membership functions as follows:

$$\mu_p(v_i) = \frac{\kappa}{1+\exp\left[-(v_i-\gamma)/q\right]}, \tag{12.22}$$

and,

$$\mu_N(v_i) = \frac{\kappa}{1+\exp\left[(v_i+\gamma)/q\right]}. \tag{12.23}$$

The greater the γ selected, the less sensitive the controller becomes to the input variables $v=[v_b \quad v_r]^T$ noise.

The design procedure is summarized in the following six steps:

1. Establish the semi-active control system desired performance.
2. Find out the vehicle information, such as mass, moment of inertia, and dimensions. Then, develop the vehicle's state space realization (see Equation (12.2)), accordingly.
3. Determine and adjust the parameters of the input Fuzzy sets (see Equations (12.22) and (12.23)). Then calculate $r(\kappa,q)$ in Equation (12.18). As pointed out earlier, proper κ and q result in a number between 1.5 and 2.5 for r. Such an outcome leads to a convenient rule-of-thumb expression for choosing r, which bypasses the entire mathematical manipulations required in this step. As a rule of thumb, r can be selected in the [1.5, 2.5] region; $r=1.5$ results in a smoother controller and softer suspension (luxury vehicles) while $r=2.5$ offers a harder suspension (sporty vehicles).
4. Consider the approximated controlled system realization, given by Equations (12.19) to (12.21). By using a well-known time or frequency domain design technique, calculate $c_{\max}$ such that eigenvalues of the corresponding state matrix A_c are placed in the proper regions of the s-plane.
5. With $c_{\max}$, determined from the previous step, implement either the on-off Skyhook strategy (Equation (12.1)) or the nonlinear Fuzzy controller (Equation (12.14)).
6. Fine-tune the $c_{\max}$ ballpark estimate during road tests to guarantee the desired ride and stability requirements.

13 Real-Time Tests of the Combined Estimator and Controller

Chapter 11 presents a nonlinear estimator, named SKF, to provide the vehicle states by fusing the measurements of a minimum number of sensors configuration. The estimated states are then processed by the Fuzzy Skyhook controller, developed in Chapter 12, to enhance the ride comfort, road handling and stability of the vehicle. In a more advanced case, the specific handling and stability-assist controllers also work in parallel with the Skyhook controller of Chapter 12[1]. The design and analysis of such controllers are out of the scope of this research.

In this chapter, the newly-proposed estimator and controller are integrated first in Section 13.1, and the stability and performance of the combined system are analyzed from a theoretical point of view. In real life, to investigate the efficiency of the integrated system, the Cadillac suspension controller is bypassed and replaced with the newly-developed estimator and controller. The real-time tests results are provided in Section 13.2.

13.1 Nonlinear Separation Theorem

Theorem 1 (Nonlinear Separation Principle). Consider a nonlinear system in the form of $\dot{x} = f(x,u)$,

– Suppose that $\exists u = g(x),\ g(0) = 0,\ g \in c^1$, and $\|\nabla_x g(x)\|$ is bounded so that the equilibrium point x_e of the $\dot{x} = f(x, g(x))$ is exponentially stable.

– Furthermore, suppose that there exists an observer $\dot{\hat{x}} = h(\hat{x}, z, u)$ which estimates the system state vector, such that the estimation error dynamics of the form, $\dot{e} = \alpha(e)$ with $e = \hat{x} - x$, is exponentially stable.

Then $\begin{bmatrix} x_e & 0 \end{bmatrix}^T$ is an exponentially stable equilibrium point of the integrated system [96],

$$\begin{bmatrix} \dot{x} \\ \dot{e} \end{bmatrix} = \begin{bmatrix} f(x, g(\hat{x})) \\ e(\alpha) \end{bmatrix}. \tag{12.24}$$

[1] The estimator is aimed to provide vehicle states required by different types of control strategies, including ride, handling and stability, not only the states needed by the Skyhook scheme (which is more effective for the ride improvement).

Theorem 1 confirms that the integrated estimator and controller loop of Figure 112, which is described by the following equation:

$$\dot{x}_s = f_s(x_s, z, w_c), \tag{12.25}$$

is exponentially stable[1] in the entire universe of discourse, and guarantees the desired performance in the vicinity of the equilibrium point $\begin{bmatrix} x_0 & 0 \end{bmatrix}^T$. The concatenated state vector in Equation (12.25) is

$$x_s = \begin{bmatrix} x \\ \hat{x} \\ \hat{c}_s \end{bmatrix}, \tag{12.26}$$

where subscript s refers to the semi-active closed-loop control system.

The real-time performance of the integrated semi-active control system, implemented on the Cadillac SRX, is studied in the next section. During the experiments, either KF or EKF is used to estimate the required states[2] of the vehicle. As explained in Section 7.1, some of the states are not precisely provided by the KF estimators; hence, the sensors' signals are filtered and directly processed (differentiated or integrated[3]) to extract those states. Nevertheless, the combination of the KF and the auxiliary filters resembles an estimator, which provides accurate estimates of all the states. The combination of such a stable estimator with the Fuzzy controller of Chapter 12 results in a stable integrated system, as Theorem 1 implies.

13.2 Real-Time Experiments of the Integrated System

As described in Chapter 7, the test vehicle, Cadillac SRX, is equipped with the MagneRide™ semi-active MR dampers. The dampers are tested in the University of Waterloo's MTS lab to characterize the damping forces with respect to the applied control current and the relative velocity across the shock. Figure 113 plots the rear dampers test results for different supplied currents. It is experimentally shown that the damper is capable of providing a wide range of damping coefficients from $200\,N.sec/m$ at 0 Amp to about $7000\,N.sec/m$ at 5 Amp.

---

1 Assumed that the estimator's stability has been already proved based on the Lyapunov's second stability theorem.

2 At the time of the real-time experiments, neither SKF nor AKF had been developed.

3 For instance, absolute velocity of the wheel-hubs is not accurately provided by the KF estimators. Therefore, signals of the wheel-hubs accelerometers are filtered by a high-pass filter to reject the DC gain and then integrated to obtain the absolute velocity states.

A semi-active control problem is defined as follows. It is desirable to find appropriate lower and upper bounds of the Skyhook control strategy, that is, $c_{\min}$ and $c_{\max}$, such that the following performance requirements are fulfilled

- soft ride on even roads/pavement (luxury style),
- controlled ride on rough roads/bumps with a settling time of around 1sec and a damping ratio of approximately $\zeta = 0.4$ (not more than two bounces after the disturbance).

Note that the design requirements are subjective and vary from one designer to the next.

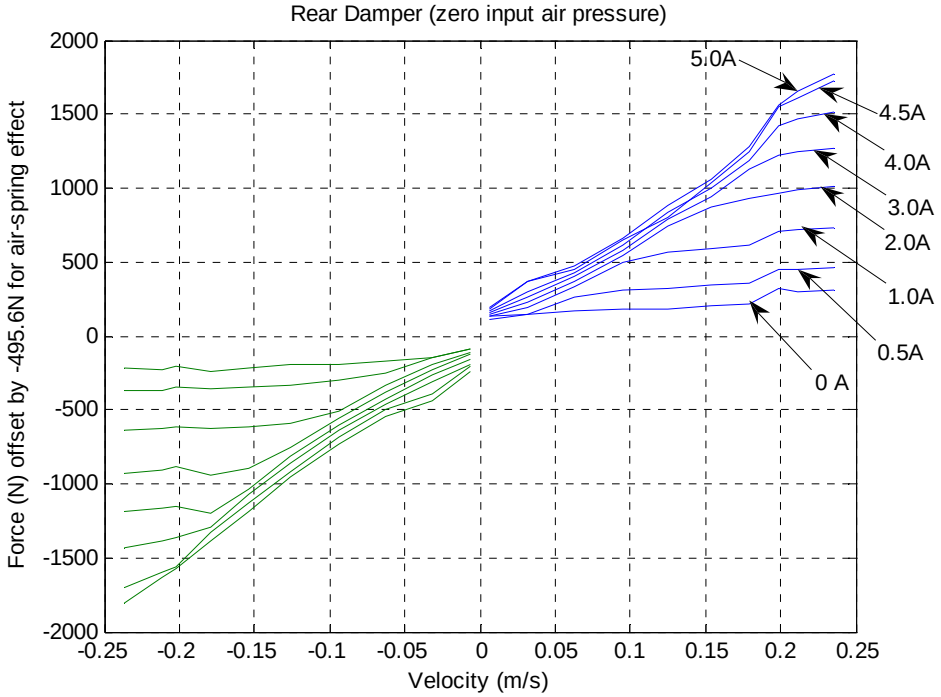

Figure 113: The behavior of the Cadillac SRX rear MR damper

By considering the design requirements, the membership functions (see Equations (12.22) and (12.23)) parameters are chosen as follows:

$$\kappa = 1,\ q = 0.01,\ \gamma = 0.05\,. \tag{12.27}$$

As mentioned previously, κ is usually selected to be 1. With q set to the small quantity of 0.01, the Fuzzy controller behaves similarly to the on-off Skyhook controller. $\gamma = 0.05$ renders the Fuzzy controller insensitive to the low amplitude vibrations of the vehicle's body/wheels, caused by weak disturbances. Consequently, the controller maintains the damping of the MR dampers at the most minimum values (around $c_{\min}$) when the vehicle is moving on the even

segments of a road. This results in a luxury-style comfortable ride. From the known parameters of Equation (12.27), r is then calculated to be 2.2.

The next step considers the approximated controlled system model (Equations (12.19) to (12.21)), and the given r to determine a proper maximum limit for the damping coefficient, $c_{\max}$. The desired closed loop poles (or regions in the s-plane) are first specified in accordance to the performance requirements. Then, by using the pole-placement technique (or any other similar design methodology), $c_{\max}$ is calculated to satisfy the requirements. For this particular semi-active control problem, $c_{\max}$ is obtained to be approximately $5500\,N.sec/m$. From the MR damper characteristic equations, it is revealed that the required upper damping is achieved at approximately 4 Amp of the supplied current. However, the lower bound of the damping coefficient, $c_{\min}$, is obtained by the damper characteristic tests and is approximately $200\,N.sec/m$ at 0.0 Amp of the supplied current.

The real-time VC++ processing platform, introduced in Chapter 7, is used to implement the integrated estimator and controller. The sensors' data are collected at 500Hz from the accelerometers and IMU and approximately 40Hz from the displacement sensors, and fed to the estimator. The computed control command is sent at the rate of approximately 20Hz[1] out of the onboard computer through an RS485 serial port to a voltage-controlled current circuit. The circuit drives a PWM amplifier which, accordingly, feeds the MR dampers. The road tests are carried out (similar to the real-time experiments of Chapter 7) on the portion of the UW's Ring Road where there are two bumps, as shown in Figure 43 and Figure 44.

The test vehicle is driven on the specified section of Ring Road (including the bump) with speeds between 20 km/hr and 50 km/hr. For each velocity, the performance of the Cadillac SRX original controller is compared with that of the designed controller. The measurements from the vertical accelerometer of the IMU (acceleration of the CG) are used as the ride-comfort measure. Figure 114 reflects the acceleration of the CG for two cases: when the benchmark control system is engaged, and when the integrated estimator and Fuzzy Skyhook controller is in-line. In comparison with the Cadillac controller, the integrated control system decreases the maximum acceleration of the vehicle's CG and also the peak-to-peak value by 19% and 13%,

[1] Theoretically, it must be at least 60Hz to effectively suppress the fast frequency components of the vehicle vibrations. However, due to the limitation of the MR damper bandwidth (approximately 10Hz), the controller command is sent at a rate of 20Hz.

respectively. The settling time of the closed-loop system is around 1.5 seconds (the bump input ends at approximately t=85sec), which is close to the desired magnitude.

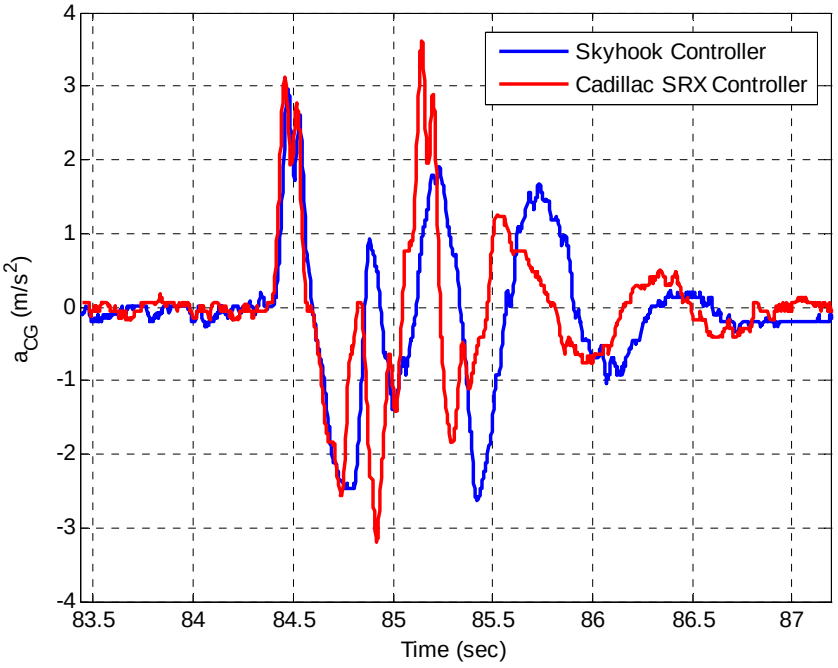

Figure 114: The graph compares the performance of the integrated control system and the Cadillac SRX original controller (the test vehicle speed is 30km/hr).

Figure 115 puts the command signal, sent by the Fuzzy Skyhook controller, and the controller inputs ($v = [v_b \quad v_r]^T$) side by side. It is apparent that the designed controller is not sensitive to the small perturbations. The low damping value, assigned by the controller on the even segments of the pavement, provides a soft and comfortable ride. Also, the controller effectively acts to reduce the effects of the bump, as seen in Figure 114. The entire processing time is evaluated as less than two milliseconds for each iteration of the integrated estimator and controller loop with the exisiting on-board processor.

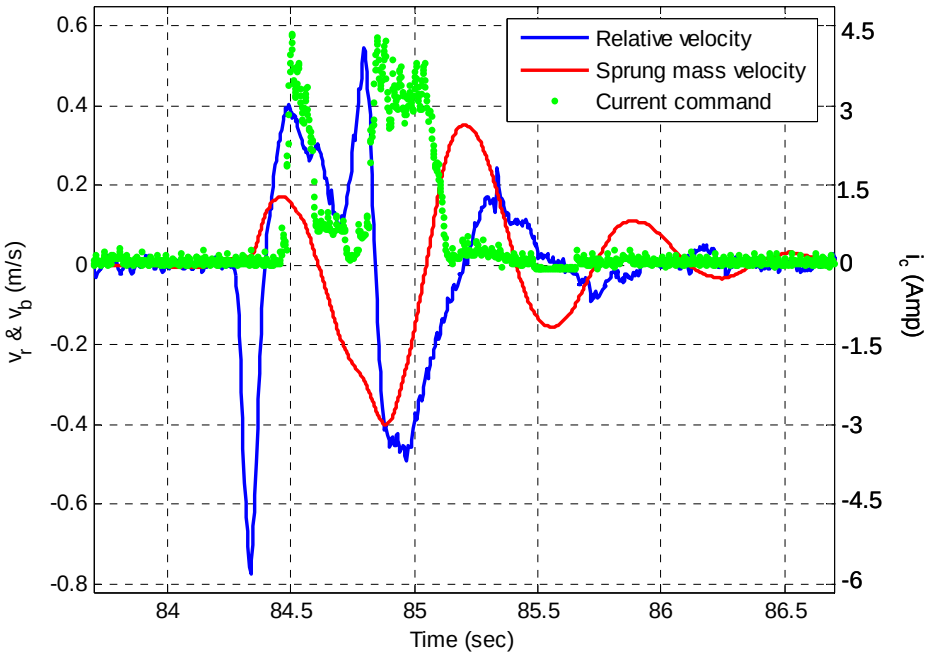

Figure 115: Absolute velocity of the front left corner of the body, relative velocity of the associated MR damper, and the control current sent to the damper.

Overall, it is observed that employing the systematic design methodology, proposed in this research, results in a semi-active suspension system whose performance is comparable to that of a commercialized industrial system. Also, it is confirmed that the proposed technique makes the semi-active control system design straightforward and free from the need of numerous trial-and-error attempts. Small modifications on the Fuzzy controller performance can be achieved by altering and adjusting the membership function parameters. However to entirely satisfy a different set of performance requirements (different settling time and transient response requirements), the design steps should be repeated to generate new values of $c_{\max}$ and $c_{\min}$.

Another semi-active control problem with different design requirements and control strategy is studied next. Consider the design requirements of the previous problem, except that the desired damping ratio is decreased by 10%. Moreover, the sub-optimal Skyhook control strategy, presented in Appendix A, is replaced by the original Skyhook strategy. By following the step by step design procedure of Chapter 12, the upper damping limit of the MR dampers, $c_{\max}$, is calculated to be around $5000\,N.sec/m$ (at approximately 3 Amp of the supplied current). The sub-optimal Skyhook, with the calculated $c_{\max}$, is then coded to the onboard

processor. The real-time experiments are carried out on the same road conditions at the same speed. Figure 116 offers a comparison of the performance of the integrated system and the Cadillac SRX original control system. It is illustrated that the integrated system with the sub-optimal Skyhook controller performs in a similar manner to the Cadillac SRX original semi-active control system.

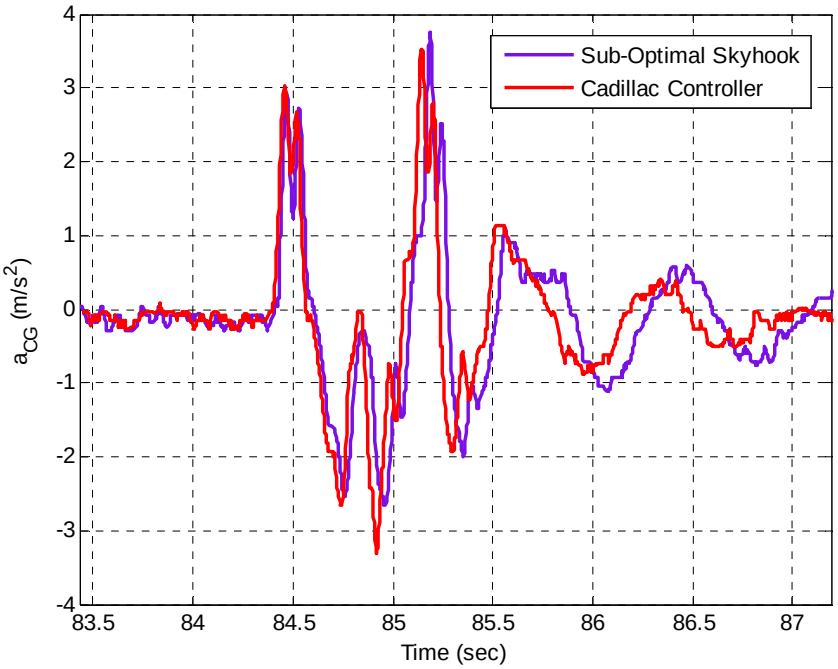

Figure 116: The graph compares the performance of the integrated system with the sub-optimal Skyhook controller, and the Cadillac SRX original semi-active control system (the test vehicle speed is 30km/hr).

To demonstrate the efficiency of the integrated control system further, Figure 117 plots the accelerations of the vehicle CG for two situations: when the integrated system is engaged and when it is off. The vehicle is driven on the same road and bump but with a different speed of 40 km/hr. It is obvious that when the suspension control system is in-line, the transmitted disturbance to the body is significantly reduced.

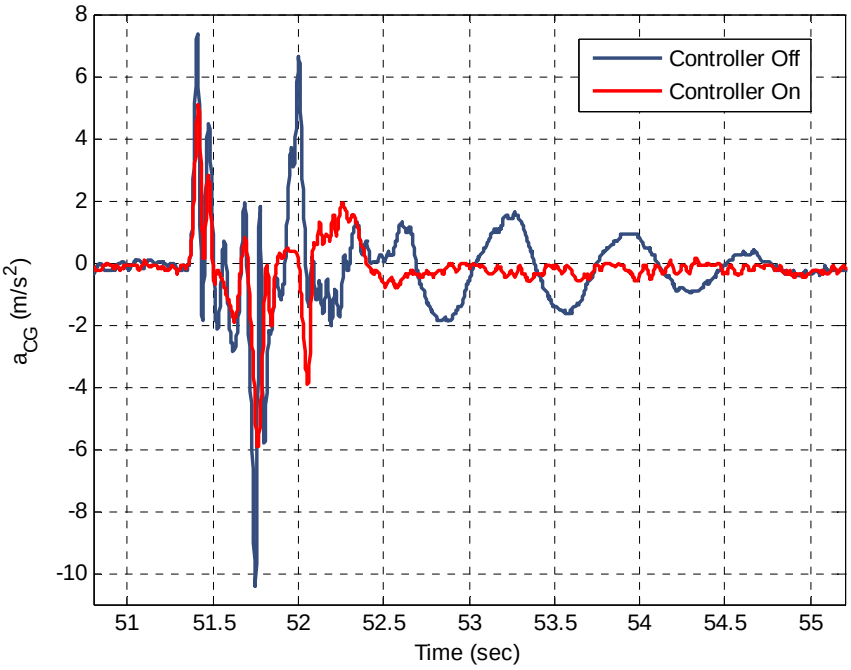

Figure 117: The graph compares acceleration of the vehicle CG for two different cases: the integrated control system is on and off (the test vehicle speed is 40km/hr).

14 Conclusions and Future Work

A solution has been given for the state estimation problem of systems with unmeasurable non-zero mean inputs/disturbances which do not satisfy the disturbance decoupling conditions. The proposed filtering scheme was then applied to the state estimation of a test vehicle model, a Cadillac SRX 2005, subjected to unknown road disturbances such as bumps. Vehicle states are required by an active or a semi-active suspension control system, which improves ride comfort, road handling, and stability of the vehicle. Due to the lack of information on road disturbances, the conventional estimation techniques such as the Kalman filter (also conventional observers such as the Luenberger observer) fail to provide accurate estimates of the states. More robust estimators, such as the particle filter, also fail as a result of the system's high-dimensional structure.

The proposed estimation algorithm, called the Supervisory Kalman Filter (SKF), consists of a Kalman filter with an extra update step, inspired by the particle filtering technique. The extra step, named the supervisory layer, can be triggered from the initial time or can be activated as soon as the unknown disturbance input is detected by a responsive sensor. It operates on the portion of the state vector that cannot be estimated by the Kalman filter. First, it produces N randomly-generated state vector – the particles – which are distributed based on the Kalman filter's last updated pdf. The other portion of the state vector that is accurately estimated by the Kalman filter remains unchanged in the particles. Then, a resampling stage is performed to collect the particles with higher probability.

The effectiveness of the SKF is demonstrated by comparing its estimation results with that of the Kalman filter and the particle filter when a test vehicle is passing over a bump. The estimation results confirm that the SKF precisely estimates those states of the vehicle that cannot be estimated by either the Kalman filter or the particle filter, without any direct measurement of the road disturbances. Although the filtering algorithm has been developed for linear systems, the same scheme can be utilised for nonlinear state estimation problems. However, for this case, instead of the Kalman filter as the base estimator, a nonlinear estimator, like the extended Kalman filter or the unscented Kalman filter, is employed.

In addition, a systematic and practical methodology has been developed for the design and implementation of vehicle semi-active suspension control systems by using simple analytical

models. The proposed methodology takes into consideration the dynamics of the semi-active dampers and those of the estimation/filtering unit. The discontinuous nature of the semi-active control strategies, including the Skyhook policy, is the principle barrier in methodical design. The first step of the new methodology is to apply the Fuzzy system theory to create a network with continuous valued outputs to emulate the discontinuous controller law. Once the original control strategy is converted to a continuous linear form, different well-established frequency or time-domain techniques can be employed to design and adjust the suspension system controller parameters (i.e., the upper and lower bounds of the Skyhook policy). If the semi-active control loop is designed to satisfy some desired ride and stability requirements, an inverse mapping offers the ultimate control law.

In the end, the entire design procedure was summarized to six steps. To demonstrate the effectiveness of the proposed methodology, it was employed in the design of a semi-active suspension control system for the Cadillac SRX test vehicle. The Cadillac original controller was then by-passed and replaced by the newly-designed controller. The road test results verified that applying the developed design technique results in a semi-active control system whose performance is comparable with that of the Cadillac SRX. It was also confirmed that the use of the newly-developed systematic design methodology reduces the time and effort required in real industrial problems.

The thesis contributions are summarized as follows:

- Development of a filtering scheme for the state estimation of systems with unknown inputs/disturbances which do not satisfy the disturbance decoupling conditions. A direct application of the proposed technique is the state estimation of terrain vehicles subjected to unknown disturbances from the road.
- Development of a systematic and practical approach to the design and implementation of vehicle semi-active suspension control systems. By using the proposed design methodology, the estimator and the controller are designed simultaneously to satisfy the desired time and frequency domain requirements.

A challenging problem that has not been addressed in this manuscript is the task of optimizing the resampling stage of the SKF to require less number of particles (and hence less

computational burden), while avoiding sample impoverishment. During sample impoverishment, all the particles will collapse to a single point within a few iterations. This problem reduces the diversity of paths of the particles, which will degrade the estimation performance significantly. Further road tests need to be conducted to study and analyze the performance of the combined SKF and the semi-active controller with the minimum sensor configuration in real life. Also, the robustness of the integrated system to different payloads and manoeuvres should be validated through real-time experiments.

It was demonstrated, through computer simulations, that the SKF has the ability to estimate the vehicle tire deflections accurately. These states are crucial for vehicle stability controllers. It is expected that, by incorporating the tire's model into the estimator's body, the estimation accuracy associated with the tire deflections will be improved. Furthermore, road tests with the wheel deflection measurements are required to confirm the SKF's real performance.

Appendices

Appendix A: Semi-active Suspension Control Strategies

A.1 1 and 2 DOF Suspension Systems Model

Figure 118-a shows a 1 DOF suspension system for a base excitation input. The equation of motion for this system is given by:

$$m\ddot{x} + c(\dot{x} - \dot{y}) + k(x - y) = 0 \tag{A.1}$$

This equation could be re-written as:

$$\ddot{x}_r + 2\xi\omega_n\dot{x}_r + \omega_n{}^2 x_r = y\omega^2 \sin(\omega t) \tag{A.2}$$

where the parameters of the above equation are:

$$\xi = \frac{c}{2\sqrt{km}}, \quad \omega_n = \sqrt{\frac{k}{m}} = 2\pi f_n, \quad x_r = x - y \tag{A.3}$$

In a harmonic base excitation system, two parameters are studied; the first one is called Displacement Transmissibility:

$$\lambda = \left|\frac{x_r}{y}\right| = \frac{\omega^2}{\sqrt{(\omega_n^2 - \omega^2)^2 + 4\zeta_s^2\omega_n^2\omega^2}} \tag{A.4}$$

This expresses the ratio of the maximum magnitude of response to the input displacement. The second parameter is called Force Transmissibility:

$$\eta = \left|\frac{\ddot{x}}{\omega_n^2 y}\right| = \frac{\omega^2\sqrt{\omega_n^2 + (2\zeta\omega_n\omega)^2}}{\omega_n^2\sqrt{(\omega_n^2 - \omega^2)^2 + 4\zeta^2\omega_n^2\omega^2}} \tag{A.5}$$

where, η is the force transmitted to the mass as a result of excitation. Using the transform method, we can find the desired parameters mentioned above with respect to frequency ratio, $\frac{\omega}{\omega_n}$, and for different damping ratio ξ.

Figure 118-b shows a 2 DOF suspension system for a base excitation input. The equations of motion for this system are given by:

$$\begin{aligned} m_b\ddot{x}_2 &= -k_1(x_2 - x_1) - c(\dot{x}_2 - \dot{x}_1) \\ m_w\ddot{x}_1 &= k_1(x_2 - x_1) + c(\dot{x}_2 - \dot{x}_1) - k_2(x_1 - y) \end{aligned} \tag{A.6}$$

The two parameters of interest in the harmonic base excitation Displacement Transmissibility and Force Transmissibility are [28]:

$$\eta = \left|\frac{\ddot{x}_b}{\omega_b^2 y}\right| = \frac{\omega^2\sqrt{A^2+B^2}}{\omega_b^2\Delta}$$
$$\lambda = \left|\frac{x_r}{y}\right| = \left|\frac{x_b - x_w}{y}\right| = \frac{\omega^2\omega_b\sqrt{\omega_b^2+(2\zeta\omega)^2}}{\Delta} \quad \text{(A.7)}$$

where the equation parameters are: $\Delta = \sqrt{C^2+D^2}$, $A = -\omega^2{}_b\omega^2{}_w$, $B = 2\omega_b\omega^2{}_w\omega\zeta$, $\omega_b = \sqrt{\frac{k_1}{m_b}}$, $\omega_w = \sqrt{\frac{k_2}{m_w}}$, $\zeta = \frac{c}{2m_b\omega_b}$, $r_m = \frac{m_b}{m_w}$ $C = \omega^4 - (r_m\omega_b^2 + \omega_w^2 + \omega_b^2)\omega^2 + \omega_w^2\omega_b^2$, and $D = 2\omega\omega_b\omega_w(\zeta\omega_w)$ $-2\omega^3(\zeta\omega_b + r_m\zeta\omega_b)$.

In the frequency domain analysis, it is common practice to compare the results based on an overall analysis obtained by RMS method. The RMS of the above-mentioned parameters are defined as:

$$RMS(\lambda) = \sqrt{\frac{1}{(r_{\max} - r_{\min})}\sum_{r_{\min}}^{r_{\max}}\lambda^2\Delta r}$$
$$RMS(\eta) = \sqrt{\frac{1}{(r_{\max} - r_{\min})}\sum_{r_{\min}}^{r_{\max}}\eta^2\Delta r} \quad \text{(A.8)}$$

in which $r_{\max}, r_{\min}$ are the frequency analysis range boundary.

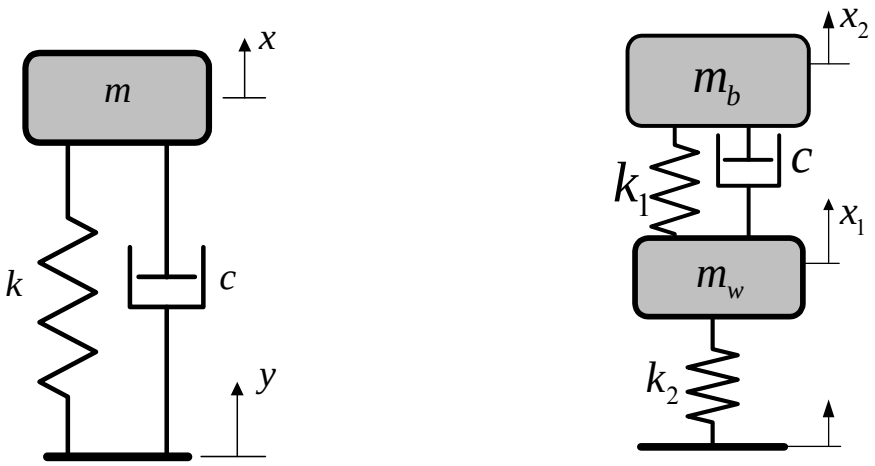

a: One Degree of Freedom System b: Two Degrees of Freedom System

Figure 118: One and Two Degrees of Freedom Systems [28]

A.2 The Semi-active Suspension Control Strategies

In this section, conventional semi-active control strategies are presented, namely: Skyhook and its modified versions, LRD, and the Rakheja-Sankar (R-S) method.

A.2.1 Skyhook Control Method

The Skyhook strategy is undoubtedly the most effective technique for the vibration suppression of a vehicle body [11], [13], and [14]. A typical Skyhook model is shown in Figure 119; the damping force provided by the Skyhook damper C_2 is always opposite to the absolute velocity of m .

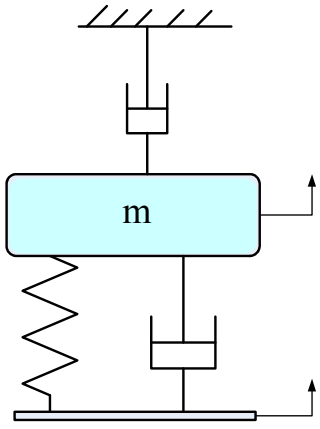

Figure 119: A schematic structure of the skyhook control system [28]

According to the Skyhook working principle [11], the semi-active on-off control law is

$$c_{sky} = \begin{cases} c_{\max} & if \quad v_r v_b \geq 0 \\ c_{\min} & otherwise \end{cases}, \tag{A.9}$$

where $v_r = \dot{x} - \dot{y}$ is the relative velocity across the shock, and $v_b = \dot{x}$ is the absolute velocity of the sprung mass. The relative velocity v_r can be obtained by differentiating the measurement of a displacement sensor.

However, measuring the absolute velocity is difficult. This is considered a negative aspect of the Skyhook control policy. Traditional methods integrate the accelerometer signal, over time, to obtain the required state. However, the quality of the resultant signal is extremely degraded by the high rate drift and noise, associated with the low-cost automotive grade MEMS sensors (<$30). Here, a modified version of the Skyhook control policy is presented which is independent of the absolute velocity states and maintains the performance of the original strategy.

A.2.2 Sub-Optimal Skyhook Control Method

Figure 120 shows the relative displacement and velocity of the vehicle LF shock, along with the absolute velocity of the sprung mass. The data are generated through the computer simulation of the 7 DOF Cadillac model, passing over the bump at 40 km/hr. From this graph and similar simulation results for the other speeds, it is discovered that the behavior of the sign change of the $v_r.v_b$ (relative velocity times the absolute velocity) is opposite to that of the $v_r.z_r$ (relative velocity and relative displacement product). This behavior is further clarified in Figure 120, where the non-zero status of the green line refers to the positive sign of the relative and absolute velocity product, while the non-zero status of the black curve refers to the negative sign of the relative velocity and the relative displacement product. It is apparent that the two curves almost overlap, which means that when the relative velocity times the absolute velocity is positive, the relative velocity times the relative displacement is negative.

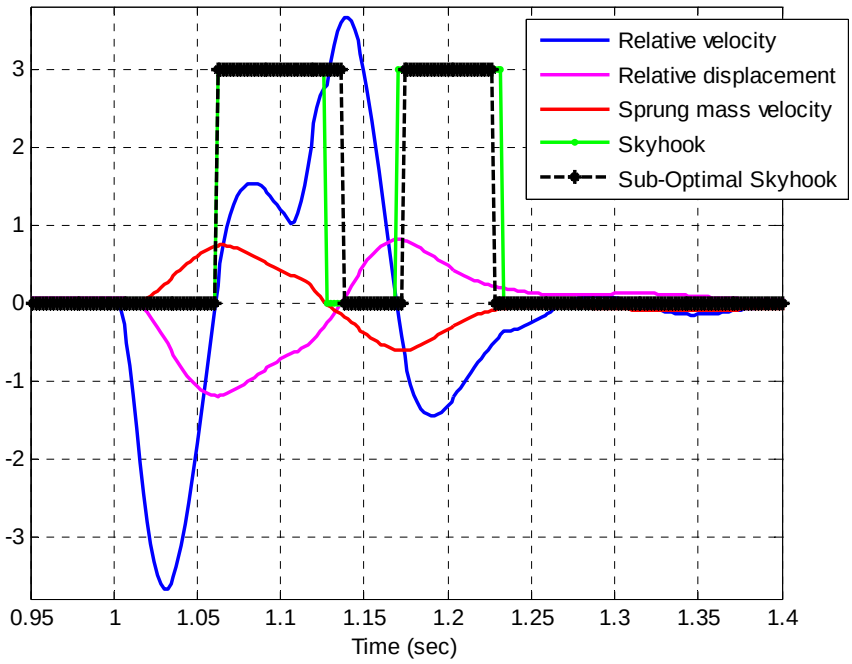

Figure 120: The graph compares signs of the relative and absolute velocity product and the relative velocity and displacement product.

Figure 120, or similar simulation results, implies that the sign of the product of the relative velocity and the relative displacement can be monitored as a replacement for the original Skyhook controller switching criterion. The proposed alternative eliminates the need for computing the sprung mass absolute velocity. However, the performance of the semi-active control system is lowered to some extent. The sub-optimal Skyhook control policy is then given by [22],

$$c_{sub\_sky} = \begin{cases} c_{\max} & if \quad v_r z_r \le 0 \\ c_{\min} & otherwise \end{cases}. \tag{A.10}$$

Now, z_r is measured by the damper displacement sensor. v_r is obtained by differentiating the filtered z_r through a low-pass filter.

Another modified version of the Skyhook strategy is presented in [28], where the sprung mass jerk $\dddot{x}$ is used instead of its absolute velocity. The control law is then modified to the following form:

$$c_{sky} = \begin{cases} c_{\max} & if \quad v_r \ddot{x} \geq 0 \\ c_{\min} & otherwise \end{cases}. \tag{A.11}$$

In this case, the sprung mass jerk, $\ddot{x}$, is obtained by differentiating the filtered acceleration of the sprung mass.

A.2.3 Groundhook Control Method

The Groundhook control strategy is described by looking at Figure 118(b). Assume that a fictitious damper is mounted between the unsprung mass and the ground to suppress the vibratory motion of the unsprung mass. The Groundhook control strategy alters the semi-active damper coefficient, c, such that the damper force be equivalent to that of the fictitious damper [13], [88] :

$$c_{sky} = \begin{cases} c_{\max} & if \quad -v_r v_w \geq 0 \\ c_{\min} & otherwise \end{cases}, \tag{A.12}$$

where $v_r = \dot{x} - \dot{y}$ is the relative velocity across the shock, and $v_w = \dot{x}_1$ is the absolute velocity of the unsprung mass.

A.2.4 Skyhook-Groundhook Control Method

The Skyhook-Groundhook method, also called the hybrid control strategy, is a combination of the Skyhook and the Groundhook strategies. With the hybrid control, it can be specified that how closely the semi-active damper emulates the Skyhook damper or the Groundhook damper. The hybrid control strategy is given by [88]:

$$\begin{aligned} c_{sky} &= \begin{cases} c_{\max} & if \quad v_r v_b \geq 0 \\ c_{\min} & otherwise \end{cases} \\ & \qquad \Rightarrow c_{hybrid} = \varepsilon c_{sky} + (1-\varepsilon) c_{Ground}, \\ c_{Ground} &= \begin{cases} c_{\max} & if \quad -v_r v_w \geq 0 \\ c_{\min} & otherwise \end{cases} \end{aligned} \tag{A.13}$$

where the variable ε is the relative ratio between the Skyhook and the Groundhook control (for $\varepsilon = 1$, the control policy is purely Skyhook, and for $\varepsilon = 0$, the control policy is purely Groundhook).

A.2.5 Limited Relative Displacement (LRD) Control Method

For the purpose of controlling the relative displacement in this control method, a mechanism is required to provide a high damping ratio when the relative displacement is above a specific threshold. Otherwise, a low damping ratio is implemented. This on-off control law can be expressed as:

$$c = \begin{cases} c_{\max} & |z_r| \geq \delta \\ c_{\min} & |z_r| < \delta \end{cases}. \tag{A.14}$$

A.2.6 Rakheja-Sankar (R-S) Control Method

The control strategy, proposed by Rakheja and Sankar [22], [28], is based on the fact that the damping force in a passive damper tends to increase the mass acceleration when it is applied in the same direction as the spring force. Ideally, a semi-active damper should not produce any damping force, or at the least a minimum value in the same direction as the spring force. Based on this concept, the following on-off control strategy is suggested:

$$F_d = \begin{cases} -\varepsilon k z_r & z_r v_r \leq 0 \\ 0 & otherwise \end{cases}, \tag{A.15}$$

where $z_r = x - y$ is the relative displacement across the shock. In practice, though, it is difficult to have the damping force properly follow the spring force. Therefore, the previous control strategy can be modified to a new form, which can be expressed as:

$$c = \begin{cases} c_{\max} & z_r v_r \leq 0 \\ c_{\min} & otherwise \end{cases}. \tag{A.16}$$

Appendix B: The Quarter Car Test Setup

Characteristics of damper, shaker control, accelerometers, and potentiometer are described as follows (see also Figure 24 and Figure 26):

B.1 Damper

RD-1097-01 is a controllable friction magnetically responsive (MR) fluid damper providing controllability and responsiveness in a lightweight package. As a magnetic field is applied to the MR fluid inside the housing, the damping characteristics of the fluid increase under 25-millisecond response time. The MR damper is especially well-suited for suspension and isolation applications.

Extended Length	7.68 inches (195 mm)
Compressed Length	9.96 inches (253 mm)
Body Diameter	1.26 inches (32 mm)
Weight	1.1 pound (0.48 kg)
Electrical Characteristics: Input Current (continuous) Input Current (intermittent) Resistance (25° C)	 0.5 amps maximum 1.0 amps maximum 20 ohms
Damper Forces: (Peak to Peak) 2 in/sec at 1 amp 8 in/sec at 0 amp	 > 22 pounds (100 N) < 2 pounds (9 N)
Mechanical Characteristics: Maximum Operating Temperature Storage Temperature Limits	 160°F (70°C) - 40° F to 212°F (-40°C to 100°C)
Response Time (amplifier and power supply dependent)	< 25 millisecond – time to reach 90% of max level during a 0 to 1 amp step input @ 2 in/sec (51 mm/sec).

B.2 Accelerometers

The characteristics of the accelerometers, mounted on the sprung and unsprung masses, are tabulated as follows:

Weight	2.1 gram
Element Style	Quartz planar shear
Sensitivity	± 10% mV/G
Range for ± 5 Volts output	± 50 G's
Frequency range	± 5% 0.5 to 10kHz
Resonant Frequency	45 KHz
Equivalent Electrical Noise Floor	0.007 G's RMS
Linearity	1% F.S.
Temperature Range	-60 to +300 °F

B.3 Potentiometer

The specifications of the potentiometer used in the QC's test rig are as follows:

Potentiometer Type	1−turn, precision, conductive plastic
Resistance: Value, Tolerance	5K ohms, ±10%
Travel: Electrical, Mechanical	340°, 340° min
Mechanical Life	100 million shaft revolutions min
Power Rating	1.0 W at 158° F (70° C)
Supply Current	12 mA max
Supply Voltage	35 VDC max (using voltage divider circuit)
Independent Linearity Error	±0.5% max per VRCI−P−100A
Output Smoothness	0.1% max
Resolution	infinite signal
Operating Temperature	−85° to +257° F (−65° to +125° C)
Temperature Coefficient	±400 ppm/°C max

B.4 Shaker Control

The purpose of environmental vibration testing is to ensure that a specific Unit Under Test (UUT) can perform its desired function when subjected to the vibration stress of its operating environment. A Shaker System allows the operator to verify this in a controlled environment. The emphasis here is on a controlled environment.

A complete Shaker System consists of seven major components:

UUT – The Unit under Test is the essential component of the system.

Fixture – The Fixture is the device that holds the UUT and simulates its normal mounting environment.

Head – The Head of the shaker is the part to which the fixture is attached.

Shaker – The Shaker converts the electronic signal that describes the desired test into vibratory motion.

Amplifier – The Amplifier multiplies the electronic signal produced by the control system. The purpose is to achieve an amplitude sufficient to "drive" the shaker at the proper levels.

Control System – The Control System compensates for the dynamics of the shaker and UUT and creates an electronic signal that causes the desired vibratory motion.

Sensors – The sensors measure the vibratory motion and convert this motion into an electronic signal that can be measured by the control system.

Appendix C: Experimental Apparatus of Real-Time Vehicle Tests

C.1 Test Vehicle

The first test vehicle was a Toyota Tercel model 1993, equipped with a complete sensor system with passive dampers (see Figure 2). In this stage, only the performance of the KF in estimating the required states of the test vehicle was examined. Then, a fully instrument Cadillac SRX model 2005 with semi-active suspension system (see also Figure 36) was utilised to analyze the performance of the combined estimation and control system.

C.2 Dampers

To control the ride comfort of a vehicle using an active or semi-active suspension system, the dampers must be modeled. That is, the resulting damping force from applied current and velocity must be known. To characterize the damping property of the existing Cadillac MR dampers, two dampers were ordered and tested separately. Different sets of tests were performed on the Cadillac SRX rear and front dampers. Damping forces, in terms of relative velocity and applied current, are shown in Figure 46 and Figure 113.

C.3 Sensors

Since acceleration and relative displacements must be measured, two types of sensors were used: MechSense^{TM} MD S 202 –U accelerometers for measuring the acceleration, and string pot for measuring the relative displacement, 0173-0161. The displacement sensors are used only as a research tool to provide truth data of the actual displacements which the accelerometers/KF will estimate. Subsequently, a comparison between the displacements measured directly from the string pots and the displacement estimates from the KF will be made to show the accuracy of the estimation. It should be noted that all accelerometers were calibrated before being mounted on the vehicle.

C.3.1 Accelerometers

MechSense Digital is a completely digital, low-cost sensing system. It integrates a two- or three-axis accelerometer with a reconfigurable signal conditioning unit, a 12-bit analog to digital converter and power regulator, all in one small, low-cost package. It also includes the MechManager™ software package that enables the user to conveniently collect, display and store data, and to re-configure the sensor's operation as required. MechSense Digital is available in ranges of ±2g and ±10g, with a typical noise floor of 200ug/√Hz. Standard applications include automotive testing, vibration monitoring, alarms and motion detection. MechSense Digital is available in a compact, mountable and hermetically-sealed 2-7/8 x 1-1/2 x 1 inch package. MechSense Digital is available with three communication interfaces.

The port powered USB interface is a 1.1/2.0 full-speed interface that allows the sensors to be meshed together for a multi-drop network of up to 64 units. A half-duplex RS-485 interface is available for greater communication lengths, even in noisy environments. With the RS-485 interface option, units can be daisy chained together to create an addressable multi-sensor network of up to 64 units. The accelerometer's signal conditioner features a fifth-order Butterworth low-pass filter that is configurable from DC-50Hz to DC-1000Hz and a gain adjustment from 1.00 to 10.00. Data sampling ranges from 1Hz to 2000Hz per channel. With the RS-232 interface option, the maximum low-pass filter adjustment is reduced to DC-500Hz and the maximum sampling rate is 1000Hz per channel.

A re-calibrate function accurately determines the zero g offset and sensitivity of each accelerometer axis. A temperature measurement can be employed by the user for a temperature compensation algorithm. A self-test function can be used for testing the unit's functionality. With the MechManager interface software, the accelerometer unit interfaces with any PC running Windows 98 or better, for capturing, plotting and storing data.

Figure 121: A MechSense 

Accelerometer.

C.3.2 Inertial Measurement Unit (IMU)

MechSense AIMU/DIMU is a completely Analog/Digital, low-cost sensing system. It integrates three accelerometers and three rate gyros with a suitable signal conditioning unit, a 12-bit analog to digital converter and a microcontroller equipped with temperature sensor, all in one small, low-cost package. It also includes the MechIMUCal™ software package that enables the user to conveniently collect, display and store data as well easily re-configure the sensor's calibration values as required.

The MechSense AIMU/DIMU accelerometers are available in any combination of the ranges ±2g and ±10g, with a typical noise floor of 200ug/√Hz. MechSense DIMU is available in a compact, mountable and hermetically-sealed package. MechSense DIMU is equipped with USB 1.1/2.0 full-speed hardware. As well, the sensors are networkable, allowing for a multi-drop network AIMU/DIMU units. The sensor's signal conditioner features sharp cut-off filters in analog and digital domains. A recalibrate function accurately determines the zero g offset and sensitivity of each accelerometer axis. A temperature sensor measurement is used for the onboard temperature compensation algorithm.

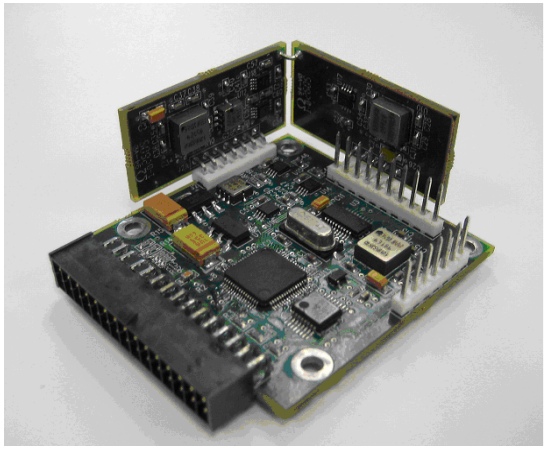

Figure 122: A MechSense IMU

C.3.3 String Potentiometer

To measure the relative displacement across the shocks, a string potentiometer Model # 0173-0161 was used. Figure 123 shows a string potentiometer and its various aspects. The specifications of the potentiometer are as follows:

Potentiometer Type	1-turn, precision, conductive plastic
Maximum Travel (Series 176)	6.5-Inch (165-mm)
Resistance: Value, Tolerance	5K ohms, ±10%
Travel: Electrical, Mechanical	340°, 340° min
Mechanical Life	100 million shaft revolutions min
Output Signal	analog signal from 0 to supply voltage (voltage divider circuit)
Power Rating	1.0 W at 158° F (70° C)
Supply Current	12 mA max
Supply Voltage	35 VDC max (using voltage divider circuit)
Resolution	infinite signal
Operating Temperature	−85° to +257° F (−65° to +125° C)
Temperature Coefficient	±400 ppm/°C max

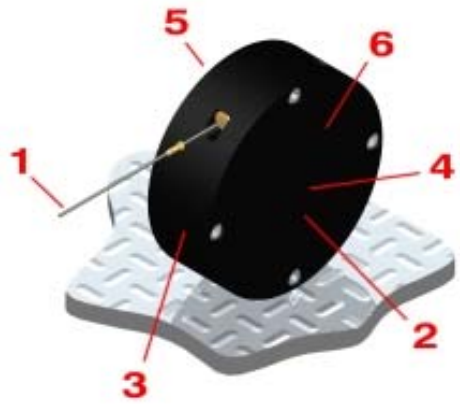

Figure 123**:** The String Potentiometer.

C.4 Sensors and IMU Data Integration

The software collects the data from the sensors, including the IMU. The data are saved in the computer and fed to the estimator. The analog output signal of each of the sensors (typically, rate gyros, accelerometers and displacement sensors) is fed into a separate configurable analog signal conditioning circuit. The conditioning circuit is inside an enclosure that may also contain additional pluralities of analog sensors "internal sensors" such as rate gyros, accelerometers and temperature sensors. The output of the each filter circuit is fed into an analog multiplexer, which is then fed to an analog-to-digital converter. The analog-to-digital converter is controlled by a processor that includes a software algorithm for additional sensor analysis as well as control of the various components within the configurable sensor.

The configurable analog signal-conditioning circuit consists of a variable gain amplifier circuit and a variable bandwidth filter. The variable gain amplifier circuit can be controlled by the processor to change the bias of the analog sensors as well as to change the gain of the sensor signal. The modified sensor signal is sent to the variable bandwidth filter. The bandwidth filter is controlled by the processor, and applies a desired low pass filter to the modified sensor signal, with a turning point selected by the processor. The filtered sensor signal is fed to a multiplexer. An embedded program in the processor configures the analog signal conditionings based upon values stored in the memory. The processor in each configurable sensor is either a microcontroller or a Digital Signal Processor (DSP). The processor controls the analog-to-digital converter, configurable filter circuit, memory, and communications interface. The

analog-to-digital converter samples each available filtered sensor signal. The memory can include both flash memory and RAM. The communications interface can include both wired and wireless communications mechanisms.

Additionally there is a power regulation circuit. The digital filtered sensor signals are analyzed by a program on the processor that can be customized for each sensor signal. The program includes a bank of configurable digital filters, observers, RMS levels calculators, peak-to-peak level calculators, and other key measures that may vary depending on the application or required criteria. The main unit can be configured to save sensor data in memory and record the time of the event, and can drive a digital-to-analog converter whose value can be read outside of the configurable sensor by a more powerful computer for further analysis and decision making. The storing of sensor data in the memory is automatic and accomplished in a method that respects the limited resources available with regard to both memory and processor resources. The sensor stores all the sensor data in a cache within the RAM so that a configurable period of the most recent sensor data is always available.

Also, the sensor is capable of operating together with other similar sensors on a shared data bus consisting either of a wired connection or a wireless connection. Since each sensor has an individual serial programmed into the memory, the sensors can be individually configured from a computer acting as the bus master. The master computer can collect the data from the sensors on the bus either in real time or by transferring data stored in the sensor memory cache. The sensors on the bus can be configured as a group and can operate in a real-time data collection mode where a few sensors send back data in pseudo real time. Individual sensors will return the contents of their cache to the master computer, reducing the communications' overhead.

Bibliography

[1] Hrovat, D., 1997, "Survey of advanced suspension developments and related optimal control applications," Automatica, vol. 33(10), pp.1781-1787.

[2] Yue, C., Busten, T., and Hedrick, J. K., 1989, "Alternative control for automotive active suspensions," ASME journal of Dynamic Systems, Measurements, and Control, vol. 111, pp. 286-290.

[3] Esmailzadeh, E., Bateni, H., 1992, "Optimal active suspensions with full state feedback control," SAE Transactions, Journal of Commercial Vehicles, vol. 101, pp.784-79.

[4] Esmailzadeh, E., Taghirad, H. D., 1996, "Active vehicle suspensions with optimal state-feedback control," SAE Transactions, Journal of Commercial Vehicles, International Journal of Mechanical Science, vol. 18, pp. 228-238.

[5] Thompson, A. G., 1976, "An active suspension with optimal linear state feedback," Vehicle System Dynamics, vol. 11, pp.187-203.

[6] Yu, F. and Crolla, D. A., 1989, "Optimal self-tuning controller for an active suspension," Vehicle System Dynamics, vol. 29, pp.51-65.

[7] Son, S. and Isik, C., 1996, "Application of Fuzzy logic to an automotive active suspension system," In proceedings of the Fifth IEEE International Conference on Fuzzy Systems, vol. 1, 8 -11, pp. 548 -553.

[8] Esmailzadeh, E. and Bateni, H., 1992, "Active vehicle suspensions with adaptive preview control," In Proceeding of the International Symposium on Robotics and Manufacturing, Santa Fe, New Mexico, USA.

[9] JR-EAST: Press Release

[10] Crosby, M.J. and Karnopp, D.C., 1973, "The active damper- a new concept for shock and vibration control," Shock and Vibration Bulletin, vol. 43.

[11] Karnopp, D. C., Crosby, M. J. and Harwood, R. A., 1974, "Vibration control using semi-active force generators," ASME Journal Eng. Ind., vol. 96, No. 2, pp 619-626.

[12] Besinger, F. H., Cebon, D., and Cole, D. J., 1995, "Force control of a semi-active damper," Vehicle System Dynamic, vol. 24, pp. 695-723.

[13] Novak, M., and Valasek, M., 1996, "A new concept of semi-active control of trucks suspension," In proceeding of AVEC 96, International Symposium on Advanced vehicle Control, Aachen University of Technology, pp.141-151.

[14] Hong, K. S., Sohn, H. C., and, Hedrick, J. K., 2002, "Modified skyhook control of semi-active suspensions: A New Model, Gain scheduling, and Hardware in the Loop Tuning," ASME Journal, vol. 124, pp 158-167.

[15] Cheok, K. C., Loh, N. K., and McGee, H. D., 1984, "Optimal suspension design with microcomputerized parameter optimizing damping,"

[16] Yokoyama, M., Hedrick, J.K., and Toyama, 2001, "A model following sliding mode controller for semi-active suspension systems with MR dampers," In proceedings of the American Control Conference, vol. 4, pp. 2652-2657.

[17] Lai, C. Y., and Liao, W. H., 2002, "Vibration control of a suspension system via a magnetorheological fluid damper," Journal of Vibration and Control, vol. 8, pp. 527-547.

[18] Rassem, R. H., 1995, A nonlinear, near optimal, observer-based control for semi-active suspension, PhD thesis, Wayne State University.

[19] Gg Liao, W. H. and Wang, D. H., 2003, "Semi-Active vibration control of train Suspension systems via magnetorheological dampers," Journal of Intelligent Material Systems and Structures, vol. 14 (3), pp.161-172.

[20] Kim, K., and Joen, D., 1999, "Vibration suppression in an MR fluid damper suspension system," Journal of Intelligent Material Systems and Structures, vol. 10, pp.779-786.

[21] Narimani, A., Jazar, N.G., and Golnaraghi, M.F., 2004, "Sensitivity analysis of the frequency response of a piecewise linear system in a frequency island," Journal of Vibration and Control, vol. 10, pp. 175-198.

[22] Rakheja, S., and Sankar, S., 1985, "Vibration and shock isolation performance of a semi-active 'on-off' damper," Journal of Vibration, Acoustics, Stress, and Reliability in Design, vol. 107(4), pp. 398-403.

[23] Mc Manus, S. J., ST. Clair, K. A., Boileau, P.E., Boutin, J., and Rakheja, S., "Evaluation of vibration and shock attenuation performance of a suspension seat with a semi-active magnetorehological fluid," Journal of Sound and Vibration, vol. 235(1), pp. 313-327.

[24] Al-Holou, N., Joo, D. S., and Shaout, A., 1996, "The development of Fuzzy logic based controller for semi-Active suspension systems," In proceeding of the 37th Midwest Symposium on Circuits and Systems, IEEE, pp. 1373-1376.

[25] Hashiyama, T., Furuhashi, T., and Uchikawa, Y., 1995, "Design of Fuzzy controllers for semi-active suspension generated through the genetic algorithm," In proceedings of Artificial Neural Networks and Expert Systems, IEEE, pp. 166 – 169.

[26] Ahmadian, M., Song, X., and Southward, S. C., 2004, "No-Jerk skyhook control methods for semi-active suspensions," ASME Journal of Vibration and Acoustics, vol. 126, pp.580-584.

[27] Savaresi, S. M., Silani, E., and Bittanti, S., 2005, "Acceleration-Driven-Damper (ADD): An optimal control algorithm for comfort-oriented semi-active suspensions," ASME Journal of Dynamic Systems, Measurement, and Control, vol. 127, pp. 218-229.

[28] Shen, Y., 2005, Vehicle Suspension Control with Magnetorheological Dampers. PhD thesis, University of Waterloo.

[29] Irmscher, S., and Hees, E., 1966, "Experience in Semi-active Damping with State Estimators," In proceeding of AVEC 96, International Symposium on Advanced Vehicle Control, Aachen University of Technology, pp. 193-206.

[30] YI, K., and Song, B. S., 1999, "Observer design for semi-Active suspension control," Vehicle System Dynamics, vol. 32, pp.129-148.

[31] Taghirad, H., and Esmailzade, E., 1997, "Automotive passenger comfort assured through LQG/LQR active suspension," Journal of Vibration and Control.

[32] Roh, H. S., and Park, Y., 1999, "Stochastic Optimal Preview Control an Active Vehicle suspension," Journal of Sound and Vibration, vol. 220(2), pp. 313-330.

[33] Lu, J. and DePoyster, M., 2002, "Multi-objective Optimal Suspension Control to Achieve Integrated Ride and Handling Performance," IEEE Transaction on Control, systems Technology, vol. 10(6).

[34] Donahue, M. D., and Hedrick, J. K., 2001, "Implementation of an Active Suspension, Preview Controller for Improved Ride Comfort,"

[35] Sayers, M. W., and Karamihas, S. M., 1998. The Little Book of Profiling; Basic Information about Measuring and Interpreting Road Profiles.

[36] Spangler, E. B., and Kelly, W. G., 1994, "Development and evaluation of the ride number concept," Vehicle-Road Interaction, ASTM STP 1225, pp 135-149.

[37] Gillespie, T. D., et al, 1980. Calibration of Response-type Road Roughness Measuring Systems. National Cooperative Highway Research Program report 228.

[38] "ZF Sachs goes mainstream with active damping," Automotive Engineering International Online: Tech Briefs, available: http://www.sae.org/automag/techbriefs/06-2004/.

[39] Fleming, W. J., 2001, "Overview of automotive sensors," IEEE Sensors Journal. vol. 1(4).

[40] Enstedt, B., 2003. Vehicle Performance Measurement Using Inertial Navigation. Royal Institute of Technology, Department of Signals, Sensors and Systems.

[41] Gelb, A., Kasper, J. F., Nash, R. A., Price, C. F., and Sutherland, A. A., 1979. Applied Optimal Estimation.

[42] Simon, D. 2006. Optimal State Estimation. John Wiley & Sons Inc. Publication.

[43] Kalman, R. E., 1960, "A new approach to linear filtering and prediction problems," Journal of Basic Engineering, pp. 35-46.

[44] Kalman, R. E., and Bucy, R. S., 1961, "New results in linear filtering and prediction Theory," Journal of Basic Engineering, pp. 95-108.

[45] Jazwinski, A. H., 1970. Stochastic processes and Filtering Theory. Academic Press.

[46] Chui, C. K., and Chen, G., 1999. Kalman Filtering with Real-time Applications. Third Edition, Springer Series in Information Sciences.

[47] Zarchan, P., and Musoff, H., 2005. Fundamentals of Kalman Filtering: A Practical Approach. Second Edition. Volume 208 Progress in Astronautics and Aeronautics.

[48] Titterton, D. H., and Weston, J. L., 2004. Strapdown Inertial Navigation Technology. Second Edition. Volume 207 Progress in Astronautics and Aeronautics.

[49] Grewal, M. S., and Andrews, A. P., 2004. Kalman Filtering: Theory and Practice. Prentice Hall.

[50] Ogata, K. 2002. Modern Control Engineering, Fourth Edition. Prentice Hall.

[51] Franklin, G. F., Powell, J. D., and Workman, M., 1998. Digital Control of Dynamic Systems. Third Edition. ADDISON WESLEY.

[52] Farrel, P. 2003. GPS/INS Integration.

[53] Julier, S., and Uhlmann, J. K., 2004, "Unscented filtering and nonlinear estimation," In proceeding of the IEEE, vol. 92, No. 3.

[54] Rictic, B., Arulampalan, S., and Gordon, N., 2004. Beyond the Kalman Filter: Particle Filters for Tracking Applications, Artech House Publishers.

[55] Arulampalam, M. S., Maskell, S., Gordon, N., and Calpp, T., 2002, "A tutorial on particle filters for online nonlinear/non-Gaussian Bayesian tracking," IEEE Transactions on Signal Processing, vol. 50, No. 2, pp. 174-188.

[56] Ho. Y., and Pepyne, D., 1964, "A Bayesian approach to problems in stochastic estimation and control," IEEE Transactions on Automatic Control, vol. AC-9, pp. 333-339.

[57] VTS40, A Permanent Magnet Shaker, available: http://www.dynsolusa.com/edshakers.htm

[58] LDS Tests and Measurements, available: http://www.lds-group.com/home.php#.

[59] Bolandhemmat, H., Clark, C., and Golnaraghi, M. F., 2006, "A distributed sensing system for vehicles states estimation," In proceedings of IMECE2006-16063. 2006 ASME International Mechanical Engineering Congress and Exposition. Chicago, Illinois, USA.

[60] Alasty, A., Ramezani, A., 2002, "Application of extended Kalman filter in simultaneous state and parameter estimation of a nonlinear full ride model", In Proceeding of the IASTED International Conference on Modelling, Identification, and Control (MIC'02), Innsbruck, Austria.

[61] Siegwart, R., and Nourbakhsh, I., 2004. Introduction to Autonomous Mobile Robots. MIT Press.

[62] Papoulis, A., and Pillai, S., 2002. Probability, Random Variables, and Stochastic Processes. McGraw-Hill, New York.

[63] Bhattacharyya, S. P., 1978, "Observer design for linear systems with unknown inputs," IEEE Transactions on Automatic Control, vol. AC-23, pp. 483-484.

[64] Bhattacharyya, S. P., 1980, "Parameter invariant observers," IEEE Transactions on Automatic Control, vol. AC-32, pp. 1127-1132.

[65] Hac, A., 1992, "Design of disturbance decoupled observer for bilinear systems," Journal of Dynamic Systems, Measurements and Control, vol. 114, pp. 556-562.

[66] Funahashi, Y., 1979, "An observable canonical form of discrete time bilinear systems," IEEE Transactions on Automatic Control, vol. AC-24, No. 5, pp. 802-803.

[67] Ali, H. S., Rafaralahy, H., Zasadzinski, M., Halabi, S., Darouach, M., 2005, "Observer design for a class of stochastic bilinear systems with multiplicative noise," American Control Conference, June 8-10, Portland, OR, USA.

[68] Cumming, S. D. G., 1969, "Design of observers of reduced dynamics," Electronic Letters, vol. 5, No. 10, pp. 213-214.

[69] Wang, S., Davison, E. J., and Dorato, P., 1975, "Observing the states of systems with unmeasurable disturbances," IEEE Transactions on Automatic Control, vol. AC-20, pp. 716-717.

[70] Hostetter, G., and Meditch, J. S., 1973, "Observing systems with unmeasurable inputs," IEEE Transactions on Automatic Control, vol. AC-18, pp. 307-308.

[71] Luenberger, D. G., 1966, "Observers for multivariable systems," IEEE Transactions on Automatic Control, vol. AC-11, pp. 190-197.

[72] Gopinath, B., 1971, "On the control of linear multiple input-output systems," Bell Systems Technology Journal.

[73] Pringler, R. M., and Rayner, A. A., 1971. Generalized Inverse Matrices. London, England: Griffin.

[74] Kudva, P., Viswanadham, N., and Ramakrishna, A., 1980, "Observers for linear systems with unknown inputs" IEEE Transactions on Automatic Control, vol. AC-25, pp. 113-115.

[75] Hou, M., and Muller, P. C., 1992, "Design of observers for linear systems with unknown inputs" IEEE Transactions on Automatic Control, vol. 37, pp. 871-874.

[76] Analog Devices, Inc. http://www.analog.com.

[77] Wabash Technologies. http://www.wabashtech.com.

[78] Mechworks Systems Inc. http://www.mechworkssys.com

[79] Delphi Corporation. http://www.delphi.com

[80] Delphi Corporation. The Delphi MagneRide™ MR shock absorber, available: http://www.delphi.com

[81] Analog Devices Specification Manual for ADXL202E Accelerometer and ADXRS401 Single Chip Rate Gyro, 2000, available: http://www.analog.com

[82] MechSense™ MD S 202 –U Accelerometer and MechTrack™ IMU data sheet, available: http://www.mechworkssys.com.

[83] Delphi Non-Contact Rotary Position Sensor Data Sheet, available: http://www.wabashtech.com.

[84] Koo, J. H., Goncalves, F. D., and Ahmadian, M. 2002, "Investigation of the response time of Magnetorheological fluid dampers,"

[85] Goncalves, F. D., Koo, J. H., and Ahmadian, M., 2003, "Experimental approach for finding the response time of MR dampers for vehicle applications," DETC 2003 19th Biennial Conference on Mechanical Vibration and noise. Chicago, IL, USA.

[86] Sharma, K., Crolla, D. A., and Wilson, D. A., 1994, "The design of a fully active suspension system incorporating a Kalman filter for state estimation," Conference Publication N0. 389, IEE.

[87] Liu, Y., Gordaninejad, F., Evrensel, C., Karakas, S., Dogruer, U., 2004, "Experimental study on Fuzzy Skyhook control of a vehicle suspension system using a Magneto-rheological fluid damper," Smart Structure and Material: Industrial and Commercial Applications of Smart Structure Technologies, in proceeding of SPIE, vol. 5388, pp. 338-347.

[88] Ahmadian, M., Goncalves, F. D., and Sandu C., 2005, "An experimental analysis of suitability of various semi-active control methods for Magneto-rheological vehicle suspensions," Smart Structure and Material: Industrial and Commercial Applications of Smart Structure Technologies, in proceeding of SPIE, vol. 5760, pp. 208-222.

[89] Ahmadian, M., 2005, "On the development of a Fuzzy Skyhook control for semi-active Magneto-rheological systems," Smart Structure and Material: Damping and Isolation, in proceeding of SPIE, vol. 5760, pp. 268-282.

[90] Lieh, J., and Li, W. J., 2004, "Adaptive Fuzzy control of vehicle semi-active suspension control," ASME J. of Dynamic Systems, Measurement and Control, vol. 61, pp.293-297.

[91] Ivers, D. E., and Miller, L. R., 2002, "Experimental comparison of passive, semi-active on/off, and semi-active continuous suspensions," SAE Technical Paper series no. 892484.

[92] Sammier, D., Sename, O. and Dugard, L., 2003, "Skyhook and H_∞ of semi-active suspensions: Some practical aspects," Vehicle System Dynamics, vol. 39, no. 4, pp.279-308.

[93] Wang, L. X., 1997. A Course in Fuzzy Systems and Control. Second Edition, Prentice Hall.

[94] Zadeh, L. A., 1973, "Outline of a new approach to the analysis of complex systems and decision processes," IEEE Transaction on Systems, Man and Cybernetics, vol. 3, pp. 28-44.

[95] Khalil, H. K., 2002. Nonlinear Systems. Third Edition, Prentice Hall.

[96] Vidyasagar, M., 1980, “On estimation of nonlinear systems using state detection,” IEEE Transaction on Automatic Control, vol. 25, pp. 504-510.

[97] SRX Standard and Optional Features, available: http://gmcanada.com.